Lehrstuhl für Steuerungs- und Regelungstechnik
Technische Universität München
Univ.-Prof. Dr.-Ing. (Univ. Tokio) Martin Buss

Advances in System Identification, Neuromuscular Modeling and Repetitive Peripheral Magnetic Stimulation

Michael Bernhardt

Vollständiger Abdruck der von der Fakultät für Elektrotechnik und Informationstechnik der Technischen Universität München zur Erlangung des akademischen Grades eines

Doktor-Ingenieurs (Dr.-Ing.)

genehmigten Dissertation.

Vorsitzender:	Univ.-Prof. Dr.-Ing. Thomas Eibert

Prüfer der Dissertation:

1. Univ.-Prof. Dr.-Ing. (Univ. Tokio) Martin Buss
2. Univ.-Prof. Dr.-Ing. Dr.-Ing. h.c. Dierk Schröder, i.R.

Die Dissertation wurde am 19.01.2009 bei der Technischen Universität München eingereicht und durch die Fakultät für Elektrotechnik und Informationstechnik am 17.07.2009 angenommen.

Foreword

This thesis is the result of almost four years of research done at the Institute of Automatic Control Engineering and within the Research Group for Sensorimotor Integration, both at the Technische Universität München. The research was funded in part by the DFG (German Research Foundation) within the project "Induction of adaptively controlled compound movements of arm and fingers by multichannel repetitive peripheral magnetic stimulation (*RPMS*) – early rehabilitation of central paresis". This work would not have been possible without the help of many different persons to which I would like to express my gratitude.

First of all, I thank my doctoral advisers Professor Martin Buss and Professor Albrecht Struppler. Martin Buss provided an excellent environment for open-minded and interdisciplinary research and had always complete confidence in me. Professor Struppler is an extraordinary researcher and man who gave me scientific and personal advice whenever I needed it.

My work was supported by many highly motivated student assistants or bachelor/master students: Bastian Buchholz, Cornelius Buchkremer, Dennis Dumke, Michael Eibl, Andreas Gasser, Daniel Gurdan, Qichen Huang, Yang Ji, Sebastian Kibler, Inga Krause, Yuanyuan Li, Adrian Lindner, Daniel Meißner, Nik Neusser, Bastian Schmitz, Thomas Spittler, and Lena Springer. Thank you for your contribution.

During my graduate studies at TUM and during my stay at the Swiss Federal Institute of Technology Zurich I collaborated with Professor Robert Riener and Dr. Martin Frey who were my scientific mentors at that time and whom I thank for teaching me so much.

I would like to thank Professor Shohreh Amini and my colleagues Martin Kuschel and Chih-Chung Chen for proofreading the thesis. Furthermore I thank my collaborators in the Research Group for Sensorimotor Integration Barbara Gebhard and Bernhard Angerer for helping me with many practical issues, for giving scientific advice and for encouraging me as friends. I am also indebted to all my colleagues at the Institute of Automatic Control Engineering and particularly to my office mates Georgios Lidoris, Moritz Große-Wentrup and Johannes Dold who provided a really joyful atmosphere and helped me with many smaller and bigger problems.

Finally I want to express my deep gratitude to my parents, my fiancée Mehrnoush and my sister Eva for their strong affection and constant support. Mehrnoush completes my life with joy and diversion.

Munich, January 2009 Michael Bernhardt

Contents

Notations

Abbreviations

APRB	Amplitude modulated pseudo random binary
ATP	Adenosine triphosphate
CNS	Central nervous system
DIP	Distal interphalangeal
DOF	Degree of freedom
EDC	Extensor digitorum communis
EIP	Extensor indices proprius
EM	Error model
EMG	Electromyography
EvMA	Estimation of voluntary muscle activity
FDP	Flexor digitorum profundus
FDS	Flexor digitorum superficialis
GN	Gauss-Newton
GS	Gradient search
ITAE	Integral time multiplied absolute error
LM	Levenberg-Marquardt
LMS	Least mean squares
LP	Linearly parameterized
l.p.e.	Linear persistent excitation/linearly persistently exciting
l.o.l.	Location of lesion
LTI	Linear time invariant
LAP	Linear adaptive prediction
m.	Musculus
MA	Moving average
MAP	Muscle action potential
MCP	Metacarpophalangeal
MIL	Matrix inversion lemma
MLP	Multi layer perceptron
MU	Motor unit
MVC	Maximum voluntary contraction
NARX	Nonlinear autoregressive with exogenous input
NFIR	Nonlinear finite impulse response
NLP	Nonlinearly parameterized
NMSE	Normalized mean square error

NRBF	Normalized radial basis function
n.l.p.e.	Nonlinear local persistent excitation
PCA	Principle component analysis
PID	Proportional-integral-derivative
PIP	Proximal interphalangeal
PSD	Power spectral density
RBF	Radial basis function
RLS	Recursive least squares
RMS	Root mean square
SNLP	Separable nonlinearly parameterized
t.s.l.	Time since lesion
wRMS	Weighted RMS
WSS	Wide sense stationary
ZDVC	Zero degree voluntary contraction

Conventions

Scalars, Vectors, and Matrices

Scalars are denoted by upper and lower case letters in italic type. *Vectors* are denoted by underlined lower case letters in italic type, as the vector $\underline{x}$ is composed of elements x_i. *Matrices* are denoted by underlined upper case letters in italic type, as the matrix $\underline{M}$ is composed of elements M_{ij} (i^{th} row, j^{th} column).

x or X	Scalar
$\underline{x}$	Vector
$\underline{X}$	Matrix
$\underline{X}^T$	Transposed of $\underline{X}$
$\underline{X}^{-1}$	Inverse of $\underline{X}$
$\underline{X}^+$	Pseudoinverse of $\underline{X}$
$f(\cdot)$	Scalar function
$\underline{f}(\cdot)$	Vector function
$\hat{x}$	Estimated or predicted value of x
$\tilde{x}$	Estimation error: $\tilde{x} = x - \hat{x}$
$\overline{x}$	Average value of x
$\|\cdot\|_p$	p-norm
$\nabla f(\underline{x}) = \frac{\partial f(\underline{x})}{\partial \underline{x}}$	Gradient vector

Symbols

General

$\underline{A}_w$	System matrix of the LTI-system $\mathcal{W}$
$\underline{b}_w$	Input vector of the LTI-system $\mathcal{W}$
$\underline{c}_w$	Output vector of the LTI-system $\mathcal{W}$
f_k	Discrete frequency variable
f_{rep}	Repetition rate of *RPMS*
f_s	Sampling rate
$G_w(s)$	Transfer function of the LTI-system $\mathcal{W}$
$G_{w,obs}(s)$	Transfer function of the Luenberger observer of the LTI-system $\mathcal{W}$
$\underline{I}$	Unity matrix
I_c	95 % confidence interval
j	Discrete time variable occurring in discrete integrals
k	Discrete time variable
k_{rep}	Discrete repetition period of *RPMS*
N	Some discrete time period
t	Time
T	A certain time period
T_1	Time constant of a PT_1-system
T_p	Pulse width of *RPMS*
T_s	Sampling time, $T_s = 0.001\,\mathrm{s}$ throughout the thesis
T_{set}	Settling time of a dynamic system
T_{sys}	System time constant of a desired polynomial
u	Input of an single input system
$\underline{v}$	Input vector of a multiple input system
$\underline{w}$	Unit vector
$\mathcal{W}$	SISO LTI-system with $\underline{A}_w$, $\underline{b}_w$, $\underline{c}_w^T$
$\mathcal{W}_{obs}$	LTI-system constituted by a Luenberger observer
$\underline{x}$	State of a dynamic system
y	System output
$\delta(k)$	Discrete Dirac Delta function
σ	Standard deviation

System Identification

$A_j(u)$	Activation function of an NRBF-network
e	Output error
e_n	Output error of the nonlinear subsystem $n(\cdot)$
e_e	Augmented error
e_{obs}	Observer error
$\underline{f}^{\hat{\theta}}$	Update term of the SLS-algorithm
$E(\cdot)$	Error criterion

g	Gain ratio of modified LM-algorithm
$\underline{g}(\cdot)$	Nonlinear function that defines the adaptive law
$\underline{h}$	Truncated impulse response
$\underline{H}$	Hessian matrix
I	Integral
$k_{d,c}$	Discrete delay time of hardware and physiological delay
k_h	Discrete time horizon of exponential forgetting
k_h	Discrete hold time of an APRB-signal
$\underline{l}$	Gain vector of a Luenberger Observer
$L(\cdot)$	Model of the error criterion $E(\cdot)$
m	Number of linear parameters
m_r	Number of orthonormal basis functions
m_{N1}	Number of radial basis functions of the nonlinearity $\hat{N}_1(\alpha)$
m_{N2}	Number of radial basis functions of the nonlinearity $\hat{N}_2(\dot{\alpha})$
$n(\cdot)$	Nonlinear Subsystem
p	Total number of parameters
$\underline{P}$	Symmetric positive definite matrix
q	Number of nonlinear parameters
r_a	Actual reduction of the error criterion
r_p	Predicted reduction of the error criterion
$\underline{Q}$	Symmetric positive definite matrix
$\underline{r}_i$	Orthonormal basis function
$\underline{R}$	Matrix of orthonormal basis functions
$\underline{R}$	Direction matrix of the LM-algorithm (damped Hessian)
s_r	Condition ratio of the modified LM-algorithm
S_i	Singular Values of the direction matrix $\underline{R}$
$T_{d,c}$	Complete delay consisting of hardware delay and physiological delay
T_h	Time horizon of exponential forgetting
T_h	Hold time of an APRB-signal
$V(\cdot)$	Lyapunov candidate
y_n	Output of a nonlinear subsystem
z	Measurement noise
β	Threshold value of the LM-algorithm
γ	Estimator gain
$\gamma_{\hat{\eta}}$	Estimator gain for nonlinear parameters (SLS-algorithm)
$\gamma_{\hat{\theta}}$	Estimator gain for linear parameters (SLS-algorithm)
δ	Damping factor of the LM-algorithm
δ_s	Damping factor of the modified LM-algorithm
ϵ	Output error of the SLS-algorithm
ϵ_{obs}	Observer error in EM C2
η	Nonlinear system parameter
θ	Linear system parameter
κ	Gain factor of the LM-algorithm
λ	Forgetting factor of exponential forgetting

ν	Threshold value of the modified LM-algorithm
ξ	General system parameter
$\Delta\xi$	Distance between two activation functions
$\underline{\Pi}$	Covariance matrix of the RLS-algorithm
$\overline{\sigma}$	Normalized smoothing parameter of an NRBF-network
τ	Time variable occurring in integrals
$\underline{\varphi}$	Input regressor
$\underline{\varphi}_f$	Filtered input regressor
$\underline{\Phi}$	Matrix of input regressors
$\underline{\chi}$	State of an LTI-system
$\underline{\psi}$	Gradient vector

Neuromuscular and Biomechanical Modeling

d_s	Specific density
D_{rel}	Damping constant of the relaxation model
E_{rel}	Elasticity constant of the relaxation model
f_l	Scaling of the force-length-curve
f_v	Scaling of the force-velocity-curve
F_M	Muscle force
F_s	Sensor force
$G_a(s)$	Transfer function of the muscle twitch model
$G_e(s)$	Transfer function of the temporal summation model
h	Tendon leverage
$I(k)$	Stimulation intensity
I_{sat}	Saturation intensity of the recruitment model
I_{thr}	Threshold intensity of the recruitment model
J	Moment of inertia
l	Tendon length
L_i	Length of the i$^{\text{th}}$ finger phalanx
m_i	Mass of the i$^{\text{th}}$ finger phalanx
$N_1(\alpha)$	Static nonlinearity of the segment dynamics
$N_2(\dot{\alpha})$	Static nonlinearity of the segment dynamics
r	Radius of the MCP-joint
R_i	Radius of the i$^{\text{th}}$ finger phalanx
$s(\alpha, \dot{\alpha})$	Spastic joint torque
$s_t(\alpha)$	Tonic component of the spastic joint torque
$s_{ph}(\dot{\alpha})$	Phasic component of the spastic joint torque
T_a	Time constant of the muscle twitch model
T_e	Time constant of the temporal summation model
$T_{d,hw}$	Hardware delay
$T_{d,ph}$	Physiological delay
T_{rel}	Time constant of the relaxation model
$u(k)$	Input of the plant "*RPMS*-stimulated muscle"
α_i	Angle of the i$^{\text{th}}$ joint

α_{sat}	Curvature parameter of the recruitment model
α_{thr}	Curvature parameter of the recruitment model
β_1, β_2	Gain and offset parameters of the recruitment model
γ_p	Pennation angle
$\rho(\cdot)$	Function of motor unit recruitment
τ_{ep}	Elastic joint torque of a muscle-tendon unit
τ_f	Friction torque
τ_g	Gravitational torque
τ_i	Torque of the i$^{\text{th}}$ joint
τ_n	Net joint torque
τ_{me}	Sensor Torque of the Fingertester
τ_M	Muscle torque
τ_{rel}	Torque of relaxation characteristics
τ_{vm}	Torque of viscous muscle-tendon properties

Applications

$a(k)$	Measure for the voluntary muscle activity
a_i	EMG-amplitude
b_j	Coefficient of the LAP-filter
$c(k)$	Raw EMG-signal
d_t	Relative difference of the tonic spasticity component evaluation
d_{ph}	Relative difference of the phasic spasticity component evaluation
K_a	Gain of the adaptive trajectory generation
K_{RMS}	Length of the RMS-filter
$s(k)$	EMG-signal inside the EvMA-cascade
S_1, S_2	Muting periods of the EMG-amplifier
w	Input of a system with state feedback
y_d	Desired output of a controlled system
$\underline{\Gamma}$	Eigenvector matrix
ι	Additive noise term
$\underline{\kappa}$	State feedback vector
κ_I	Gain of the integral controller
λ_i	Eigenvalues of the covariance matrix
$\underline{\Lambda}$	Diagonal matrix of eigenvalues
ν	Virtual system input
$\underline{\Xi}$	Transformation matrix of PCA
χ_I	State variable of the integral controller
υ	Weighting factor of the wRMS-filter
$\underline{\Psi}$	Covariance matrix
ω_0	Characteristic frequency of an ITAE-polynomial

Abstract

In this thesis, novel methods of nonlinear system identification and new approaches in physiological modeling and rehabilitation engineering are presented. Thereby, a contribution to the advancement of the repetitive peripheral magnetic stimulation (*RPMS*) is made. The *RPMS* is an innovative approach in rehabilitation of sensorimotor deficits like paresis and spasticity, e.g. after stroke. The key issues of the current *RPMS*-research are the further analysis of the underlying therapeutic mechanisms and the optimization of the proprioceptive afferent input patterns by inducing functional synergistic-antagonistic movements in the arm, hand and fingers.

First of all, new methods for parameter identification in the presence of linear, nonlinear and separable nonlinear parameterization are introduced. Conditions for parameter convergence are developed using a stability framework from nonlinear dynamic system theory. The proposed theoretic framework is generic and can be applied to a variety of problems. Here, it is used to identify the plant of the *RPMS*-induced index finger extension and flexion. For this purpose, an adequate biomechanical and neurophysiological model is developed that includes the *RPMS*-induced force generation, the segment dynamics, the dynamic relaxation effect as well as a simplified model of the spastic joint torque. This approach yields the basis for three applications that contribute to the above mentioned key issues: System identification-based therapy assessment and monitoring, dual channel position controlled *RPMS* and EMG-driven position control.

Zusammenfassung

In der vorliegenden Arbeit werden neue Methoden der nichtlinearen Systemidentifikation und neue Ansätze der physiologischen Modellbildung und des Rehabilitation Engineering vorgestellt. Hierdurch wird auch ein Beitrag zur Weiterentwicklung der repetititiven peripheren Magnetstimulation (*RPMS*) geleistet. Die *RPMS* ist eine innovative Methode zur Rehabilitation sensomotorischer Defizite wie Parese und Spastik infolge eines Schlaganfalls. Die Kernpunkte der aktuellen *RPMS*-Forschung sind die weitere Aufschlüsselung der therapeutischen Wirkungsmechanismen sowie die Optimierung des propriozeptiven Afferenzenmusters durch Induktion funktioneller synergistisch-antagonistischer Bewegungen in Arm, Hand und Fingern.

Es werden zunächst neue Methoden der Parameteridentifikation bei linearer, nichtlinearer und separierbarer nichtlinearer Parametrierung vorgestellt. Asymptotische Stabilität der vorgestellten Ansätze wird mit Hilfe von Methoden aus der Theorie nichtlinearer dynamischer Systeme bewiesen. Die vorgestellte Theorie ist generisch und kann somit bei einer Vielzahl praktischer Probleme zum Einsatz kommen. In dieser Arbeit wird sie zur Identifikation der Regelstrecke „*RPMS* induzierte Zeigefingerextension und -flexion“ eingesetzt. Hierfür wird ein biomechanisches und neuromuskuläres Modell entwickelt, das die *RPMS* induzierte Krafterzeugung, die Segmentdynamik, den dynamischen Relaxationseffekt sowie ein vereinfachtes Modell für das spastische Gelenkmoment umfasst. Der gewählte Gesamtansatz stellt die Grundlage für drei beispielhafte Anwendungen dar, die einen Beitrag zu den oben genannten Kernpunkten leisten: Therapieevaluierung und -monitoring basierend auf Systemidentifikation, zweikanalige positionsgeregelte *RPMS* und EMG-gesteuerte Positionsregelung.

1 Introduction

This chapter aims to introduce the reader to the research areas that are within the scope of this thesis: *Stroke rehabilitation*, *nonlinear system identification*, *physiological modeling* and *rehabilitation engineering*. This introduction does not provide a comprehensive overview of the related state of the art since this issue is covered at the beginning of each of the subsequent chapters.

1.1 Motivation

A *stroke* is a sudden, temporary insufficiency of the cerebral[1] blood supply that may be caused by thrombosis, embolism or a hemorrhage. As a consequence, the affected brain area can be irretrievably damaged, leading to sensorimotor deficits like *paresis* on one side of the body (*hemiparesis*), one-sided *spasticity*, deficits in speech, and one-sided visual dysfunctions. In Germany, each year approximately 150,000 people suffer a stroke [57] and this number is increasing. About 90 % of the stroke survivors suffer a persistent hemiparesis of the upper extremities, and in 30 %-40 % the paresis is so severe that the affected limb con no longer be used [65]. Particularly a paresis of the arm and hand impairs daily life activities and thus, the quality of life is reduced dramatically. This emphasizes the necessity of innovative techniques in rehabilitation of central paresis.

Cortical reorganization abilities[2] form the basis of *relearning the lost motor functions*. In order to activate a beneficial reorganization process, the lost *proprioceptive input* should be reactivated. Conventional physiotherapy aims to achieve such an activation through externally applied movements [160]. Thus, the sensors in muscles, tissue and skin are activated and send *proprioceptive information* to the *central nervous system* (CNS) which facilitates a relearning process. In order to assist the physiotherapists during these exercises, robots have been developed and applied for rehabilitation of lower and upper extremities (see e.g. [136; 161]). Apart from applying peripheral limb manipulation to a passive patient, physiotherapy tries to allow the patient to *actively participate* as far as possible. As an example, the "Constraint Induced Movement Therapy" (CIMT, [168; 169]) forces the patient to use his/her paretic arm and hand by strapping the other one. A similar goal is pursued with the development of *patient-cooperative rehabilitation robotics* [138; 139].

However, the muscles of those patients that do not have the ability of voluntary participation will not be activated during classical physiotherapy. In this case, muscle activation can be achieved by *artificial muscle stimulation* that represents a different approach of mo-

[1] Fundamental terms concerning the sensorimotor system and sensorimotor deficits are explained in Appendix B.

[2] The ability of the human brain to perform structural reorganization is called plasticity. The human brain remains plastic until old age.

tor rehabilitation. Aside from the well-known functional electrical stimulation (FES, [159]), there exists the repetitive peripheral magnetic stimulation (*RPMS*, [166]). With both methods terminal motor branches are depolarized by applying external electric fields so that the respective muscle contracts. Thus, adequate (indirect) efferent[3] signals by means of activation of mechanoreceptors as well as inadequate (direct) efferent signals by means of antidromic[4] conduction are elicited. Due to the combination of adequate and inadequate input to the CNS, the muscle stimulation therapy has a great potential to supplement the motor rehabilitation. A comprehensive review of the clinical uses of FES in the context of motor rehabilitation is presented in [159].

Though the FES activates somatosensory nerve fibers, a major drawback consists of the equal activation of cutaneous receptors. Apart from leading to pain, this may also result in an additional increase of spasticity. Hence, the use of FES for therapeutic purposes appears limited, see [28], e.g.. Contrary to FES, the *RPMS* is a deep penetrating, focused and painless stimulation method. Its application to stroke rehabilitation is developed within the Sensorimotor Research Group, Technische Universität München (TUM) under the responsibility of Professor em. Dr. med. Albrecht Struppler.

Numerous clinical experimental studies showed that the proprioceptive inflow induced by *RPMS* elicits conditioning effects on various levels of the sensorimotor and cognitive systems: *RPMS* can effectively suppress spasticity [166; 167], has a modulatory effect on the postural component of motor performances like the stabilization of the elbow joint in a relaxed state [165], and can improve higher (integrative) sensory functions like spatial cognition in patients [80; 81]. Also, recognition errors of different tactile stimuli can be clearly reduced after *RPMS* [63]. In [215], a PET H_2O^{15}-study showed an increase of activation of the parieto-premotor network following *RPMS*-treatment which indicates a significant conditioning effect of *RPMS* on the cortical level.

Stroke researchers agree that it is yet unclear which of the available methods and technologies are the best to be used, and that the answer to this question might differ from patient to patient (see e.g. [161]). They also agree that available methods often yield an unsatisfactory therapeutic outcome. Therefore, there is a strong demand for research on stroke rehabilitation. Due to the functional variety of open questions in this working field, research on rehabilitation is undertaken best in teamwork of neurologists, engineers and physiotherapists. This thesis has evolved in an interdisciplinary working environment provided by tight collaboration of the Institute of Automatic Control Engineering and the Sensorimotor Research Group, both at TUM. It was the goal of the presented work to develop and apply control engineering methods that will ultimately yield improvements of the *RPMS*-therapy. To this end, fundamental research in system identification in physiological modeling has been performed.

The discipline of *system identification* can be broken down into mathematical *modeling* and *parameter identification*. System identification represents an essential interface between control engineering and medicine. Models are a substitute for the original system and are used in the context of physical, biomedical, chemical or economical processes. A

[3] Afferent nerve signals propagate from receptors and sense organs toward the CNS, while efferent nerve signals propagate in opposite direction.

[4] An orthodromic impulse propagates along an axon in its normal direction, away from the soma. Antidromic impulses run in the direction opposite to normal.

good model accurately describes the system characteristics of interest, and hence, yields a comprehensive, convenient and inexpensive possibility to investigate the properties of the original system. In medical research, there are in general two applications for models: *Analysis* and *control*. In the analysis application, the model is often employed for simulations that aim to gain insight into the system, supplement diagnostics and to reduce the number experiments performed in human subjects. If the model is embedded into an on-line system identification procedure, it can be used for model-based patient monitoring. In the control application where the human is part of the plant, models can be used for controller design or they can even be embedded into the underlying control algorithm.

Models of physiological systems are often of *macroscopic character* since the underlying microscopic processes may be highly complex. It is therefore a challenging task to develop a model that is only as detailed as necessary to describe the dominant characteristics with sufficient accuracy. Further challenges in modeling physiological systems are *nonlinearities*, *time variant behavior* and *inter- and intrapersonal differences*. Hence, the model parameters have to be adapted to the respective subject once a mathematical formulation is found that qualitatively approximates the system.

Methods for parameter identification have been a field of research for several decades, now. A parameter identification method is required to *converge* to the *optimal parameter values* in a reasonable amount of time with a reasonable computational effort. It is the purpose of fundamental research on parameter identification to provide generic methods that have been formally proven to converge under well defined conditions. Thus, the user can apply *theoretically verified algorithms* which he/she can rely on. Another aim of fundamental research is to utilize theoretical insight into the underlying adaptive systems in order to formulate design rules that can be easily applied by the user. As will be explained in Chapter 2, mathematical models where the parameters occur nonlinearly can be treated much less generally than *linearly parameterized models*. In case of *nonlinear parameterization*, often a system-by-system investigation is necessary since there is no general theoretic framework. This becomes obvious if one remembers that the unimpressive term "nonlinear" really means "everything except linear", and thus covers a huge number of system classes. Since nonlinear parameterization is intrinsic to many plants there is still a strong demand for research on nonlinear parameter identification.

1.2 Contributions and Outline of this Thesis

To develop a *successful stroke rehabilitation*, the following components are required: Understanding of the underlying pathophysiological mechanisms, methods for *objective therapy assessment*, *optimization of the proprioceptive input patterns* and *incorporation of the patients' voluntary efforts* as far as possible. The central goal of this thesis is to provide methods and techniques that have the capability to contribute to all of the abovementioned components. Fig. 1.1 illustrates the integration of the proposed techniques into an *RPMS*-therapy environment. The development of the methods, models and exemplary applications presented in this thesis was inspired by the application framework illustrated in Fig. 1.1. However, it is also the goal of this thesis to present generic results that can also be applied to other problems. The parameter identification algorithms are derived as

general methods and thus can be applied to any arbitrary system identification problem that meets the respective mathematical constraints. Further the proposed neuromuscular and biomechanical models will be useful in different contexts and applications.

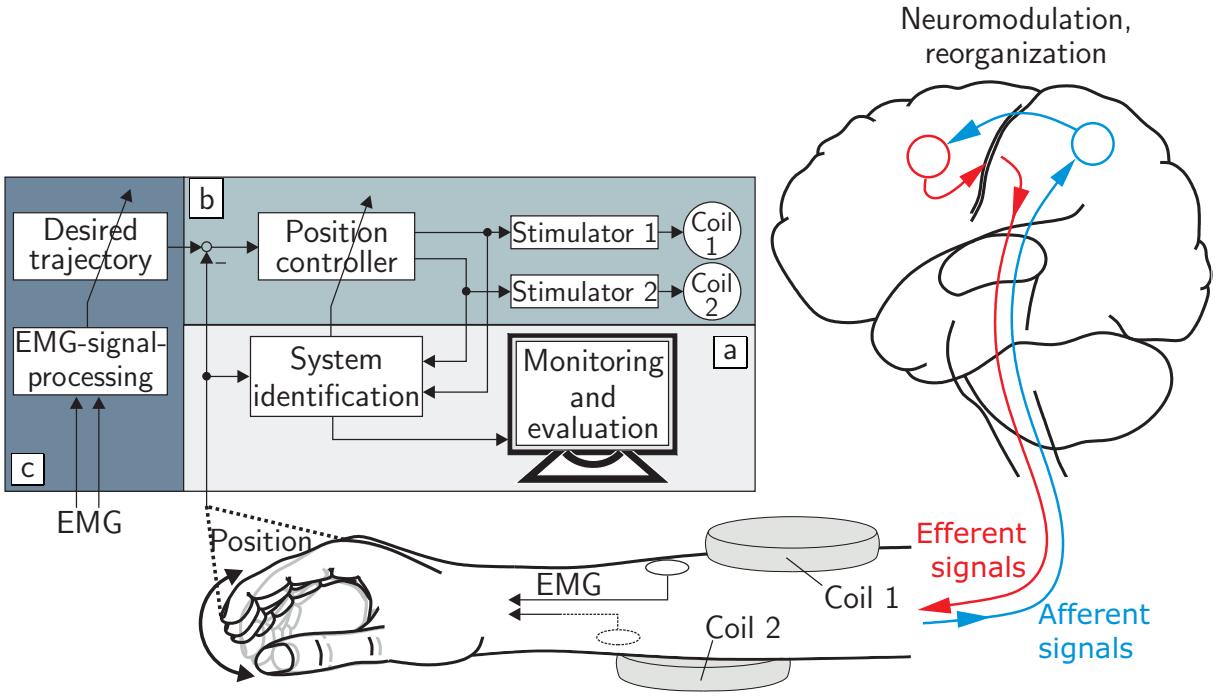

Fig. 1.1: Schematic of an integrated therapy environment: (a) Automated therapy monitoring and assessment by means of system identification. (b) Position controlled induction of functional movements using multiple stimulators. (c) Incorporation of the patient's effort using EMG-signal processing.

The following four paragraphs correspond to the Chapters 2-5 and summarize the main scientific contributions of each chapter:

Parameter Identification in the Presence of Linear, Nonlinear and Separable Nonlinear Parameterization

In Chapter 2, *parameter identification methods* are presented, that enhance the current methodical state of the art. As will be shown, it is an essential distinction whether the parameters occur linearly of nonlinearly in the model equation. Therefore, three different classes of parameterization are systematically treated. The focus is on plant configurations where an unknown subplant whose output is not directly measurable but filtered a known LTI-transfer function is to be identified. This structure occurs in many kinds of mechanical, electromechanical and biomechanical systems. The applied adaptive laws that govern the parameter convergence, are based on the *recursive least squares algorithm* and *gradient based methods* like the *Levenberg-Marquardt algorithm*. The parameter convergence of the adaptive systems is proved using stability concepts of nonlinear differential equations. Based on Lyapunov's theory, conditions are derived that guarantee asymptotic stability, i.e. convergence of the model parameters to their true value.

Model of the Spastic Index Finger
In Chapter 3, a *neuromuscular and biomechanical model* of the *RPMS*-induced index finger movement is developed. It comprises the submodels "force generation", "force transmission", "length-velocity-dependencies", "segment dynamics" and "spastic joint torque". The model is developed based on numerous experiments that were conducted with a reasonable number of participants in order to obtain representative parameters. The models of "force transmission" and the "length-velocity-dependencies" were taken from literature since there exist well-established results. The "force generation" is described in Hammerstein-structure with activation delay. The "segment dynamics" are approximated with differential equations of motion including static nonlinear functions as it is known from robotics, e.g.. Additionally, a *relaxation effect* is taken into account by means of a dynamic velocity feedback. Most available biomechanical limb models describe "big" limbs like the forearm, thigh and shank with relatively high inertia, and high gravitational force components such that the relaxation effect is neglected. Our experiments show that this simplification does not apply for "small" limbs like the index finger. The "spastic joint torque" model is derived based on force-torque measurements carried out with stroke patients that suffer from spasticity in the finger flexors.

All proposed submodels are successfully verified by means of model output error evaluations. Thus, a qualitative model is obtained that approximates an "average plant" of the *RPMS*-induced index finger movement.

Automated Model Individualization
In Chapter 4, the scientific innovations presented in the previous chapters are combined: The *qualitative index finger model* is *individualized* to the respective subjects using the proposed parameter identification methods. For this purpose, the index finger model is transformed into a mathematical formulation that conforms with the structures of the appropriate error models of Chapter 2.

Due to the macroscopic character of the index finger model, inconsistencies and structural uncertainties are inevitable. The proposed mathematical formulation addresses this problem with the *incorporation of a priori knowledge* as long as it exists and with *flexibility to structural and parametric uncertainties* where a priori knowledge is poor. The derivation of appropriate equations is facilitated if the designer has the freedom to use nonlinear parameterization. Thus, the parameter identification methods for nonlinear and separable nonlinear parameterization ultimately enable the proposed approach.

Based on the stability conditions formally derived in Chapter 2, persistently exciting input sequences are developed that finally guarantee parameter convergence.

Techniques for the Improvement of the RPMS-Therapy
In Chapter 5, the three goals summarized in Fig. 1.1 are exemplarily realized:

- System identification-based extraction of the patient parameters spasticity level and muscular fatigue during *RPMS*
- Position controlled induction of the index finger extension and flexion using two stimulators

- Patient driven position control taking into account the patient's voluntary muscle activation

The parameter identification presented in Chapter 4 yields the basis for all three applications. In a pilot study with stroke patients, it is shown that a *system identification-based spasticity quantification* during *RPMS* is possible. The experimental results are controlled with biomechanical reference measurements. The identification of *muscular fatigue* is carried out with healthy subjects. Based on the identified model, a *linearizing computed torque controller* with a *linear state feedback* control cascade is implemented for *dual coil RPMS*. Experiments with healthy subjects show a good controller performance and the general feasibility of the position control concept. The position controller is combined with an *adaptive trajectory generation* that is *driven by the patient*. An EMG-signal processing cascade is presented that has the capability to detect *voluntary muscle activity at the stimulated muscle*. This information is used to implement an *RPMS*-supported index finger extension that facilitates the motion intended by the patient similar to servo steering. The concept is tested and evaluated with healthy subjects. The tests show the feasibility of the approach.

2 Parameter Adaptation and Stable Error Models

2.1 Introduction

System identification is the discipline of constructing mathematical models from observing the input/output behavior of an in general nonlinear dynamic system. It is of great interest to engineering, physics, biology, chemistry and economics [163]. In all these fields, models play an important role. They predict the behavior of the real system and are useful, often essential for system analysis, process design, process optimization, supervision and fault detection. In biomedical research, there are in general two applications for such models: On the one hand they help to gather a deeper insight into physiological processes which are of importance for the analysis of pathophysiologies. Thus, the number of experiments performed in human can be reduced and diagnostics and patient monitoring can be improved. On the other hand, simulations based on models are used in the context of control strategies where the human is part of the plant.

The procedure of system identification can roughly be divided into the choice of the model structure, i.e. complexity, order, dynamics and parameter identification, i.e. finding the optimal model parameters. The theory of established methods has been well investigated [97; 118; 122]. An overview of the application to physiological and biomedical systems is given in [83; 180]. It is essential to distinguish whether the parameters occur linearly or nonlinearly in the equation. In the case of linearly parameterized models, there exists an extensive theoretical framework that allows analyzing generic system classes in terms of stability and performance of the parameter identification. These results have been reported in [8; 90; 106; 118; 144; 158].

However, nonlinear parameterization is often intrinsic to physical and biological systems. Some examples are friction models [7], nonlinear damper models [85], a fermentation process [17], biochemical processes [18] and neural systems [31]. One of the possible approaches is to use a suitable diffeomorphism which yields a linearly parameterized transformed model. However, finding the transformation may be nontrivial which substantially limits the applicability. Furthermore, linear parameterization of systems where the parameters occur nonlinear increases the dimension of the parameter space which can result in overparameterization. If the original constitutive equations of a modeled process can be maintained for identification, the parameters keep their physical integrity. Thus, it is easier to analyze the identification results with respect to plausibility and initial parameter estimates can be meaningfully determined.

Since nonlinearly parameterized models do not share many properties, often system by system investigations are necessary. As a consequence, there is a strong demand for

research that aims to provide general methods for analysis and design of parameter adaptation algorithms for nonlinearly parameterized models. This conclusion can be emphasized by searching the scientific database `http://isiknowledge.com`: The search entry "System Identification" OR "Parameter Identification" OR "Parameter Adaptation" OR "Adaptive Systems" yields yearly increasing numbers of journal publications (725 articles in 2007).

Parameter identification can be done either off-line or on-line. While off-line identification may be useful if the plant parameters are constant on-line methods have the capability of tracking (at least slowly) time-varying parameters. On-line identification is applied for adaptive and self-tuning control purposes as well as for monitoring, supervision and failure detection in a large variety of application areas. In the following, only on-line algorithms will be considered.

In this chapter, methods for system identification dealing with certain classes of linear, nonlinear and a mixed linear/nonlinear parameterization are introduced. The focus is on a configuration where the output signal of the system to be identified is not directly accessible but only the response of a known LTI-plant $\mathcal{W}$ can be observed. This structure occurs in many kinds of mechanical, electromechanical and biomechanical systems. The problem has first been addressed for linearly parameterized systems in [118] by introducing the so called error models 1-4.

The most important results of the last decade for nonlinear parameterization can be found in [22; 100; 173; 174]. In [100], the Min-Max-Algorithm is introduced that fits the derivative of a Lyapunov-candidate to specific algebraic inequalities leading to asymptotic stability, i.e. parameter convergence. The known LTI-system has to be of relative degree one and the nonlinear parameters occur through additive scalar nonlinear functions. In [22], the Min-Max-method is advanced so that the known dynamic system $\mathcal{W}$ may be nonlinear but first order, and the parameters may occur in a general nonscalar nonlinear function. In [174] and [173], a method is introduced, where nonlinear parameters of nonlinear dynamic input affine systems are identified. The proposed method applies to a class of nonlinear parameterizations satisfying a specific monotonicity constraint. The adaptation method is a gradient based switching algorithm.

The novel scientific contributions introduced in this chapter are:

- Introduction of a modified Levenberg-Marquardt algorithm for numerically robust parameter identification.
- Enhancement of error models 1-4 [118] by replacing the gradient search adaptive law by a Recursive Least Squares algorithm.
- Formulation of conditions that provide parameter convergence for nonlinear parameter identification using gradient based algorithms. Specifically the configuration in series with a known LTI-system mentioned above will be considered.
- Formulation of conditions that provide parameter convergence for mixed linear/nonlinear parameterization using the separable least squares algorithm. Again, the configuration with a known LTI-system is specifically considered.

This chapter is organized as follows: In Section 2.2 a fundamental theoretical framework and state of the art theory of relevant parameter identification methods that will be used

Fig. 2.1: Block diagram representation of signals and LTI-systems: Thick signal arrows (block diagram on the right) represent a vector of signals, i.e. $\underline{u}(t) = [u_1(t) \dots u_r(t)]$, e.g.. In this case, the LTI-block $\mathcal{L}$ represents r independent SISO LTI-systems so that $[y_1(t) \dots y_r(t)]^T = \mathcal{L}(\underline{u}(t)) := [\mathcal{L}(u_1(t)) \dots \mathcal{L}(u_r(t))]^T$.

throughout this chapter are introduced. Subsequently, theory of linear, nonlinear and mixed linear/nonlinear parameterization is described in Sections 2.3, 2.5 , and 2.6, respectively. Section 2.7 concludes this chapter with a summary and discussion.

2.2 Fundamentals and Definitions

The theory of system and parameter identification is often treated in discrete time formulation. This is motivated by the fact that the adaptation algorithms are usually implemented in discrete time and furthermore, the discrete time representation of dynamic systems can easily be transformed into a convenient model equation formalism (see Section 2.2.1).

The analysis of convergence and stability properties of the proposed adaptation algorithms will be done with stability concepts of continuous time nonlinear differential equations. Therefore, continuous time formulation will be used. Since for analysis and design, digital control systems can be treated as continuous time systems if high sampling rates are used, the derived stability properties apply for discrete implementation, too. Time continuous signals will be denoted as $s(t)$, their discrete equivalents as $s(k)$ with $k \mathrel{\widehat{=}} kT_s$, whereas T_s is the sampling time of the discrete implementation. This is a slight revision of notation for sake of a better readability. Further continuous time variables are τ and T with their respective discrete equivalents given by j and N. If either a property applies for both time domains, or the domain is clear from the context, the time argument may be skipped.

Furthermore, operator notation will be used in order to describe the response or an LTI-system $\mathcal{L}$ to its input signal $u(t)$ as $y(t) = \mathcal{L}(u(t))$. The operator notation is defined for SISO systems only. For sake of a better readability, the abbreviation $[y_1(t) \dots y_r(t)]^T = \mathcal{L}(\underline{u}(t)) := [\mathcal{L}(u_1(t)) \dots \mathcal{L}(u_r(t))]^T$ is defined. The corresponding graphical representation is depicted in Fig. 2.1.

The system $\mathcal{L}$ can be characterized either in state space with $\{\underline{c}_L^T, \underline{A}_L, \underline{b}_L\}$ and with its state $\underline{\chi} \in \mathbb{R}^n$ or as transfer function $G_L(s) = \underline{c}_L^T(s\underline{I} - \underline{A}_L)^{-1}\underline{b}_L$.

2.2.1 Identification Structure, Error Models and Model Equations

Output Error Configuration and Error Transfer Functions

Throughout the thesis, parameter identification is accomplished with supervised learning methods in output error configuration as depicted in Fig. 2.2. Plant, model and adaptation

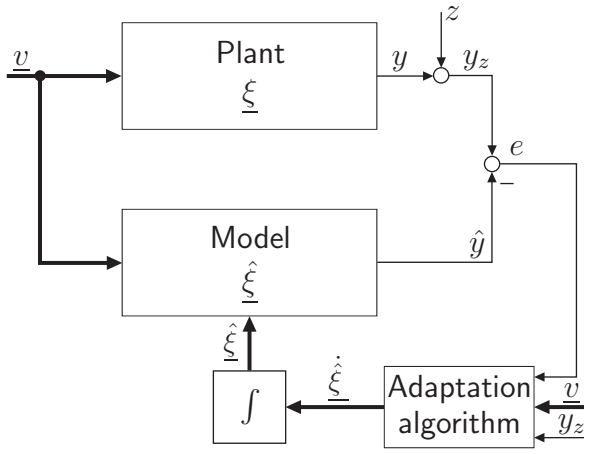

Fig. 2.2: Basic structure of parameter identification: Output error configuration. All estimated variables are labeled with a "ˆ".

algorithm constitute an adaptive system with the input $\underline{v} \in \mathbb{R}^r$, the output y, the measured output y_z, the measurement noise z, the plant parameters $\underline{\xi} \in \mathbb{R}^p$, the output error $e = y_z - \hat{y}$, and the parameter error $\tilde{\underline{\xi}} = \underline{\xi} - \hat{\underline{\xi}}$. It is the objective of supervised learning to minimize a measure of the output error (prediction error) e by finding the optimal parameter estimates $\hat{\underline{\xi}}_{\text{opt}}$. If the model approximates the plant exactly and in the noise free case ($z = 0$), we have $\hat{\underline{\xi}}_{\text{opt}} = \underline{\xi}$. Since the output error e is measurable it is used to tune the unknown but adjustable parameter error $\tilde{\underline{\xi}}$.

The main focus of this chapter is on plants that can be divided into an unknown part $n(\underline{\xi}, \underline{v})$ with output y_n in series with a known SISO LTI-system $\mathcal{W}$ (see Fig. 2.3) whereas $\mathcal{W}$ is defined as

$$\begin{aligned} \dot{\underline{\chi}} &= \underline{A}_w \underline{\chi} + \underline{b}_w y_n, \quad \underline{\chi} \in \mathbb{R}^n \\ y &= \underline{c}_w^T \underline{\chi} \ . \end{aligned} \tag{2.1}$$

Note that the subsystem $n(\underline{\xi}, \underline{v})$ can be static as well as dynamic. Since the output y_n is not measurable, the error $e_n = y_n - \hat{y}_n$ cannot be calculated. However, the known LTI-system $\mathcal{W}$ can be simulated in order to filter $\hat{y}_n$ as depicted in Fig 2.3, and to obtain $\hat{y}$. Thus, the output error $e = y - \hat{y}$ can be calculated and used for parameter identification. If $\underline{\chi}(0) = \hat{\underline{\chi}}(0)$, the output error is given by

$$e = \mathcal{W}(y_n - \hat{y}_n) \ . \tag{2.2}$$

The dynamics between $e_n = y - y_n$ and e is denominated as error transfer function $G_w(s)$ with $G_w(s) = \underline{c}_w^T (s\underline{I} - \underline{A}_w)^{-1} \underline{b}_w$. The plant state error is defined as $\tilde{\underline{\chi}} = \underline{\chi} - \hat{\underline{\chi}}$ and hence, the state of an adaptive system structured according to Fig. 2.3 is given as $\underline{x}^T = [\tilde{\underline{\chi}}^T \ \tilde{\underline{\xi}}^T] \ \underline{x} \in \mathbb{R}^{n+p}$.

Error Models

As mentioned before, it is the aim of the adaptive systems considered in this chapter to drive the parameter error $\underline{\tilde{\xi}}$ to zero, i.e. $\lim_{t\to\infty} \underline{\tilde{\xi}} = 0$. In order to analyze the convergence behavior of an adaptive system, often the underlying error model that describes the dynamic relationship between the parameter error and the output error is examined. Considering the configuration of Fig. 2.3, the error equation

$$\begin{aligned} \dot{\underline{\tilde{\chi}}} &= \underline{A}_w \underline{\tilde{\chi}} + \underline{b}_w (y_n(\underline{v}) - \hat{y}_n(\underline{\hat{\xi}}, \underline{v})) \\ e &= \underline{c}_w^T \underline{\tilde{\chi}} \end{aligned} \tag{2.3}$$

can be derived whereas it is assumed that $\underline{\hat{\chi}}(0) = \underline{\chi}(0)$. The adaptation algorithm (compare to Fig. 2.2) can be written as

$$\begin{aligned} \dot{\underline{\hat{\xi}}} &= \underline{g}(e, y, \underline{v}) \\ \dot{\underline{\tilde{\xi}}} &= -\dot{\underline{\hat{\xi}}} \end{aligned} \tag{2.4}$$

Eq. (2.3) together with Eq. (2.4) constitute the error model (EM) of the adaptive system. Its state is defined by $\underline{x}^T = [\underline{\tilde{\chi}}^T \ \underline{\tilde{\xi}}]$. This definition has first been introduced in [119]. The EM is stable if $\underline{\tilde{\xi}}$ remains bounded, asymptotically stable if $\lim_{t\to\infty} \underline{\tilde{\xi}} = 0$, and unstable otherwise.

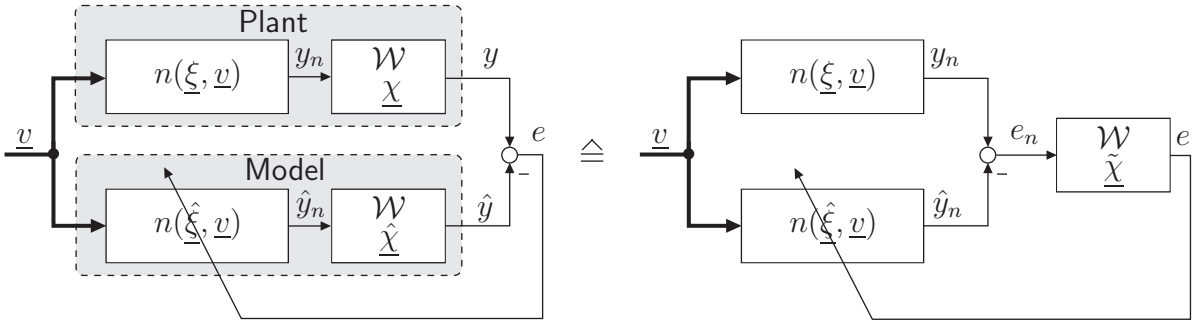

Fig. 2.3: Output error configuration with a plant that can be structured as subsystem $n(\underline{\xi}, \underline{v})$ with unknown parameters whose output y_n is not directly measurable but filtered with a known LTI-system $\mathcal{W}$. If $\underline{\chi}(0) = \underline{\hat{\chi}}(0)$, the block diagram manipulation that leads to the graph on the right is formally correct and thus, $\underline{\tilde{\chi}} = \underline{\chi} - \underline{\hat{\chi}}$ and $e_n = y_n - y$. The measurable output error e can be interpreted as the actual error e_n filtered by the error transfer function $G_w(s)$.

Model Equations

The model equations $\hat{y}_n = n(\hat{\underline{\xi}}, \underline{v})$ can be distinguished with respect to their parameterization. In the following, three classes are considered:

$$n = \hat{\underline{\theta}}^T \underline{\varphi}(\underline{v}) \tag{2.5a}$$
$$n = n(\hat{\underline{\eta}}, \underline{v}) \tag{2.5b}$$
$$n = \hat{\underline{\theta}}^T \underline{\varphi}(\hat{\underline{\eta}}, \underline{v}) \tag{2.5c}$$

A linear regression (LP-) model (2.5a) can be expressed as scalar product of a vector of "linear parameters" $\hat{\underline{\xi}} = \hat{\underline{\theta}} \in \Omega_\theta \subset \mathbb{R}^m$ and an input regressor $\underline{\varphi}(\underline{v})$. In a nonlinear regression (NLP-) model (2.5b) the parameters $\hat{\underline{\xi}} = \hat{\underline{\eta}} \in \Omega_\eta \subset \mathbb{R}^q$ occur nonlinear. Ω_θ and Ω_η are closed and bounded subsets of $\mathbb{R}^m$ and $\mathbb{R}^q$, respectively. The parameters of a separable nonlinear regression (SNLP-) model (2.5c) can be separated into linear and nonlinear parameters ($\hat{\underline{\xi}}^T = [\hat{\underline{\theta}}^T \; \hat{\underline{\eta}}^T]$). The total number of parameters in (2.5c) is given as $p = q + m$.

If $\hat{y}_n(\hat{\underline{\xi}}, \underline{v})$ is a purely static nonlinearity, the equations (2.5a)-(2.5c) apply for continuous time as well as for discrete time domain. If $\hat{y}_n(\hat{\underline{\xi}}, \underline{v})$ represents the approximation of dynamic behavior, it is convenient to use discrete time formulation. Then, the dynamics can be incorporated either with a difference equation or with a truncated convolution sum. The former leads to an input regressor $\underline{\varphi}(\underline{v}(k)) = [\hat{y}(k)\, \hat{y}(k-1) \ldots \hat{y}(k-n_y)\, \underline{v}(k)\, \underline{v}(k-1) \ldots \underline{v}(k-n_u)]^T$ and the model results in a NARX- (nonlinear autoregressive with exogenous input) structure. With $\underline{\varphi} = [\underline{v}(k)\, \underline{v}(k-1) \ldots \underline{v}(k-n_u)]^T$ as input regressor of the latter, a NFIR- (nonlinear finite impulse response) model is obtained. Details can be found in [122], e.g..

2.2.2 The Neural Observer

The neural observer is an extension of the error transfer function method illustrated in Fig. 2.3. It has first been introduced in [151] and [69]. The dynamic behavior of the error transfer function $G_w(s)$ is important for the convergence properties of the adaptive system. By using an observer structure (Fig. 2.4) instead of a pure parallel model (Fig. 2.3), the properties of $G_w(s)$ can be designed. The block diagram manipulation of Fig. 2.4 applies for the initial conditions $\underline{\chi}(0) = \hat{\underline{\chi}}(0)$ and yields the error transfer function

$$G_{w,obs}(s) = \underline{c}_w^T (s\underline{I} - \underline{A}_w + \underline{l}\underline{c}_w^T)^{-1} \underline{b}_w \quad .$$

Thus, the poles can be placed arbitrarily by adapting the observer gain vector $\underline{l}$. The observer error e_{obs} is fed into the adaptation algorithm (2.4).

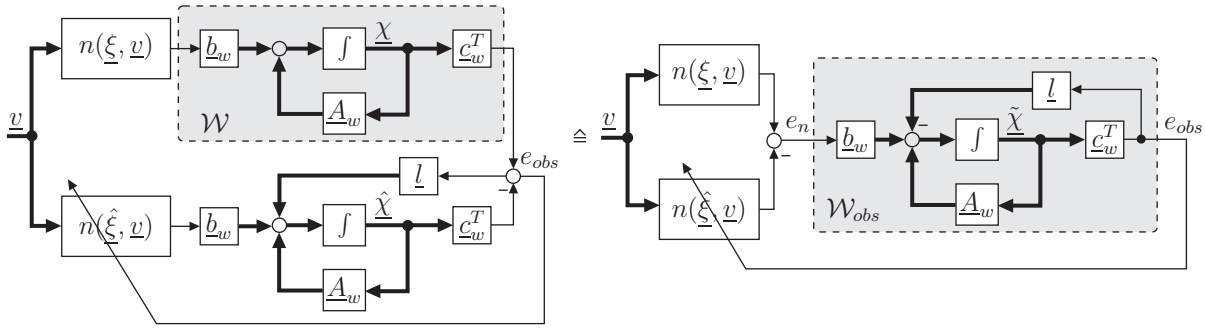

Fig. 2.4: Neural observer: Manipulation using block diagram algebra. The dynamic relation between e_n and e_{obs} is governed by $e_{obs}(s) = G_{w,obs}(s)e_n(s)$.

2.2.3 Parameter Identification Algorithms

Least Squares Optimization

The well-known least squares method was first developed by Gauss in 1795. The optimal parameters are defined by the optimization problem

$$\hat{\underline{\xi}}_{\text{opt}} = \arg\min_{\hat{\underline{\xi}}} E(\hat{\underline{\xi}}) \quad . \tag{2.6}$$

If the error criterion $E(\hat{\underline{\xi}})$ is defined as a quadratic function of the output error e, which is by far the most common criterion in practice, Eq. (2.6) represents a least squares problem. For on-line identification, there exist well-known least squares optimization methods that are shortly summarized in Tab. 2.1. Detailed derivations can be found in [98; 122] (discrete time) and in [162] (continuous time). Here, the derivation of the discrete time algorithms is shortly sketched following the explanation of the recursive maximum likelihood algorithm as it is referred to in [98]. In order to track time varying parameters, the error criterion should weight more recent data higher. This is achieved by using the forgetting factor λ ($0 < \lambda \leq 1$) that determines the decay of previous data. Thus, the cost function

$$E_k(\hat{\underline{\xi}}) = \frac{1}{2} \sum_{j=0}^{k} \lambda^{k-j} e(\hat{\underline{\xi}}, j)^2 \tag{2.7}$$

is introduced with the model error $e(\hat{\underline{\xi}}, k) = y(k) - \hat{y}(\hat{\underline{\xi}}, k)$.

Let $\hat{\underline{\xi}}(k)$ be a be the latest available estimate that minimizes $E_{k-1}(\hat{\underline{\xi}})$. In order to compute $\hat{\underline{\xi}}(k+1)$, the second order Taylor expansion $L_k(\hat{\underline{\xi}})$ is considered as a model of the behavior of E_k in the neighborhood of the current estimate $\hat{\underline{\xi}}(k)$:

$$E_k(\hat{\underline{\xi}}) \approx L_k(\hat{\underline{\xi}}) = E_k(\hat{\underline{\xi}}(k)) + E_k'(\hat{\underline{\xi}}(k))[\hat{\underline{\xi}} - \hat{\underline{\xi}}(k)] + \frac{1}{2}[\hat{\underline{\xi}} - \hat{\underline{\xi}}(k)]^T E_k''(\hat{\underline{\xi}}(k))[\hat{\underline{\xi}} - \hat{\underline{\xi}}(k)] \quad . \tag{2.8}$$

In order to find $\hat{\underline{\xi}}(k+1)$, the minimum of the quadratic model function L is computed by setting $L' = 0$. This leads to

$$\hat{\underline{\xi}}(k+1) = \hat{\underline{\xi}}(k) - \left[E_k''(\hat{\underline{\xi}}(k))\right]^{-1} E_k'(\hat{\underline{\xi}}(k))^T \quad . \tag{2.9}$$

Differentiating Eq. (2.7) with respect to $\hat{\underline{\xi}}$ yields

$$\begin{aligned} E_k'(\hat{\underline{\xi}}) &= -\sum_{j=0}^{k} \lambda^{k-j} \underline{\psi}(\hat{\underline{\xi}}, j) e(\hat{\underline{\xi}}, j) \\ &= \lambda E_{k-1,2}'(\hat{\underline{\xi}}) - \underline{\psi}(\hat{\underline{\xi}}, k) e(\hat{\underline{\xi}}, k) \\ &\approx -\underline{\psi}(\hat{\underline{\xi}}, k) e(\hat{\underline{\xi}}, k) \quad , \end{aligned} \tag{2.10}$$

with the gradient vector

$$\underline{\psi}(\hat{\underline{\xi}}, k) = -\frac{\partial e(\hat{\underline{\xi}}, k)}{\partial \hat{\underline{\xi}}} = \nabla \hat{y}(\hat{\underline{\xi}}, k) \quad . \tag{2.11}$$

This approximation follows from the assumption that $\hat{\underline{\xi}}(k)$ is indeed the optimal estimate at time $t-1$, i.e. $E_{k-1,2}'(\hat{\underline{\xi}}) = 0$. Note, that the gradient is a row vector since it is defined as a single-line Jacobian. Differentiating once more gives

$$E_k''(\hat{\underline{\xi}}) \approx \underline{H}(k) = \lambda \underline{H}(k-1) + \underline{\psi}(\hat{\underline{\xi}}, k)^T \underline{\psi}(\hat{\underline{\xi}}, k) \quad . \tag{2.12}$$

This approximation $\underline{H}(k)$ of the Hessian Matrix $E_k''(\hat{\underline{\xi}})$ is usually taken in order to reduce computational load (see [123],[98], e.g.). With these simplifications the update law for the nonlinear parameters can be written as

$$\hat{\underline{\xi}}(k+1) = \hat{\underline{\xi}}(k) + \underline{H}(k)^{-1} \underline{\psi}(\hat{\underline{\xi}}, k)^T e(\hat{\underline{\xi}}, k) \quad . \tag{2.13}$$

which corresponds to the GN-algorithm in Tab. 2.1. Note that replacing $\underline{H}(k)$ with the unity matrix $\underline{I}$ results in the GS-algorithm and replacing $\underline{H}(k)$ with $\underline{R}(k) = \underline{H}(k) + \delta \underline{I}$ leads to an LM-update law. The damping factor δ decides whether to make a parameter update in GN-direction (small δ) or a small step in gradient direction (big δ) which will be explained in more detail in Section 2.3. It is worth noting that the GS-algorithm and the GN-algorithm are equivalent to LMS and RLS, respectively, when applied to an LP-Problem. In the relevant literature, GS, GN and LM from Tab. 2.1 are often referred to as gradient based recursive adaptation algorithms.

The correspondence between the continuous forgetting factor λ_c and discrete forgetting factor λ_d can easily be derived as

$$\lambda_d = \frac{1}{1 - T_s \ln \lambda_c} \tag{2.14}$$

as it is explained in Appendix A.3. The subscript may be dropped in the following if the meaning is clear from the context. The estimator gain γ influences the adaptation speed.

Tab. 2.1: Error criteria and adaptive laws for on-line least squares optimization: The laws LMS and RLS relate to LP-models (2.5a) whereas the laws GS, GN and LM have to be applied in case of NLP-equations (2.5b).

	Discrete time	Continuous time
Error criterion	$E(\hat{\underline{\xi}},k) = \frac{1}{2}\sum_{j=0}^{k}(y(j)-\hat{y}(\hat{\underline{\xi}},j))^2$	$E(\hat{\underline{\xi}},t) = \int_0^t(y(\tau)-\hat{y}(\hat{\underline{\xi}},\tau))^2 d\tau$
Error criterion with forgetting factor	$E(\hat{\underline{\xi}},k) = \frac{1}{2}\sum_{j=0}^{k}\lambda_d^{k-j}(y(j)-\hat{y}(\hat{\underline{\xi}},j))^2$	$E(\hat{\underline{\xi}},t) = \int_0^t\lambda_c^{t-\tau}(y(\tau)-\hat{y}(\hat{\underline{\xi}},\tau))^2 d\tau$
Least Mean Squares (LMS)	$\hat{\underline{\theta}}(k+1) = \hat{\underline{\theta}}(k) + \gamma\underline{\varphi}(k)e(k)$	$\dot{\hat{\underline{\theta}}} = \gamma\underline{\varphi}(t)e(t)$
Recursive Least Squares (RLS)	$\hat{\underline{\theta}}(k+1) = \hat{\underline{\theta}}(k) + \gamma\underline{\Pi}(k)\underline{\varphi}(k)e(k)$ $\underline{\Pi}(k)^{-1} = \lambda_d\underline{\Pi}(k-1)^{-1} + \underline{\varphi}(k)\underline{\varphi}(k)^T$	$\dot{\hat{\underline{\theta}}}(t) = \gamma\underline{\Pi}(t)\underline{\varphi}(t)e(t)$ $\underline{\Pi}(t)^{-1} = \int_0^t\lambda_c^{t-\tau}\underline{\varphi}(\tau)\underline{\varphi}(\tau)^T d\tau$
Gradient Search (GS)	$\hat{\underline{\eta}}(k+1) = \hat{\underline{\eta}}(k) + \gamma\nabla\hat{y}(k)^T e(k)$	$\dot{\hat{\underline{\eta}}}(t) = \gamma\nabla\hat{y}(t)^T e(t)$
Gauss-Newton Algorithm (GN)	$\hat{\underline{\eta}}(k+1) = \hat{\underline{\eta}}(k) + \gamma\underline{H}(k)^{-1}\nabla\hat{y}(k)^T e(k)$ $\underline{H}(k) = \lambda_d\underline{H}(k-1) + \nabla\hat{y}(k)^T\nabla\hat{y}(k)$	$\dot{\hat{\underline{\eta}}}(t) = \gamma\underline{H}(t)^{-1}\nabla\hat{y}(t)^T e(t)$ $\underline{H}(t) = \int_0^t\lambda_c^{t-\tau}\nabla\hat{y}(\tau)^T\nabla\hat{y}(\tau)d\tau$
Levenberg-Marquardt Algorithm (LM)	$\hat{\underline{\eta}}(k+1) = \hat{\underline{\eta}}(k) + \gamma\underline{R}(k)^{-1}\nabla\hat{y}(k)^T e(k)$ $\underline{H}(k) = \lambda_d\underline{H}(k-1) + \nabla\hat{y}(k)^T\nabla\hat{y}(k)$ $\underline{R}(k) = \underline{H}(k) + \delta(k)\underline{I}$	$\dot{\hat{\underline{\eta}}}(t) = \gamma\underline{R}(t)^{-1}\nabla\hat{y}(t)^T e(t)$ $\underline{H}(t) = \int_0^t\lambda_c^{t-\tau}\nabla\hat{y}(\tau)^T\nabla\hat{y}(\tau)d\tau$ $\underline{R}(t) = \underline{H}(t) + \delta(t)\underline{I}$

The Separable Least Squares Algorithm

A separable nonlinear least squares problem is represented by a model equation according to (2.5c). This separable problem was first addressed in [55] with the introduction of the Separable Least Squares (SLS-) Algorithm. On-line versions have first been introduced in [35] and [123]. For the derivation, the off-line algorithm is discussed first.

With the vector/matrix notations

$$\underline{y} = \begin{bmatrix} y(1) \\ \vdots \\ y(N) \end{bmatrix} \quad \text{and} \quad \underline{\Phi}(\hat{\underline{\eta}}) = \begin{bmatrix} \underline{\varphi}^T(\hat{\underline{\eta}},\underline{v}(1)) \\ \vdots \\ \underline{\varphi}^T(\hat{\underline{\eta}},\underline{v}(N)) \end{bmatrix} \tag{2.15}$$

the off-line error criterion of a SNLP-model can be written as

$$E_{N,1}(\hat{\underline{\xi}}) = \frac{1}{2N}\left\|\underline{y} - \underline{\Phi}(\hat{\underline{\eta}})\hat{\underline{\theta}}\right\|_2^2 \quad , \tag{2.16}$$

$\hat{\underline{\xi}}^T = [\hat{\underline{\theta}}^T \; \hat{\underline{\eta}}^T]$.

With this notation, it is easy to see that if the nonlinear parameters $\hat{\underline{\eta}}$ were known, the linear parameters $\hat{\underline{\theta}}$ could be calculated by solving the linear least squares problem

$$\hat{\underline{\theta}}_{opt} = \underline{\Phi}(\hat{\underline{\eta}})^+ \underline{y} \tag{2.17}$$

with the pseudoinverse $\underline{\Phi}(\hat{\underline{\eta}})^+ := (\underline{\Phi}(\hat{\underline{\eta}})^T \underline{\Phi}(\hat{\underline{\eta}}))^{-1} \underline{\Phi}(\hat{\underline{\eta}})^T$. By replacing $\hat{\underline{\theta}}$ in (2.16) with (2.17), an error criterion

$$E_{N,2}(\hat{\underline{\eta}}) = \frac{1}{2N} \left\| \underline{y} - \underline{\Phi}(\hat{\underline{\eta}}) \underline{\Phi}(\hat{\underline{\eta}})^+ \underline{y} \right\|_2^2 \tag{2.18}$$

is obtained, where the linear parameters have been eliminated. Golub and Perreyra set up the following theorem (proof see [55]):

If $\hat{\underline{\eta}}_{opt}$ is a minimizer of $E_{N,2}(\hat{\underline{\eta}})$, and $\hat{\underline{\theta}}_{opt} = \underline{\Phi}^+(\hat{\underline{\eta}}_{opt})\underline{y}$, then, $\hat{\underline{\xi}}_{opt} = [\hat{\underline{\theta}}_{opt}^T \; \hat{\underline{\eta}}_{opt}^T]^T$ also minimizes the original error criterion $E_{N,1}(\hat{\underline{\xi}})$ and thus, $E_{N,2}(\hat{\underline{\eta}}_{opt}) = E_{N,1}(\hat{\underline{\xi}}_{opt})$.

Therefore, the SLS-algorithm divides the calculation of $\hat{\underline{\xi}}_{opt}$ into two steps:

1. Minimize $E_{N,2}(\hat{\underline{\eta}})$ in order to obtain $\hat{\underline{\eta}}_{opt}$.
2. Use the optimal value $\hat{\underline{\eta}}_{opt}$ to calculate $\hat{\underline{\theta}}_{opt}$ with linear regression according to Eq. (2.17).

Hence, the minimization using an iterative nonlinear search algorithm can be accomplished within a reduced parameter set.

Remark 2.2.1 *The minimization problem defined with the error criterion* (2.16) *could in principle be solved by applying nonlinear optimization algorithms to the full functional without exploiting the SLS-structure. An advantage of the SLS-method lies in the reduced computational cost. The main advantage however, is the reduction of the dimension of the optimization problem. This contributes significantly to the performance of the estimation process [134]. In [89] it could be shown that the SLS-scheme always converges faster than the minimization of the full functional* (2.16).

The on-line algorithm is introduced following the derivation in [123]. The reformulation of (2.18) in summation form at the time instance k yields

$$\begin{aligned} E_{k,2}(\hat{\underline{\eta}}) &= \frac{1}{2} \sum_{j=0}^{k} \lambda^{k-j} \left(y(j) - \underline{\varphi}(\hat{\underline{\eta}}, j)^T \left(\sum_{n=0}^{k} \lambda^{k-n} \underline{\varphi}(\hat{\underline{\eta}}, n) \underline{\varphi}(\hat{\underline{\eta}}, n)^T \right)^{-1} \right. \\ &\quad \left. \cdot \left(\sum_{n=0}^{k} \lambda^{k-n} \underline{\varphi}(\hat{\underline{\eta}}, n) y(n) \right) \right)^2 \\ &= \frac{1}{2} \sum_{j=0}^{k} \lambda^{k-j} (y(j) - \hat{y}(\hat{\underline{\eta}}, j))^2 \\ &= \frac{1}{2} \sum_{j=0}^{k} \lambda^{k-j} \epsilon^2(\hat{\underline{\eta}}, j) \quad . \end{aligned} \tag{2.19}$$

By applying the steps (2.10)- (2.12) to the SLS-error criterion (2.19), the update law

$$\underline{\hat{\eta}}(k+1) = \underline{\hat{\eta}}(k) + \underline{H}(k)^{-1}\underline{\psi}(\underline{\hat{\eta}},k)^T\epsilon(\underline{\hat{\eta}},k) \quad . \tag{2.20}$$

is derived, which corresponds to the GN-algorithm in Tab. 2.1. Again, replacing $\underline{H}(k)$ with $\underline{I}$ results in the GS-algorithm and replacing $\underline{H}(k)$ with $\underline{R}(k) = \underline{H}(k) + \delta\underline{I}$ leads to an LM-update law. It remains to calculate the gradient vector $\underline{\psi}(\underline{\hat{\eta}},k)$. From Eq. (2.19) and with the definitions

$$\begin{aligned}\underline{\Pi}(k)^{-1} &= \sum_{n=0}^{k}\lambda^{k-n}\underline{\varphi}(\underline{\hat{\eta}},n)\underline{\varphi}(\underline{\hat{\eta}},n)^T \\ &= \lambda\underline{\Pi}(k-1)^{-1} + \underline{\varphi}(\underline{\hat{\eta}},k)\underline{\varphi}(\underline{\hat{\eta}},k)^T \end{aligned} \tag{2.21}$$

and

$$\begin{aligned}\underline{f}^{\hat{\theta}}(k) &= \sum_{n=0}^{k}\lambda^{k-n}\underline{\varphi}(\underline{\hat{\eta}},n)y(n) \\ &= \lambda\underline{f}^{\hat{\theta}}(k-1) + \underline{\varphi}(\underline{\hat{\eta}},k)y(k) \end{aligned} \tag{2.22}$$

it follows

$$\epsilon(\underline{\hat{\eta}},k) = y(k) - \underline{\varphi}(\underline{\hat{\eta}},k)^T\underline{\Pi}(k)\underline{f}^{\hat{\theta}}(k) \quad . \tag{2.23}$$

Thus, the i$^{\text{th}}$ component of the gradient vector $\underline{\psi}(\underline{\hat{\eta}},k)$ is

$$\begin{aligned}\psi(\underline{\hat{\eta}},k)_i &= \frac{\partial\underline{\varphi}(\underline{\hat{\eta}},k)^T}{\partial\hat{\eta}_i}\underline{\Pi}(k)\underline{f}^{\hat{\theta}}(k) + \underline{\varphi}(\underline{\hat{\eta}},k)^T\frac{\partial\underline{\Pi}(k)\underline{f}^{\hat{\theta}}(k)}{\partial\hat{\eta}_i} \\ &= \underline{\varphi}_i(\underline{\hat{\eta}},k)^T\underline{\Pi}(k)\underline{f}^{\hat{\theta}}(k) + \underline{\varphi}(\underline{\hat{\eta}},k)^T\underline{\Pi}(k) \\ &\quad \cdot(\underline{f}_i^{\hat{\theta}}(k) - \underline{\Pi}_i(k)^{-1}\underline{\Pi}(k)\underline{f}^{\hat{\theta}}(k)) \,, \end{aligned} \tag{2.24}$$

whereas

$$\underline{\Pi}_i(k)^{-1} = \lambda\underline{\Pi}_i(k-1)^{-1} + \underline{\varphi}_i(\underline{\hat{\eta}},k)\underline{\varphi}(\underline{\hat{\eta}},k)^T + \underline{\varphi}(\underline{\hat{\eta}},k)\underline{\varphi}_i(\underline{\hat{\eta}},k)^T \tag{2.25}$$

and

$$\underline{f}_i^{\hat{\theta}}(k) = \lambda\underline{f}_i^{\hat{\theta}}(k-1) + \underline{\varphi}_i(\underline{\hat{\eta}},k)y(k) \tag{2.26}$$

and with

$$\underline{\varphi}_i(\underline{\hat{\eta}},k) = \frac{\partial\underline{\varphi}(\underline{\hat{\eta}},k)}{\partial\eta_i} \quad .$$

For the update of the linear parameters it follows

$$\underline{\hat{\theta}}(k+1) = \underline{\Pi}(k)\underline{f}^{\hat{\theta}}(k) \tag{2.27}$$

from (2.23), which is the same as the RLS-algorithm (derivation see Appendix A.1).

2.3 A Modified Levenberg-Marquardt Algorithm

Due to its fast convergence and robustness, the LM-algorithm is one of the most commonly used techniques for nonlinear local optimization. However, the choice of the damping factor δ requires expertise and insight into mechanisms of gradient based iterative optimization. The rules for the choice of δ proposed in literature (see [114; 124; 179], e.g.) are derived for off-line identification and do not address problems specific to recursive adaptation. Therefore, rules for adjusting the damping factor of the LM-algorithm will be derived which address particular problems of on-line identification. A simple example is given to illustrate the benefit of the proposed method.

2.3.1 Method

The following considerations are based on the derivation of the recursive GS-, GN- and LM-adaptation algorithms in Section 2.2.3. It is well known that simple gradient search may converge very slowly: One would like to make large steps down the gradient when the gradient is small and small steps when the gradient is large to avoid going too far. The GS-update rule does just the opposite of this. The GN-algorithm approximates the cost function with a quadratic function and jumps to the minimum of this approximation in one step. Hence, if this approximation is proper, the GN-algorithm may converge very fast. Usually, this is the case close to the minimum. Far from the minimum where the cost function often tends to be linear, gradient search will perform better. Obviously, these two methods are complementary in the advantages they provide. Therefore, Levenberg [96] and Marquardt [107] suggested a damped GN-method where in the parameter update of Eq. (2.13) the Hessian matrix is replaced by

$$\underline{R}(k) = \underline{H}(k) + \delta(k)\underline{I},$$

with the unity matrix $\underline{I}$ and the so called damping factor δ. The effect of the damping factor can be explained intuitively:

1. For large values of δ
$$(\underline{H}(k) + \delta(k)\underline{I})^{-1} \approx \frac{1}{\delta(k)}\underline{I}$$
is obtained which yields a short step into the steepest descent direction. This may perform well if the current estimate $\hat{\underline{\xi}}(k)$ is far from the solution, where the curvature of the error criterion is often small and thus, a linear approximation is good.

2. If δ is very small
$$(\underline{H}(k) + \delta(k)\underline{I})^{-1} \approx \underline{H}(k)^{-1}$$
is obtained which yields a GN-parameter update which may perform well close to the minimum where the error criterion can often be approximated with a parabolic function.

There is a possibility to adjust δ by evaluating the model $L_k(\hat{\underline{\xi}}(k))$ (2.8) of the actual cost function as it is proposed in [124]. This can be achieved by calculating the gain ratio

$$g = \frac{r_a}{r_p} = \frac{E_k(\hat{\underline{\xi}}(k)) - E_k(\hat{\underline{\xi}}(k+1))}{L_k(\hat{\underline{\xi}}(k)) - L_k(\hat{\underline{\xi}}(k+1))} \tag{2.28}$$

which is the relation between the actual reduction r_a and the predicted reduction r_p of the cost function. For the on-line identification, the following updating rules are proposed:

- If $g \leq \beta$ (with $0 \leq \beta \leq 1$, $\beta = 0.25$, e.g.) the approximation L_k is considered as inappropriate and $\delta(k+1)$ should be increased by a factor κ in order to reduce step size and go more into gradient direction.
- If $g \geq 1 - \beta$ the approximation L_k is considered as proper. Hence, $\delta(k+1)$ should be increased by a factor κ in order to enlarge the step size and to go more into GN-direction.

During off-line identification, the search algorithm is stopped, when the minimum is found. The on-line algorithm is continuously functional, since the plant parameters might change. This may lead to near singular Hessian matrices $\underline{H}(k)$ close the minimum. If the model equation $\hat{y}(\hat{\underline{\xi}}, k)$ is overparametrized, $\underline{H}(k)$ will always be singular at the minimum, since there exists an infinite number of solutions. In order to avoid this, it is proposed to evaluate a condition number of $\underline{R}(k)$ before inverting the matrix. The invertibility can be evaluated by calculating the ratio

$$s_r = \frac{\max(S_i)}{\min(S_i)}$$

of the largest and the smallest singular value of $\underline{R}(k)$ (see [5], e.g.). The following rule is formulated in order to avoid a singular Hessian matrix:

- If the condition number $s_r(k) > \nu$ the diagonal elements will be strengthened by adjusting $\delta(k)$ to $\delta(k) + \delta_s$.

This rule is applied consecutively to the update rules for the damping parameter $\delta(k)$.

Remark 2.3.1 *The calculation of the gain ratio g according to Eq.* (2.28) *may be computationally expensive. It is therefore advisable, not to compute the full functional* (2.7) *but only*

$$E_k(\hat{\underline{\xi}}) = \frac{1}{2} \sum_{j=k-k_h}^{k} \lambda^{k-j} e(\hat{\underline{\xi}}, j)^2 \ ,$$

whereas the time horizon $T_h = T_s k_h$ should not be chosen longer than the time horizon of exponential forgetting.

2.3.2 Simulative Example

In the following example, the modified LM-algorithm has been applied for the adaptation of the nonlinear parameter estimates $\hat{\underline{\eta}}$ of an SNLP-model (2.5c). The plant is formulated in discrete time with a static nonlinear function

$$w(v(k)) = \eta_1 v(k) + \eta_2 v(k)^2 + \eta_3 v(k)^3 \tag{2.29}$$

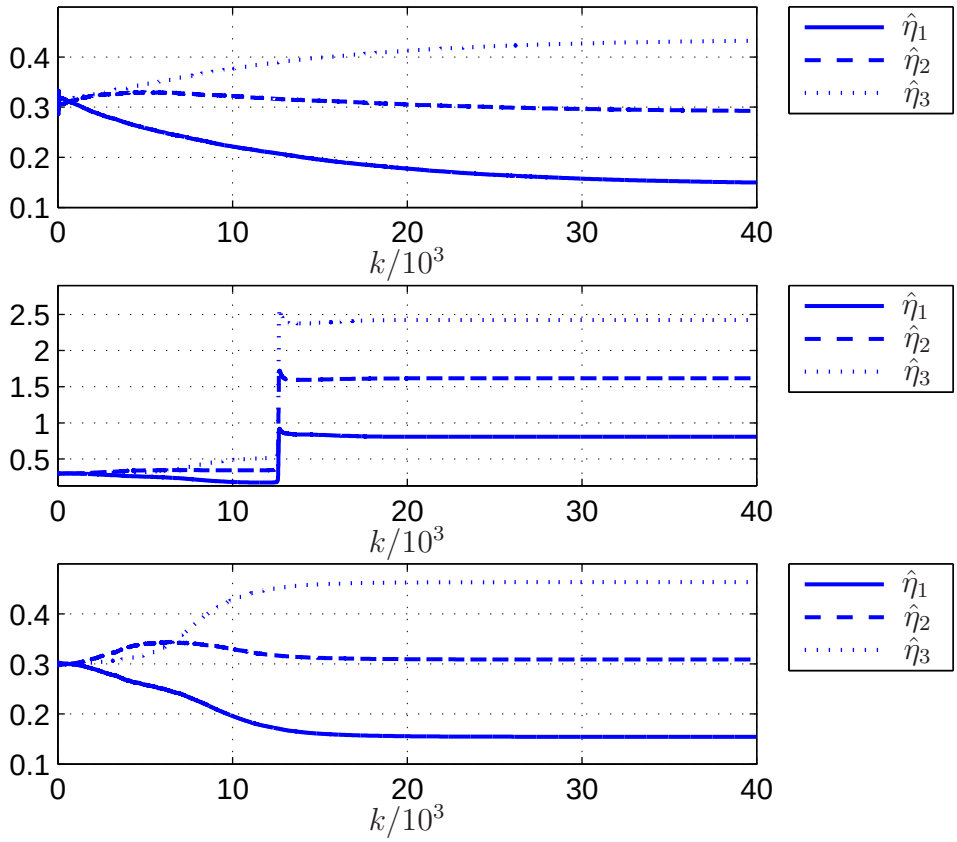

Fig. 2.5: Parameter swarms $\hat{\underline{\eta}}(k)$ obtained with the GS-, LM-, and the modified LM-algorithm.

in series with a PT_1-system

$$y(k) = \theta_1 y(k-1) + \theta_2 w(v(k)) \quad . \tag{2.30}$$

Thus, the model equation can be formulated as

$$\hat{y}(\hat{\underline{\xi}}, k) = \hat{\underline{\theta}}^T \underline{\varphi}(\hat{\underline{\eta}}, v) = [\hat{\underline{\theta}}_1 \; \hat{\underline{\theta}}_2] \begin{bmatrix} y(k-1) \\ w(\hat{\underline{\eta}}, v(k)) \end{bmatrix} \tag{2.31}$$

which is a NARX-model in SNLP-form. Note that the "nonlinear parameters" $\underline{\eta}$ actually occur linearly in the plant equation. Nevertheless, the SLS-structure can be exploited.

The plant parameters have been chosen to $\eta_1 = 1$, $\eta_2 = 2$, $\eta_3 = 3$, $\theta_1 = 0.99$ and $\theta_2 = 1 - \theta_1$. This plant has been chosen, since its overparameterization is easy to see: The gain of the complete plant is a product of the gain of $w(v(k))$ and the gain of the PT_1-system. I.e., there exist an infinite number of solutions for the model (2.31). The parameter adaptation has been implemented according to the SLS-algorithm introduced in Section 2.2.3 with a sample rate of $T_s = 0.001\,\mathrm{s}$. Three different adaptation-algorithms for the identification of $\hat{\eta}$ have been implemented: GS, LM and the modified LM. The design variables have been chosen to $\gamma = 1$, $\beta = 0.25$, $\kappa = 1.1$, $\nu = 1000$, and $\delta_s = 0.1$. The parameter swarms $\hat{\underline{\eta}}(k)$ are depicted in Fig. 2.5.

2.3.3 Discussion

All three algorithms converge to a solution on the line $c[1\,2\,3]^T$. The simple gradient search is by far the slowest. The LM-algorithm is fastest, but close to the minimum, a huge parameter update occurs and the algorithm converges to a different solution. This inappropriate behavior is due to numerical problems caused by a poorly conditioned Hessian matrix. The bottom graph illustrates the result obtained with the modified LM. It shows fast convergence but remedies the numerical problems of the conventional LM-algorithm.

2.4 Error Models for Linear Parameterization

In this section, the parameter identification of LP-models (2.5a) in the configuration as illustrated in Fig. 2.3 is discussed. In [118], four error models (EM 1-4) have been introduced. They are summarized as block diagrams with their respective error model equations in Fig. 2.6. Since EM 2 is a special case of EM3, it is not considered at this point. The adaptive law that is used for EMs 1-4 is the gradient search algorithm (LMS, respectively since LP-models are considered). In [118], the EMs 1-4 are proven to be asymptotically stable, i.e. $\lim_{t\to\infty} \underline{\tilde{\theta}} = 0$ using a Lyapunov approach. In the following, the error models A1-A3 are introduced and asymptotic stability is proven. They correspond to EMs 1, 2 and 4, but instead of gradient search the RLS-algorithm is applied as adaptive law. Note, that EM A1 is by no means new, but just the pure RLS-algorithm analyzed with the error model approach. It is introduced since the theoretical derivations are fundamental for EM A2 and EM A3.

2.4.1 Error Model A1

From the block diagram in Fig. 2.7, the equations of EM A1 can be inferred as

$$\begin{aligned} e &= \underline{\tilde{\theta}}^T \underline{\varphi}(\underline{v}) \\ \underline{\dot{\hat{\theta}}} &= -\underline{\dot{\tilde{\theta}}} = \gamma \underline{\Pi}(t) \underline{\varphi}(\underline{v}) e \quad , \end{aligned} \tag{2.32}$$

and the state is defined as $\underline{x} = \underline{\tilde{\theta}}$. The update law for $\underline{\Pi}(t)^{-1}$ is given with

$$\underline{\Pi}(t)^{-1} = \int_0^t \lambda^{t-\tau} \underline{\varphi}(\tau) \underline{\varphi}(\tau)^T d\tau \tag{2.33}$$

(compare to Tab. 2.1).

In order to prove asymptotic stability of (2.32) the Lyapunov candidate

$$V(\underline{x}) = \underline{\tilde{\theta}}^T \underline{\Pi}(t)^{-1} \underline{\tilde{\theta}} \tag{2.34}$$

is proposed. The time derivative of (2.34) evaluated along the parameter drift (2.32) yields

$$\dot{V}(\underline{x}) = \underline{\dot{\tilde{\theta}}}^T \underline{\Pi}(t)^{-1} \underline{\tilde{\theta}} + \underline{\tilde{\theta}}^T \frac{d}{dt}(\underline{\Pi}(t)^{-1}) \underline{\tilde{\theta}} + \underline{\tilde{\theta}}^T \underline{\Pi}(t)^{-1} \underline{\dot{\tilde{\theta}}} \tag{2.35}$$

Using the Leibniz rule, the time derivative $^{d}/_{dt}(\underline{\Pi}(t)^{-1})$ can be calculated as

$$\frac{d}{dt}(\underline{\Pi}(t)^{-1}) = \underline{\varphi}(\underline{v})\underline{\varphi}(\underline{v})^T + \ln\lambda \int_0^t \lambda^{t-\tau}\underline{\varphi}(\underline{v}(\tau))\underline{\varphi}(\underline{v}(\tau))^T d\tau \quad . \tag{2.36}$$

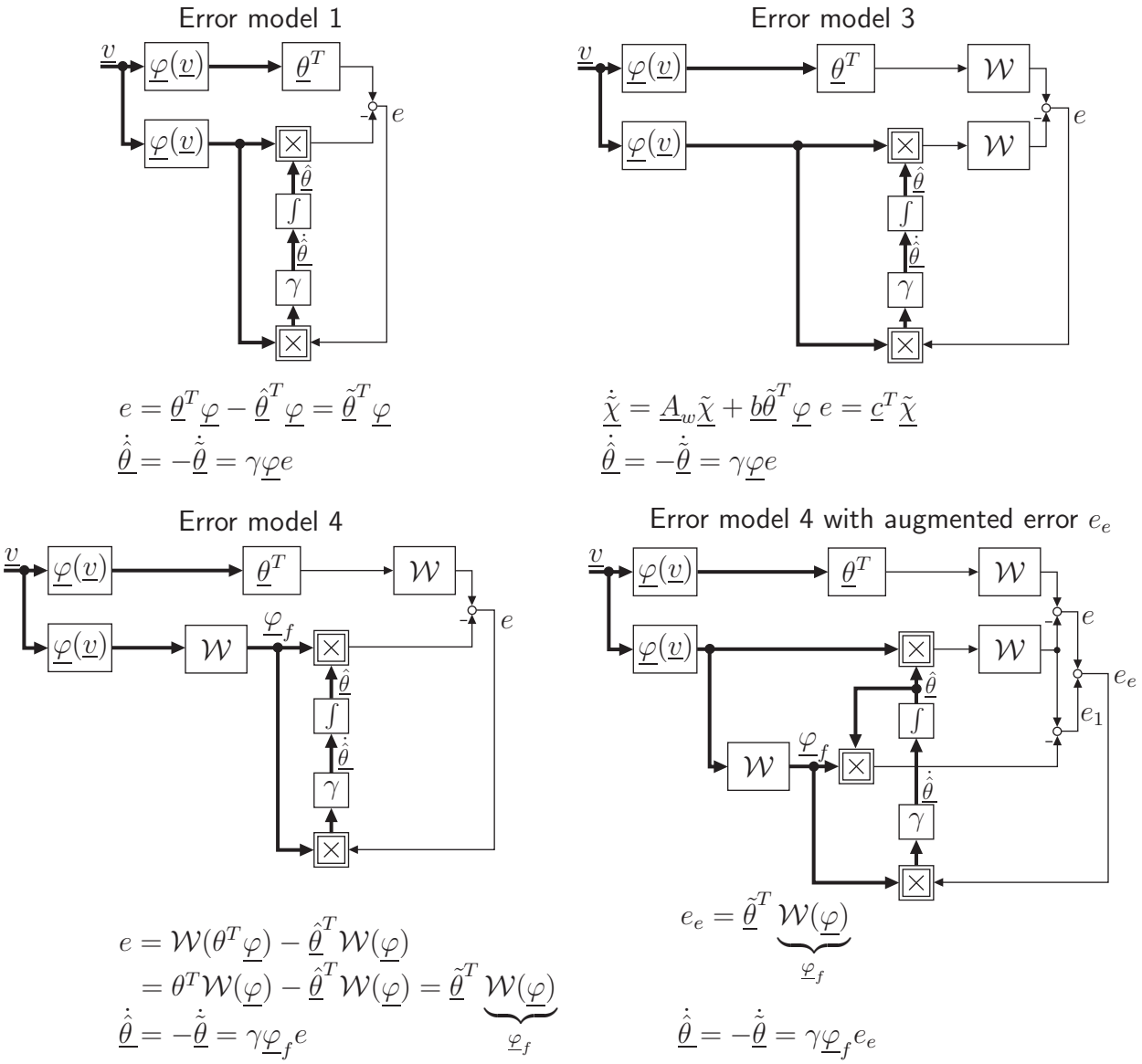

Fig. 2.6: Error models 1,3 and 4: In EM 4 the "filtered regressor" $\underline{\varphi}_f = \mathcal{W}(\underline{\varphi})$ is defined. EM 4 with augmented error e_e can be shown to be equivalent to EM4 by applying block diagram manipulation. The motivation for the error augmentation will be explained in the context of EM A3 in Section 2.4.3.

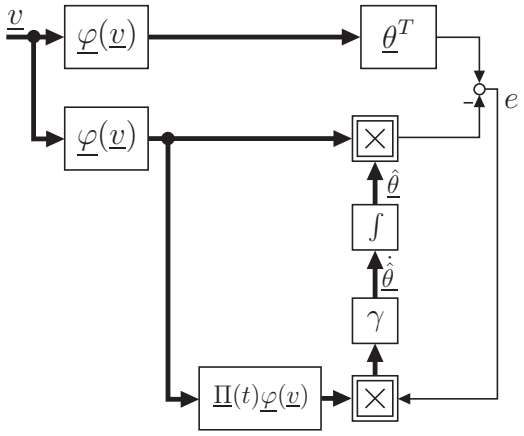

Fig. 2.7: Block diagram of error model A1.

Inserting (2.36) into (2.35) yields

$$\begin{aligned}\dot{V}(\underline{x}) &= -\gamma e \underline{\varphi}(\underline{v})^T \underline{\Pi}(t)^T \underline{\Pi}(t)^{-1} \tilde{\underline{\theta}} \\ &\quad + \tilde{\underline{\theta}}^T \Big(\underline{\varphi}(\underline{v}) \underline{\varphi}(\underline{v})^T + \ln\lambda \int_0^t \lambda^{t-\tau} \underline{\varphi}(\underline{v}(\tau)) \underline{\varphi}(\underline{v}(\tau))^T d\tau \Big) \tilde{\underline{\theta}} \\ &\quad - \gamma \tilde{\underline{\theta}}^T \underline{\Pi}(t)^{-1} \underline{\Pi}(t) \underline{\varphi} e \quad . \end{aligned} \tag{2.37}$$

With $\underline{\Pi}$ and $\underline{\Pi}^{-1}$ symmetric, $\dot{V}(\underline{x})$ is calculated as

$$\begin{aligned}\dot{V}(\underline{x}) &= -\gamma e^2 + e^2 - |\ln\lambda| V(\underline{x}) - \gamma e^2 \\ &= (1-2\gamma) e^2 - |\ln\lambda| V(\underline{x}) \quad \leq \quad 0 \end{aligned} \tag{2.38}$$

for $\gamma > 1/2$. From this result it can be concluded that the EM (2.32) is stable and hence, $\tilde{\underline{\theta}}$ is bounded. Asymptotic stability cannot be concluded since $\dot{V}(\underline{x})$ is only negative semidefinite ($e = \tilde{\underline{\theta}}^T \underline{\varphi}(\underline{v})$ can be zero for $\tilde{\underline{\theta}}$ and $\underline{\varphi}$ linearly dependent). For further considerations, $\dot{V}(\underline{x})$ is bounded from above with $(1-2\gamma)e^2 \geq \dot{V}(\underline{x})$. Hence, integrating $\dot{V}(\underline{x})$ over a time interval T yields

$$\int_{t_0}^{t_0+T} \dot{V}(\underline{x},\tau) d\tau = V(t_0+T) - V(t_0) \;\leq\; (1-2\gamma) \int_{t_0}^{t_0+T} (\tilde{\underline{\theta}}(\tau)^T \underline{\varphi}(\underline{v}(\tau))^2 d\tau \quad . \tag{2.39}$$

By applying the Cauchy-Schwarz inequality to the integral on the right hand side of (2.39) it can be bounded from below:

$$\begin{aligned}\int_{t_0}^{t_0+T} (\tilde{\underline{\theta}}(\tau)^T \underline{\varphi}(\underline{v}(\tau))^2 d\tau \int_{t_0}^{t_0+T} 1^2 d\tau &\geq \left(\int_{t_0}^{t_0+T} |\tilde{\underline{\theta}}(\tau)^T \underline{\varphi}(\underline{v}(\tau)) 1| \right)^2 \\ &\Leftrightarrow \\ \int_{t_0}^{t_0+T} (\tilde{\underline{\theta}}(\tau)^T \underline{\varphi}(\underline{v}(\tau))^2 d\tau &\geq \frac{1}{T} \Big(\underbrace{\int_{t_0}^{t_0+T} |(\tilde{\underline{\theta}}(\tau)^T \underline{\varphi}(\underline{v}(\tau))| d\tau}_{I} \Big)^2 \quad . \end{aligned} \tag{2.40}$$

In [118], it has been shown that the integral I relaxes the inequality $I \geq \epsilon > 0$ for some positive constant ϵ if the input regressor $\underline{\varphi}(\underline{v}(t))$ satisfies

$$\frac{1}{T}\int_{t_0}^{t_0+T} |\underline{w}^T \underline{\varphi}(\underline{v}(\tau)| d\tau \geq \epsilon_1 \tag{2.41}$$

for every unit vector $\underline{w} \in \mathbb{R}^m$ and for a positive constant ϵ_1. The proof of (2.41) is mathematically involved and is described in detail in [118]. Condition (2.41) is also known as "linear persistent excitation" condition ([118], e.g.). If (2.41) holds, the input regressor is said to be linear persistently exciting (l.p.e.). With $I \geq \epsilon > 0$ it follows

$$V(t_0+T) - V(t_0) \leq \underbrace{(1-2\gamma)\frac{\epsilon^2}{T}}_{-\kappa} < 0 \;\text{ for }\; \gamma > \frac{1}{2} \;. \tag{2.42}$$

Since the estimator gain γ is a design parameter, κ can be chosen arbitrarily with $0 < \kappa \leq V(t_0)$ and it follows:

$$\forall \kappa \;\text{ with }\; 0 < \kappa \leq V(t_0) \;\; \exists\, T > 0 \;\; \Rightarrow \;\; V(t) \leq V(t_0) - \kappa \;\; \forall\, t \geq t_0 + T, \text{ i.e. } \lim_{t\to\infty} V(t) = 0 \;. \tag{2.43}$$

For (2.34) to be a Lyapunov function, the matrix $\underline{\Pi}^{-1}$ has to be strictly positive definite. As shown in Appendix A.2, matrices of the form $\underline{M} = \underline{a}\underline{a}^T$ are positive semidefinite and not necessarily positive definite, and therefore, $\underline{\Pi}(t)^{-1}$ can become positive semidefinite. Using the l.p.e.-condition (see [162], e.g.)

$$\int_{t_0}^{t_0+T} \underline{\varphi}(\underline{v}(\tau))\underline{\varphi}(\underline{v}(\tau))^T d\tau \geq \alpha \underline{I} \tag{2.44}$$

for any $t_0 > 0$, with α and T positive constants and with the unity matrix $\underline{I}$, it can be concluded that $\underline{\Pi}(t)^{-1}$ is positive definite in case of a linearly persistently exciting input regressor $\underline{\varphi}(\underline{v}(t))$. Note that according to the derivations in [118], the l.p.e.-condition (2.44) is equivalent to (2.41). The update rule of the matrix $\underline{\Pi}^{-1}$ incorporates exponential forgetting. Using the derivations in Appendix A.3, the matrix update can as formulated in Laplace domain as

$$\underline{\Pi}^{-1}(s) = \frac{K}{1+sT_1}(\underline{\varphi}\underline{\varphi}^T)(s)$$

with $K = {}^{-1}\!/_{\ln\lambda}$ and $T_1 = {}^{-1}\!/_{\ln\lambda}$. For $0 < \lambda < 1$ the PT_1 system is asymptotically stable and the output $\underline{\Pi}^{-1}$ remains bounded for a bounded input $\underline{\varphi}\underline{\varphi}^T$. From the above derivations it can be concluded that (2.34) is a Lyapunov function with $\lim_{t\to\infty} V(t) = 0$. It is radially unbounded and decrescent since $\underline{\Pi}^{-1}(t)$ is bounded. Hence, the origin $\underline{x} = \underline{0}$ of EM A1 defined with Eq. (2.32) is globally uniformly asymptotically stable, i.e. the parameter error $\underline{\tilde{\theta}}$ converges to zero.

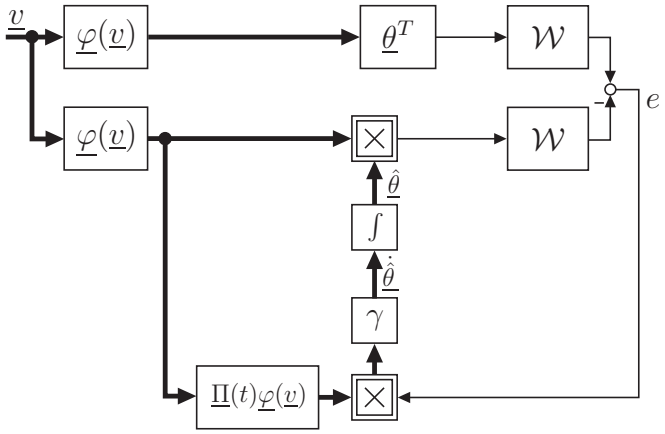

Fig. 2.8: Block diagram of error model A2.

2.4.2 Error Model A2

Using the derivations and definitions of Section 2.2.1, the equations of EM A2 (Fig. 2.8) are given with

$$\begin{aligned} \dot{\underline{\tilde{\chi}}} &= \underline{A}_w \underline{\tilde{\chi}} + \underline{b}_w (\underbrace{\underline{\tilde{\theta}}^T \underline{\varphi}(\underline{v})}_{e_n}) \\ e &= \underline{c}_w^T \underline{\tilde{\chi}} \end{aligned} \tag{2.45}$$

and

$$\dot{\underline{\hat{\theta}}} = -\dot{\underline{\tilde{\theta}}} = \gamma \underline{\Pi}(t) \underline{\varphi}(\underline{v}) e \ . \tag{2.46}$$

The state of EM A2 is defined as $\underline{x}^T = [\underline{\tilde{\chi}}^T \ \ \underline{\tilde{\theta}}^T]$. It is assumed that the LTI-system $\mathcal{W}$ is strict positive real (SPR) and therefore, the famous Kalman-Yakubovich-Lemma (KYL) applies: For an SPR-system $\{\underline{c}^T, \ \underline{A}, \ \underline{b}\}$ there exist symmetric positive definite matrices $\underline{P}$ and $\underline{Q}$ that satisfy

$$\underline{A}^T \underline{P} + \underline{P} \underline{A} = -\underline{Q} \tag{2.47a}$$

$$\underline{P} \underline{b} = \underline{c} \ . \tag{2.47b}$$

For a positive real (PR-) system, a positive semi-definite Matrix $\underline{Q} = \underline{Q}^T$ satisfies (2.47a). Note that an asymptotic stable LTI-system that is not PR still satisfies (2.47a) with $\underline{P} = \underline{P}^T > 0$ and $\underline{Q} = \underline{Q}^T > 0$.

The stability of EM A2 is analyzed with the Lyapunov candidate

$$V(\underline{x}) = \underline{\tilde{\chi}}^T \underline{P} \underline{\tilde{\chi}} + \underline{\tilde{\theta}}^T \underline{\Pi}(t)^{-1} \underline{\tilde{\theta}} \ . \tag{2.48}$$

Using Eq. (2.36) and the KYL, the time derivative of (2.48) evaluated along the parameter drift (2.46) yields

$$\begin{aligned}
\dot{V}(\underline{x}) &= \dot{\underline{\tilde{\chi}}}^T \underline{P}\underline{\tilde{\chi}} + \underline{\tilde{\chi}}^T \underline{P}\dot{\underline{\tilde{\chi}}} + \dot{\underline{\tilde{\theta}}}^T \underline{\Pi}^{-1}\underline{\tilde{\theta}} + \underline{\tilde{\theta}}^T \frac{d}{dt}(\underline{\Pi}^{-1})\underline{\tilde{\theta}} + \underline{\tilde{\theta}}^T \underline{\Pi}^{-1}\dot{\underline{\tilde{\theta}}} \\
&= (\underline{A}_w\underline{\tilde{\chi}} + \underline{b}_w e_n)^T \underline{P}\underline{\tilde{\chi}} + \underline{\tilde{\chi}}^T \underline{P}(\underline{A}_w\underline{\tilde{\chi}} + \underline{b}_w e_n) \\
&\quad -\gamma e \underline{\varphi}^T \underline{\Pi}^T \underline{\Pi}^{-1}\underline{\tilde{\theta}} \\
&\quad +\underline{\tilde{\theta}}^T \Big(\underline{\varphi}\underline{\varphi}^T + \ln\lambda \int_0^t \lambda^{t-\tau}\underline{\varphi}\underline{\varphi}^T d\tau\Big)\underline{\tilde{\theta}} \\
&\quad -\gamma \underline{\tilde{\theta}}^T \underline{\Pi}^{-1}\underline{\Pi}\underline{\varphi} e \\
&= \underline{\tilde{\chi}}^T(\underline{A}_w^T\underline{P} + \underline{P}\underline{A}_w)\underline{\tilde{\chi}} + e_n \underline{b}_w^T \underline{P}\underline{\tilde{\chi}} + \underline{\tilde{\chi}}^T \underline{P}\underline{b}_w e_n \\
&\quad -2\gamma e \underline{\tilde{\theta}}^T \underline{\varphi} + (\underline{\tilde{\theta}}^T \underline{\varphi})^2 - |\ln\lambda| \underline{\tilde{\theta}}^T \underline{\Pi}^{-1}\underline{\tilde{\theta}} \\
&= -\underline{\tilde{\chi}}^T \underline{Q}\underline{\tilde{\chi}} + 2(1-\gamma)e_n e + e^2 - |\ln\lambda| \underline{\tilde{\theta}}^T \underline{\Pi}^{-1}\underline{\tilde{\theta}} \qquad (2.49)
\end{aligned}$$

with $0 < \lambda < 1$. The term $e_n e$ is not positive $\forall\, t$ and thus, (2.49) is indefinite. Therefore, (2.48) is not a Lyapunov function. Bounding $\dot{V}(\underline{x})$ from above with $2(1-\gamma)e_n e + e^2 \geq \dot{V}(\underline{x})$ and integrating $\dot{V}(\underline{x})$ over time yields

$$\int_0^t \dot{V}(\underline{x}(\tau))d\tau = V(\underline{x}(t)) - V(\underline{x}(0)) \;\leq\; 2(1-\gamma) \underbrace{\int_0^t e_n(\tau)e(\tau)d\tau}_{I_1} + \underbrace{\int_0^t e(\tau)^2 d\tau}_{I_2} \quad . \qquad (2.50)$$

For all t, $I_2 \geq 0\ \forall t$ holds. Integral I_1 can be bounded from below, too according to

$$\int_0^t e_n(\tau)e(\tau)d\tau = \int_0^t e_n(\tau)\mathcal{W}(e_n(\tau))d\tau \geq 0\ \forall\, t \qquad (2.51)$$

if $\underline{\tilde{\chi}}(0) = \underline{0}$. Eq. (2.51) follows from an important property of positive real systems: Given a PR system $\mathcal{S}$ with input $\underline{u}$, output $\underline{y}$ and state $\underline{z}$, then

$$\int_0^t \underline{u}(\tau)^T \underline{y}(\tau)d\tau = \int_0^t \underline{u}(\tau)^T \mathcal{S}(\underline{u}(\tau))d\tau \geq 0\ \forall\, t \ \text{ if } \ \underline{z}(0) = \underline{0} \ . \qquad (2.52)$$

The proof can can be found in [82], e.g.. It can further be guaranteed that $I_1 > 0$ if either of the following conditions applies:

i) $e_n(t) > 0\ \ \forall\, t$

ii) $e_n(t) < 0\ \ \forall\, t$

Assuming that either condition i) or ii) applies and choosing the estimator gain

$$\gamma > \frac{I_2}{2I_1} + 1 \qquad (2.53)$$

it follows

$$V(\underline{x}(t)) - V(\underline{x}(0)) \leq -\kappa \ \text{ with } \ 0 < \kappa \leq V(\underline{x}(0)) \qquad (2.54)$$

and therefore,

$$\forall\kappa \text{ with } 0 < \kappa \leq V((\underline{x}(0))\ \exists\, T > 0 \ \Rightarrow\ V(\underline{x}(t)) \leq V(\underline{x}(0)) - \kappa \ \ \forall\, t \geq T, \text{ i.e. } \lim_{t\to\infty} V(t) = 0\ . \qquad (2.55)$$

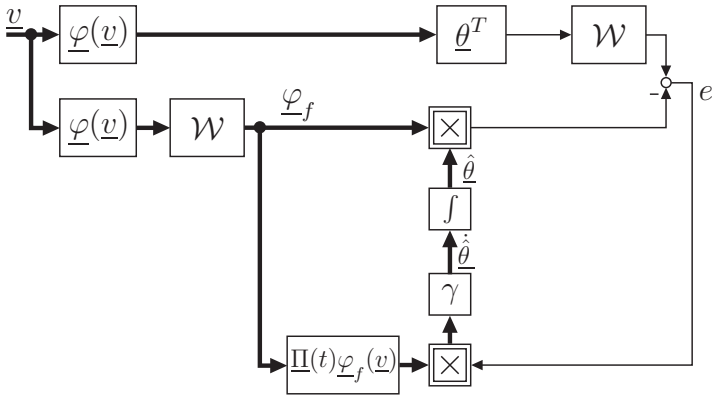

Fig. 2.9: Block diagram of error model A3.

Following the considerations for EM A1, it can be concluded that the radially unbounded storage function (2.48) is positive definite in case of an l.p.e. input regressor $\underline{\varphi}(\underline{v})$ (see (2.41) or(2.44)). Furthermore, $\underline{\Pi}(t)^{-1}$ is bounded and hence, (2.48) is a decrescent function.

Thus, if $\underline{\varphi}(\underline{v})$ is l.p.e. and either of the conditions i) or ii) applies, the origin $\underline{x} = \underline{0}$ of EM A2 is globally uniformly asymptotically stable.

2.4.3 Error Model A3

If the LTI-system $\mathcal{W}$ is not SPR but asymptotically stable, the error model A3 is proposed. It is obtained by replacing the gradient algorithm in EM 4 (Fig. 2.6) with the RLS-adaptation law. Its structure is depicted in Fig. 2.9.

With the definition of the filtered regressor

$$\underline{\varphi}_f(\underline{v}) = \mathcal{W}(\underline{\varphi}(\underline{v})) \tag{2.56}$$

the equations

$$\begin{aligned} e &= \mathcal{W}(\underline{\theta}^T\underline{\varphi}(\underline{v})) - \underline{\hat{\theta}}^T\mathcal{W}(\underline{\varphi}(\underline{v})) = \underline{\theta}^T\mathcal{W}(\underline{\varphi}(\underline{v})) - \underline{\hat{\theta}}^T\mathcal{W}(\underline{\varphi}(\underline{v})) = \underline{\tilde{\theta}}^T\underline{\varphi}_f(\underline{v}) \\ \dot{\underline{\hat{\theta}}} &= -\dot{\underline{\tilde{\theta}}} = \gamma\underline{\Pi}(t)\underline{\varphi}_f(\underline{v})e \end{aligned} \tag{2.57}$$

constitute the EM A3 with

$$\underline{\Pi}(t)^{-1} = \int_0^t \lambda^{t-\tau}\underline{\varphi}_f(\tau)\underline{\varphi}_f(\tau)^T d\tau \quad . \tag{2.58}$$

The transformation $\mathcal{W}(\underline{\theta}^T\underline{\varphi}(\underline{v})) = \underline{\theta}^T\mathcal{W}(\underline{\varphi}(\underline{v}))$ in (2.57) applies since the parameter vector $\underline{\theta}$ is constant.

Asymptotic stability of $\mathcal{W}$ is required since the filtered regressor $\underline{\varphi}_f$ might not be bounded and could not be computed uniquely otherwise. Hence, in case of an asymptotically stable system $\mathcal{W}$, the equations (2.57) are formally equivalent to the equations (2.32) of EM A1. Therefore, the stability proof of EM A1 also applies to EM A3 and it can be concluded that the origin of (2.57) is globally uniformly asymptotically stable if $\underline{\varphi}(\underline{v})$ is l.p.e. and if $\mathcal{W}$ is asymptotically stable.

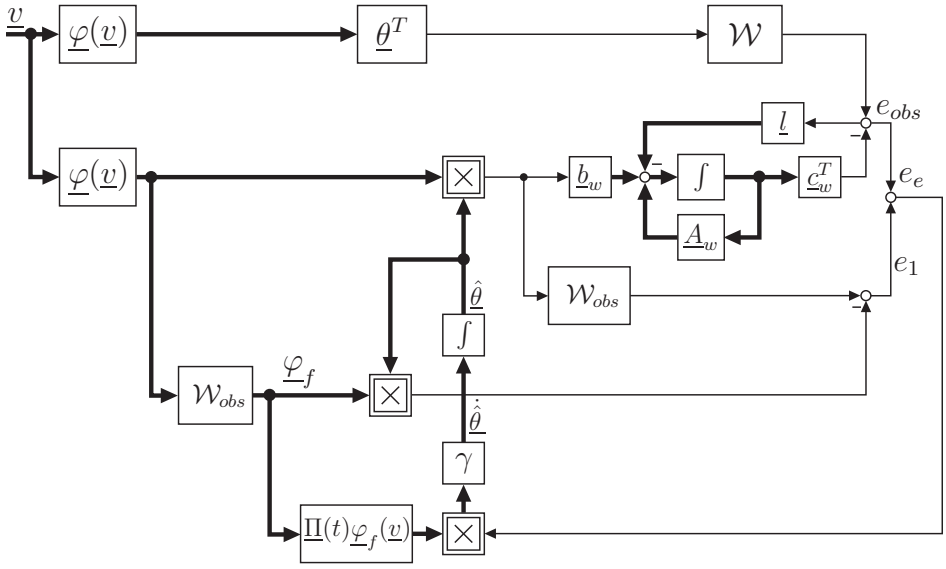

Fig. 2.10: Error model A3 with augmented error e_e in combination with a neural observer.

In practical applications the known LTI-system $\mathcal{W}$ often appears as double integrator with $G_w(s) = \frac{1}{s^2}$ which does not meat the requirement of asymptotic stability. In the following, it is shown how EM A3 can still be applied by using a neural observer (Section 2.2.2).

Inspired by the EM 4 with augmented error e_e (Fig. 2.6), the configuration illustrated in Fig. 2.10 is proposed. The LTI-Blocks $\mathcal{W}_{obs}$ are equivalent to the dynamic system $\mathcal{W}_{obs}$ in Fig. 2.4. With the appropriate choice of the observer gain $\underline{l}$, the system $\mathcal{W}_{obs}$ is asymptotically stable.

The augmented error e_e is given by

$$\begin{aligned} e_e &= \underbrace{\mathcal{W}_{obs}((\underline{\theta}^T - \hat{\underline{\theta}}^T)\underline{\varphi})}_{e_{obs}} + \mathcal{W}_{obs}(\hat{\underline{\theta}}^T \underline{\varphi}) - \hat{\underline{\theta}}^T \mathcal{W}_{obs}(\underline{\varphi}) \\ &= \underline{\theta}^T \mathcal{W}_{obs}(\underline{\varphi}) - \hat{\underline{\theta}}^T \mathcal{W}_{obs}(\underline{\varphi}) \\ &= \tilde{\underline{\theta}}^T \underline{\varphi}_f \end{aligned} \tag{2.59}$$

with $\underline{\varphi}_f = \mathcal{W}_{obs}(\underline{\varphi})$. For the derivation of (2.59), the block diagram manipulation of Fig. 2.4 is used to calculate e_{obs}.

The augmented error e_e and the filtered regressor $\underline{\varphi}_f = \mathcal{W}_{obs}(\underline{\varphi})$ are fed into the parameter adaptation algorithm and thus, the adaptive law

$$\dot{\hat{\underline{\theta}}} = -\dot{\tilde{\underline{\theta}}} = \gamma \underline{\Pi}(t) \underline{\varphi}_f e_e \tag{2.60}$$

is obtained with $\underline{\Pi}(t)^{-1}$ according to (2.58). Equations (2.59) and (2.60) are equivalent to (2.57) and hence, the configuration of Fig. 2.10 yields and implementable version of the EM A3 combined with a neural observer.

2.4.4 Discussion

The RLS-algorithm with forgetting factor is in practice the most common method for the identification of linearly parameterized time varying plant. Compared to the LMS-algorithm, it shows much faster convergence. Furthermore, the RLS-algorithm is less sensitive to noise and disturbances than LMS. Therefore, the error models 1-4 introduced in [118] have been modified by using the RLS-algorithm as adaptive law instead of the LMS-algorithm. The new error models are called EM A1-A3. On the basis of the fundamental theory of the error model framework introduced in [118], the convergence behavior of EM A1-A3 has been analyzed and conditions have been formulated that guarantee asymptotic stability. Similar to the EM 4 in [118], EM A3 is the most general case since the error transfer function $G_w(s)$ does not need to be SPR. The dynamics of $G_w(s)$ may even be unstable, since they can be stabilized when combining EM A3 with a neural observer.

2.5 Error Models for Nonlinear Parameterization

In this section, parameter identification of NLP-models according to Eq. (2.5b) is considered. Particularly, systems whose output y_n is not directly measurable but filtered by a known LTI-system (compare configuration Fig. 2.3) are analyzed. However, in order to derive important convergence conditions for certain classes of NLP-models, first, the case of an accessible output $\hat{y}_n$ is investigated. Throughout this section, parameter convergence is analyzed within the error model framework introduced in Section 2.2.1.

2.5.1 Error Model B1

EM B1 is depicted in Fig. 2.11. In the following, the adaptation laws GS and GN (see Tab. 2.1) will be considered and the respective error models will be referred to as EM B1-GS and EM B1-GN. It is well known that the parameter error of EM B1 will converge if the quadratic error criterion (see Tab. 2.1) is convex. In the following, different conditions that guarantee stability will be derived.

Error Model B1-Gradient Search

The EM B1-GS is given by the equations

$$\begin{aligned} e &= y - \hat{y} = n(\underline{\eta}, \underline{v}) - n(\hat{\underline{\eta}}, \underline{v}) \\ \dot{\hat{\underline{\eta}}} &= -\dot{\tilde{\underline{\eta}}} = \gamma \nabla n^T e \ . \end{aligned} \tag{2.61}$$

Its state is defined by $\underline{x} = \tilde{\underline{\eta}}$. With the decrescent radially unbounded Lyapunov candidate

$$V(\underline{x}) = \frac{1}{2} \tilde{\underline{\eta}}^T \tilde{\underline{\eta}} \tag{2.62}$$

it follows

$$\dot{V}(\underline{x}) = \tilde{\underline{\eta}}^T \dot{\tilde{\underline{\eta}}} = -\gamma \tilde{\underline{\eta}}^T \nabla n^T e \ . \tag{2.63}$$

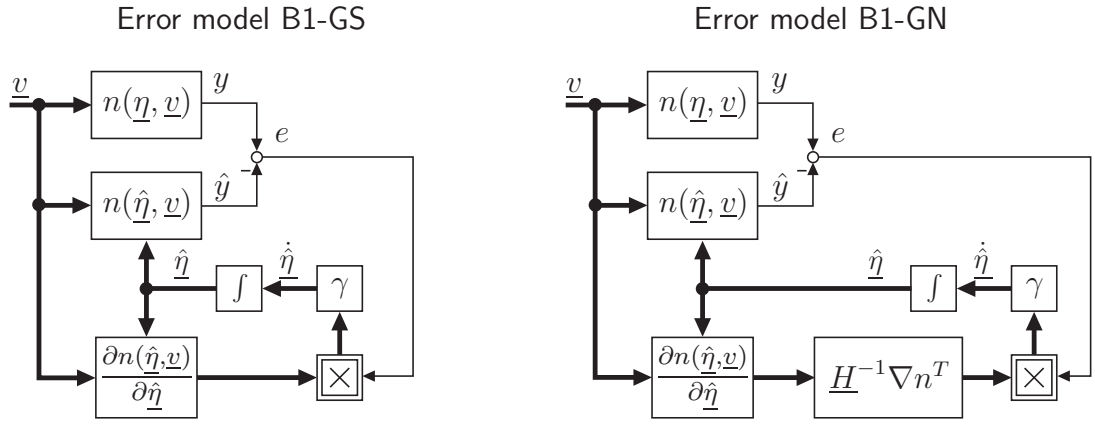

Fig. 2.11: Error models B1-GS and B1-GN: Note that the gradient $\frac{\partial n(\hat{\underline{\eta}},\underline{v})}{\partial \hat{\underline{\eta}}} = \nabla n$ is a row vector.

It can be seen that the stability condition $\dot{V}(\underline{x}) \leq 0$ cannot be generally guaranteed.

In order to derive constraints for $n(\hat{\underline{\eta}},\underline{v})$ that will guarantee stability, first, scalar parameterization ($q = 1$) is considered, i.e. $\hat{y} = n(\hat{\eta},\underline{v})$. Let's assume that $n(\hat{\underline{\eta}},\underline{v})$ is strictly monotonic with respect to $\hat{\eta}$, i.e. ${}^{\partial n(\hat{\eta},\underline{v})}/_{\partial\hat{\eta}} > 0 \; \forall \; \hat{\eta}$ or ${}^{\partial n(\hat{\eta},\underline{v})}/_{\partial\hat{\eta}} < 0 \; \forall \; \hat{\eta}$. Fig. 2.12 illustrates a strictly monotonically decreasing function $n(\hat{\underline{\eta}},\underline{v}^*)$ at a particular input $\underline{v}^*$. For case 1 and case 2 it follows

$$\begin{aligned} \text{sign}(\tilde{\eta}_1)\text{sign}(\nabla n)\text{sign}(e_1) &= 1 \\ \text{sign}(\tilde{\eta}_2)\text{sign}(\nabla n)\text{sign}(e_2) &= 1 \; . \end{aligned}$$

The same result is obtained when considering a strictly monotonically increasing function. Hence, with a positive estimator gain γ we have

$$\dot{V}(x) = -\gamma\tilde{\eta}\nabla n e < 0 \; \forall \; \tilde{\eta}\backslash\{0\} \quad , \tag{2.64}$$

i.e., in the scalar case, the origin $\tilde{\eta} = 0$ of (2.61) is globally uniformly asymptotically stable for strictly monotonic parameterization.

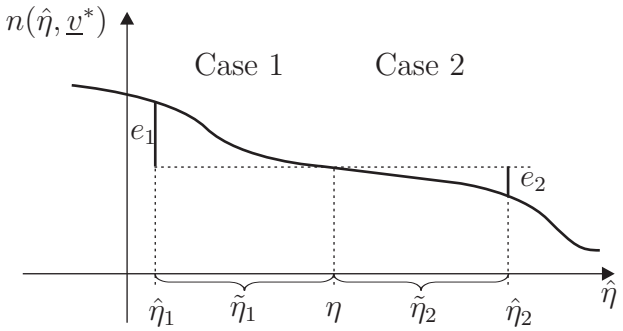

Fig. 2.12: Example of a monotonically decreasing parameterized function $n(\hat{\eta},\underline{v}^*)$.

In the nonscalar case we have

$$\underline{\tilde{\eta}}^T \nabla n e = \tilde{\eta}_1 \nabla n_1 e + \ldots + \tilde{\eta}_q \nabla n_q e \tag{2.65}$$

and the condition of strictly monotonic parameterization does not imply $\text{sign}(\underline{\tilde{\eta}}^T \nabla n e) = 1$.

For further considerations, the definition of local parameterization is introduced:

Definition 2.5.1 Local Parameterization
Given a function $n(\underline{\hat{\eta}}, \underline{v}) : \mathbb{R}^q \times \mathbb{V} \to \mathbb{R}$ with $\mathbb{V} \subset \mathbb{R}^r$. For every parameter $\hat{\eta}_i,\ i = 1 \ldots q$, there is a region $\mathbb{V}_i$ with $\mathbb{V}_i \subset \mathbb{V}$ and with $\mathbb{V}_i \cap \mathbb{V}_j = 0$ for $i \neq j$. A parameter $\underline{\hat{\eta}}_i$ is called local if its value affects the value of $n(\underline{\hat{\eta}}, \underline{v})$ only if $\underline{v}$ is element of the region $\mathbb{V}_i$, i.e.

$$\frac{\partial n(\underline{\hat{\eta}}, \underline{v})}{\partial \hat{\eta}_i} = \nabla n_i \approx 0 \ \text{ for } \ \underline{v} \notin \mathbb{V}_i \ .$$

The region $\mathbb{V}_i$ is denoted as the activation region of the parameter $\hat{\eta}_i$.

If the function $\hat{y} = n(\underline{\hat{\eta}}, \underline{v})$ is locally parameterized, Eq. (2.65) is given with

$$\underline{\tilde{\eta}}^T \nabla n^T e \approx 0 + \ldots + \tilde{\eta}_i \nabla n_i e + \ldots 0 \tag{2.66}$$

for $\underline{v} \in \mathbb{V}_i,\ i = 1 \ldots q$. Furthermore, in case of local and strictly monotonic parameterization we have

$$\underline{\tilde{\eta}}^T \nabla n^T e \approx \tilde{\eta}_i \nabla n_i e > 0 \tag{2.67}$$

for $\underline{v} \in \mathbb{V}_i,\ i = 1 \ldots q$. Thus, the time derivative $\dot{V}(\underline{x})$ (2.63) is negative semidefinite function and stability can be concluded for EM B1-GS. It can clearly be seen that $\dot{V} = 0$ only if $\tilde{\eta}_i = 0$ and $\underline{v} \in \mathbb{V}_i$ or $\underline{v} \notin \mathbb{V}_i,\ i = 1 \ldots q$. If it can be guaranteed that during the time interval $[t_0, t_0 + T]$, the input $\underline{v}(t)$ has been element of every activation region $\mathbb{V}_i$ we have

$$\int_{t_0}^{t_0+T} \dot{V}(\underline{x}, \tau) d\tau = V(t_0 + T) - V(t_0) \leq -\kappa \text{ with } \kappa < 0 \ . \tag{2.68}$$

Definition 2.5.2 *Nonlinear Local Persistent Excitation (n.l.p.e.)*
Given a locally parameterized function $n(\underline{\hat{\eta}}, \underline{v}) : \mathbb{R}^q \times \mathbb{V} \to \mathbb{R}$ with the input space $\mathbb{V} \subset \mathbb{R}^r$. The input $\underline{v}(t)$ is nonlinearly locally persistently exciting (n.l.p.e.) if during every consecutive finite time interval $[t_k, t_k + T]$ with $t_{k+1} = t_k + T$ and $k = 0, 1, 2 \ldots \infty$, $\underline{v}(t)$ passes through every activation region $\mathbb{V}_i$.

If $\underline{v}$ is n.l.p.e it can be concluded that

$$\forall \kappa \ \text{ with } \ 0 < \kappa \leq V(t_0) \ \ \exists\, \delta > 0 \ \ \Rightarrow \ \ V(t) \leq V(t_0) - \kappa \ \ \forall\, t \geq \delta, \text{ i.e. } \lim_{t \to \infty} V(t) = 0 \tag{2.69}$$

and thus, the following corollary can be formulated:

Corollary 2.5.3
Given a function $y = n(\underline{\eta}, \underline{v})$ with unknown parameters $\underline{\eta}$ and its approximation $\hat{y} = n(\underline{\hat{\eta}}, \underline{v})$: With local and strict monotonic parameterization of $n(\underline{\hat{\eta}}, \underline{v})$ and with the bounded input signal $\underline{v}(t)$ being n.l.p.e., the gradient search algorithm yields uniformly globally asymptotically stable parameter adaptation, i.e. $\lim_{t \to \infty} \underline{\tilde{\eta}} = \underline{0}$.

Error Model B1-Gauss-Newton

The equations

$$\begin{aligned} e &= y - \hat{y} = n(\underline{\eta}, \underline{v}) - n(\hat{\underline{\eta}}, \underline{v}) \\ \dot{\hat{\underline{\eta}}} &= -\dot{\tilde{\underline{\eta}}} = \gamma \underline{H}(t)^{-1} \nabla n^T e \end{aligned} \tag{2.70}$$

constitute the error model B1-GN. The state is defined as $\underline{x} = \tilde{\underline{\eta}}$. The matrix $\underline{H}(t)$ is an approximation of the Hessian of the error criterion $E(\hat{\underline{\eta}}, t) = \int_0^t \lambda^{t-\tau}(y(\tau) - \hat{y}(\hat{\underline{\eta}}, \tau))^2 d\tau$ and is calculated as $\underline{H}(t) = \int_0^t \lambda^{t-\tau} \nabla \hat{y}(\tau)^T \nabla \hat{y}(\tau) d\tau = \int_0^t \lambda^{t-\tau} \nabla n(\tau)^T \nabla n(\tau) d\tau$ (see Tab. 2.1). Note that $\underline{H}(t)$ as well as $\underline{H}(t)^{-1}$ are symmetric as well as positive semidefinite. If condition (2.44) applies for the gradient vector ∇n, i.e.

$$\int_{t_0}^{T+t_0} \nabla n(\underline{v}(\tau))^T \nabla n(\underline{v}(\tau)) \geq \alpha I \text{ for } \alpha > 0 \quad , \tag{2.71}$$

$\underline{H}(t)$ and $\underline{H}^{-1}$ are even positive definite.

For the analysis of the convergence properties, the Lyapunov candidate

$$V(\underline{x}) = \tilde{\underline{\eta}}^T \underline{H}(t) \tilde{\underline{\eta}} \tag{2.72}$$

is proposed. It is radially unbounded and if (2.71) is relaxed, $V(\underline{x})$ is positive definite and decrescent. The time derivate evaluated along the parameter drift $\dot{\tilde{\underline{\eta}}}$ yields

$$\begin{aligned} \dot{V}(\underline{x}) &= \dot{\tilde{\underline{\eta}}}^T \underline{H}(t) \tilde{\underline{\eta}} + \tilde{\underline{\eta}}^T \dot{\underline{H}}(t) \tilde{\underline{\eta}} + \tilde{\underline{\eta}}^T \underline{H}(t) \dot{\tilde{\underline{\eta}}} \\ &= -2\gamma \tilde{\underline{\eta}}^T \nabla n^T e + (\tilde{\underline{\eta}}^T \nabla n^T)^2 - |\ln \lambda| V(\underline{x}) \\ &\leq (\tilde{\underline{\eta}}^T \nabla n^T)^2 - 2\gamma \tilde{\underline{\eta}}^T \nabla n^T e \quad . \end{aligned} \tag{2.73}$$

This inequality is obtained following the argumentation for the derivation of (2.49). Considering the integral equation

$$\int_{t_0}^{t_0+T} \dot{V}(\underline{x}, \tau) d\tau = V(t_0+T) - V(t_0) \leq \underbrace{\int_{t_0}^{t_0+T} (\tilde{\underline{\eta}}(\tau)^T \nabla n(\tau)^T)^2 d\tau}_{I_1} - 2\gamma \underbrace{\int_{t_0}^{t_0+T} \tilde{\underline{\eta}}(\underline{\tau})^T \nabla n(\tau) e(\tau) d\tau}_{I_2} \tag{2.74}$$

it follows that $V(t_0+T) - V(t_0) < 0$ if $\underline{v}$ is n.l.p.e and if $n(\hat{\underline{\eta}}, \underline{v})$ is strict monotonically parameterized and with $\gamma > \frac{I_1}{2I_2}$. Thus, conclusion (2.69) applies also for EM B1-GN and the following corollary can be formulated:

Corollary 2.5.4
Given a function $y = n(\underline{\eta}, \underline{v})$ with unknown parameters $\underline{\eta}$ and its approximation $\hat{y} = n(\hat{\underline{\eta}}, \underline{v})$. With strict local an monotonic parameterization of $n(\hat{\underline{\eta}}, \underline{v})$ and with a bounded input signal $\underline{v}(t)$ being n.l.p.e. and being such that the gradient vector $\nabla n(\underline{v})$ meets the condition (2.71)*, the Gauss-Newton algorithm yields uniformly globally asymptotically stable parameter adaptation, i.e.* $\lim_{t \to \infty} \tilde{\underline{\eta}} = \underline{0}$.

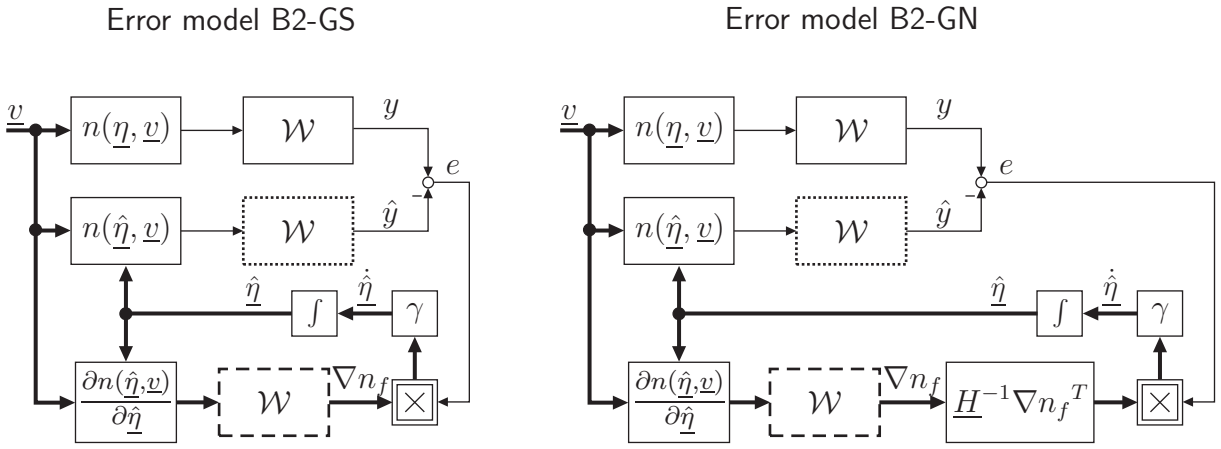

Fig. 2.13: Error models B2-GS and B2-GN: The dashed block is applied only if the parameterization of $n(\underline{\hat{\eta}},\underline{v})$ is quasilinear. Otherwise the gradient is not filtered and the dotted block is replaced with a neural observer (see Section 2.2.2).

2.5.2 Error Model B2

With error model B2 the case of a non measurable output $y_n = n(\underline{\eta},\underline{v})$ is considered whereas it is assumed, that the nonlinearity $n(\underline{\eta},\underline{v})$ is locally and strict monotonically parameterized. The system output $y = \mathcal{W}(y_n)$ is measurable whereas $\mathcal{W}$ is an asymptotically stable and known LTI-system. Similarly to Section 2.5.1, two different adaptation laws will be distinguished and the corresponding error models will be referred to as error model B2 - Gradient Search and Error Model B2 - Gauss-Newton (See Fig. 2.13).

Error Model B2 - Gradient search

The equations of EM B2-GS can be derived analogous to EM A2 and are given by

$$\begin{aligned} \dot{\tilde{\underline{\chi}}} &= \underline{A}_w\tilde{\underline{\chi}} + \underline{b}_w(\underbrace{n(\underline{\eta},\underline{v}) - n(\hat{\underline{\eta}},\underline{v})}_{e_n}) \\ e &= \underline{c}_w^T\tilde{\underline{\chi}} \end{aligned} \tag{2.75}$$

and

$$\dot{\hat{\underline{\eta}}} = -\dot{\tilde{\underline{\eta}}} = \gamma\nabla n_f e \ , \tag{2.76}$$

whereas the filtered gradient is introduced as $\nabla n_f = \mathcal{W}(\nabla n)$. This is inspired by the filtered regressor $\underline{\varphi}_f$ that occurs in EM 4. The state of EM B2-GS is defined as $\underline{x}^T = [\tilde{\underline{\chi}}^T\ \tilde{\underline{\eta}}^T]$.

In order to analyze the convergence behavior of EM B2-GS, the positive definite and radially unbounded Lyapunov candidate

$$V(\underline{x}) = \underline{\tilde{\chi}}^T \underline{P} \underline{\tilde{\chi}} + \frac{1}{2} \underline{\tilde{\eta}}^T \underline{\tilde{\eta}} \tag{2.77}$$

with $\underline{P} = \underline{P}^T > 0$ is proposed. The time derivative evaluated along the parameter drift $\dot{\underline{\hat{\eta}}}$ can be calculated as

$$\dot{V}(\underline{x}) = -\underline{\tilde{\chi}}^T \underline{Q} \underline{\tilde{\chi}} + 2 \underline{\tilde{\chi}}^T \underline{P} \underline{b} e_n - \gamma \underline{\tilde{\eta}}^T \nabla {n_f}^T e \tag{2.78}$$

whereas property (2.47a) is applied. Eq. (2.78) is indefinite and hence, (2.77) is not a Lyapunov function. The last term of (2.78) can be written as

$$\gamma \underline{\tilde{\eta}}^T \nabla {n_f}^T e = \gamma \underline{\tilde{\eta}}^T \mathcal{W}(\nabla n^T) \mathcal{W}(e_n) \quad . \tag{2.79}$$

Since $\hat{y} = n(\underline{\hat{\eta}}, \underline{v})$ is locally and strict monotonically parameterized, the relation of the signs of ∇n_i and e_n is

$$\nabla n_i e_n = \begin{cases} > 0 \;\text{ if }\; \text{sign}(\underline{\tilde{\eta}}_i) > 0 \\ < 0 \;\text{ if }\; \text{sign}(\underline{\tilde{\eta}}_i) < 0 \end{cases} \tag{2.80}$$

as it is illustrated in Fig. 2.12.

It is obvious that this relation is generally not maintained for the filtered signals $\mathcal{W}(\nabla n_i^T)$ and $\mathcal{W}(e_n)$. Since this relation is crucial for parameter convergence, two conditions are given where each of them provides maintenance of (2.80) in case of filtering with $\mathcal{W}$:

i) The bandwidth of the signals $\nabla n_i(\underline{\hat{\eta}}, \underline{v})$ and $e_n(\underline{\hat{\eta}}, \underline{v})$ is small compared to the bandwidth of the LTI-System $\mathcal{W}$.

ii) The parameterization of $\hat{y}_n$ is quasilinear, i.e. $\hat{y}_n \approx n(\underline{\hat{\eta}}^*, \underline{v}) + \nabla n(\underline{\hat{\eta}}^*, \underline{v})(\underline{\hat{\eta}} - \underline{\hat{\eta}}^*)$.

If condition i) applies, the filtering with $\mathcal{W}$ can be approximated with a multiplication by a constant K. Thus, the filtering of the gradient (dashed block in Fig, 2.13) can be omitted and we have $\nabla n_i \mathcal{W}(e_n) \approx K \nabla n_i e_n$ and the sign-condition (2.80) applies also to for the filtered signal $\mathcal{W}(e_n)$. This condition can be relaxed by either applying an appropriate input signal $\underline{v}$ or by applying a neural observer.

In case ii) we have $e_n = y_n - \hat{y}_n \approx (\eta_i - \hat{\eta}_i) \nabla n_i$. Note, that this approximation is exact for LP-systems. Thus, $\mathcal{W}(\nabla n_i)\mathcal{W}(e_n) \approx \mathcal{W}(\nabla n_i)\mathcal{W}((\eta_i - \hat{\eta}_i)\nabla n_i)$ and for a parameter change $\underline{\hat{\eta}}(t)$ that is slow in the sense that the bandwidth of $\underline{\hat{\eta}}(t)$ is smaller than the bandwidth of $\mathcal{W}$, we can write $\mathcal{W}(\nabla n_i)\mathcal{W}((\eta_i - \hat{\eta}_i)\nabla n_i) \approx (\eta_i - \hat{\eta}_i)\mathcal{W}(\nabla n_i)^2$. Thus, condition (2.80) can be relaxed.

Integrating (2.78) over a time period yields

$$\int_{t_0}^{t_0+T} \dot{V}(\underline{\tilde{\eta}}, \tau) d\tau = V(t_0+T) - V(t_0) \leq 2 \underbrace{\int_{t_0}^{t_0+T} \underline{\tilde{\chi}}^T(\tau) \underline{P} \underline{b} e_n(\tau) d\tau}_{I_1} - \gamma \underbrace{\int_{t_0}^{t_0+T} \underline{\tilde{\eta}}(\tau)^T \nabla {n_f}(\tau)^T e(\tau) d\tau}_{I_2} \tag{2.81}$$

since $\underline{\tilde{\chi}}^T \underline{Q} \underline{\tilde{\chi}}$ is positive definite. If either condition i) or ii) applies, and in case of $\underline{v}$ being n.l.p.e, the integral I_2 is strictly positive. It follows that $V(t_0+T) - V(t_0) < 0$ if $\gamma > \frac{2I_1}{I_2}$. Therefore, (2.69) applies also for EM B1-GN and the following can be concluded:

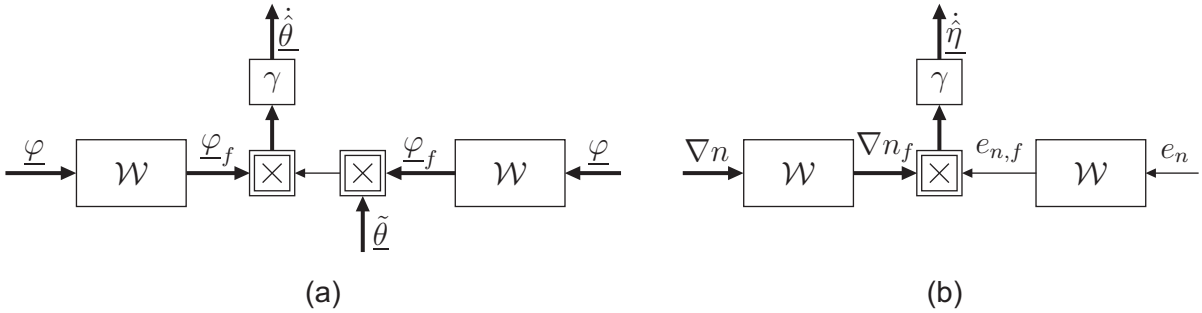

Fig. 2.14: Block diagrams of adaptation laws for error model 4 (a) and Error model B2-GS (b).

The origin $\underline{x} = 0$ of EM B2-GS is globally uniformly asymptotically stable, i.e. the parameter error converges to zero, if the input $\underline{v}$ is n.l.p.e. and if either condition i) or condition ii) applies. Since conditions i) and ii) are derived in a nonformal descriptive manner the convergence of EM B2-GS has not formally been proven, but design rules that guarantee parameter convergence are provided by means of obvious conclusions.

Remark 2.5.5 *The reasoning for the filtering method applied for EM 3 and EM 4 [118] as well as for the error models introduced in this chapter can be explained in an illustrative manner. For the actual least mean squares algorithm the update law is given with* $\dot{\hat{\underline{\theta}}} = \gamma\underline{\varphi}e_n$ *with* $e_n = \tilde{\underline{\theta}}\underline{\varphi}$*. In case of a non-measurable error* e_n *the update law is given as* $\dot{\hat{\underline{\theta}}} = \gamma\underline{\varphi}e$ *with* $e = \mathcal{W}(e_n) = \mathcal{W}(\tilde{\underline{\theta}}^T\underline{\varphi})$ *in case of EM 3. For EM 4, the output error is calculated as* $e = \tilde{\underline{\theta}}\mathcal{W}(\underline{\varphi})$*. Since for EM 3, the LTI-System* $\mathcal{W}$ *is required to be SPR, the phase shift between* e *and* e_n *is less than* $\pi/2$*, and hence the products* $\varphi_i e$ *have mostly the same sign as the products of the actual update law* $\varphi_i e_n$*. I.e., the direction of the parameter drift* $\dot{\hat{\underline{\theta}}}$ *remains correct. If* $\mathcal{W}$ *is not SPR, the phase shift can only be guaranteed to be less than* π *so that the product* $\underline{\varphi}e$ *may yield a wrong parameter update direction. In order to find a remedy, the filtered regressor* $\underline{\varphi}_f = \mathcal{W}(\underline{\varphi})$ *(see Fig. 2.14 (a)) is introduced that is exactly in phase with* $e = \tilde{\underline{\theta}}\mathcal{W}(\underline{\varphi})$ *and thus, the direction of parameter adjustment is maintained.*

In the NLP case, the filtering of the gradient (Fig. 2.14 (b)) does not necessarily yield in phase condition of $e_{n,f}$ *and* ∇n_f *since the signals* e_n *and* ∇n *have in general different spectra and thus, they are delayed differently by the filter* $\mathcal{W}$*. If quasilinear conditions apply (condition ii)), two signals with similar spectra, namely* ∇n_i *and* $(\eta_i - \hat{\eta}_i)\nabla n_i$ *(see above) are filtered with* $\mathcal{W}$ *so that in-phase conditions can be guaranteed.*

Error Model B2 - Gauss-Newton

The equations

$$\begin{aligned} \dot{\tilde{\underline{\chi}}} &= \underline{A}_w\tilde{\underline{\chi}} + \underline{b}_w\underbrace{(n(\underline{\eta},\underline{v}) - n(\hat{\underline{\eta}},\underline{v}))}_{e_n} \\ e &= \underline{c}_w^T\tilde{\underline{\chi}} \end{aligned} \tag{2.82}$$

and

$$\dot{\underline{\hat{\eta}}} = -\dot{\underline{\tilde{\eta}}} = \gamma \underline{H}(t)^{-1} \nabla n_f e \quad . \tag{2.83}$$

constitute the EM B2-GN. Its state is defined as $\underline{x}^T = [\underline{\tilde{\chi}}^T \ \underline{\tilde{\eta}}^T]$ and the matrix $\underline{H}(t)$ is calculated as $\underline{H}(t) = \int_0^t \nabla n_f(\tau)^T \nabla n_f(\tau) d\tau$. The time derivative of the Lyapunov candidate

$$V(\underline{x}) = \underline{\tilde{\chi}}^T \underline{P} \underline{\tilde{\chi}} + \underline{\tilde{\eta}}^T \underline{H}(t) \underline{\tilde{\eta}} \tag{2.84}$$

evaluated along the parameter drift (2.83) yields

$$\begin{aligned} \dot{V}(\underline{x}) &= -\underline{\chi}^T \underline{Q} \underline{\chi} + 2\underline{\tilde{\chi}}^T \underline{Pb} e_n - 2\gamma \underline{\tilde{\eta}}^T \nabla {n_f}^T e + \underline{\tilde{\eta}}^T (\nabla {n_f}^T \nabla n_f + \ln \lambda \underline{H}(t)) \underline{\tilde{\eta}} \\ &= -\underline{\chi}^T \underline{Q} \underline{\chi} - |\ln \lambda| \underline{\tilde{\eta}}^T \underline{H}(t) \underline{\tilde{\eta}} + 2\underline{\tilde{\chi}}^T \underline{Pb} e_n + (\underline{\eta}^T \nabla {n_f}^T)^2 - 2\gamma \underline{\tilde{\eta}}^T \nabla {n_f}^T e \\ &\leq 2\underline{\tilde{\chi}}^T \underline{Pb} e_n + (\underline{\eta}^T \nabla {n_f}^T)^2 - 2\gamma \underline{\tilde{\eta}}^T \nabla {n_f}^T e \end{aligned} \tag{2.85}$$

whereas the time derivative of $\underline{H}(t)$ is calculated analogous to (2.36). Integrating (2.85) over a time period yields

$$\begin{aligned} \int_{t_0}^{t_0+T} \dot{V}(\underline{x}, \tau) d\tau &= V(t_0 + T) - V(t_0) \\ &\leq \underbrace{\int_{t_0}^{t_0+T} \left(2\underline{\tilde{\chi}}^T(\tau) \underline{Pb} e_n(\tau) + (\underline{\eta}^T \nabla {n_f}^T)^2 \right) d\tau}_{I_1} - 2\gamma \underbrace{\int_{t_0}^{t_0+T} \underline{\tilde{\eta}}(\tau)^T \nabla n_f(\tau)^T e(\tau) d\tau}_{I_2} \end{aligned} \tag{2.86}$$

With the same reasoning as for EM B2-GS conclusion (2.69) applies if $\gamma > \frac{I_1}{2I_2}$. Thus, if ∇n_f relaxes condition (2.71) and if the input $\underline{v}$ is n.l.p.e, and if either condition i) or ii) applies, the origin $\underline{x} = \underline{0}$ is globally uniformly asymptotically stable. Hence, the parameter error $\underline{\tilde{\eta}}$ converges to zero.

2.5.3 Discussion

For a certain class of nonlinearly parameterized models, it could be shown that gradient based parameter identification methods are asymptotically stable and hence, converge to the global minimum.

The EM B1 has been investigated in order to derive the corollaries 2.5.3 and 2.5.4 that are fundamental for the analysis of EM B2. Furthermore, the corollaries 2.5.3 and 2.5.4 can be useful in case of a measurable output y_n as it is assumed in EM B1, too since the analytic proof of locality and monotonicity of the model equation might be simpler then the convexity proof of the quadratic error criterion.

With EM B2, conditions have been formulated that yield asymptotically stable parameter identification of a locally and monotonically parameterized system whose output y_n is not directly accessible, but filtered by a known LTI-system $\mathcal{W}$. If $\mathcal{W}$ is asymptotically stable, the adaptation converges either in case of quasilinear parameterization, or if the bandwidth of $\mathcal{W}$ is fast compared to the bandwidth of the signal y_n. If this condition is

not met, or if $\mathcal{W}$ is not asymptotically stable, the dynamics of the error transfer function can be modified with the implementation of a neural observer.

It is worth to test the property of quasilinearity and thus the necessity of a neural observer, since its usage is accompanied by the amplification of sensor noise. The measured plant output y is amplified by the observer gain $\underline{l}$ and thus, the measurement noise is amplified as well. If a fast dynamic performance is required, a high observer gain $\underline{l}$ has to be chosen which causes a high sensitivity with respect to noise. In practice, it is advisable to implement an observer in any case since it provides an additional degree of freedom for the design of the adaptive system. However, the poles of the error transfer function should be placed just as far into the left half of the s-plane as necessary.

Gradient based adaptation algorithms like the GS-, GN- and LM-method are easy to implement and furthermore, they are integrated as ready-to-use routines in many software packages like Matlab and Simulink [109]. Therefore, it was the aim of the above derivations to broaden the classes of parameter adaptation problems to which they are applicable.

2.6 Error Models for Separable Nonlinear Parameterization

In this section, methods that have been derived for EM A and EM B will be applied to SNLP-model equations (2.5c). First, the SLS-algorithm introduced in Section 2.2.3 will be rewritten with continuous time equations, and in the error model framework. Depending on the adaptive law applied for the identification of $\underline{\eta}$, it is referred to as EM C1-GS/GN. Note, that EMs C1-GS/GN are not new but introduced as recursive SLS-algorithm in [123]. The formulation in the error model framework yields the basis for further derivations explained in this section. Subsequently, EM-C2-GS/GN will be introduced as a method to identify SNLP-plants whose output is not directly measurable, but filtered by a known LTI-system $\mathcal{W}$. The EM-C2 is developed following the derivations and arguments introduced for the error models A3 and B1.

2.6.1 Error Model C1

Error Model C1-GS

The error model C1 is given by the error equation

$$\epsilon = \underline{\theta}^T \underline{\varphi}(\underline{\eta}, \underline{v}) - \hat{\underline{\theta}}(\hat{\underline{\eta}})^T \underline{\varphi}(\hat{\underline{\eta}}, \underline{v}) = \underline{\theta}^T \underline{\varphi} - \hat{\underline{\theta}}(\hat{\underline{\eta}})^T \hat{\underline{\varphi}} \tag{2.87}$$

and by the adaptive laws

$$\dot{\hat{\underline{\theta}}} = -\dot{\tilde{\underline{\theta}}} = \gamma_{\hat{\theta}} \underline{\Pi} \hat{\underline{\varphi}} \epsilon \tag{2.88}$$

and

$$\dot{\hat{\underline{\eta}}} = -\dot{\tilde{\underline{\eta}}} = \gamma_{\hat{\eta}} \underline{\psi}^T \epsilon \ . \tag{2.89}$$

The state is defined as $\underline{x}^T = [\tilde{\underline{\theta}}^T \ \ \tilde{\underline{\eta}}^T]$. The block diagram is depicted in Fig. 2.15. The corresponding time continuous update equations of (2.21), (2.22), (2.25) and (2.26) are

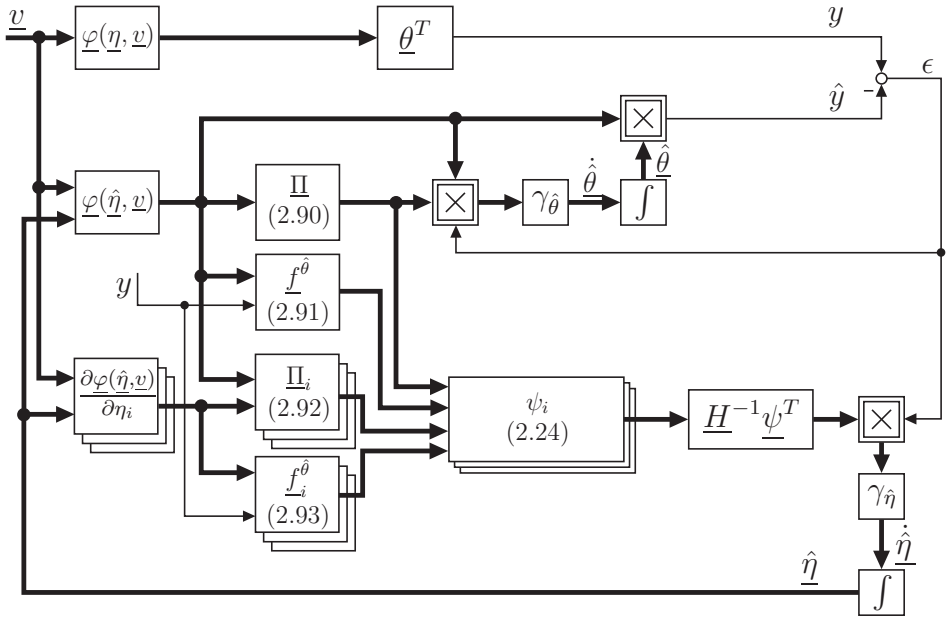

Fig. 2.15: Error Model C1: Replacing the inverse approximate Hessian matrix $\underline{H}^{-1}$ with the unity matrix $\underline{I}$ results in EM C1-GS. Calculating $\underline{H}$ as $\underline{H}(t) = \int_0^t \lambda^{t-\tau}\underline{\psi}(\tau)^T\underline{\psi}(\tau)d\tau$ results in EM C1-GN.

given with

$$\underline{\Pi}(t)^{-1} = \int_0^t \lambda^{t-\tau}\underline{\varphi}(\hat{\underline{\eta}},\underline{v})\underline{\varphi}(\hat{\underline{\eta}},\underline{v})^T d\tau \quad , \tag{2.90}$$

$$\underline{f}^{\hat{\theta}}(t) = \int_0^t \lambda^{t-\tau}\underline{\varphi}(\hat{\underline{\eta}},\underline{v})y(\tau)d\tau \quad , \tag{2.91}$$

$$\underline{\Pi}_i(t)^{-1} = \int_0^t \lambda^{t-\tau}\left(\underline{\varphi}_i(\hat{\underline{\eta}},\underline{v})\underline{\varphi}(\hat{\underline{\eta}},\underline{v})^T + \underline{\varphi}(\hat{\underline{\eta}},\underline{v})\underline{\varphi}_i(\hat{\underline{\eta}},\underline{v})^T\right)d\tau \quad , \tag{2.92}$$

and

$$\underline{f}_i^{\hat{\theta}}(t) = \int_0^t \lambda^{t-\tau}\underline{\varphi}_i(\hat{\underline{\eta}},\underline{v})y(\tau)d\tau \quad . \tag{2.93}$$

The elements of the gradient vector $\underline{\psi}$ are calculated according to (2.24). The RLS-parameter update (2.88) is equivalent to the update formula (2.27) as proposed in [123] which is shown for the discrete time domain in Appendix A.1. The formulation (2.88) is chosen instead of (2.27) to be consistent with the formulae of EM A.

If $\tilde{\underline{\eta}}$ converges to zero, the convergence analysis of $\tilde{\underline{\theta}}$ is equivalent to EM A1. Therefore, as a necessary condition for asymptotic stability of the origin $\underline{x} = \underline{0}$ the input regressor $\underline{\varphi}(\hat{\underline{\eta}},\underline{v})$ has to be l.p.e..

In order to analyze the convergence of the nonlinear parameters $\hat{\underline{\eta}}$, the Lyapunov approach of EM B1 is used and analogous to Eq. (2.62) the Lyapunov candidate

$$V(\underline{x}) = \frac{1}{2}\tilde{\underline{\eta}}^T\tilde{\underline{\eta}} \tag{2.94}$$

is proposed. The time derivative evaluated along (2.89) is obtained as

$$\dot{V}(\underline{x}) = -\gamma_\theta \tilde{\underline{\eta}} \underline{\psi}^T \epsilon \ . \tag{2.95}$$

For further analysis, first, the property of local parameterization is investigated. The SLS-algorithm minimizes the error criterion (2.19) that solely depends on the nonlinear parameters $\hat{\underline{\eta}}$. It incorporates the model error $\epsilon(\hat{\underline{\eta}}, k)$ that is given with Eq. (2.23). From rewriting the right side of (2.23) as

$$y - \underline{\varphi}(\hat{\underline{\eta}})^T \underline{\Pi} \underline{f}^{\hat{\theta}} = y - \underline{\varphi}(\hat{\underline{\eta}})^T \hat{\underline{\theta}}(\hat{\underline{\eta}})$$

a model equation that solely depends on $\hat{\underline{\eta}}$ can be inferred as

$$\hat{y}(\hat{\underline{\eta}}) = \underline{\varphi}(\underline{\eta})^T \hat{\underline{\theta}}(\hat{\underline{\eta}}) = \underline{\varphi}(\hat{\underline{\eta}})^T \underline{\Pi} \underline{f}^{\hat{\theta}} \ . \tag{2.96}$$

Rewriting Eq. (2.24) as

$$\psi_i = \frac{\partial \left(\underline{\varphi}(\hat{\underline{\eta}})^T \hat{\underline{\theta}}(\hat{\underline{\eta}}) \right)}{\partial \hat{\eta}_i} = \frac{\partial \underline{\varphi}^T(\hat{\underline{\eta}})}{\partial \underline{\eta}_i} \hat{\underline{\theta}}(\hat{\underline{\eta}}) + \underline{\varphi}(\hat{\underline{\eta}})^T \frac{\partial \hat{\underline{\theta}}(\hat{\underline{\eta}})}{\partial \hat{\eta}_i} \tag{2.97}$$

illustrates how the gradient vector $\underline{\psi}$ implicitly incorporates the change of the linear parameters $\hat{\underline{\theta}}$ that is caused by a change of $\hat{\underline{\eta}}$. From the assumption of $\hat{y} = \hat{\underline{\theta}}^T \underline{\varphi}(\hat{\underline{\eta}}, \underline{v})$ being locally parameterized, it follows that $\underline{\varphi}_i = {}^{\partial \underline{\varphi}}/_{\partial \underline{\eta}_i} \approx \underline{0}$ for $\underline{v} \notin \mathbb{V}_i$. As a consequence, $\underline{\Pi}_i$ and $\underline{f}_i^{\hat{\theta}}$ will decay to zero due to exponential forgetting. Thus, $\psi_i \approx 0$ after a decaying time if $\underline{v} \notin \mathbb{V}_i$. Since the forgetting factor λ is a design parameter, it can be chosen appropriately. From the above considerations, the following corollary is deduced:

Corollary 2.6.1 *Given the approximation $\hat{y}(\hat{\underline{\theta}}, \hat{\underline{\eta}}) = \hat{\underline{\theta}}^T \underline{\varphi}(\hat{\underline{\eta}}, \underline{v})$ of the plant $y = \underline{\theta}^T \underline{\varphi}(\underline{\eta}, \underline{v})$. If $\hat{y}(\hat{\underline{\theta}}, \hat{\underline{\eta}})$ is locally parameterized with respect to $\hat{\underline{\eta}}$, then, also the transformed model equation* (2.96) *is locally parameterized. This conclusion holds under the assumption that the bandwidth of exponential forgetting is greater than the bandwidth of the input signal $\underline{v}$. The time constant of exponential forgetting is determined by forgetting factor λ.*

From Corollary 2.6.1 it follows

$$\dot{V}(\underline{x}) \approx -\gamma_\theta (0 + \ldots + \tilde{\eta}_i \psi_i \epsilon + \ldots + 0) \tag{2.98}$$

for $\underline{v} \in \mathbb{V}_i$, whereas according to Definition 2.5.1, $\mathbb{V}_i$ is the activation region of the i$^{\text{th}}$ nonlinear parameter. If furthermore, Eq. (2.96) is strictly monotonically parameterized, the stability analysis of the origin $\tilde{\underline{\eta}} = \underline{0}$ follows the reasoning of EM B1 (Section 2.5.1). Thus, in case of an l.p.e input regressor $\underline{\varphi}(\hat{\underline{\eta}}, \underline{v})$ and a n.l.p.e. input $\underline{v}$, the origin of EM C1 $\underline{x} = \underline{0}$ is uniformly globally asymptotically stable if the original model equation $\hat{y}(\hat{\underline{\theta}}, \hat{\underline{\eta}})$ is locally parameterized and if the transformed model equation (2.96) is monotonically parameterized.

Unfortunately, it could not generally be shown that monotonicity of Eq. (2.96) with respect to $\hat{\eta}_i$ follows from monotonicity of the original model equation $\hat{y}(\hat{\underline{\theta}}, \hat{\underline{\eta}})$.

Error Model C1-GN

EM C1-GN (Fig. 2.15) is given by the error equation (2.87), the adaptive laws (2.88) and

$$\dot{\underline{\hat{\eta}}} = -\dot{\underline{\tilde{\eta}}} = \gamma_{\hat{\eta}} \underline{H}^{-1} \underline{\psi}^T \epsilon \tag{2.99}$$

whereas the approximate Hessian $\underline{H}$ is calculated as

$$\underline{H}(t) = \int_0^t \lambda^{t-\tau} \underline{\psi}(\tau)^T \underline{\psi}(\tau) d\tau \quad . \tag{2.100}$$

Following the derivations of EM B1-GN, the derivative of the Lyapunov candidate $V(\underline{\hat{\eta}}) = \underline{\tilde{\eta}}^T \underline{H}(t) \underline{\tilde{\eta}}$ can be calculated as

$$\dot{V}(\underline{\tilde{\eta}}) \leq -2\gamma_{\hat{\eta}} \underline{\tilde{\eta}}^T \underline{\psi}^T \epsilon + (\underline{\tilde{\eta}}^T \underline{\psi}^T)^2 \quad . \tag{2.101}$$

Therefore, if the model equation $\hat{y} = \underline{\hat{\theta}}^T \underline{\varphi}(\underline{\hat{\eta}}, \underline{v})$ is locally parameterized with respect to $\underline{\hat{\eta}}$ and if (2.96) is strictly monotonically parameterized, the stability concept of EM B1-GS applies to EM C1-GS, as well.

2.6.2 Error Model C2

In this section, SNLP-plants with unknown parameters $\underline{\theta}$ and $\underline{\eta}$ whose output y_n is not directly measurable but filtered by a known LTI-system $\mathcal{W}$ are considered. A configuration is proposed where the method of error augmentation in combination with a neural observer is applied (Fig. 2.16) in order to obtain an asymptotically stable error transfer function whose poles are placed such that its bandwidth is greater than the bandwidth of the signals to be filtered. Thus, EM C2 can be reduced to EM C1.

Error Model C2-GS

As it can be inferred from the block diagram in Fig. 2.16, the EM C2-GS is constituted by the equations

$$\epsilon_e = \underbrace{\mathcal{W}_{obs}(\underline{\theta}^T \underline{\varphi}(\underline{\eta}, \underline{v}) - \underline{\hat{\theta}}^T \underline{\varphi}(\underline{\hat{\eta}}, \underline{v}))}_{\epsilon_{obs}} + \mathcal{W}_{obs}(\underline{\hat{\theta}}^T \underline{\varphi}(\underline{\hat{\eta}}, \underline{v})) - \underline{\hat{\theta}}^T \mathcal{W}_{obs}(\underline{\varphi}(\underline{\hat{\theta}}, \underline{v})) \tag{2.102}$$

$$= \underline{\theta}^T \underbrace{\mathcal{W}_{obs}(\underline{\varphi}(\underline{\eta}, \underline{v}))}_{\underline{\varphi}_f} - \underline{\hat{\theta}}^T \underbrace{\mathcal{W}_{obs}(\underline{\varphi}(\underline{\hat{\eta}}, \underline{v}))}_{\underline{\hat{\varphi}}_f} \quad , \tag{2.103}$$

$$\dot{\underline{\hat{\theta}}} = -\dot{\underline{\tilde{\theta}}} = \gamma_{\hat{\theta}} \underline{\Pi} \underline{\hat{\varphi}}_f \epsilon_e \tag{2.104}$$

and

$$\dot{\underline{\hat{\eta}}} = -\dot{\underline{\tilde{\eta}}} = \gamma_{\hat{\eta}} \underline{\psi}^T \epsilon_e \quad . \tag{2.105}$$

In order to calculate $\underline{f}^{\hat{\theta}}$ and $\underline{f}_i^{\hat{\theta}}$ according to (2.91) and (2.93) the signal

$$y_{obs} = \epsilon_{obs} + \mathcal{W}_{obs}(\hat{y}_n) = \mathcal{W}_{obs}(y_n) \tag{2.106}$$

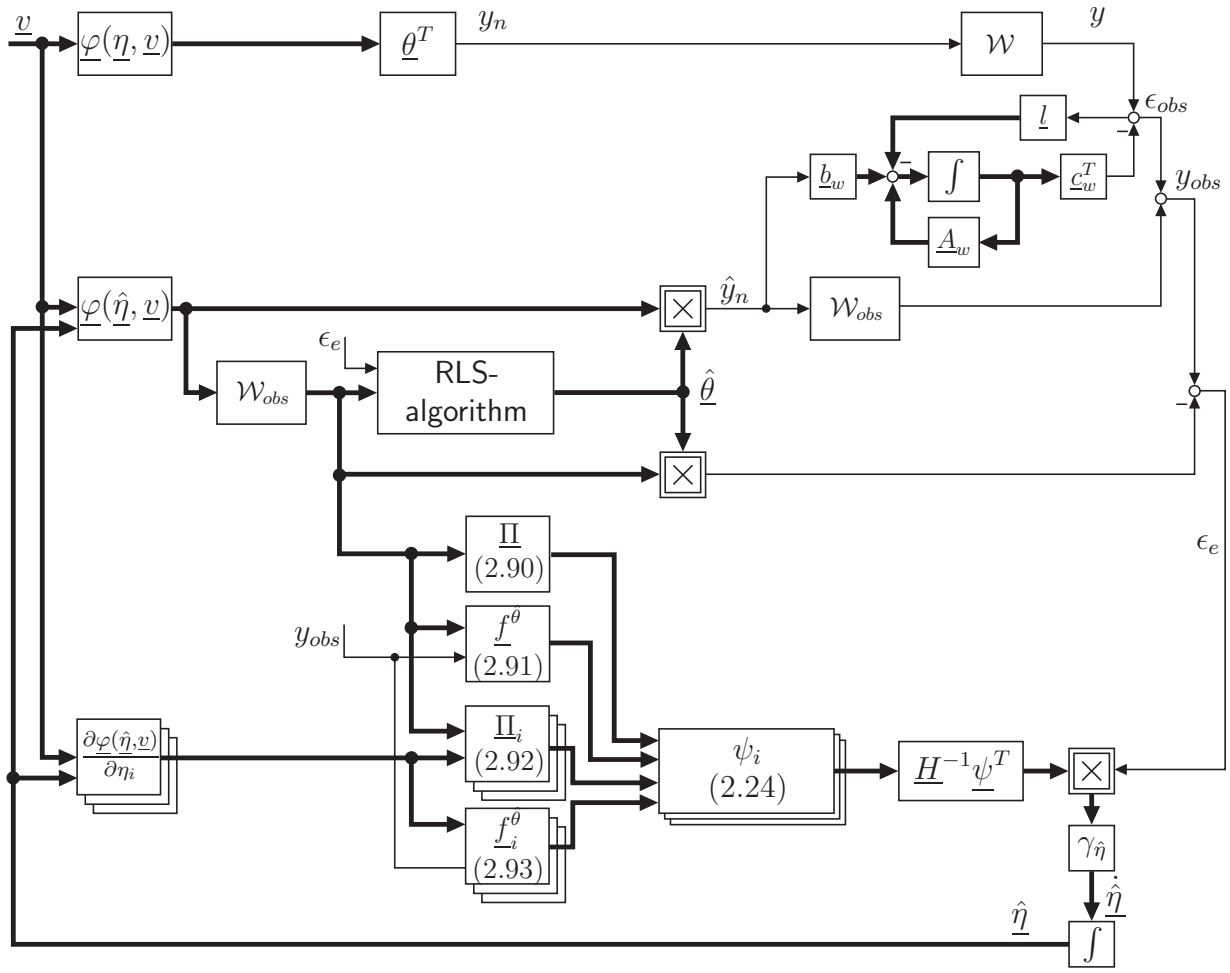

Fig. 2.16: Block diagram of EM C2: Replacing the inverse approximate Hessian matrix $\underline{H}^{-1}$ with the unity matrix $\underline{I}$ results in EM C2-GS. Calculating $\underline{H}$ as $\underline{H}(t) = \int_0^t \lambda_{\hat{\eta}}^{t-\tau} \underline{\psi}(\tau)^T \underline{\psi}(\tau) d\tau$ results in EM C2-GN. The method of error augmentation in combination with a neural observer is used in order to change the bandwidth of the error transfer function and to obtain the signal $y_{obs} = \mathcal{W}_{obs}(y_n)$

is used instead of y.

If the observer poles are placed such that the dynamics of resulting error transfer function are fast compared to the bandwidth of the occurring signals, we have $\underline{\varphi}_f \approx K\underline{\varphi}$, $\hat{\underline{\varphi}}_f \approx K\hat{\underline{\varphi}}$ and $y_{obs} \approx Ky_n$ with K representing the static gain of $\mathcal{W}_{obs}$. Therefore, EM C2-GS approximates EM C1-GS. Thus, the convergence properties of EM C1-GS apply to EM C2-GS, as well.

Note that even with unstable dynamics of $\mathcal{W}$, the proposed method can be applied as long as the error transfer function is asymptotically stable.

Error Model C2-GN

The equations of EM C2-GN (Fig. 2.16) are given by (2.102), (2.104) and the adaptive law

$$\dot{\underline{\hat{\eta}}} = -\dot{\underline{\tilde{\eta}}} = \gamma_{\hat{\eta}} \underline{H}^{-1} \underline{\psi}^T \epsilon \tag{2.107}$$

with $\underline{H}$ according to (2.100). If the observer is designed such that the bandwidth of the error transfer function is greater than the bandwidth of the signals involved, EM C2-GN approximates EM C1-GN and thus the stability results of EM C1-GN apply to EM C2-GN, as well.

2.6.3 Discussion

The SLS-algorithm is a very efficient method for the identification of mixed-linear-nonlinear parameterized model equations. It incorporates standard adaptive laws such as the RLS-algorithm for the linear parameters and gradient based methods for the nonlinear parameters. Therefore, it can be easily implemented using standard routines.

With Corollary 2.6.1, the locality condition of EM B applies to EM C, as well. Hence, asymptotically stable parameter identification can be guaranteed by the monotonicity constraint together with local parameterization just as derived for EM B. With the presented theory, the number of parameter adaptation problems to which the SLS-algorithm is applicable could be enlarged. The analytic monotonicity analysis of the transformed model equation (2.96) might not be trivial. However, in practice, a simulative examination of the monotonicity condition is sufficient.

By implementing a neural observer and using the method of error augmentation, the SLS-algorithm can be applied to SNLP-models whose output y_n is not directly measurable but filtered by a known LTI-system. With EM C2 this method is introduced within the error model framework. With the application of the EMs C1 and C2 to a physiological system in Chapter 4, an example is given where the methods derived in this chapter will be exemplified.

2.7 Summary and Conclusions

In this chapter, on-line parameter identification in the presence of linear, nonlinear and separable nonlinear parameterization has been addressed. The focus has been on the identification of plants with unknown parameters whose output y_n is not directly measurable but filtered by a known LTI-system $\mathcal{W}$. The measurable output of $\mathcal{W}$ is fed into an adaptation algorithm in order to drive the parameter error to zero. Throughout the chapter, the method of error augmentation in combination with a neural observer is used: To either place the poles of the error transfer function such that it can be approximated as a constant gain, or in order to stabilize error transfer functions that are not asymptotically stable.

For identification in the presence of linear parameterization, the error model A has been developed. It can be considered as add-on to the fundamental error models 1, 3 and 4 introduced in [118]. Global asymptotic stability, i.e. convergence of the parameter error to zero could be formally proven. The adaptation law is of RLS-type and hence, yields

superior convergence properties compared to the LMS-type law applied with EM 1,3 and 4. The RLS-algorithm is known to converge faster and to be less sensitive to measurement noise. If the error transfer function is not asymptotically stable, error augmentation in combination with a neural observer can be applied to allow identification anyhow.

In case of NLP-plants, global asymptotic stability of GS-Type and GN-Type algorithms could be proven for local monotonic parameterization. If the NLP-part is quasilinear parameterized, the filtered gradient is introduced in order to generate in-phase conditions for the adaptation law. This method is inspired by the filtered regressor of EM 4. If quasilinearity does not apply, a neural observer can be used in order to increase the bandwidth of the error transfer function. Then, the algorithm converges not only for local monotonic parameterization but also if the quadratic error criterion can be considered as benign. I.e., in a certain region around the global minimum, the criterion is strictly decreasing so that there are neither plateaus nor local minima. Of course, local parameterization reduces the requirements on the input signal in order to be persistently exciting.

Also in case of quasilinear parameterization it might be beneficial to apply a neural observer if the error transfer function lowpasses information in the signal y_n. The poles of the neural observer have to be placed carefully since fast poles lead to a high observer gain $\underline{l}$ which amplifies measurement noise.

Finally, the identification of SNLP-plants has been addressed. The usage of SNLP-models allows combining the advantages of linear and nonlinear parameter identification methods. On the one hand, a priori knowledge can be incorporated by using nonlinear parameterized nonlinear model equations whose shape is similar to the curve to be approximated. On the other hand, linear parameterized models like polynomials or NRBF-networks for static approximation of FIR-model for dynamics plants can be applied where a priori knowledge is poor. It could be shown that from local parameterization of the plant $y = \underline{\theta}^T \underline{\varphi}(\underline{\eta}, \underline{v})$ with respect to $\underline{\eta}$ it follows locality of the model equation $\hat{y}(\underline{\hat{\eta}})$ that solely depends on the nonlinear parameters. This result can be useful when designing persistently exciting input signal, since monotonic parameterization allows applying an n.l.p.e. input signal. If $\hat{y}(\underline{\hat{\eta}})$ is strictly monotonically parameterized, the convergence condition of EM B apply to EM C, too. Unfortunately monotonicity of $\hat{y}(\underline{\hat{\eta}})$ cannot be concluded from monotonicity of the original equation $y_n = \underline{\theta}^T \underline{\varphi}(\underline{\eta}, \underline{v})$ and thus, monotonicity has to be verified separately. Convergence can also be guaranteed, if the error criterion is benign. The adaptation laws are of RLS-type for the linear parameters and of GS/GN-type for the nonlinear parameters. The input signal has to be l.p.e. with respect to the input regressor $\underline{\varphi}(\underline{\hat{\eta}}, \underline{v})$ and n.(l.)p.e. depending on the type of nonlinear parameterization. By combining the methods of error augmentation and neural observer with EM C1, the error model EM C2 is obtained that allows to apply the SLS-algorithm to SNLP-model whose output is not directly measurable but filtered by a known LTI-system.

It is important to note that the stability properties derived for GN-type adaptive laws apply to the Levenberg-Marquardt algorithm, as well. This is due to the positive definiteness of the damped Hessian $\underline{R} = \underline{H} + \delta \underline{I}$ that occurs in the LM-parameter update law.

The most important results of this chapter are summarized in Fig. 2.17 together with the existing related fundamental methods. It illustrates the enhancement of the current state of the art that has been created by the introduction of the error models A,B and C.

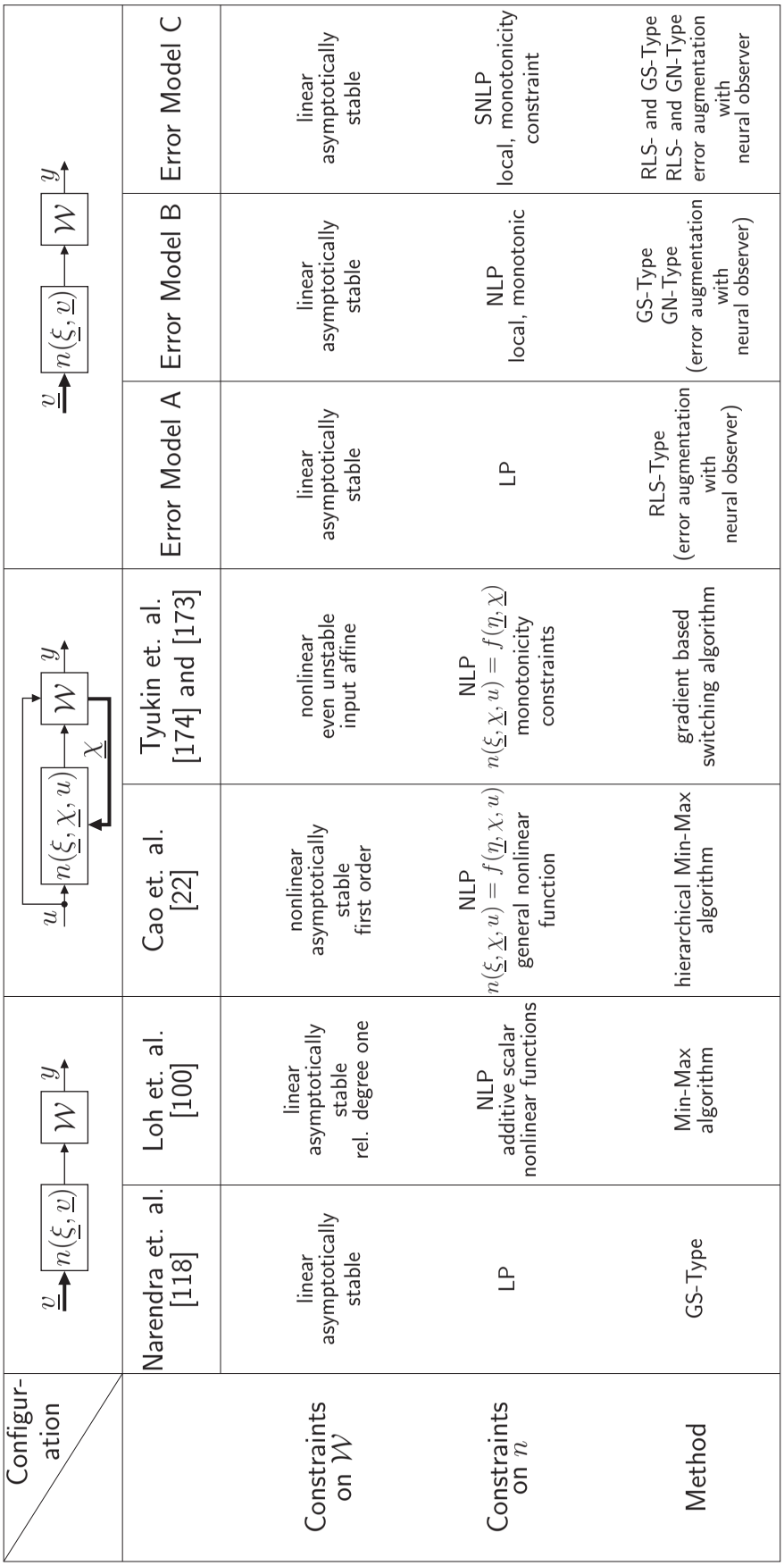

Fig. 2.17: Comparison of the related state of the art with the error models A, B and C.

3 Neuromuscular and Biomechanical Modeling

3.1 Introduction

In this chapter, a model of *RPMS*-induced index finger i.e. the relationship between the peripherally applied magnetic field pulses the resulting movements is developed. This model represents the basis for the three applications developed in this thesis: System identification based therapy evaluation, induction of position-controlled limb motion and patient driven *RPMS*-therapy. The model developed in this chapter predicts the behavior of the plant qualitatively and is used for the development, the simulative implementation and the evaluation of the above mentioned applications.

The plant of the muscle stimulation induced limb motion will be subdivided into the blocks "force generation" (often called muscle activation dynamics), "force transmission" (tendon leverage, e.g.), "segment dynamics", "length-velocity-dependencies" (the ability of the muscle to generate force depending on its length and its change of length), and "spastic joint torque" as illustrated in Fig. 3.1. The last block accounts for the limb motion-dependent increase of muscle tone called spasticity (see Appendix B.4) that may occur after neurological damages.

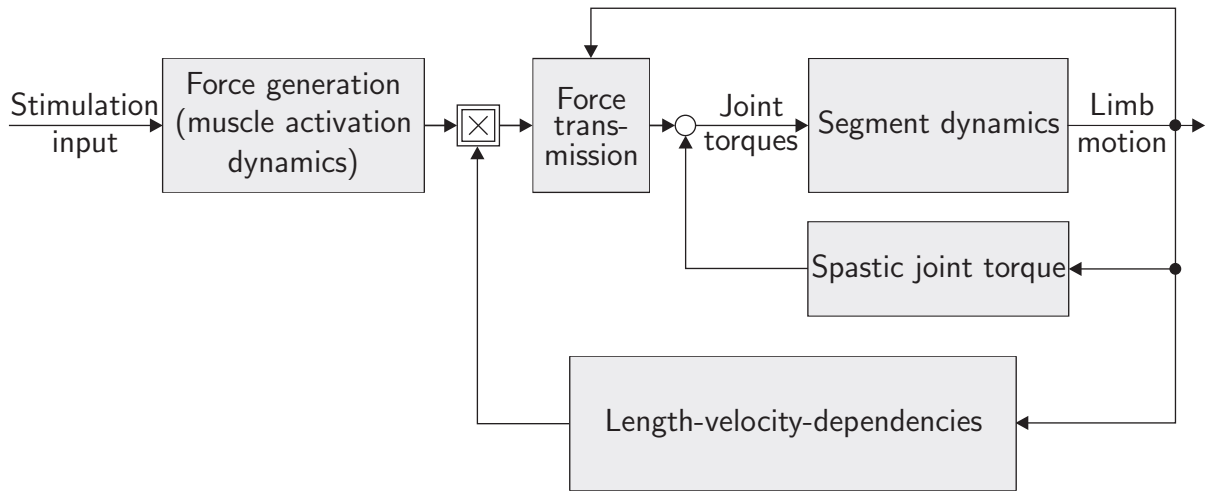

Fig. 3.1: Block diagram overview of the plant "muscle stimulation induced limb motion".

Neuromuscular and biomechanical models have been developed for general muscle force driven limb motion caused by physiological muscle activation. Reviews are given in standard biomechanics literature (see [86], e.g.). In the framework of muscle stimulation, these

models have been applied to FES-induced limb motion (see [140; 176], e.g.) as well as to *RPMS*-induced motion of the elbow joint [6].

The most widely used biomechanical muscle model was developed by A.V. Hill in 1938 [67; 68]. The Hill-type muscle model accounts for passive elastic and passive viscous properties of the muscle with spring- and damper-elements in parallel to an active contractile element. Often, these passive elements, as well as the model for the length-velocity dependencies are summarized as "muscle contraction dynamics" (see [135], e.g.). Here, the passive muscle properties are considered within the block "segment dynamics". Also the torques caused by spasticity will be mathematically integrated within the equation of the segment dynamics. Although these modifications do not strictly represent the physiological structure of the considered plant, they result in a mathematical description that is formally equivalent to the Hill-type topology. These modifications provide a simpler model structure that is advantageous for the system identification that will be presented in Chapter 4. Differences and similarities of the proposed structure in Fig. 3.1 compared to models that reflect the plant topology will be discussed within the following sections.

The novel scientific contributions presented in this chapter are the proposition and verification of models for the force generation, the segment dynamics and the spastic joint torque in the index finger. The classical modeling approach for the segment dynamics is extended to account for a relaxation phenomenon and thus, a much better approximation accuracy is obtained. It is shown that the spastic joint torque occurring with spastic paretic patients can be approximated by a simple static model that can easily be integrated into the segment dynamics. The models are parameterized and verified by means of measurements carried out with healthy subjects as well as with spastic paretic patients.

This chapter is structured as follows: In Section 3.2 fundamentals like the principle of the *RPMS*-induced neural excitation, a mathematical formulation of the magnetic pulses, anatomical terms and coordinate systems are introduced. In the Sections 3.3 - 3.7, models for every block of the overview in Fig. 3.1 are proposed. The order mainly follows the chain of action from the stimulation input to the limb motion. The block "force transmission" is prefaced, since it introduces fundamental terms.

3.2 Fundamentals and Definitions

3.2.1 Neuromuscular Excitation with RPMS

In order to stimulate a muscle or a muscle group with RPMS, magnetic field pulses are applied with a magnet coil placed above the respective innervation zone. This results in the depolarization of the terminal motor branches. The functional principle is depicted in Fig. 3.2. In Fig. 3.3 two typical coil configurations are illustrated as they are used for *RPMS*-induced elbow and index finger movements.

The relevant physiological aspects of nervous conduction and muscle contraction are summarized in appendix B.1. In this section, technical and physical aspects as well as the mathematical abstraction of the magnetic field pulses as a system input will be described.

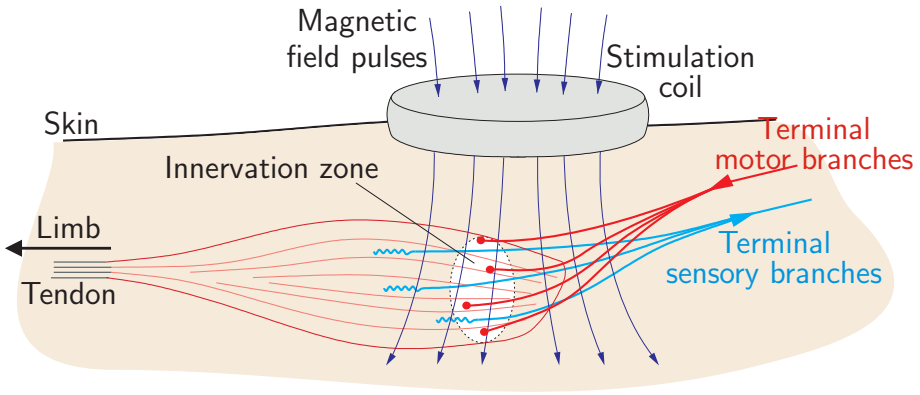

Fig. 3.2: Principle of the peripheral magnetic stimulation: A magnet coil is placed above the innervation zone of the respective muscle. The magnetic field pulses induce an electrical field inside the tissue which results in a depolarization of the terminal motor branches. Thus, the muscle contracts and exerts a force that is transmitted via a tendon to the respective limb.

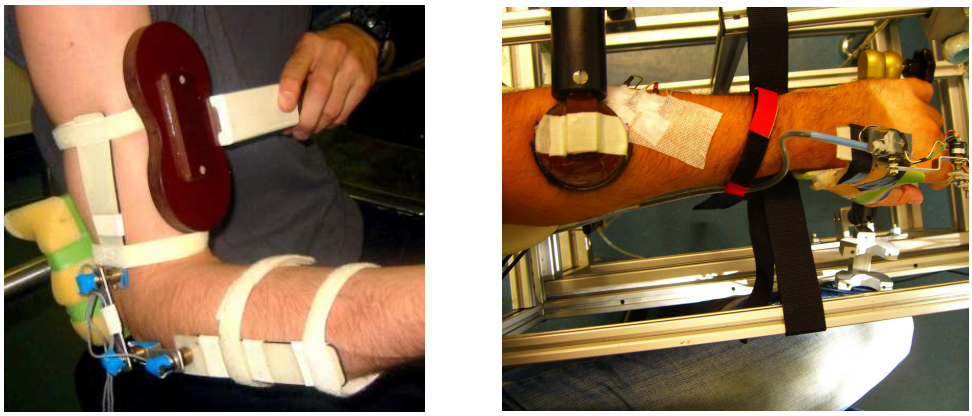

(a) (b)

Fig. 3.3: Different coil configurations: (a) A butterfly coil placed above the biceps muscle for the *RPMS*-induced elbow flexion. (b) A small circular coil placed above the innervation zone of the finger extensors.

Pulse Generation

A stimulation unit for peripheral as well as for transcranial magnetic stimulation consists of a stimulator whose circuits produce current pulses which is attached to a magnet coil. Fig. 3.4 illustrates the schematic of the stimulator circuit. A trigger signal fires the thyristor. Thus, the capacitor is discharged and a current pulse flows through the coil. The stimulators used by the Sensorimotor Research Group [175], feeds the coil current back into the capacitor in order to reduce energy consumption. Therefore, the pulses occur in

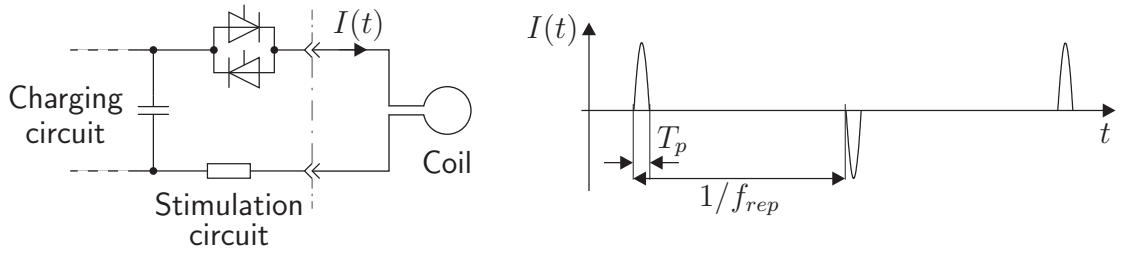

Fig. 3.4: Left: Functional schematic of the stimulation unit: The most important elements are a capacitor and a thyristor-circuit that together with the stimulation coil act as a controllable LC-oscillator. Details about the stimulators used for the experiments of this thesis are presented in [175; 181]. Right: In order to optimize the energy consumption of the stimulator, alternating current pulses are applied to the coil [175]. The pulse width T_p of the sinusoidal half waves amounts 90 μs and the repetition rate f_{rep} is variable up to 30 Hz. The peak value of $I(t)$ goes up to 3 kA which corresponds to a magnetic flux density of approx. 2 T, depending on the particular coil.

alternating polarity as depicted in Fig. 3.4. These devices are able to generate current pulses with a repetition rate of $f_{rep} = 30\,\mathrm{Hz}$.

The stimulation coil consists of isolated copper windings, a temperature sensor to prevent overheating, a plastic coating, and a handle. There exist different coil geometries (round and butterfly, e.g.) and different sizes (typical diameter: 90 mm). Specifications of commercially available coils can be found in [104] and [105].

Neural Activation

The underlying physical principle of magnetic stimulation is the electromagnetic induction that is governed by Faraday's law:

$$\vec{\nabla} \times \vec{E} = -\frac{\partial \vec{B}}{\partial t} \quad . \tag{3.1}$$

It states that an electrical field $\vec{E}$ is induced inside the tissue by a time varying magnetic field $\vec{B}$ (see Fig. 3.5).

By means of magnetic stimulation, only myelinated axons (see Appendix B.1.2 and B.1.3) are depolarized whereas thin nerve fibers like nociceptors are hardly activated [27] (see also Tab. B.1). The mechanism of the enforced depolarization can be explained with the equivalent circuit illustrated in Fig. 3.5. The electrical field $\vec{E}$ can be divided into a component $\vec{E}_{||}$ parallel to the axon, and a component $\vec{E}_{\perp}$ perpendicular to the axon. According to [182], the intensity of an electrical field induced by magnetic stimulation is less than $10^4\,\mathrm{V/m}$. Since the intensity of the electrical field caused by the membrane potential (modeled with capacitor C_M) ranges up to $10^7\,\mathrm{V/m}$, the field component $\vec{E}_{\perp}$ is comparatively small and has no depolarization effect.

In Fig. 3.5, only the component $\vec{E}_{||}$ is depicted. For sake of simplicity, it is assumed, that the intensity of $\vec{E}_{||}$ is constant between two adjacent nodes of Ranvier which are

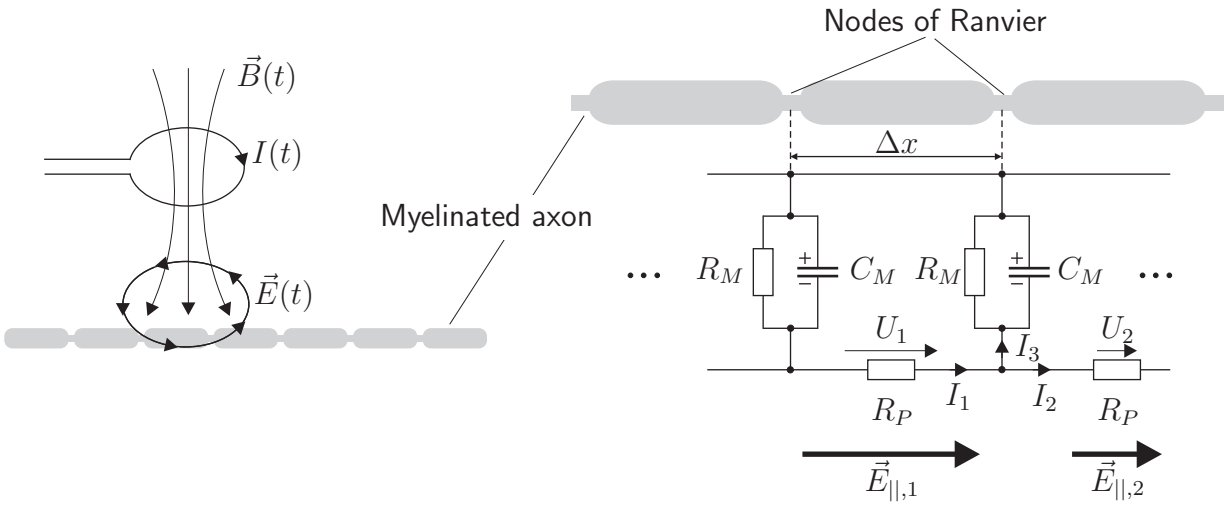

Fig. 3.5: Left: The current pulse $I(t)$ in the coil generates a magnetic field pulse $\vec{B}(t)$ that induces the electrical field $\vec{E}(t)$. A myelinated axon passes the induction zone. Right: Simplified equivalent circuit of the axon (modified from [182]): The nerve can be modeled as a cylindrical capacitor with the myelin as electrically-insulating dielectric layer. The capacity of a single section with length Δx is modeled by the capacitor C_M and the leakage is modeled by a parallel resistor R_M. The conductivity of the axon plasma is modeled with the resistor R_P. See Appendix B.1 for anatomical and physiological background knowledge.

equidistantly allocated, i.e. $\Delta x = \text{const.}$. Therefore, $\vec{E}_{||,1}$ results in a voltage $U_1 = \vec{E}_{||,1}\Delta x$ and induces a current $I_1 = \frac{U_1}{R_P}$. With $\vec{E}_{||_1} > \vec{E}_{||_2}$ it follows $U_1 > U_2$ and $I_3 = I_1 - I_2 > 0$, and the positive current I_3 neutralizes the capacitor C_M. If the gradient of the electrical field $\vec{E}_{||}$ is big enough, the capacitor C_M is discharged above the depolarization threshold and an action potential is elicited that propagates along the axon as explained in Appendix B.1.3. By physiological elicitation, the action potential starts at the soma and only propagates in orthodromic direction. However, the *RPMS*-elicited action potential starts at the axon and propagates in orthodromic as well as in antidromic directions.

The model of Fig. 3.5 is an oversimplification of the nerve and the surrounding tissue. In reality, peripheral nerves are situated in highly non-homogeneous structures with anisotropic conductivities [87] which have significant influence on the current densities. Taking these properties into consideration requires extensive modeling of the tissue and the electromagnetic propagation. Using *RPMS*, a muscle can be selectively activated simply by observing the movements of the respective limbs during stimulation and by replacing the coil if necessary. Therefore, no research on field propagation is done by the Sensorimotor Research Group. Nevertheless, the prediction of the field distribution inside the tissue can be of importance for diagnostic and therapeutic stimulation. For further information the reader is referred to [11; 87; 112; 116; 143; 154].

Repetitive Magnetic Field Pulses as Model Input

A magnetic field pulse has a pulse width T_p of approximately $90\,\mu$s and activates motor units of the stimulated muscle. The number of recruited motor units nonlinearly depends on the magnetic flux density. In the following, the strength of magnetic pulses will be referred to as stimulation intensity I that varies within the range $0 \leq I \leq 100\,\%$. The maximum value $I = 100\,\%$ corresponds to the maximum magnetic flux density which the respective stimulation unit can generate. The pulses are mathematically described as discrete Dirac Delta functions representing the system input u that is calculated in discrete time as

$$u(k) = \sum_{j=0}^{\infty} I(k)\delta(k - jk_{rep}) \tag{3.2}$$

with $k_{rep} = \frac{1}{f_{rep}T_s}$. As described in the beginning of Chapter 2, simulations and algorithms are implemented in discrete time with a sampling time $T_s = 0.001\,\mathrm{s}$.

3.2.2 Bones, Joints, Muscles and Tendons

Bones and Joints

Like all four digits of the human hand, the index finger consists of three bones that are interconnected by rotational 1DOF joints. They are referred to as phalanx bones and are attached to the metacarpal bones that are located in the palm. The bones and the joints are illustrated and labeled in Fig. 3.6.

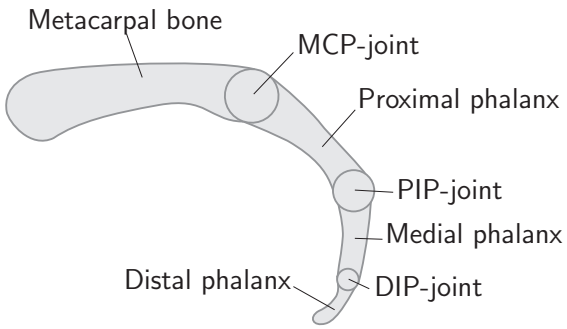

Fig. 3.6: Bones and Joints of the index finger: The metacarpal bone is located in the palm. The three joints are known as the metacarpophalangeal (MCP), the proximal interphalangeal (PIP), and the distal interphalangeal (DIP) joint.

Muscles and Tendons

The muscles involved in the index finger flexion and extension are the musculus (m.) extensor indices proprius (EIP, index finger extensor) the m. extensor digitorum communis (EDC) and the m. flexor digitorum profundus/superficialis (FDP/FDS, finger flexors), see Fig. 3.7. Muscles are connected to bones via tendons and the EDC is attached to four tendons that branch to all four digits. Hence, an isolated extension of either little finger,

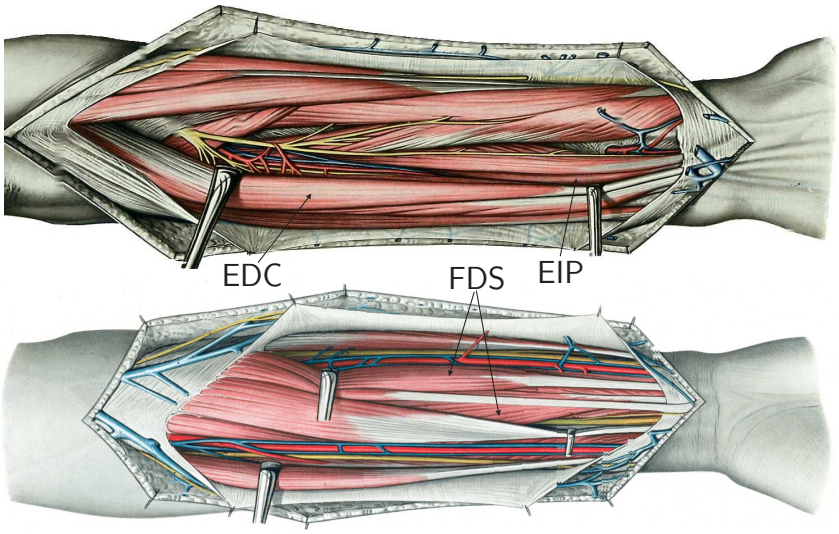

Fig. 3.7: Muscles involved in the index finger movement (Modified from [178]): Upper picture: Extensor side of the lower arm with the m. extensor digitorum communis (EDC) and the m. extensor indices proprius (EIP). Lower picture: Flexor side of the lower arm with the m. flexor digitorum superficialis (FDS). The m. flexor digitorum profundus (FDP) is not visible. It is located just below the FDS.

ring finger or middle finger is a complex interaction of EDC and FDP/FDS. Even though it is possible to activate certain areas of these muscles more than others, most humans are not capable of performing proper isolated extension movements. Only the index finger is connected to a separate muscle, the EIP, whose tendon runs in parallel to the tendon of the EDC. There is no separate flexor muscle but all four digits are connected with the FDP/FDS. Fig. 3.9 illustrates the tendon arrangement of the extrinsic[1] EIP-muscles in a lateral view.

The *RPMS*-induced index finger extension is achieved by stimulating the EIP. The flexion is accomplished by placing the coil above the innervation area of the FDP and FDS and hence, an isolated *RPMS*-induced index finger flexion is not possible since the other three digits are flexed, as well.

3.2.3 Coordinate Systems

The kinematics and the dynamics of the index finger are formulated using the coordinate systems introduced in Fig. 3.10. Each of the three finger segments is characterized by its length L_i, radius R_i, mass m_i and the coordinate system S_{i+1}, with $i = 1 \ldots 3$.

[1] An extrinsic muscle does not originate in the limb in which it is inserted whereas origin and insertion of an intrinsic muscle are in the same limb.

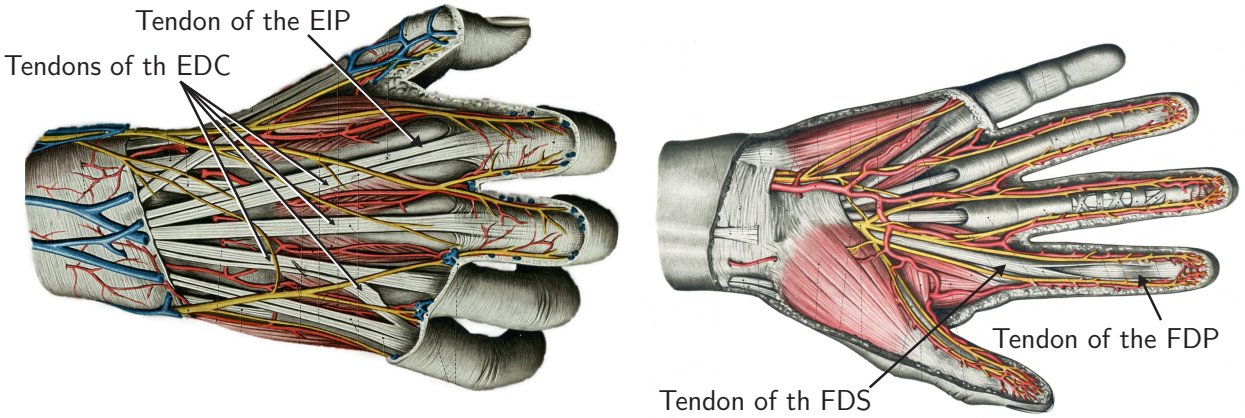

Fig. 3.8: Tendons involved in extension and flexion of the digits (Modified from [178]).

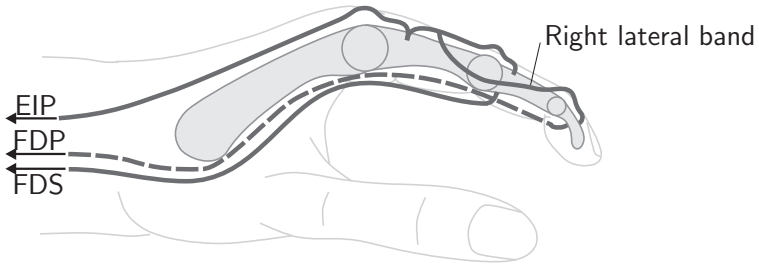

Fig. 3.9: Schematic anatomy of the tendons attached to the extrinsic muscle at the index finger: The tendon of the EIP spans over the MCP-joint and is primarily attached at the proximal phalanx. Subsequently, it spans over the PIP-joint and is finally attached to the medial phalanx. Additionally, two lateral bands are branching on the right and on the left side of the PIP-joint, span over the DIP-joint, and are attached to the distal phalanx. The tendon of the FDS is attached to the medial phalanx. The FDP-tendon passes through a slot of the FDS-tendon and connects to the distal phalanx.

3.3 Force Transmission

The muscle force F_M is transmitted via a tendon to the respective joint. The muscle joint torque τ_M is induced depending on the tendon leverage h according to $\tau_M = F_M h$. For the following considerations, it is assumed that the tendon strain can be neglected. This assumption is justified by the small tendon forces that occur during extension and flexion of the index finger in a normal range. A tendon strain model is introduced in [141], e.g.. Since viscous dissipative effects of the muscle-tendon unit are taken into account in the model of the segment dynamics (Section 3.6), the force transmission can be modeled as lossless.

The tendon leverage h results from the respective muscle and joint geometry. In general, it is a function of angles $\alpha_1 \dots \alpha_n$ of all joints the tendon spans. If the biomechanical geometry is known such that the length l_j of a muscle-tendon unit j is given as a function

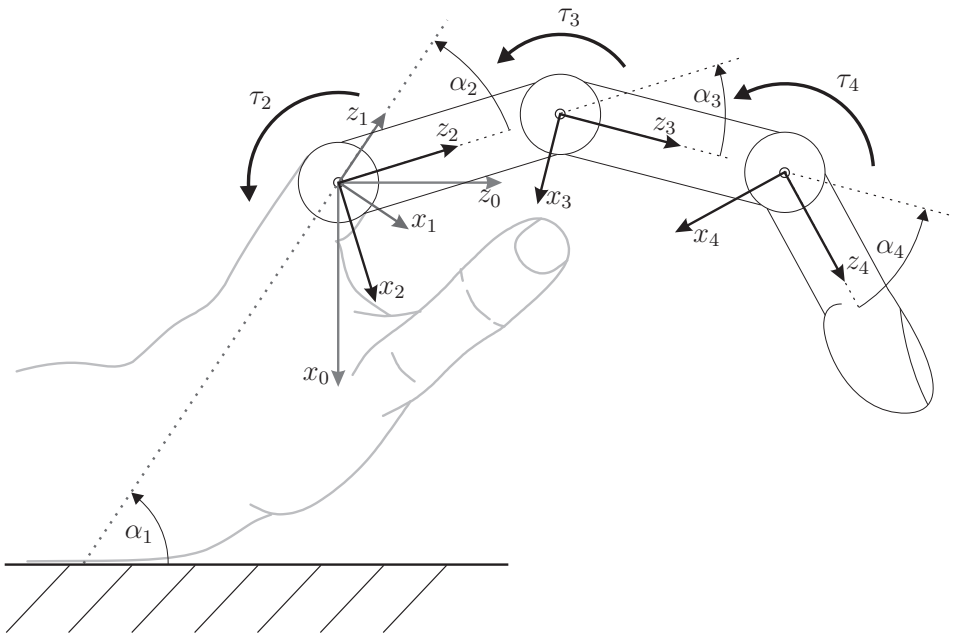

Fig. 3.10: Coordinate systems of the palm and index finger: The world coordinate system is given with x_0 and z_0. It is assumed that the finger is not abducted (straddled) and hence, the y-axes of all coordinate systems are in parallel. The z_0-axes is parallel to the ground, the z_1-axes is in parallel to the back of the hand, the z_2-, z_3- and z_4-axis are in parallel to the respective finger segments. The torques τ_i, denote the muscular driving torques τ_{M_i} acting on the MCP-, PIP-, and DIP-joint, respectively (see Section 3.2.2).

$l_j(\alpha_1 \dots \alpha_n)$ of the relevant joint angles, the leverages can easily be calculated using the principle of virtual work. The leverage $h_{i,j}(\alpha_1 \dots \alpha_n)$ of the j$^{\text{th}}$ muscle acting on the i$^{\text{th}}$ joint is given as

$$h_{i,j}(\alpha_1 \dots \alpha_n) = \frac{\partial l_j(\alpha_1 \dots \alpha_n)}{\partial \alpha_i} \quad . \tag{3.3}$$

For further derivations see [135].

In the following, the functions $l_j(\alpha_1 \dots \alpha_n)$ for the EIP, FDS and FDP are derived from a literature review.

3.3.1 Tendon Leverage of the Index Finger Extension

In [14], a model of the length of the muscle-tendon unit of the middle finger extensor is introduced. So far, it is the only model that takes into account the lateral bands (see Fig. 3.9) i.e. the angle α_4. Motivated by the anatomical similarity, it is assumed that the proposed model applies to the index finger, as well. Since the EIP-tendon (including the lateral bands) is attached to all three phalanges, its elongation is given as

$$\Delta l_{EIP} = \Delta l_{EIP,2}(\alpha_2) + \Delta l_{EIP,3}(\alpha_3) + \Delta l_{lat}(\alpha_3, \alpha_4), \tag{3.4}$$

whereas we have $\Delta l_{lat}(\alpha_3, \alpha_4) \approx 0$ for $\alpha_3 > -40°$ since in this configuration there is no tension on the lateral bands (see [212] for more detailed derivations). Furthermore, it is assumed that during extension of the MCP-joint with constant angle α_3, most of the force is induced at the tendon attachment at the proximal phalanx.

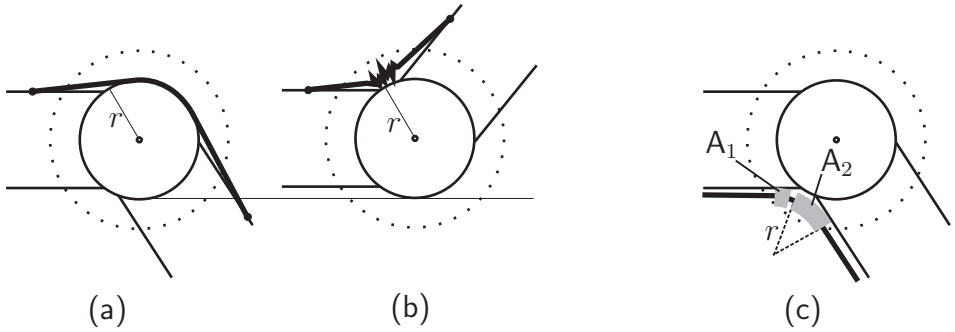

Fig. 3.11: (a) Pulley model of the EIP-tendon guidance over the MCP-joint in flexion configuration. (b) The pulley model does not apply to extension configuration. (c) Pulley model of the flexor tendons of the FDS and FDP as it is introduced in [101].

During *RPMS*, only the MPC-joint is extended. Our measurements demonstrated that the PIP-joint of a relaxed index finger has an average flexion of $\alpha_3 > -35°$. Therefore, the tendon elongation during *RPMS* can be simplified as

$$\Delta l_{EIP} = \Delta l_{EIP,2}(\alpha_2) \ . \tag{3.5}$$

The MCP-joint can be approximated as a pulley with radius r that guides the tendon (Fig. 3.11 (a)). This assumption is confirmed in [4], [14] and [47] but only applies to $\alpha_2 \leq 0$. If $\alpha_2 > 0$ (Fig. 3.11 (b)), it is not possible to find a relation by simple geometrical considerations. During *RPMS*, the index finger is hardly in extension, i.e. $\alpha_2 \leq 0$ and thus, the relation (3.5) is given as

$$\Delta l_{EIP} = -r\Delta\alpha_2 \ . \tag{3.6}$$

Thus, using Eq. (3.3), the leverage h_{EIP} is given as $-r$. The MCP-joint of the middle finger has an average radius of $r = 8\,\text{mm}$ [4; 14].

3.3.2 Tendon Leverage of the Index Finger Flexion

The tendons of the FDS and FDP are guided underneath the MCP-joint through the annular ligaments (also called pulleys) A_1 and A_2 (see Fig. 3.11 (c)). In flexion configuration, this guideway can be modeled as a pulley with radius r that is equal to the radius of the EIP-tendon pulley [101] (compare Fig. 3.11 (a)). Also the very fundamental investigation with cadaver fingers reported in [4] describes a nearly constant tendon leverage (approx. 8 mm) of FDS and FDP with respect to the MCP-joint.

FDS and FDP are connected to the distal and to the medial phalanges (Fig. 3.9) and flex the MCP-joint only indirectly when the mechanical resistance of PIP-joint and DIP-joint exceeds the resistance of the MCP joint. Therefore, a delay occurs when flexing

the MCP-joint with stimulation of the FDS/FDP. However, once the MCP-joint begins to flex, the configuration of the PIP-joint and DIP-joint remains almost constant and the elongation of the muscle-tendon units is given as

$$\Delta l_{FDS} = \Delta l_{FDP} \approx -r\Delta\alpha_2 \ . \tag{3.7}$$

Using Eq. (3.3), the tendon leverages are given as $h_{FDS} = h_{FDP} = -r$.

3.3.3 Discussion

The average radius r of the MCP-joint of the middle finger might differ from that of the index finger. Reliable data for the index finger could not be found. However, the linear force-torque relation r can be considered as a constant gain of the force generation model and thus, it will be automatically adapted to the respective subject using the system identification approach explained in Chapter 4.

3.4 Force Generation

The following derivations are based on the results in [6; 188; 191; 192] which are so far the only publications that include *RPMS*-modeling. The transcutaneous functional electrical stimulation (FES), see [129], e.g., is a related field of research where muscle activation models have been derived (see [30; 135; 147; 176], e.g.). However, as shown in [6], there exist fundamental differences in the nervous activation mechanisms of FES and *RPMS* such that on cannot conclude that the models proposed for FES apply to *RPMS*. The *RPMS*-activation model in [6] has been proposed for the m. biceps brachii (elbow flexor). In this section, the activation dynamics of the EIP are modeled. Because of anatomical differences between m. biceps brachii and EIP (size of muscle fibers and ratio of muscle fiber types, e.g.), it is expected that the models differ from each other.

All experiments discussed in this section are performed under isometric conditions. The terms isometric and non-isometric measurements will be used throughout this section and therefore, a short clarification appears necessary: Under isometric conditions, the length of the stimulated muscle remains nearly unchanged since the respective limb is attached to a fixed, immobile force sensor. Hence, the measured response to stimulation represents the muscle force. Under non-isometric conditions, the limb will move and therefore, the position of the limb will represent the measured system output.

By means of isometric measurements, the plant of muscle force generation can be analyzed aside from the segment dynamics and muscle contraction dynamics. As shown in [6], the Hammerstein structure (Fig. 3.12) that is often used to describe FES-induced muscle activation dynamics qualitatively applies to *RPMS*, as well.

The subsystem "force generation" (Fig. 3.1) consists of a physiological delay, the recruitment characteristics, and the dynamic force response as illustrated in Fig. 3.13. The recruitment is modeled with a static nonlinear function that describes the number of recruited motor units depending on the stimulation intensity I. The dynamic force response

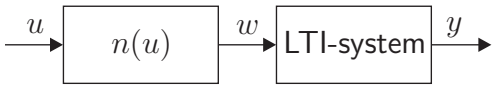

Fig. 3.12: Hammerstein cascade: A block structured nonlinear system that consists of a static nonlinearity with input u in series with an LTI-system with output y.

of a single recruited motor unit to a magnetic stimulus can be described with an LTI-system.

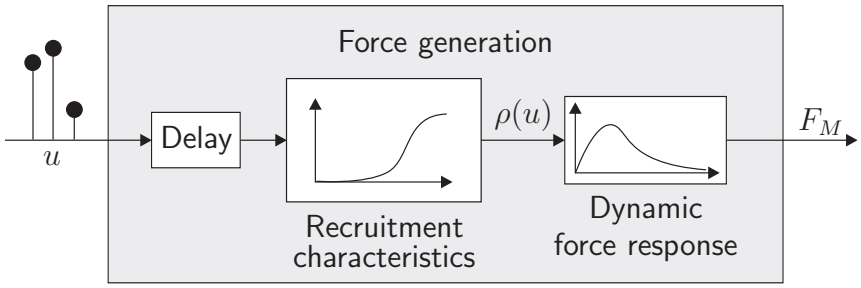

Fig. 3.13: Hammerstein structure of the force generation model: The input u is given with the magnetic stimulation pulses according to Eq. (3.2), the recruitment curve is denominated with $\rho(u)$ and the muscle force F_M represents the model output.

3.4.1 Experimental Setup

The experiments explained in the following were performed with the setup depicted in Fig. 3.14. During the experiments, all subjects were asked to relax their respective arm, hand and fingers as much as possible, in order to avoid artifacts. The force sensor was placed such that it touches the PIP-joint of the index finger when the MCP-joint is at its equilibrium position $\alpha_{2,0}$. Therefore, during stimulation, the MCP-joint angle remained constant and the length EIP-muscle-tendon unit did not change.

The relation between the sensor force F_s and the driving joint torque τ_2 is given with $\tau_2 = L_1 F_s$. Thus, the muscle force F_M can be calculated as

$$F_M = \frac{\tau_2}{r\cos(\gamma_P)} = F_s \frac{L_1}{r\cos(\gamma_P)} \quad . \tag{3.8}$$

This formula takes into account the tendon leverage r as introduced in Section 3.3 and the EIP pennation angle [95] γ_P. It describes the angle between the alignment of the muscle fibers and the line of action along the tendon. In [95], an average value of $\gamma_P = 6.3°$ was determined.

In the following, the output signal F_s of the force sensor unit will be directly interpreted as muscle force F_M instead of using Eq. (3.8). Since the overall gain of the measured forces is irrelevant for the following considerations, this is done for sake of a simpler notation but without loss of generality.

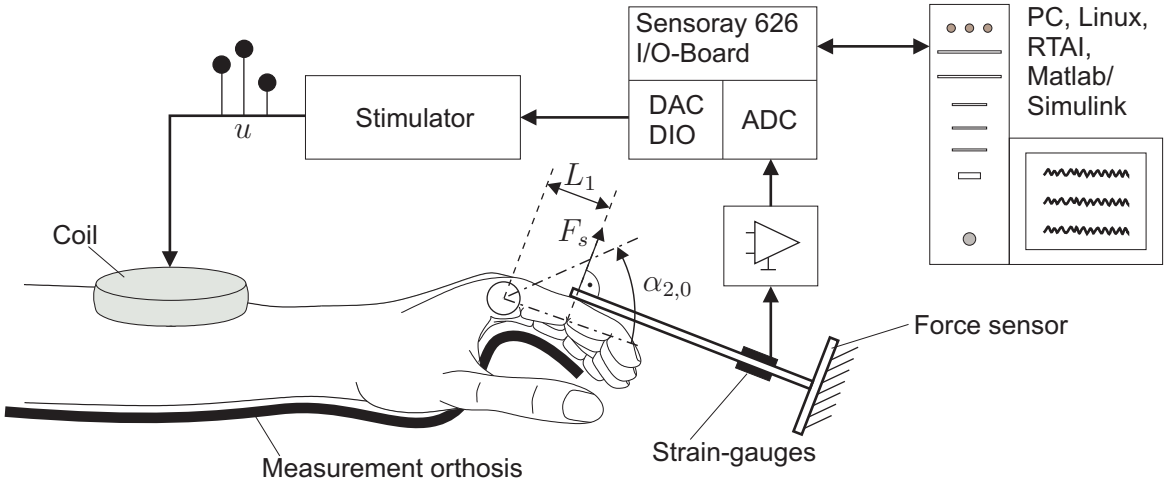

Fig. 3.14: Experimental setup for isometric *RPMS* of the EIP: The subject's hand is locked into position with a measurement orthosis. The force F_s is measured with a self built strain-gauge beam arrangement. The measurement signal of the strain-gauge full bridge is amplified, filtered with an anti-aliasing filter and sampled with a Sensoray 626 multichannel I/O board [157]. The filter is a simple RC-low pass with a corner frequency of 40 Hz. The I/O board is mounted on a Linux-PC with the real-time operating system "Real-Time Application Interface" (RTAI). The stimulator is driven by a program that runs in real-time on the PC. The sample rate f_s for all experiments is set at $f_s = 1\,\text{kHz}$. A magnetic pulse is fired when a trigger signal is sent. The stimulation intensity I of every pulse can be chosen arbitrarily with an analogue control signal. Due to technical properties of the stimulation device, there exists a hardware delay $T_{d,hw}$ between the trigger signal and the actual pulse. In [212], this delay been determined to $T_{d,hw} = 2.6\,\text{ms}$.

3.4.2 Physiological Delay

Physiology

The increase of muscle tension follows the muscle action potential (MAP) with a delay $T_{d,ph}$ (see Fig. B.4 and Appendix B.1.6). This delay is mainly due to the relatively slow MAP conduction velocity of $2-6\,\text{m/s}$. In [6], the delay occurring during FES and *RPMS* at the biceps muscle has been analyzed in a comparative study. It could be shown, that the FES-delay is more than twice as long (approx. 25 ms) and shows a greater inter-personal variance compared to *RPMS*. These differences can be explained by the propagation mechanisms of both stimulation methods. In contrast to the magnetic field, the propagation of the electrical current stimulus strongly depends on the properties of the tissue. In particular, the nonlinear and time varying resistive and capacitive skin properties play an important role in this process [34].

In [6], it could also be shown, that the physiological *RPMS*-delay depends neither on the pulse width nor on the stimulation intensity. Therefore, all experiments described in

the next paragraphs were conducted with the standard pulse width of our stimulators of $T_p = 90\,\mu$s and with a stimulation intensity of $I = 100\,\%$.

Data Acquisition and Data Processing

The delay $T_{d,ph}$ is defined as the time between the actual magnetic pulse and the onset of the force response $F_M(t)$, which is detected as the first positive zero crossing of $\dot{F}_M(t)$ after the magnetic pulse (Fig. 3.15). The hardware delay $T_{d,hw}$ is compensated by delaying the trigger signal that is considered for data processing by 2.6 ms.

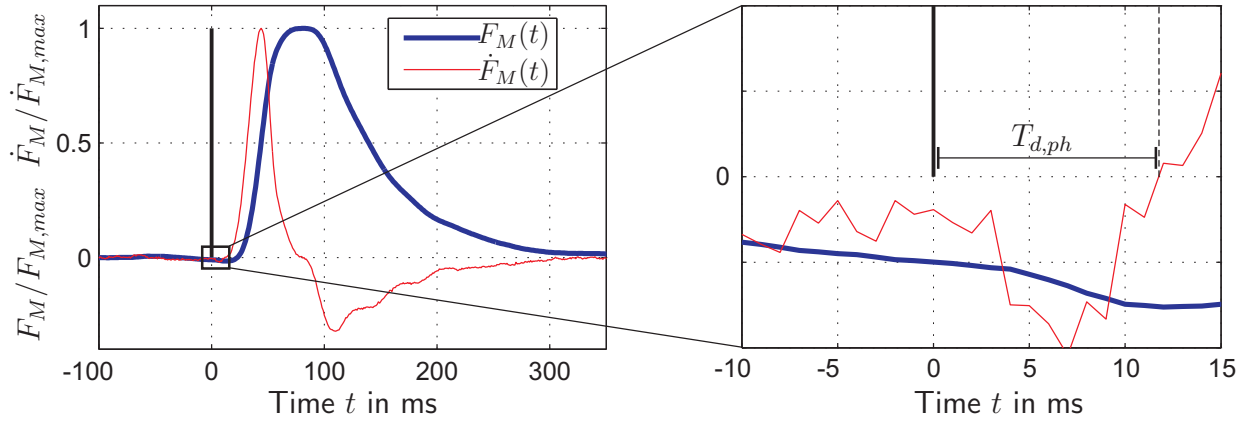

Fig. 3.15: Determination of the physiological delay $T_{d,ph}$. The instant at which the magnetic pulse is applied is labeled with a thick vertical line at $t = 0$. For a better illustration, the sensor force F_M and its time derivative $\dot{F}_M$ are normalized with respect to their maximum values.

As explained in Section 3.4.1, the force signal is filtered with a first order 40 Hz low pass filter for noise reduction and anti-aliasing. This filtering causes an additional delay that would bias the determination of $T_{d,ph}$. Therefore, the force signals are filtered backwards in an off-line procedure with a digital 40 Hz low pass filter in order to compensate for the delay caused by the hardware filter.

Experimental results

The experiments were conducted with 14 healthy subjects. From every subject, 30 pulses were recorded. For every pulse the delay $T_{d,ph}$ was determined according to Fig. 3.15. The average delay $\overline{T}_{d,ph}$ of a subject was calculated by averaging over 30 measurements of $T_{d,ph}$. The results are summarized in Tab. 3.1.

Tab. 3.1: Average delay and standard deviation $\overline{T}_{d,ph} \pm \sigma_{T_{d,ph}}$ calculated over 30 pulses applied to each subject. Also the average delay $\overline{\overline{T}}_{d,ph}$ over all values $\overline{T}_{d,ph}$, the standard deviation $\sigma_{\overline{T}_{d,ph}}$, and the 95 % confidence interval I_c [43] of $\overline{T}_{d,ph}$ have been calculated.

Subject	$\overline{T}_{d,ph} \pm \sigma_{T_{d,ph}}$ in ms
LS (f,23)	10.2 ± 3.6
BB (m,22)	9.3 ± 3.3
FH (m,22)	11.9 ± 3.1
DD (m,27)	11.0 ± 1.9
JS (f,21)	15.0 ± 3.3
DH (m,22)	12.3 ± 4.6
MK (m,24)	11.7 ± 3.5
TW (f,23)	14.8 ± 3.0
BG (m,24)	12.8 ± 4.1
CA (f,23)	11.6 ± 4.0
JM (m,23)	11.9 ± 3.8
AL (m,25)	14.4 ± 4.3
KS (f,23)	13.6 ± 4.2
AE (m,18)	12.9 ± 3.5
$\overline{\overline{T}}_{d,ph} \pm \sigma_{\overline{T}_{d,ph}}$	12.3 ± 1.7
I_c	[11.3 13.3]

3.4.3 Dynamic Force Response to a Single Stimulus

Physiology

When a motor unit is activated, the muscle fibers contract and exert a force, as explained in Appendix B.1.5. The force response, called twitch, is dynamic with a characteristic shape as depicted in Fig. B.4. It decays after a period called contraction time.

Model

In the following, the muscle twitch is referred to as its force response $F_{M,a}(t)$. It can be modeled as an impulse response of an LTI-system. Since $F_{M,a}(t)$ does not show any oscillating behavior (see Fig. 3.16, e.g.), it can be concluded that the transfer function of the impulse response model has real poles, only. In [6], model error analysis led to the conclusion that a third order model yields a sufficiently accurate approximation. Therefore, the transfer function

$$G_a(s) = \frac{K_a}{(1 + sT_a)^3} \tag{3.9}$$

is used as a model for the muscle twitch $F_{M,a}(t)$ of a recruited motor unit. The time constant T_a adapts the model to the actual contraction time and K_a is a gain factor. The time domain equation of (3.9) is calculated as

$$\hat{F}_{M,a}(t) = \frac{K_a}{2T_a^3} t^2 e^{\frac{-t}{T_a}} \quad . \tag{3.10}$$

For further considerations, Eq. (3.10) is time discretized and defined for negative and positive time separately which yields

$$\hat{F}_{M,a}(k) = \begin{cases} 0 & \text{for} \quad k < 0 \\ \frac{K_a}{2T_a^3}(kT_s)^2 e^{\frac{-kT_s}{T_a}} & \text{for} \quad k \geq 0 \end{cases} \quad . \tag{3.11}$$

Data Acquisition and Data Processing

The experiment was conducted with 14 healthy subjects. From every subject, 30 muscle twitches were recorded. In [6], it was shown that the time constant T_a depends neither on the stimulation intensity, nor the magnetic pulse width. Therefore, all pulses were applied with $I = 100\,\%$ in order to achieve the best possible signal-to-noise ratio and with the standard pulse width $T_p = 90\,\mu$s.

To fit the model (3.11) to the measured data, all twitches were normalized such that their peak value is equal to one. In Fig. 3.16, the normalized muscle twitches of every subject are plotted. For a better illustration, every subject's average muscle twitch $\overline{F}_{M,a}$ obtained from averaging over all 30 measurements is depicted. The time domain equation (3.10) has to be normalized accordingly which yields

$$\hat{F}_{M,a}(k) = \begin{cases} 0 & \text{for} \quad k < 0 \\ \frac{1}{(2T_a)^2 e^{-2}}(kT_s)^2 e^{\frac{-kT_s}{T_a}} & \text{for} \quad k \geq 0 \end{cases} \quad . \tag{3.12}$$

The optimal time constant $\overline{T}_{a,opt}$ of each subject was determined by initially minimizing the quadratic error criterion

$$E(T_a) = \|\underline{e}(T_a)\|_2^2 = \left\| \underline{F}_{M,a} - \underline{\hat{F}}_{M,a}(T_a) \right\|_2^2 \tag{3.13}$$

for all 30 pulses, whereas $\underline{e} = [e(0)\, e(T_s)\, e(2T_s) \ldots e(kT_s)]^T$. Minimizing Eq. (3.13) is a nonlinear least squares problem that has been solved using the MATLAB-function "`lsqnonlin`" [109]. Secondly, the 30 resulting time constants of each patient were averaged to $\overline{T}_{a,opt}$.

Experimental Results

Every muscle twitch was fitted to the model (3.12) in order to determine its time constant $T_{a,opt}$. The subjects' time constants were averaged to $\overline{T}_{a,opt}$. The model accuracy was calculated for every subject with the NMSE($\underline{F}_{M,a}, \underline{\hat{F}}_{M,a}(T_{a,opt})$) (see Appendix A.4). The results are summarized in Tab. 3.2.

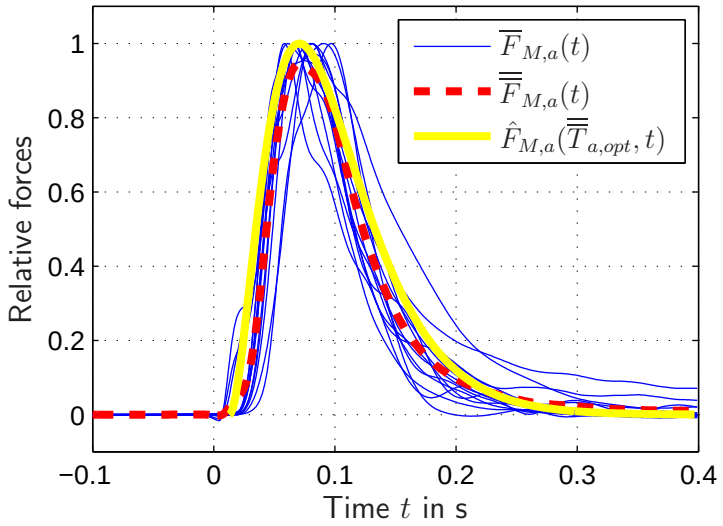

Fig. 3.16: The graphs show the average muscle twitches $\overline{F}_M(t)$ of every subject, the average response $\overline{\overline{F}}_M(t)$ over all data sets $\overline{F}_M(t)$, and the PT_3-approximation $\hat{F}_M(\overline{\overline{T}}_{a,opt}, t)$ calculated with the average time constant $\overline{\overline{T}}_{a,opt}$ obtained from all experiments with 14 subjects.

3.4.4 Dynamic Force Response to Repetitive Stimuli

Physiology

When a muscle is activated by a magnetic pulse train with a repetition rate f_{rep}, the muscle twitches merge to an unfused or fused tetanus. This effect is called temporal summation (see Appendix B.1.6). Examples are illustrated in Fig. 3.17.

Model

In contrary to physiological muscle activation, during magnetic stimulation, all recruited motor units are activated synchronously. Therefore, the muscle force generation during *RPMS* can simply be modeled as temporal summation of Eq. (3.11)

$$\hat{F}_{M,rep}(k) = \sum_{j=0}^{\infty} \hat{F}_{M,a}(k - jk_{rep}) \quad , \tag{3.14}$$

with $k_{rep} = {}^{1}/_{(f_{rep}Ts)}$. In [6] it has been shown that the model (3.14) describes the temporal summation with excellent accuracy.

Remark 3.4.1 *There are also nonlinear repetition rate dependent characteristics of the temporal summation (doublet- and triplet-effect [140]) that are not taken into account in* (3.14)*. In [6], the nonlinear temporal summation is built into the recruitment model. Here, these effects are not considered, since only the repetition rate* $f_{rep} = 20\,Hz$ *is of interest.*

Tab. 3.2: Time constants and accuracy of the PT_3 muscle twitch approximation. For every subject, the average value $\overline{T}_{a,opt}$ and its standard deviation $\sigma_{T_{a,opt}}$ is calculated from 30 twitches. The $\overline{\text{NMSE}}$ represents the approximation quality averaged over 30 NMSEs calculated for every twitch of the particular subject. In the last two lines, the average time constant $\overline{\overline{T}}_{a,opt} \pm \sigma_{\overline{T}_{a,opt}}$ the average $\overline{\overline{\text{NMSE}}}$ of the whole sample, and the 95 % confidence interval I_c [43] are presented.

Subject	$\overline{T}_{a,opt} \pm \sigma_{T_{a,opt}}$ in ms	$\overline{\text{NMSE}}$ in %
LS (f,23)	30.8 ± 1.5	3.0
BB (m,22)	28.7 ± 1.4	9.0
FH (m,22)	30.9 ± 1.1	4.6
DD (m,27)	29.5 ± 1.2	2.3
JS (f,21)	26.5 ± 1.3	5.3
DH (m,22)	24.9 ± 2.2	7.8
MK (m,24)	32.3 ± 1.2	4.2
TW (f,23)	27.0 ± 1.7	4.8
BG (m,24)	35.5 ± 1.3	5.5
CA (f,23)	27.0 ± 1.5	2.9
JM (m,25)	29.2 ± 1.5	19.7
AL (m,23)	26.3 ± 1.7	12.4
KS (f,23)	26.4 ± 1.7	10.1
AE (m,18)	29.9 ± 1.2	7.6
$\overline{\overline{T}}_{a,opt} \pm \sigma_{\overline{T}_{a,opt}}$, $\overline{\overline{\text{NMSE}}}$	28.4 ± 2.2	7.2
I_c	[27.1 29.7]	

The examples in Fig. 3.17 are force responses to repetitive stimulation with stimulation intensity of $I(k) = 100\%\,\sigma(k)$. Whereas $\sigma(k)$ denotes the discrete Heaviside Step Function. In the following, these force responses are referred to as step responses. After approx. 0.7 s the step responses reach a plateau. In this "steady state" $F_{M,rep}$ can be expressed as superposition of a periodic part and a constant part $F_{M,\overline{rep}}$. From the model equation (3.14), the constant part $\hat{F}_{M,\overline{rep}}$ can be derived as

$$\hat{F}_{M,\overline{rep}} = \frac{1}{k_{rep}} \sum_{k=0}^{k_{rep}-1} \sum_{j=0}^{\infty} \hat{F}_{M,a}(k - jk_{rep} + {}^{f_s}/_{1\text{Hz}}) \approx \frac{1}{k_{\text{rep}}} \sum_{k=0}^{{}^{f_s}/_{1\text{Hz}}} \hat{F}_{M,a}(k) \quad , \tag{3.15}$$

whereas it is assumed that the muscle twitch $\hat{F}_{M,a}(k)$ is decayed after 1 s or $k = {}^{f_s}/_{1\text{Hz}}$ samples. The complete derivation of Eq. (3.15) can be found in [6]. In the following, the constant part $\hat{F}_{M,\overline{rep}}$ will also be denominated as gain of the temporal summation.

Besides the dynamics of every single muscle twitch, the temporal summation shows a dynamic behavior, as well. The step responses of Fig. 3.17 can be interpreted as a

superposition of a periodic ripple caused by the muscle twitch dynamics with an aperiodic rise that will be referred to as dynamics of the temporal summation. These dynamics can be approximated with a PT_1 system and hence, the the equivalent model

$$G_e(s) = \frac{K_e}{1 + sT_e} \tag{3.16}$$

with its step response

$$\hat{F}_{M,e}(t) = K_e(1 - e^{\frac{t}{T_e}}) \tag{3.17}$$

is proposed. For further considerations, Eq. (3.17) is time discretized and defined for negative and positive time separately which yields

$$\hat{F}_{M,e}(k) = \begin{cases} 0 & \text{for} \quad k < 0 \\ K_e(1 - e^{\frac{kT_s}{T_e}}) & \text{for} \quad k \geq 0 \end{cases} . \tag{3.18}$$

The force $\hat{F}_{M,e}(k)$ directly depends on the repetition rate $f_{rep} = {}^1/_{(k_{rep}T_s)}$ as it can be inferred from Eq. (3.14), and thus, the time constant T_e is specific to the particular choice of f_{rep}. During therapy and during all our experiments, f_{rep} is chosen to 20 Hz. Therefore, only this repetition rate is considered.

Data Acquisition and Data Processing

During the experiments, 30 step responses were recorded from each of the 14 healthy subjects. Since the temporal summation model (3.14) was shown to be valid in [6] and the PT_3 time constant T_a is independent of I and T_p, it is obvious that also the PT_1 time constant T_e is independent of I and T_p. Thus, also during the step response experiments, the stimulation parameters were chosen to $I = 100\,\%$ and $T_p = 90\,\mu$s.

The model (3.17) was fitted to every measured step response by adapting time constant T_e. Therefore, the force signals were normalized with respect to the steady state value $F_{M,\overline{rep}}$ and the gain of model (3.18) was set to $K_e = 1$. In Fig. 3.17 the normalized results of every subject are plotted. For a better illustration, every subject's average step response $\overline{F}_{M,rep}$ obtained from averaging over all 30 measurements is depicted.

The identification of the optimal time constants $T_{e,opt}$ for every step response and the average time constants $\overline{T}_{e,opt}$ for every subject followed exactly the procedure as described for the impulse response $F_{M,a}(t)$. The model evaluation was done by calculating the NMSE($\underline{F}_{M,rep}, \underline{\hat{F}}_{M,rep}(T_{e,opt})$) according to Eq. (A.11) as explained in Appendix A.4.

Experimental results

Every subject's time constant $\overline{T}_{e,opt}$ was determined by averaging over 30 constants $T_{e,opt}$ obtained from fitting the model (3.16) measured step responses. The model was evaluated by calculating the $\overline{\text{NMSE}}$ as the average over all 30 NMSEs calculated for every model fit. The results are summarized in Tab. 3.3.

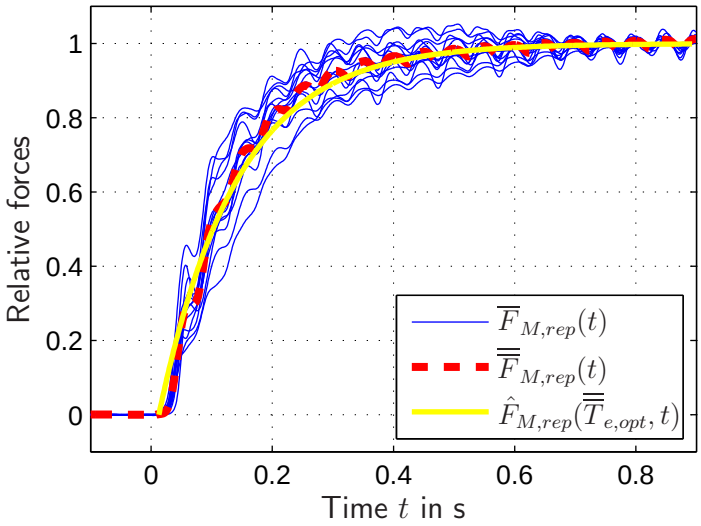

Fig. 3.17: The graph shows the average step responses $\overline{F}_{M,rep}(t)$ of every subject, the average response $\overline{\overline{F}}_{M,rep}(t)$ over all data sets $\overline{F}_{M,rep}(t)$, and the PT_1-approximation $\hat{F}_{M,e}(\overline{\overline{T}}_{e,opt}, t)$ calculated with the average time constant $\overline{\overline{T}}_e$ obtained from all experiments with 14 subjects.

3.4.5 Motor Unit Recruitment

Physiology

The number of recruited motor units (MUs) can be modulated with the stimulation intensity I. This relationship is called recruitment characteristics (see Fig. 3.13). The modulation of the muscle force with the number of recruited motor units is also called spatial summation (see also Appendix B.1.5). Due to the all-or-none principle of action potential elicitation, no MU is recruited when stimulating with an intensity below a certain threshold value I_{thr}. In the same manner, there exists a saturation value I_{sat} at which all motor units are active such that a further increase of I has no effect on the recruitment.

Model

To analytically describe the static nonlinear recruitment curve, the formula

$$\hat{\rho}(I) = \beta_1 \Big((I - I_{thr}) \arctan(\alpha_{thr}(I - I_{thr})) - (I - I_{sat}) \arctan(\alpha_{sat}(I - I_{sat})) \Big) + \beta_2 \quad (3.19)$$

is used that has been originally introduced in [135] as a model of the recruitment behavior during FES. The parameters I_{thr} and I_{sat} determine the threshold and saturation as explained above. With α_{thr} and α_{sat} the curvature in the region of I_{thr} and I_{sat} can be adapted and β_1, β_2 are gain and offset values.

Tab. 3.3: Time constants and accuracy of the PT_1 approximation of the step response: For every subject the average value $\overline{T}_{e,opt}$ and its standard deviation $\sigma_{T_{e,opt}}$ is calculated from 30 twitches. The $\overline{\text{NMSE}}$ gives the approximation quality averaged over 30 NMSEs calculated for every twitch of the particular subject. In the last two lines the average time constant $\overline{\overline{T}}_{e,opt} \pm \sigma_{\overline{T}_{e,opt}}$, the average $\overline{\overline{\text{NMSE}}}$ of the whole sample, and the 95 % confidence interval I_c [43] of $\overline{T}_{e,opt}$ are given.

Subject	$\overline{T}_{e,opt} \pm \sigma_{T_{e,opt}}$ in ms	$\overline{\text{NMSE}}$ in %
LS (f,23)	176.8 ± 25.2	0.2
BB (m,22)	125.7 ± 20.1	0.2
FH (m,22)	173.0 ± 22.1	0.2
DD (m,27)	113.4 ± 12.0	0.3
JS (f,21)	112.4 ± 16.5	0.2
DH (m,22)	145.4 ± 11.8	0.2
MK (m,24)	114.3 ± 9.3	0.2
TW (f,23)	96.1 ± 18.1	0.2
BG (m,24)	102.3 ± 9.5	0.3
CA (f,23)	125.9 ± 7.9	0.2
JM (m,25)	111.7 ± 38.3	0.5
AL (m,23)	145.2 ± 18.9	0.2
KS (f,23)	123.7 ± 31.4	0.7
AE (m,18)	138.1 ± 24.6	0.3
$\overline{\overline{T}}_{e,opt} \pm \sigma_{\overline{T}_{e,opt}}$, $\overline{\overline{\text{NMSE}}}$	128.9 ± 24.4	0.3
I_c	[114.8 143.0]	

Data Acquisition and Data Processing

For the experimental determination of the recruitment characteristics it is assumed that the number of recruited motor units is proportional to the constant part $F_{M,\overline{rep}}$ of the isometric force in steady state (compare to Eq. (3.14)). Therefore, the absolute recruitment characteristics are defined as

$$\rho(I) = F_{M,\overline{rep}}(I) \ . \tag{3.20}$$

It is important to note that with this definition, ρ is actually not the number of recruited motor units but a function that reflects its immediate effect. Thus, strictly speaking, Eq. (3.19) is a gray box model for the cause and effect relationship between stimulation intensity and isometric steady state force. In order to make the recruitment curves of different subjects comparable the relative recruitment

$$\rho_r(I) = \frac{\rho(I)}{F_{M,\overline{rep}}(20\,\text{Hz}, 100\,\%)} \tag{3.21}$$

was introduced. The value $F_{M,\overline{rep}}(100\,\%)$ was obtained as the constant part of the force response in steady state during stimulation with $I = 100\,\%$ and $f_{rep} = 20\,\mathrm{Hz}$.

The measurement was conducted by modulating the stimulation intensity according to $I(t) = 100\,\% \sin(\frac{t}{T})$ with $0 \leq t \leq \frac{T}{2}$. The periodic time was chosen to $T = 80\,\mathrm{s}$. Thus, the variation of intensity was much slower than the dynamics $G_e(s)$ that describes the dynamics of the temporal summation occurring during repetitive stimulation with $f_{rep} = 20\,\mathrm{Hz}$.

Experimental results

The recruitment characteristics was determined for four healthy subjects. In Fig. 3.18 (a), a measurement result from subject MB is depicted. The model (3.19) has been adapted to the measured relative recruitment (3.21) by finding the optimal parameters I_{thr}, I_{sat}, α_{thr} and α_{sat}. This optimization problem has been solved using the MATLAB-function "`fminsearch`" [109]. Exemplary parameter sets obtained from 4 different subjects are summarized in Tab. 3.4.

In contrary to the parameters of the activation dynamics, recruitment parameters that are specific to a particular subject cannot be determined since the recruitment curve is very sensitive to the position and orientation of the coil. This sensitivity is illustrated in Fig. 3.18 (b).

Tab. 3.4: Model parameters and model evaluation for the recruitment characteristics: The parameters have been determined by adapting the recruitment model to measurements obtained from four subjects. The model is evaluated with the calculation of the NMSE$(\rho(I), \hat{\rho}(I))$ according to Eq. (A.11).

Subject	I_{thr} in %	I_{sat} in %	α_{thr}	α_{sat}	NMSE in %
MB	59.4	92.1	11.1	8.6	0.25
BB	38.9	71.1	10.3	5.5	0.36
DM	61.1	91.9	5.7	8.3	1.21
BG	65.1	120.2	6.3	7.9	0.8

3.4.6 Complete Model

The complete model is obtained by integrating the physiological delay $T_{d,ph}$, the temporal summation $\hat{F}_{M,rep}$ and the recruitment $\hat{\rho}(I)$ into a common model in Hammerstein structure as depicted in 3.13. The equation is given as

$$\begin{aligned} \hat{F}_M(k) &= \frac{1}{\hat{F}_{M,\overline{rep}}(100\,\%)} \left[\sum_{j=0}^{\infty} \hat{\rho}(jk_{rep}) \hat{F}_{M,a}(k - k_{d,ph} - jk_{rep}) \right] \\ &= \frac{1}{\hat{F}_{M,\overline{rep}}(100\,\%)} \left[\hat{\rho}(0) \hat{F}_{M,a}(k - k_{d,ph}) + \hat{\rho}(k_{rep}) \hat{F}_{M,a}(k - k_{rep} - k_{d,ph}) + \ldots \right] , \end{aligned} \tag{3.22}$$

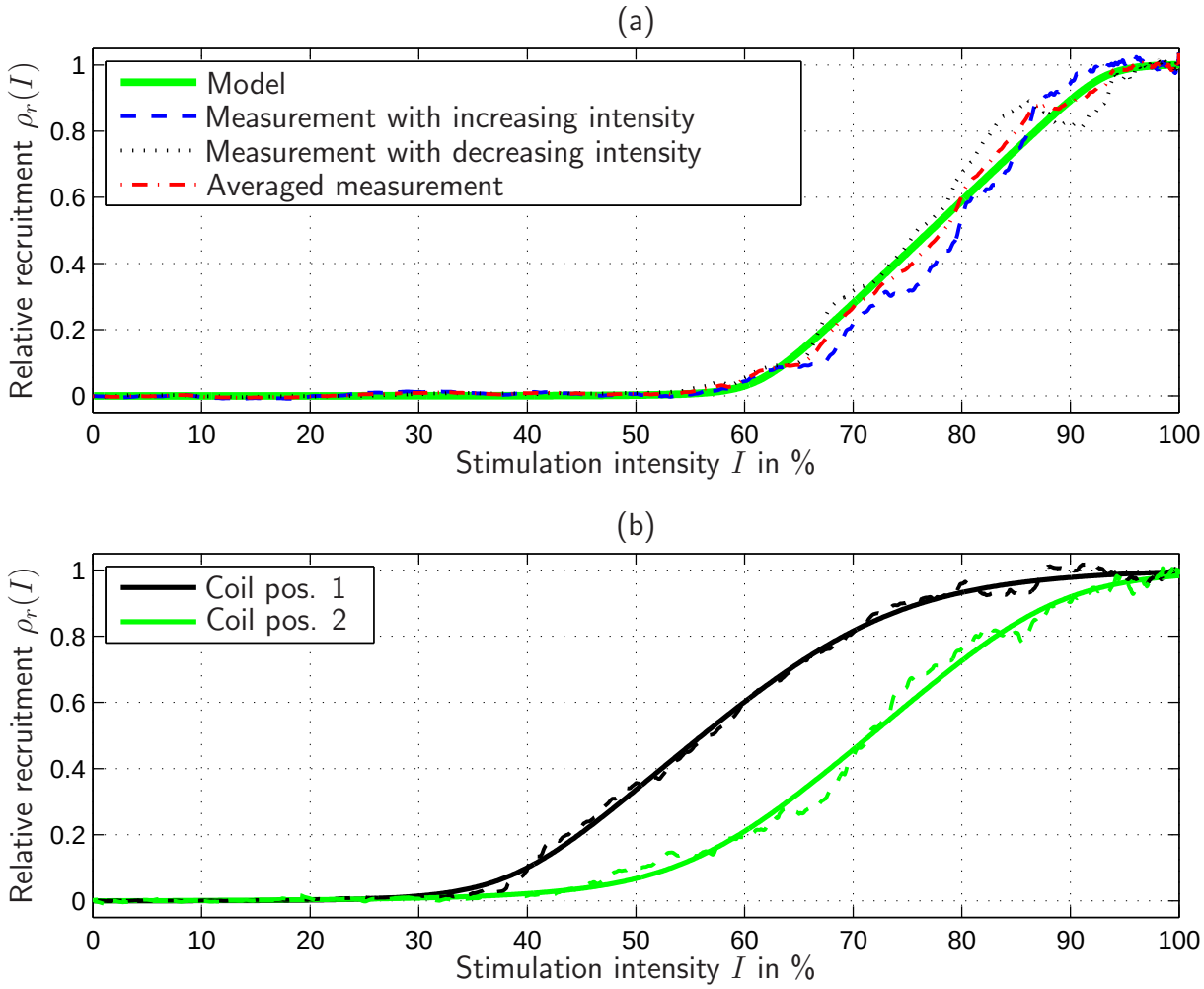

Fig. 3.18: (a) Measurement results and model of the relative recruitment of subject MB: As explained before, during the measurement, the stimulation intensity has been slowly increased from 0 % to 100 % and decreased backwards with a sinusoidal signal $I(t)$. Both, the measurement during increasing and the measurement during decreasing intensity are depicted. The model has been adapted to the curve obtained by averaging both measurements. (b) Relative recruitment of subject BB: Coil position 1 was determined by searching for a position that yielded a very good recruitment. Then, the coil was slightly moved into position 2. For both positions, the averaged recruitment measurements are plotted with dashed lines, and the models are plotted with solid lines.

whereas the physiological delay $T_{d,ph}$ is approximated with $k_{d,ph} = \text{round}(T_{d,ph}/T_s)$. Using Eq. (3.2), the recruitment value $\hat{\rho}(jk_{rep})$ is calculated as

$$\begin{aligned}\hat{\rho}(jk_{rep}) = \hat{\rho}(u(jk_{rep})) &= \hat{\rho}\Big(\sum_{i=0}^{\infty} I(jk_{rep})\delta(jk_{rep} - ik_{rep})\Big) \\ &= \begin{cases} \hat{\rho}(I(jk_{rep})) & \text{for} \quad i = j \\ 0 & \text{else} \end{cases} . \end{aligned} \tag{3.23}$$

According to Eq. (3.20), the gain of the linear temporal summation is included in the absolute recruitment. Since this gain is also inherently included in the formula

$$\sum_{j=0}^{\infty} F_{M,a}(k - jk_{rep})$$

that describes the temporal summation, the normalization with $\hat{F}_{M,\overline{rep}}(100\,\%)$ is necessary.

Remark 3.4.2 *A correct gain of the model* (3.22) *could also be achieved by combining the relative recruitment* $\hat{\rho}_r$ *with impulse responses* $\hat{F}_{M,a}$ *that are scaled to approximate a muscle twitch with* $I = 100\,\%$*. The chosen definition is advantageous because the absolute recruitment directly indicates the stimulation intensity steady state force* $F_{M,\overline{rep}}(I)$*.*

3.4.7 Discussion

The average physiological delay $\overline{\overline{T}}_d = 12.3\,\text{ms}$ shows a relative average interpersonal standard deviation of 13.8 %. Within 12.3 ms, the MAPs propagate a distance of 2.5-7.2 cm, considering a propagation velocity of 2-6 m/s (see Appendix B.1.6). Considering an EIP-length of 9-13 cm, this distance is within a reasonable range.

The force response to a single stimulus, also called muscle twitch, is modeled with a PT_3 system. The average time constant $\overline{\overline{T}}_a = 28.4\,\text{ms}$ shows a relative average interpersonal standard deviation of 7.7 % and a spans between 26.3 ms and 35.5 ms. A parameter adaptation will be introduced in Chapter 4 that will individualize the dynamic muscle twitch model to the respective subject. As the NMSE-evaluation indicates, the PT_3-system shows a very good approximation performance. In [6], the same model has been successfully applied to the m. biceps brachii. The average time constant has been determined with 38.4 ms. Or rather, the m. biceps brachii has an average contraction time of 450 ms whereas the EIP contraction time has been determined to 350 ms. This result can be ascribed to the different sizes of the respective muscles, since in a bigger muscle, the MAPS have to overcome longer distances.

The enhancement of the mathematical description of the force response for repetitive stimulation is trivial since the principle of temporal summation can be mathematically expressed as summation of muscle twitches. This summation is possible since during *RPMS* all motor units are recruited simultaneously. In [6], the excellent accuracy of the summation approach (3.14) has already been shown. Here, the dominant dynamics of the temporal summation are investigated. These dynamics depend on the repetition rate f_{rep} and have only been analyzed for $f_{rep} = 20\,\text{Hz}$ since this repetition rate is our standard during therapy, system identification and position-controlled movement induction. The proposed equivalent system $G_e(s)$ shows excellent model accuracy. The average time constant $\overline{\overline{T}}_e = 128.9\,\text{ms}$ has a relative average interpersonal standard deviation of 18.9 %. The transfer function $G_e(s)$ can be interpreted as an equivalent system with continuous input that approximates the dominant dynamic behavior of the force produced by the repetitively stimulated muscle. The knowledge of this dynamic behavior is important for tuning of the on-line parameter identification of Chapter 4, and the design of the position-controlled movement induction as it will be introduced in Chapter 5.

Also the recruitment model yields a very good accuracy, as the model evaluation indicates. The measurements of the recruitment characteristics show a large variation. This can indeed be due to interpersonal differences of muscle sizes and muscle geometries. However, the position and the orientation of the coil has an even larger influence on the recruitment curve. Therefore, the recruitment model has to be adapted each time the coil is placed differently and the coil has to be fixated properly during parameter identification.

The complete model will be used for simulative studies. Since the simulations are implemented in discrete time, a time discrete model is derived. When integrating the recruitment curve and activation dynamics into one model equation, it has to be considered that the gain of the temporal summation (compare to Eq. 3.15) is incorporated in the absolute recruitment model (3.20), and is also inherently included in Eq. (3.14). This is taken into account in Eq. (3.22) with the normalization with respect to $\hat{F}_{M,\overline{rep}}(100\,\%)$.

It is important to note, that the proposed model has a macroscopic character that does not explicitly model the electrophysiological processes in the motor unit. Nevertheless, the input-output behavior of the *RPMS*-induced force generation can be predicted with a good accuracy that is sufficient for the simulative studies used in Chapter 4 and 5. Also an explicit model of muscle fatigue, as it is introduced in [135] has not been derived. In Chapter 5, it will be shown how muscle fatigue can be identified with an on-line parameter identification of the model introduced in this section. Experiments that determine the model parameters of the flexor muscles FDP/FDS have not been accomplished since it is assumed that the proposed EIP model qualitatively applies to the flexors, too, and the parameters are individualized by means of system identification, anyway.

3.5 Length-Velocity-Dependencies

Under non-isometric conditions, the length of the muscles attached to the moving limb changes. As explained in Appendix B.1.6, the muscle's capability of force generation depends on its length and its velocity. This dependency is modeled with the force-length curve (f_l) and the force-velocity curve (f_v) and is included into the model with the block "length-velocity-dependencies" (see Fig. 3.1). Under isometric conditions, the output of this subsystem remains constant and can be considered as a constant gain of the muscle force generation.

The first mathematical model was introduced by Hill [67]. Since then, many slight modifications of Hill's muscle model were published and the most important contributions are summarized in [135]. Most models were proposed on the basis of experiments with frog leg muscle fibers. A break down of the block "length-velocity-dependencies" of 3.1 is depicted in Fig. 3.19. The gain factor that scales the output of the block "muscle force generation" is calculated as $f_l(\alpha_2)f_v(\dot{\alpha}_2)$.

3.5.1 Simulative Quantification

In order to simulate the force-length- and the force-velocity-behavior for the index finger movements, the models proposed in [19; 20] were used. The main differences compared with the models proposed in the publications summarized in [135] are: Experimental data

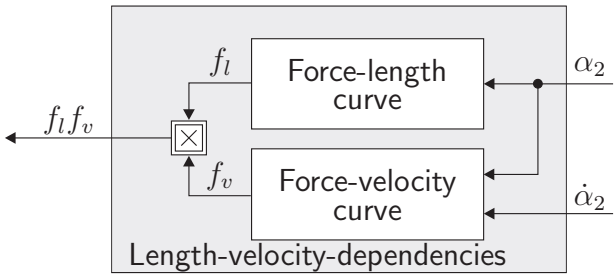

Fig. 3.19: Break down of the block "length-velocity-dependencies" of Fig. 3.1.

were obtained from rabbit muscles that are more comparable to human muscles than frog muscles. Furthermore, the proposed force-velocity-curve includes a muscle length dependency, too, which yields a better approximation than a pure velocity dependency.

The formulae are given as

$$\tilde{f}_l(\overline{l}) = \exp\left(-\left| \frac{(\overline{l})^{\,b_1} - 1}{b_2} \right|^{b_3} \right) \tag{3.24}$$

and

$$\tilde{f}_v(\overline{l}, \overline{v}) = \begin{cases} \dfrac{c \;-\; \overline{v}}{c + (d_{v1} + d_{v2}\overline{l})\,\overline{v}} & \text{for } \overline{v} \leq 0 \\ \dfrac{e \;-\; (f_{v0} + f_{v1}\overline{l} + f_{v2}\overline{l}^{\,2})\,\overline{v}}{e \;+\; \overline{v}} & \text{for } \overline{v} > 0 \end{cases}, \tag{3.25}$$

whereas $\overline{l} = {}^{l}/_{l_{opt}}$ and $\overline{v} = v\,{}^{1\mathrm{s}}/_{l_{opt}}$, with the muscle length l, the velocity $v = {}^{dl}/_{dt}$ and the optimal length l_{opt} at which the muscle can exert maximum force. The model parameters are summarized in Tab. 3.5.

Tab. 3.5: Parameters of the $\tilde{f}_l$ and $\tilde{f}_v$ curves according to [19]: The model distinguishes slow twitch fibers (Type I) and fast twitch fibers (Type II), see also Appendix B.1.6.

Muscle fiber type	b_1	b_2	b_3	c	d_{v1}	d_{v_2}	e	$f_{v,0}$	$f_{v,1}$	$f_{v,2}$
Type I	2.30	1.26	1.62	-4.06	5.88	0	0.18	-4.70	8.41	-5.34
Type II	1.55	0.81	2.12	-7.39	-3.21	4.17	1.05	-1.52	0	0

The optimal lengths l_0 for the relevant muscles were taken from [95] and are as follows: EIP: 105 mm, FDP: 149 mm and FDS: 140 mm. The functions $\tilde{f}_l$ and $\tilde{f}_v$ depend on l and v. In order to obtain functions f_l and f_v that depend on α_2 and $\dot{\alpha}_2$, the relationships (3.6) and (3.7) have to be applied. The models (3.24) and (3.25) were simulated with position and velocity ranges that definitely give lower and upper bounds for the MCP-joint motion during *RPMS*. With $-70\,^\circ \leq \alpha_2 \leq 10\,^\circ$ and $-150\,^\circ/\mathrm{s} \leq \dot{\alpha}_2 \leq -150\,^\circ/\mathrm{s}$ the factor $f_l f_v$ was bounded with $0.94 < f_l f_v < 1.06$ for all three muscles involved. The ratio between Type I and Type II fibers was chosen at 50 %.

3.5.2 Discussion

This simulation result shows that during non-isometric *RPMS*, the scaling with $f_l f_v$ changes the output of the block "muscle force generation" by less then 6 %. Hence, for the model-based parameter identification applied to the plant "*RPMS*-induced index finger extension and flexion", as it will be described in Chapter 4, the length-velocity-dependencies will be neglected.

3.6 Segment Dynamics

In this section, a model is proposed that simulates the dynamic relationship between the exerted muscle forces and the resulting motion of the index finger. In particular, the MCP-joint of the index finger is considered. During all experiments described in the following, the subject, its arm and its wrist remain in a fixed position, so that the coordinate system S_1 (Fig. 3.10) is stationary. It is furthermore assumed that the angles α_3 and α_4 remain constant. Thus, the segment dynamics of the index finger are given with the second order differential equation

$$\ddot{\alpha}_2 = \frac{1}{J}\tau_n = \frac{1}{J}(\tau_2 - N_1(\alpha_2) - N_2(\dot{\alpha}_2) - \tau_{rel}) \quad . \tag{3.26}$$

The block diagram representation is illustrated in Fig. 3.20. The net torque τ_n acts on the moment of inertia J and accelerates the finger. The nonlinearities $N_1(\alpha_2)$ and $N_2(\dot{\alpha}_2)$ that subtract from the muscular driving torque τ_2 are explained in the following. Our experiments have shown that the elastic joint properties are not purely static but are characterized by relaxation effects. This is taken into account by the block "relaxation dynamics" that is explained in detail in Section 3.6.3.

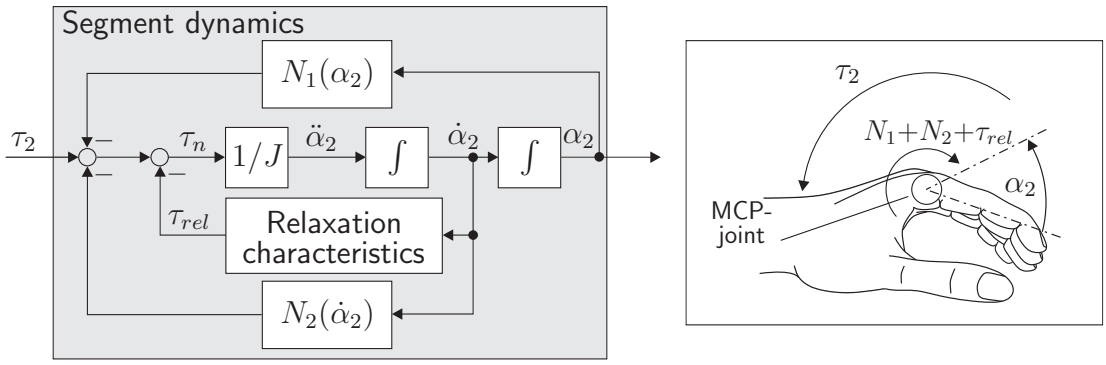

Fig. 3.20: Block diagram representation of the segment dynamics of the index finger motion at the MCP-joint and sign conventions according to the directions of α_2 and τ_2 defined in Fig. 3.10.

3.6.1 Moment of Inertia

In order to calculate a J, the finger phalanges are modeled as solid homogeneous cylinders with length L_i and radius R_i (see Section 3.2.3). Thus, the mass m_i of the i^{th} phalanx is calculated as

$$m_i = \pi R_i^2 L_i d_s \tag{3.27}$$

with the specific density $d_s = 1.1\frac{\text{g}}{\text{cm}^3}$ [184]. The moment of inertia of each cylinder with respect to the axis of rotation y_2 is denoted with $J_{i,y2}$ and hence, J can be calculated as

$$\begin{aligned} J &= J_{1,y_2} + J_{2,y_2} + J_{3,y_2} \\ &= m_1\,(\frac{R_1^2}{4} + \frac{L_1^2}{3}) + \\ &\quad + m_2\left(L_1^2 + \frac{L_2^2}{3} + \frac{R_2^2}{4} + L_1 L_2 \cos\alpha_3\right) + \\ &\quad + m_3\left(L_1^2 + L_2^2 + \frac{R_3^2}{4} + \frac{L_3^2}{3} + L_2 L_3 \cos\alpha_4 + 2L_1 L_2 \cos\alpha_3 + L_1 L_3 \cos(\alpha_3 + \alpha_4)\right) \ . \end{aligned} \tag{3.28}$$

The derivation of Eq. 3.28 can be found in A.5.

3.6.2 The Nonlinearities $N_1(\alpha_2)$ and $N_2(\dot{\alpha}_2)$

The static nonlinear function $N_1(\alpha_2)$ summarizes the gravitational torque $\tau_g(\alpha_2)$ and the elastic properties $\tau_{ep}(\alpha_2)$ of the joint and of the attached muscle-tendon units and is given with

$$N_1(\alpha_2) = \tau_g(\alpha_2) + \tau_{ep}(\alpha_2) \ . \tag{3.29}$$

The gravitational component can be approximated using the cylinder model as used for the moment of inertia J. The elastic joint and muscle properties $\tau_{ep}(\alpha_2)$ can be approximated with a double exponential function as

$$\tau_{ep}(\alpha_2) = a(e^{b(\alpha_2 - \alpha_{2,r})} - e^{c(\alpha_2 - \alpha_{2,r})}),$$

with the equilibrium joint angle $\alpha_{2,r}$ and the design constants a, b and c (see [37], e.g.). Fig. 3.21 illustrates a typical curve that shows a nearly linear behavior in a region around the equilibrium angle.

The static nonlinear function $N_2(\dot{\alpha}_2)$ comprises the joint friction $\tau_f(\dot{\alpha}_2)$, as well as viscous dissipative properties of the muscle-tendon unit $\tau_{vm}(\dot{\alpha}_2)$ and is given as

$$N_2(\dot{\alpha}_2) = \tau_f(\dot{\alpha}_2) + \tau_{vm}(\dot{\alpha}_2) \ . \tag{3.30}$$

The actual friction occurring in the joints is negligible compared to the viscous muscle-tendon properties. The latter are typically approximated as

$$\tau_{vm} \propto \text{sign}(\dot{l}_m)|\dot{l}_m|^{1/2},$$

with the muscle contraction speed $\dot{l}_m$ (see [58; 60], e.g.). According to Eq. (3.6) and Eq. (3.7), the muscle contraction speed $\dot{l}_m$ is proportional to $\dot{\alpha}_2$ and the approximation

$$\tau_{vm}(\dot{\alpha}_2) \propto \text{sign}(\dot{\alpha}_2)|\dot{\alpha}_2|^{1/2}$$

applies (see Fig. 3.21).

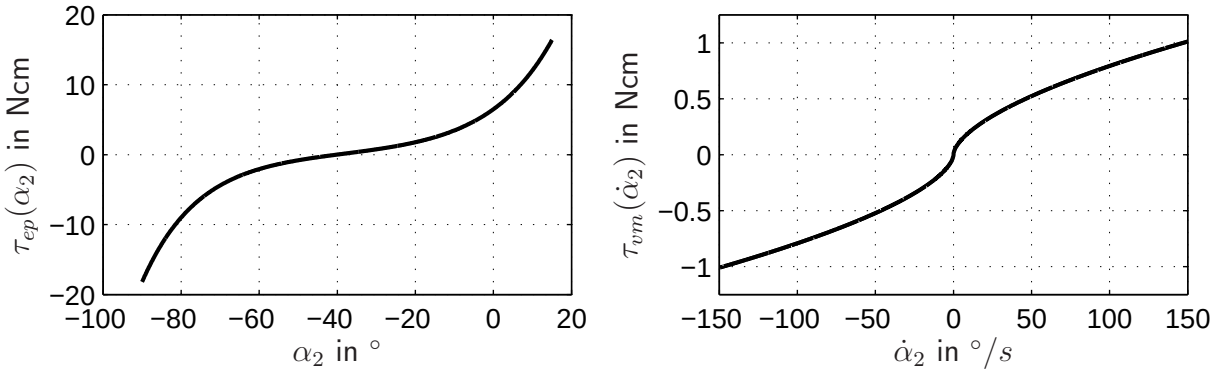

Fig. 3.21: Left: Model of the elastic joint properties τ_{ep} in the index finger according to [37]. Typically, the torque increases rapidly near -90° flexion and in extension configuration ($\alpha_2 > 0.$) Right: Model of the viscous dissipative properties of the muscle-tendon-unit according to [58].

Average parameters of τ_g, τ_{ep}, and τ_{vm} are not determined in experimental studies since the nonlinear functions $N_1(\alpha_2)$ and $N_2(\dot{\alpha}_2)$ will be adapted to the respective subjects using a system identification approach as presented in Chapter 4.

Remark 3.6.1 *As mentioned in the introduction of this chapter, the elastic and the viscous muscle properties are usually modeled with separate equations and summarized together with the length-velocity-dependencies as muscle contraction dynamics. Here, they are integrated into the segment dynamics in order to summarize all static nonlinear functions, that are not involved in active muscle force generation, within the nonlinearities $N_1(\alpha_2)$ and $N_2(\dot{\alpha}_2)$. This is formally correct but does not reflect the topology of the plant since the segment dynamics only describe the kinetics of the limb itself. Nevertheless, this approach simplifies the mathematical description, and will be advantageous for the system identification that will adapt the qualitative model to the respective subject as described in Chapter 4.*

3.6.3 Relaxation Characteristics

Our observations have shown that the approximation of the passive elastic properties with a static function $\tau_{ep}(\alpha_2)$, which is a sufficiently accurate model for the knee joint or the elbow joint, e.g., does not suffice when modeling the passive elastic joint properties of the MCP-joint. Instead, the passive torque is subject to a relaxation phenomenon that has to be approximated with a dynamic model. In order to determine the relaxation characteristics,

torque-position-measurements are carried out. For these measurements, the Fingertester depicted in Fig. 3.22 has been developed (see also Appendix C and [214]). It moves the MCP-joint of the index finger in a horizontal plane along a predefined trajectory and measures the exerted torque τ_{me}, whereas the direction of τ_{me} is defined equally to the direction of τ_2.

Phenomenon

If the MCP-joint is moved along a sinusoidal trajectory ($\dot{\alpha}_2 \approx 20°/s$), a hysteresis-shaped torque τ_{me} is recorded which significantly differs from a purely static approximation (Fig. 3.23, left). The graph on the right hand side of Fig. 3.23 shows the measured torque response to a position step $\Delta\alpha_2$. As indicated with the dashed curve, τ_{me} can be approximated with a exponentially decaying process with the relaxation time constant T_{rel}.

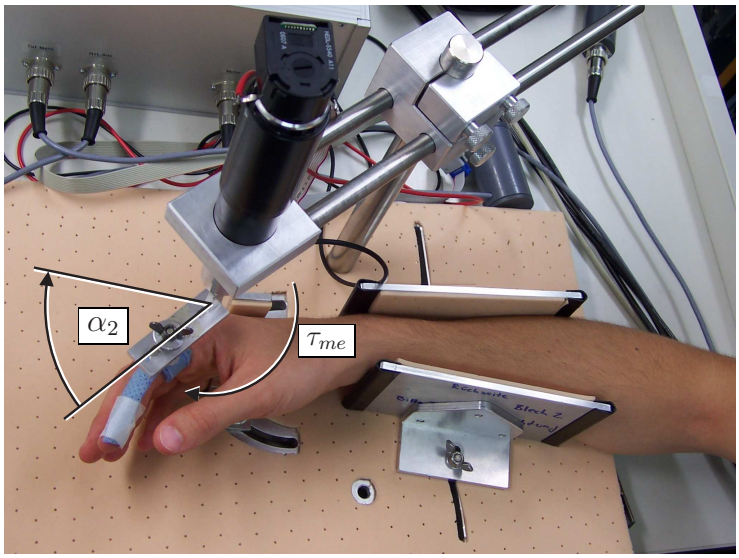

Fig. 3.22: The Fingertester: Self built measurement device that measures angle-torque-curves of the MCP-joint.

Model

A Maxwell element is proposed as a model of the relaxation behavior illustrated in Fig. 3.23. It consists of a linear damper in series with a linear spring. A schematic of the MCP-joint with a mechanical equivalent is depicted in Fig. 3.24. Spring and damper of the Maxwell element are characterized by the damping constant D_{rel}, and by the spring constant E_{rel}. Based on the element equations $\tau_E = E_{rel}\alpha_E$ and $\tau_D = D_{rel}\alpha_D$ and the deformation constraints $\alpha_2 = \alpha_E + \alpha_D$ and $\tau_E = \tau_D = \tau_{rel}$, the constitutive equation

$$\dot{\tau}_{rel} = E_{rel}\dot{\alpha}_2 - \frac{1}{T_{rel}}\tau_{rel} \tag{3.31}$$

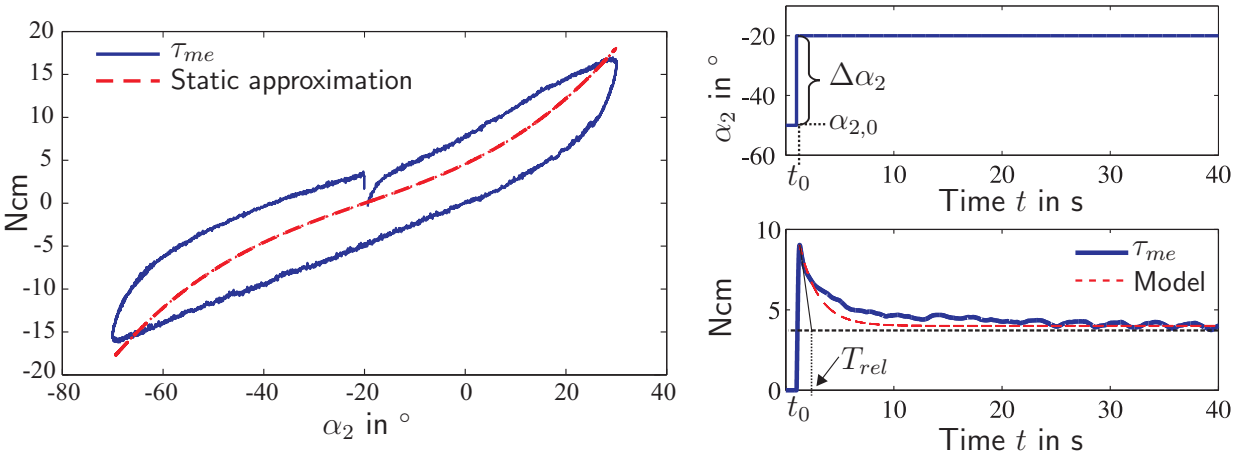

Fig. 3.23: Left: Measured torque τ_{me} during sinusoidal movement of the MCP-joint compared to a static approximation. Right: Step response experiment and first order model. The MCP-joint has been moved along a position step $\Delta\alpha_2$. The initial angle $\alpha_{2,0}$ is given with the equilibrium position at which the finger remains without applying muscle forces or external forces, i.e. $N_1(\alpha_{2,0}) = 0$.

can be easily derived with the relaxation constant $T_{rel} = {}^{D_{rel}}/_{E_{rel}}$. This differential equation can be integrated into the segment dynamics (Fig. 3.20) with the PT_1 transfer function

$$\frac{\tau_{rel}(s)}{s\alpha_2(s)} = \frac{E_{rel}}{s + {}^1/_{T_{rel}}} \quad . \tag{3.32}$$

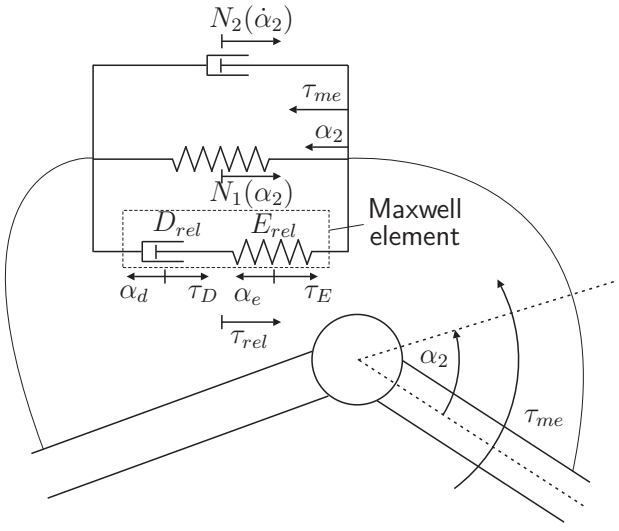

Fig. 3.24: Proposed model of the passive joint properties: The nonlinearities $N_1(\alpha_2)$ and $N_2(\dot{\alpha}_2)$ are modeled as nonlinear spring and nonlinear damper. The Maxwell element in parallel connection approximates the relaxation behavior.

3.6.4 Model Identification and Verification

To identify the parameters of moment of inertia and relaxation and the nonlinearities $N_1(\alpha_2)$ and $N_2(\dot{\alpha}_2)$, experiments with 18 healthy subjects were accomplished. The moment of inertia was determined simply by collecting anthropometric data, whereas the relaxation and the nonlinear functions were analyzed in a two stage system identification process. The model was verified and evaluated by calculation of the relative model error.

Moment of Inertia

The lengths L_i and the radii R_i of the index finger segments of 15 subjects were measured. Subsequently, the moment of inertia J was calculated according to Eq. (3.28). The average configuration of the PIP- and the DIP-joint were assumed to be $\alpha_3 = -30°$ and $\alpha_4 = -10°$ if wrist and fingers are in a relaxed position. The anthropometric data are summarized in Tab. 3.6.

Tab. 3.6: Anthropometric data of the left index finger taken from 15 healthy subjects. Every subject's sex and age is indicated in parenthesis in the first column. Units: L_i and R_i in mm, J in 10^{-5}kgm^2. The last two lines indicate the average values μ, the standard deviations σ, and the 95 % confidence interval I_c [43].

Subject	L_1	L_2	L_3	R_1	R_2	R_3	J
LS (f,23)	46	26	22	19	16	14	3.2
BB (m,22)	43	25	25	20	17	16	3.3
FH (m,22)	52	33	23	22	18	16	6.5
DD (m,27)	50	27	26	21	18	16	5.1
JS (f,21)	42	22	22	19	16	15	2.5
DH (m,22)	52	30	26	21	18	15	6.8
PB (f,50)	44	25	21	18	16	15	2.9
MK (m,24)	57	32	25	19	18	17	7.1
TW (f,23)	51	28	22	20	17	14	4.6
BG (m,24)	50	27	23	20	17	15	4.4
CA (f,23)	45	24	23	18	16	15	2.8
JM (m,23)	49	22	22	19	17	10	3.2
AL (m,25)	41	30	24	21	18	16	3.7
KS (f,23)	40	26	23	18	15	14	2.2
BES (m,22)	54	31	22	21	18	17	6.8
AE (m,18)	51	27	26	25	21	16	6.9
RH (m,18)	40	27	24	21	18	16	3.2
BS (m,18)	52	30	28	22	19	17	6.7
$\mu \pm \sigma$	47.7±5.2	27.3±3.2	23.7±1.9	20.2±1.8	17.4±1.4	15.2±1.6	4.6 ± 1.8
I_c	-	-	-	-	-	-	[3.7 5.4]

Relaxation characteristics and the Nonlinearities $N_1(\alpha_2)$ and $N_2(\dot{\alpha}_2)$

The relaxation parameters and static nonlinearities were identified in a two stage identification process. The Fingertester (Fig. 3.22) was attached to the subject's index finger. During the measurements the subjects were asked to relax as much as possible so that no muscular driving torque τ_2 is applied. Thus, the finger was moved only with the driving torque of the measurement device that is equal to measured torque τ_{me}.

In the first stage, the relaxation parameters were determined with a step response experiment (see Fig. 3.23, graph on the right). The applied angular trajectory consisted of three steps from the subject's equilibrium position $\alpha_{2,0}$ to $\alpha_{2,0} + \Delta\alpha_2$ and three steps in opposite direction, back into the equilibrium position. Each step was followed by a 70 s period of constant position. The step size was chosen to $\Delta\alpha_2 = 30\,^\circ$. The relaxation curves recorded for each hand were averaged in order to reduce sensor noise and measurement artifacts.

Immediately after the position step at time t_0^+, the damper can be considered as stiff and hence, the exerted torque is calculated as

$$\tau_{me}(t_0^+) = E_{rel}\Delta\alpha_2 + N_1(\alpha_{2,0} + \Delta\alpha_2) \quad . \tag{3.33}$$

Subsequently, the damper becomes active until the spring E_{rel} is completely relaxed. Therefore, $N_1(\alpha_{2,0} + \Delta\alpha_2)$ can be inferred as $\tau_{me}(t \to \infty)$ and the parameter E_{rel} can be calculated from Eq. (3.33). The relaxation time constant T_{rel} is obtained with the tangent method as indicated in Fig. 3.23. The parameter identification results are summarized in Tab. 3.7.

Since the mean values $\overline{T}_{rel}$ and $\overline{E}_{rel}$ did not show significant differences between right and left hand, further evaluations can be done with a calculation basis of 30 experiments. The 95 % confidence intervals as well as the mean values with standard deviation calculated with a basis of 30 experiments are summarized in Tab. 3.8.

In the second stage, the static functions $N_1(\alpha_2)$ and $N_2(\dot{\alpha}_2)$ were estimated using a system identification approach that approximates $N_1(\alpha_2)$ and $N_2(\dot{\alpha}_2)$ with normalized radial basis function (NRBF-) networks (see Section 4.3.1). The model parameters were adapted in output error configuration (see Section 2.2.1). Since the relaxation dynamics were already identified, they were integrated as known subplant into the model, and only the parameters of the estimated functions $\hat{N}_1(\alpha_2)$ and $\hat{N}_2(\dot{\alpha}_2)$ were subject to identification (see Fig. 3.25). Using Eq. (3.26) with τ_2 replaced by τ_{me}, yields

$$\tau_{me} = J\ddot{\alpha}_2 + N_1(\alpha_2) + N_2(\dot{\alpha}_2) + \tau_{rel} \quad .$$

Since the finger was moved along a trajectory with low acceleration and the moment of inertia J is very small, the term $J\ddot{\alpha}_2$ can be neglected.

As parameter identification, a Levenberg-Marquardt algorithm was applied (see [211]). Details about the NRBF-approximation, the output error configuration and the LM-adaptation are given in Chapters 2 and 4.

The identification results are depicted in Figs. 3.26 and 3.27. The position dependent component $\hat{N}_1(\alpha_2)$ follows the typical double exponential characteristics of the model il-

Tab. 3.7: Experimentally identified relaxation time constants T_{rel} and spring constants E_{rel} from 15 healthy subjects. Sex and age of every subject are written in parenthesis in the first column.The last two lines indicate the mean values $\overline{T}_{rel}$ and $\overline{E}_{rel}$, and the standard deviations σ_{Trel} and σ_{Erel}.

	Left hand		Right hand	
Subject	T_{rel} in s	E_{rel} in Ncm/°	T_{rel} in s	E_{rel} in °
AV (m, 39)	0.73	0.11	0.58	0.34
BS (f, 23)	0.38	0.12	0.41	0.16
DM (m, 23)	0.87	0.19	0.76	0.13
DD (m, 22)	0.76	0.14	0.58	0.15
EV (f, 37)	0.73	0.11	0.57	0.19
FK (m, 28)	0.54	0.09	0.49	0.22
JH (m, 33)	0.75	0.14	0.56	0.13
ML (f, 29)	0.93	0.07	0.95	0.03
MS (m, 23)	0.49	0.17	0.99	0.10
MR (m, 24)	1.29	0.10	1.25	0.09
MB (m, 28)	0.58	0.10	0.53	0.16
ME (m, 26)	1.05	0.18	1.03	0.18
MJ (m, 25)	0.59	0.13	0.53	0.14
SE (f, 22)	0.53	0.06	0.70	0.08
SS (f, 23)	0.42	0.09	0.91	0.07
$\overline{T}_{rel}$ and $\overline{E}_{rel}$	0.71	0.12	0.72	0.14
σ_{Trel} and σ_{Erel}	0.25	0.04	0.25	0.07

Tab. 3.8: Mean values $\overline{T}_{rel}$, $\overline{E}_{rel}$ and standard deviations σ_{Trel} and σ_{Erel} and the respective 95 % confidence intervals I_c [43] calculated with a basis of 30 experiments.

	T_{rel} in s	E_{rel} in Ncm/°
$\overline{T}_{rel}$ and $\overline{E}_{rel}$	0.72	0.13
σ_{Trel} and σ_{Erel}	0.25	0.05
I_c	$[0.63 \;\; 0.81]$	$[0.11 \;\; 0.15]$

lustrated in Fig. 3.21. Since the movement was accomplished in a range that is convenient for the subjects, the recorded curve barely exceeds the linear region. A nonlinear increase of the reset torque can be observed for angles $\alpha_2 < -60\,°$, only.

The velocity dependent component $\hat{N}_2(\dot{\alpha}_2)$ does not coincide with the model of Fig. 3.21. Only for angular velocities $|\dot{\alpha}_2| < 50\,°/\text{s}$ the amount $|\hat{N}_2(\dot{\alpha}_2)|$ of mechanical resistance increases. Every subject shows strong nonlinearities even with a decrease of mechanical resistance for $|\dot{\alpha}_2| > 50\,°/\text{s}$. It is therefore assumed that the curves $\hat{N}_2(\dot{\alpha}_2)$ identified by

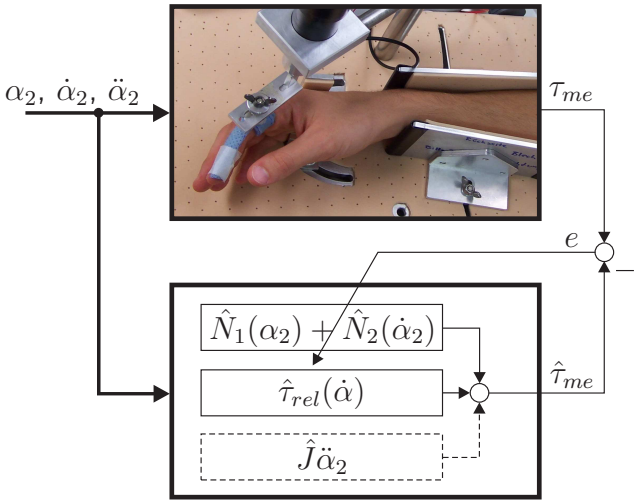

Fig. 3.25: Output error configuration for the identification of the static nonlinearities N_1 and N_2. All estimated values and functions are indicated with "$\hat{}$". The dashed lines indicate that the term $\hat{J}\ddot{\alpha}$ is neglected.

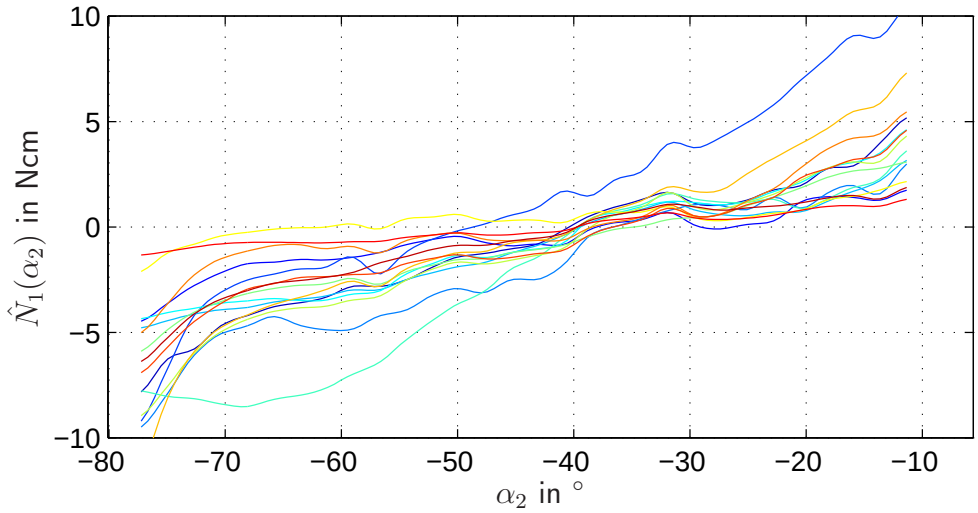

Fig. 3.26: Identification results of the position dependent passive joint torque $N_1(\alpha_2)$ from the right hand of 15 healthy subjects.

the parameter estimation algorithm reflect not only passive viscous properties but also phasic muscle stretch reflex activity (see Appendix B.3.4) occurring for angular velocities $|\dot{\alpha}_2| > 50\,°/\mathrm{s}$.

Model Verification

The model for the relaxation behavior and the static nonlinearities is verified by evaluating the NMSE($\underline{\tau}_{me}, \underline{\hat{\tau}}_{me}$) (see Appendix A.4) for every subject, whereas $\underline{\tau}_{me}$ =

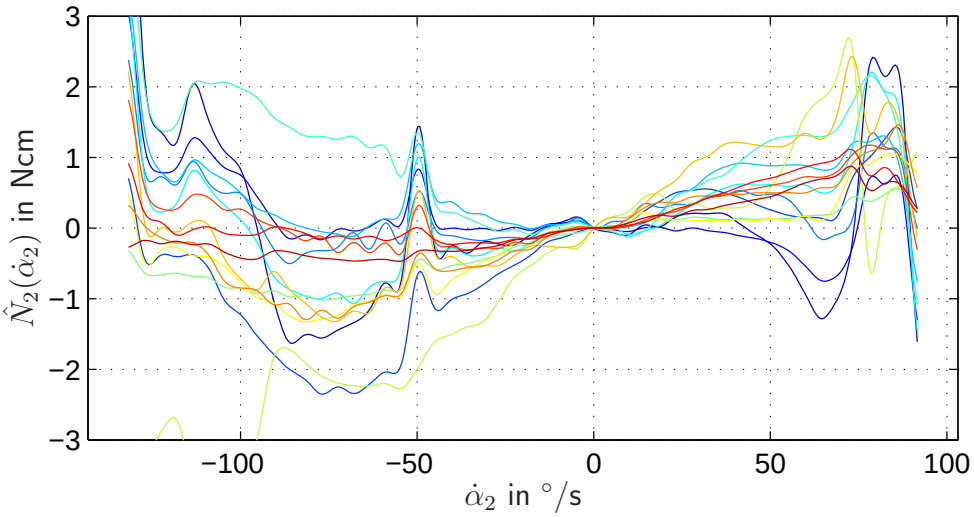

Fig. 3.27: Identification results of the velocity dependent passive joint torque $N_2(\dot{\alpha}_2)$ from the right hand of 15 healthy subjects.

$[\tau_{me}(0)\,\tau_{me}(T_s)\,\tau_{me}(2T_s)\ldots\tau_{me}(kT_s)]^T$. In Fig. 3.28, the model error e is plotted during the process of parameter identification. The NMSE is calculated, once the parameters have converged to their final value. The results are summarized in Tab. 3.9. Averaging over all 30 results of Tab. 3.9 yields $\overline{\text{NMSE}} = 0.41\,\%$. In order to evaluate, whether the average values $\overline{T}_{rel}$ and $\overline{E}_{rel}$ of Tab. 3.8 provide a sufficiently accurate approximation for every subject, the calculation NMSE of the was repeated when parameterizing the relaxation model with $\overline{T}_{rel}$ and $\overline{E}_{rel}$ instead of using the individual parameters identified in the first stage. Then, the mean NMSE increased slightly to $\overline{\text{NMSE}} = 0.45\,\%$.

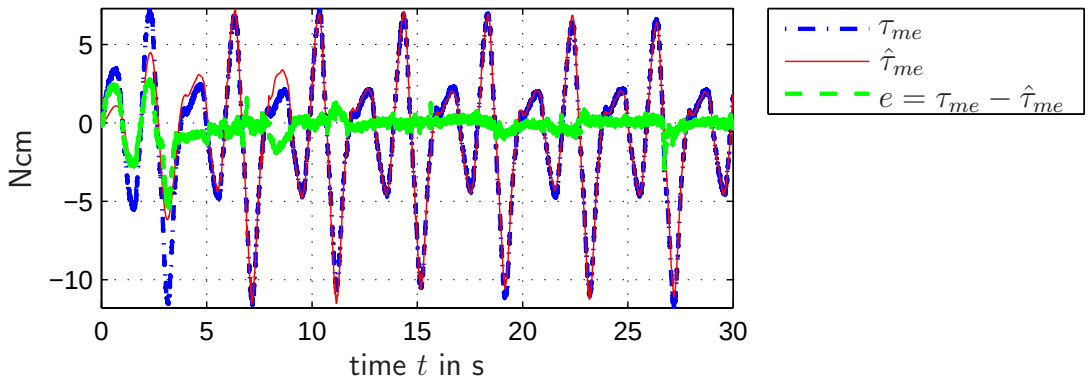

Fig. 3.28: Exemplary illustration of the measured torque τ_{me} compared with the model output $\hat{\tau}_{me}$ during parameter adaptation.

Tab. 3.9: NMSE($\underline{\tau}_{me}, \underline{\hat{\tau}}_{me}$) of the left and right hands of all 15 subjects, calculated according to Eq. (A.11).

Subject	1	2	3	4	5	6	7	8	9	10	11	12	13	14	15
e_{rel} left in %	0.5	0.4	0.3	0.5	0.4	0.5	0.4	0.4	0.3	0.7	0.4	0.3	0.3	0.4	0.4
e_{rel} right in %	0.4	0.4	0.3	0.5	0.4	0.3	0.4	0.3	0.7	0.6	0.4	0.4	0.4	0.4	0.3

3.6.5 Discussion

The typical segment dynamics model consisting of a double integrator and two static nonlinearities turns out to be insufficient for the MCP-joint of the index finger. As shown in [209], a purely static approximation of τ_{me} yields in average $\overline{\text{NMSE}} = 2.9\,\%$. The respective relative model error (see Eq. A.13) was calculated as $\overline{e}_r = 40,3\,\%$. When including the relaxation model, the average NMSE can be reduced to $\overline{\text{NMSE}} = 0.41\,\%$. Considering that this corresponds to an average model error $\overline{e}_r = 6.71\,\%$, it is clear that taking into account the relaxation effect significantly improves the model accuracy. When parameterizing the relaxation model with the average parameters $\overline{T}_{rel}$ and $\overline{E}_{rel}$ that have been experimentally determined from measurements of 30 hands the NMSE increases slightly to $\overline{\text{NMSE}} = 0.45\,\%$. From these results, it can be concluded that the average values $\overline{T}_{rel}$ and $\overline{E}_{rel}$ obtained experimentally from a sample of 30 hands yield a valid general approximation of the relaxation characteristics of the MCP-joint. The incorporation of the relaxation model is crucial for the system identification of the *RPMS*-induced index finger movement as introduced in Chapter 4. This can be easily understood when looking at force-torque curve depicted in Fig. 3.23, and the output error configuration depicted in Fig. 3.25. Similar to what will be implemented for the nonisometric identification described in Chapter 4, the estimate $\hat{\tau}_{rel}$ of the relaxation torque is used to compensate for τ_{rel} within the model (lower branch of output error configuration in Fig. 3.25). If the relaxation is not compensated, the hysteresis-shaped curve of τ_{me} (left plot of Fig. 3.23) yields ambiguous measurements for the same positions α_2 which is an inconsistency the identification algorithm cannot cope with.

The identified static nonlinearities $\hat{N}_1(\alpha_2)$ depicted in Fig. 3.26 show the typical shape of the double exponential model as it can be observed in the relevant literature. However, the identification result of the velocity dependent component $\hat{N}_2(\dot{\alpha}_2)$ (Fig. 3.27) differs from the typical friction model where the frictional reset torque τ_{vm} increases monotonically with the joint velocity. Since this deviation has similar characteristics among the majority of the subjects this deviation cannot be ascribed to voluntary muscle activity. Instead, it is likely that phasic reflex activity occurring when muscle stretch velocity exceeds a certain threshold is reflected in $\hat{N}_2(\dot{\alpha}_2)$. Since the functions $\hat{N}_1(\alpha_2)$ and $\hat{N}_2(\dot{\alpha}_2)$ show large interpersonal differences, they are be subject to system identification as presented in Chapter 4.

3.7 Spastic Joint Torque

Spasticity is defined as a velocity dependent increase of muscle tone during muscle stretch [92]. The current state of the art concerning the underlying mechanisms is explained and summarized in Appendix B.3.4 and B.4. Since model-based spasticity quantification is a goal of this thesis, in this section, a simple spasticity model is derived and qualitatively verified.

3.7.1 Simplified Model

The schematic in Fig. 3.29 illustrates in a simplified manner, how spasticity results from a lesion in the CNS (compare with Fig. B.13). As a result of a stroke or a spinal cord injury, the input from higher levels (sensorimotor cortex, e.g.) may be reduced or completely lost. Therefore, the activity of the muscle stretch reflex cannot be sufficiently regulated any more. This is called reflex disinhibition. The clinical appearance is a nonphysiological flexion of the affected limbs. The resulting spastic joint torque depends on the muscle length and on the muscle velocity since Ia- and II-afferents are involved in the reflex loops. The muscle length depends on the angle of the respective limb. Therefore, in the case of the MCP-joint of the index finger, the spastic joint torque $s(\alpha_2, \dot{\alpha}_2)$ is introduced as a function of α_2 and $\dot{\alpha}_2$. Since the position and the velocity information of the Ia- and II-afferents is encoded with the firing rate of action potentials that are summed at the α-Motoneuron, it is reasonable to model $s(\alpha_2, \dot{\alpha}_2)$ as a sum of a tonic and a phasic component:

$$s(\alpha_2, \dot{\alpha}_2) = s_t(\alpha_2) + s_{ph}(\dot{\alpha}_2) \quad . \tag{3.34}$$

This approach allows the integration of the spastic joint torque into the static nonlinearities of the segment dynamics that are extended to

$$N_1(\alpha_2) = \tau_g(\alpha_2) + \tau_{ep}(\alpha_2) + s_t(\alpha_2) \tag{3.35a}$$

$$N_2(\dot{\alpha}_2) = \tau_f(\dot{\alpha}_2) + s_{ph}(\dot{\alpha}_2) \quad . \tag{3.35b}$$

Remark 3.7.1 *Integrating the spasticity into the segment dynamics is physiologically inconsistent since the spastic joint torque is generated by the effected muscles and therefore, it should be integrated into the plant of muscle force generation. However, the proposed model structure allows the application of a highly capable system identification approach as it is discussed in Chapter 4. Furthermore, in the real plant, the relation between α_2, $\dot{\alpha}_2$ and $s(\alpha_2, \dot{\alpha}_2)$ is not static, since the reflex loop causes a delay, and the muscle activation is a dynamic process. Though, during RPMS-induced movements, the bandwidth of the joint angle signal $\alpha_2(t)$ and the angular velocity signal $\dot{\alpha}_2(t)$ is small compared to the bandwidth of the muscle activation dynamics. Thus, a static approximation is reasonable. Static spasticity models have been proven valid in [38; 39; 150], e.g..*

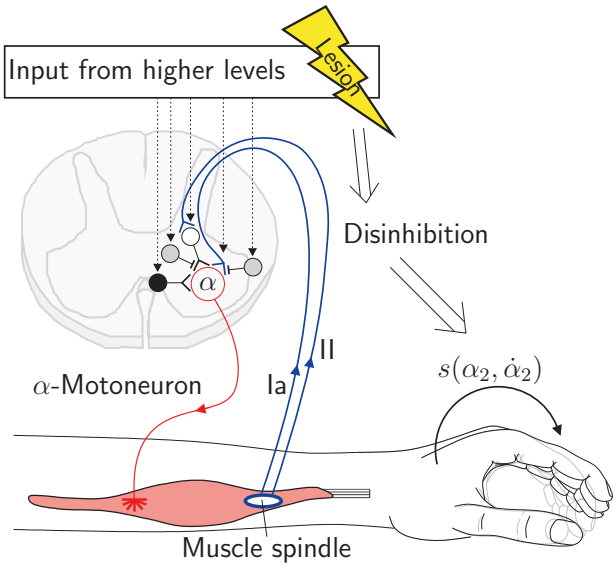

Fig. 3.29: Simplified spasticity schematic: A lesion in the central nervous system may decrease the input from higher levels that inhibits the stretch reflex activity. This disinhibition results in a spastic joint torque $s(\alpha_2, \dot{\alpha}_2)$. An explanation of the illustrated muscle stretch reflex can be found in Fig. B.13.

3.7.2 Qualitative Model Verification

In order to verify, whether the separation of $s(\alpha_2, \dot{\alpha}_2)$ according to Eq. (3.34) is valid, measurements with six patients were accomplished. Patient 1-5 have been suffering from spastic paresis as a consequence of a stroke. Patient 6 has suffered from a dystonia[2] by birth. During the measurement, the MCP-joint torque was recorded while extending the index finger with the Fingertester (see Appendix C). The velocity dependence of the spastic joint torque was examined by extending the index finger at three different angular velocities $\dot{\alpha}_2$: 15, 30 and 60 °/s. The measuring results are depicted in Fig. 3.30.

Compared with the curves of $\hat{N}_1(\alpha_2)$ that have been obtained as a system identification result from healthy subjects, the curves measured from spastic patients show a higher amount of reset torque. A qualitative inspection of the measurement results shows, that τ_{me} increases when increasing $\dot{\alpha}_2$. Furthermore, it can be seen, that the increase τ_{me} remains nearly constant over the complete range of α_2. Therefore, it can be concluded, that the velocity dependency of spasticity is to a certain extent independent of the muscle length. Thus, the approach (3.34), i.e. the separation of the spastic joint torque into a sum of a purely position dependent and a purely velocity dependent component, can be considered as valid, at least for the spasticity in the index finger flexors.

[2]Dystonia is a neurological disorder that affects the motor system: Muscle contractions may cause twisting movements of the limbs or abnormal postures.

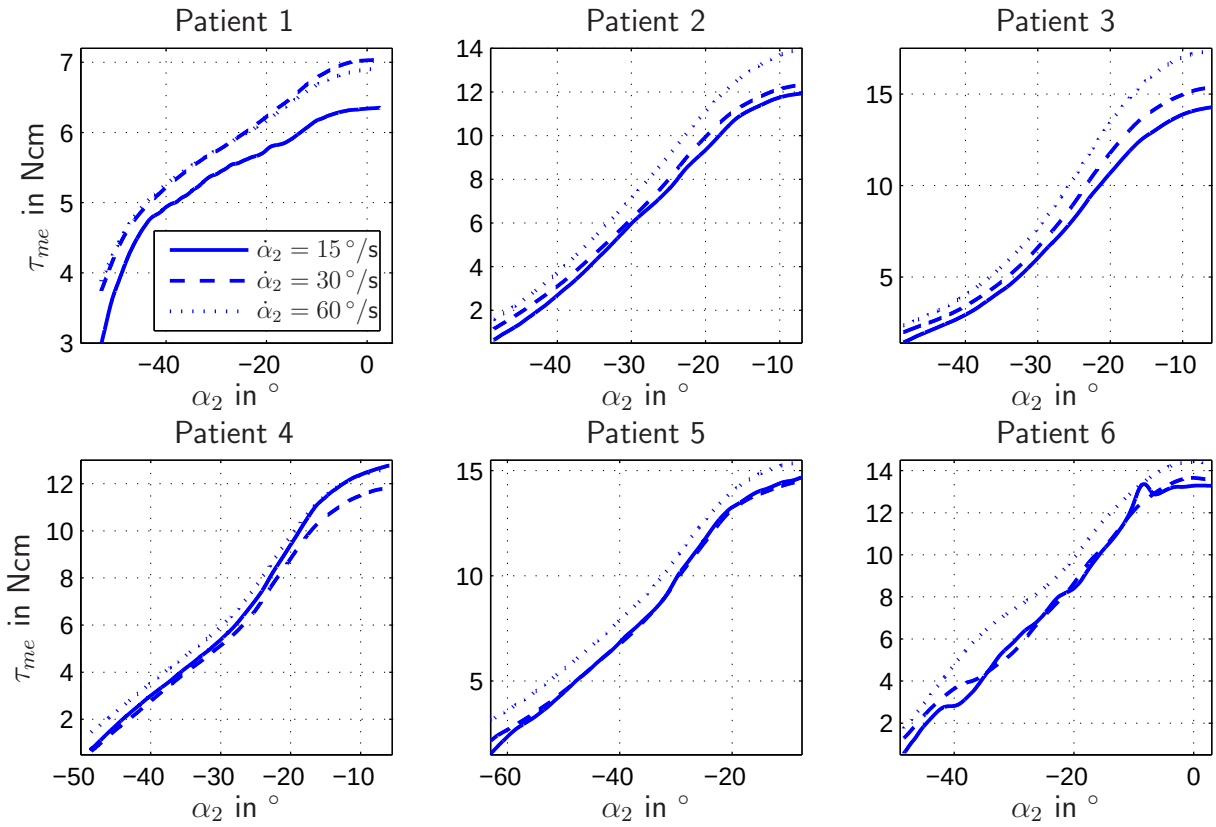

Fig. 3.30: Measured MCP-joint torque τ_{me} of six patients: Patient 1-5 suffer from spastic paresis as a consequence of a stroke, patient 6 suffers from a dystonia by birth. Each patient's index finger of the affected hand has been extended with three different angular velocities.

3.7.3 Discussion

According to measurements at six spastic paretic stroke patients the spastic joint torque in the MCP-joint can be separated into a tonic and phasic component. This separation is inspired by the physiology of the stretch reflex that is dependent on I- and II-afferents. It is important to note the this assumption has been verified by qualitative evaluation and for the index finger, only. Therefore, the proposed model cannot be assumed to be valid in general. Nevertheless, it is a useful approach for the special case considered in this thesis. The result of this section allows a system identification based monitoring of changes in spasticity with a break down into position and velocity dependent components. This can be achieved simply by tracking the nonlinear functions $\hat{N}_1(\alpha_2)$ and $\hat{N}_2(\dot{\alpha}_2)$.

3.8 Summary and Conclusions

In this chapter, a model of the *RPMS*-induced index finger extension has been proposed. For this purpose, the subplants illustrated in the general overview of Fig. 3.1 have been considered separately.

The force transmission as well as the muscle contraction dynamics have been modeled using existing knowledge gathered from a literature review, since a lot of research has been done in this area and there exist well established results.

The segment dynamics are modeled using a combination of the classical structure of a double integrator with static position and velocity feedback with a dynamic position feedback that takes into account the strong relaxation effect in the index finger. The relaxation model has been experimentally parameterized and verified. Compared to a segment dynamics model with purely static velocity feedback, the incorporation of the relaxation yields a decrease of the relative prediction error by more than 30 %. This improvement is crucial for the system identification introduced in Chapter 4.

Measurements with spastic patients have verified the simple model of the spastic joint torque in the MCP-joint of the index finger. This model expresses the spasticity as a sum of a purely static and phasic component and can therefore integrated into the equations of the segment dynamics. These equations are subject to system identification as explained in Chapter 4 and therefore, this approach provides the basis for the spasticity quantification as it is presented in Chapter 5.

The proposed force generation model is based on the fundamental work presented in [6]. Model parameters that are specific to the EIP have been determined from experimental studies and it was verified that the model structure of [6] provides an excellent prediction of the input-output behavior. Additionally, a simplified model that predicts the dominant dynamic behavior of the force generated during repetitive stimulation has been proposed and experimentally verified. The detailed EIP-model based on [6] can be used for studies which require an accurately simulated plant. The simplified model provides useful information for controller design.

For the verification and the parameterization of the different models, biomechanical measurements were conducted. During the experiments, the subjects were required to relax as much as possible to avoid artifacts and biasing. This is possible only, if the experimental setup allows the subjects to adopt a convenient and relieving posture. Therefore, our measurement devices, like the measurement orthosis, the force sensor (Fig. 3.14) and the Fingertester (Appendix C), were carefully designed and constructed to meet not only the technical requirements like resolution and accuracy, but also ergonomic aspects. All measurements were repeated multiple times with the same subject in order to reduce random errors as much as possible.

4 System Identification During RPMS

4.1 Introduction

The system identification during *RPMS* yields the basis for the three goals formulated in Chapter 1: Automated therapy monitoring and assessment during simulation, position controlled induction of functional movements and the EMG-driven therapy mode.

The identification of the input-output properties of stimulated muscles and the attached limbs has been a topic of active research for several decades. The resulting muscle-limb models can be used for simulations that are useful in the context of neural prostheses design, e.g.. For this purpose, qualitative knowledge of the model behavior obtained from off-line identification is sufficient. If the model is used for adaptive control or monitoring of patient parameters, like muscular fatigue, on-line parameter estimation methods have to be applied. The identification can be conducted under isometric or nonisometric conditions (see also Section 3.4). Under isometric conditions, the plant of force generation can be identified, whereas under nonisometric conditions, additional information about the segment dynamics and the passive elastic properties of joints muscles and tendon can be inferred. Although muscle fatigue could be observed with isometric experiments, movement dependent phenomena like spasticity can only be identified under nonisometric conditions.

In [6], a nonisometric on-line identification of an *RPMS*-induced elbow flexion and extension was developed. With the exception of this study, the current state of the art comprises identification of electrically stimulated muscles only. In [53; 54], isometric muscle models were identified by means of experiments using rabbit muscles. In [41], isometric experiments with the human quadriceps muscle (shank extensor) were conducted. In [48] and [133], the quadriceps was modeled, too and identified under isometric as well as under nonisometric conditions. In all five studies off-line identifications were carried out. On-line identification of the quadriceps under nonisometric conditions is described in [23] and [147]. The parameter identification algorithm of the former requires either direct measurement of the angular acceleration or its numerical computation. The measurement of acceleration requires an additional sensor. The numerical computation limits the on-line capability since extensive filtering is necessary in order to obtain useful signals. The latter approach only adapts the model parameters of the force generation and assumes the remaining plant to be known. For the system identification based spasticity quantification as it will be presented in Chapter 5 this assumption does not hold.

In this chapter, the system identification of the *RPMS*-induced index finger extension will be introduced. The model that has been developed in Chapter 3 yields only qualitative information. In order to obtain quantitative information that is specific to a subject, the model has to be individualized. For this purpose, on-line parameter adaptation algorithms based on the error models derived in Chapter 2 will be applied. First, isometric conditions

are investigated in order to test and evaluate the identification of the force generation plant separately. Secondly, nonisometric identification will be carried out. In both cases, first simulations are implemented in order to test the performance, accuracy and robustness of the proposed approach. Subsequently, the identification schemes are applied to data obtained from real experiments with healthy subjects.

The novel scientific contributions introduced in this Chapter are the transfer of the theoretical results derived in Chapter 2 into a real application on the one hand, and the nonisometric on-line system identification of the *RPMS*-induced index finger extension with a macroscopic model on the other hand.

This chapter is organized as follows: In Section 4.2, the isometric case is considered, and a model equation is derived that will be formulated in SNLP-structure (compare to Eq. (2.5c)). An identification scheme according to EM C1 will be presented. In Section 4.3, the model equation is enhanced for the nonisometric case. The identification will be implemented according to EM C2. Due to sampled data acquisition, input-output observations are in discrete time and hence, the adaptive systems are implemented in discrete time, too. Therefore, throughout this chapter, discrete time signals are used that are denoted as $s(k)$ with $k \mathrel{\widehat{=}} kT_s$, whereas $T_s = 1\,\text{ms}$ is the sampling time of the discrete implementation.

4.2 Identification under Isometric Conditions

In isometric configuration, only the force generation part of the complete plant is considered (compare Fig. 3.1 and Fig. 3.13). In order to integrate the plant of Fig. 3.13 into an adaptive system, first a parametric model equation will be derived. The physiological delay between the applied magnetic stimulus and the onset of the muscle twitch (see Section 3.4.2) will not be integrated into the model equation. Instead, it will be taken into account in the implementation of the identification algorithm as explained in Section 4.2.2.

4.2.1 Model Equation

Muscle Twitch

The muscle twitch (dynamic force response) can be approximated by a third order LTI-system as verified in Section 3.4. Thus, it seems appropriate to utilize the coefficients of a third order difference equation for parameter identification. This formulation has two main drawbacks: Firstly, it predefines the model order that is in reality unknown. The third order approximation is only a trade- off between model complexity and performance. The shapes of the measured muscle twitches illustrated in Fig. 3.16 clearly show that an exact reproduction could only be achieved with much higher order. As explained in [121], e.g., the predefinition of the model order when not exactly known may yield poor identification results. Secondly, the difference equation approach yields a NARX-model equation that has to be identified in equation error configuration [121] which is much more sensitive to sensor noise.

For these reasons, an FIR equation is proposed that approximates the muscle twitch with the truncated impulse response $\underline{\hat{h}} = [h(0) \ldots h(m)]$. Thus, the muscle force $\hat{F}_M$ can

be calculated as convolution of $\underline{\hat{h}}$ with the output of the recruitment function $\hat{\rho}(u(k))$:

$$\hat{F}_M(k) = \sum_{i=0}^{m} \hat{h}(i)\hat{\rho}(u(k-i)) \quad . \tag{4.1}$$

A contraction time of approx. 350 ms and a sample time $T_s = 1\,\text{ms}$ yields $m = 350$ and thus model (4.1) comprises 351 parameters that have to be adapted. In order to remedy this shortcoming the number of parameters is reduced by expressing $\underline{\hat{h}}$ as a linear combination of orthonormal basis functions (OBFs) [121].

As explained in [6] warped sine-functions

$$\begin{aligned} & r_1(i) = \left(\tfrac{m}{2}\right)^{-0.5} \exp\left(-(i-0.5)/\zeta\right) && \text{with} \quad i = 0 \ldots m \\ \text{and} \quad & r_l(i) = \left(\tfrac{m}{2}\right)^{-0.5} \sin\left(\left(l-1\right)\pi\left(1-\exp\left(-(i-0.5)/\zeta\right)\right)\right) && \text{with} \quad \begin{matrix} i = 0 \ldots m \\ l = 2 \ldots m_\text{r} \end{matrix} \end{aligned} \tag{4.2}$$

are well suited basis functions for the approximation of the muscle twitch. These functions were initially introduced in [84; 91]. The variable m_r determines the number of basis functions and the variable ζ is the so called form factor that determines the degree of warping. The choice of m_r and ζ is heuristic. However, in [91], the following rules of thumb are given for the approximation non-oscillating systems like the muscle twitch: Choose $\zeta \cong {}^{T_{63}}/_{T_s}$ whereas T_{63} is the time at which the system reaches 63 % of its steady state value of its step response and choose $m_r \cong 6$. Using matrix notation, the basis functions can be summarized as

$$\underline{R} = \begin{bmatrix} r_1(0) & r_1(1) & \ldots & r_1(m) \\ r_2(0) & r_2(1) & \ldots & r_2(m) \\ \vdots & \vdots & \ddots & \vdots \\ r_{m_r}(0) & r_{m_r}(1) & \ldots & r_{m_r}(m) \end{bmatrix} = \begin{bmatrix} \underline{r}_1^T \\ \underline{r}_2^T \\ \vdots \\ \underline{r}_{m_r}^T \end{bmatrix} \quad . \tag{4.3}$$

For a unique parameter identification the basis functions have to be orthonormal [121]. An orthonormalized matrix $\underline{\tilde{R}}$, i.e. $\underline{\tilde{R}}\underline{\tilde{R}}^T = \underline{I}$, can be obtained using the Cholesky orthonormalization

$$\begin{aligned} & \underline{R}^T = \underline{\tilde{R}}^T\,\underline{C} \quad \text{with} \quad \underline{R}\,\underline{R}^T = \underline{C}^T \underbrace{\underline{\tilde{R}}\,\underline{\tilde{R}}^T}_{\stackrel{!}{=}\underline{I}}\,\underline{C} = \underline{C}^T\,\underline{C} \\ & \Rightarrow \underline{\tilde{R}}^T = \underline{R}^T\,\underline{C}^{-1} \quad \Rightarrow \quad \underline{\tilde{R}} = \begin{bmatrix} \tilde{r}_1(0) & \ldots & \tilde{r}_1(m) \\ \vdots & \ddots & \vdots \\ \tilde{r}_{m_r}(0) & \ldots & \tilde{r}_{m_r}(m) \end{bmatrix} = \begin{bmatrix} \underline{\tilde{r}}_1^T \\ \vdots \\ \underline{\tilde{r}}_{m_r}^T \end{bmatrix} = \left(\underline{C}^T\right)^{-1}\,\underline{R} \end{aligned} \tag{4.4}$$

whereas the matrix $\underline{C}$ summarizes the so called Cholesky factors (see [56],e.g.). It can be computed using the MATLAB-function "`chol`" [109].

With the impulse response

$$\hat{h}(i) = \sum_{l=1}^{m_r} \hat{\theta}_{M,l}\tilde{r}_l(i) \;\; \forall \;\; i = 0 \ldots m \tag{4.5}$$

Eq. (4.1) can be written as

$$\hat{F}_M(k) = \sum_{i=0}^{m} \sum_{l=1}^{m_r} \hat{\theta}_{M,l} \tilde{r}_l(i) \hat{\rho}(u(k-i)) \quad . \tag{4.6}$$

whereas the number of parameters $\hat{\theta}_{M,l}$ has been reduced from m to m_r.

Recruitment Characteristics

The recruitment curve is modeled according to Eq. (3.19) with the following modifications: The gain β_1 is set to $\beta_1 = 1$ since the gain of the complete Hammerstein model is implicitly included in Eq. (4.6), already. Since it is clear from physiology that $\hat{\rho}(0) = 0$, the offset value β_2 is chosen appropriately. With the parameter vector $\underline{\hat{\eta}}^T = [\hat{I}_{thr}\ \hat{I}_{sat}\ \hat{\alpha}_{thr}\ \hat{\alpha}_{sat}]$ the model equation of the recruitment curve is given as

$$\begin{aligned} \hat{\rho}(\underline{\hat{\eta}}, u(k)) \;=\; & (u(k) - \hat{\eta}_1) \arctan(\hat{\eta}_3 (u(k) - \hat{\eta}_1)) - (u(k) - \hat{\eta}_2) \arctan(\hat{\eta}_4 (u(k) - \hat{\eta}_2)) \\ & + \underbrace{\hat{\eta}_1 \arctan(-\hat{\eta}_3 \hat{\eta}_1) - \hat{\eta}_2 \arctan(-\hat{\eta}_4 \hat{\eta}_2)}_{\beta_2} \quad . \end{aligned} \tag{4.7}$$

Complete Model Equation

The recruitment model is integrated into the muscle twitch model by inserting Eq. (4.7) into Eq. (4.6) which yields

$$\begin{aligned} \hat{F}_M(k) \;&=\; \sum_{i=0}^{m} \sum_{l=1}^{m_r} \hat{\theta}_{M,l} \tilde{r}_l(i) \hat{\rho}(\underline{\hat{\eta}}, u(k-i)) \\ &=\; \sum_{l=1}^{m_r} \hat{\theta}_{M,l} \sum_{i=0}^{m} \tilde{r}_l(i) \hat{\rho}(\underline{\hat{\eta}}, u(k-i)) \\ &=\; \sum_{l=1}^{m_r} \hat{\theta}_{M,l} \Big[\tilde{r}_l(0) \hat{\rho}(\underline{\hat{\eta}}, u(k)) + \ldots + \tilde{r}_l(m) \hat{\rho}(\underline{\hat{\eta}}, u(k-m)) \Big] \quad . \end{aligned} \tag{4.8}$$

With $\underline{u}(k) = [u(k) \ldots u(k-m)]^T$, $\underline{\hat{\rho}}(\underline{\hat{\eta}}, \underline{u}(k))^T = [\hat{\rho}(\underline{\hat{\eta}}, u(k)) \ldots \hat{\rho}(\underline{\hat{\eta}}, u(k-m))]$ and with $\underline{\hat{\theta}}_M^T = [\hat{\theta}_{M,1} \ldots \hat{\theta}_{M,m_r}]$ it follows

$$\begin{aligned} \hat{F}_M(k) \;&=\; \sum_{l=1}^{m_r} \hat{\theta}_{M,l} \left[\underline{\tilde{r}}_l^T \underline{\hat{\rho}}(\underline{\hat{\eta}}, \underline{u}(k)) \right] \\ &=\; \hat{\theta}_{M,1} \underline{\tilde{r}}_1^T \underline{\hat{\rho}}(\underline{\hat{\eta}}, \underline{u}(k)) + \ldots + \hat{\theta}_{M,m_r} \underline{\tilde{r}}_{m_r}^T \underline{\hat{\rho}}(\underline{\hat{\eta}}, \underline{u}(k)) \\ &=\; \underline{\hat{\theta}}_M^T \left[\underline{\tilde{r}}_1^T \underline{\hat{\rho}}(\underline{\hat{\eta}}, \underline{u}(k)) \ldots \underline{\tilde{r}}_{m_r}^T \underline{\hat{\rho}}(\underline{\hat{\eta}}, \underline{u}(k)) \right]^T \\ &=\; \underline{\hat{\theta}}_M^T \left[\underline{\tilde{R}} \underline{\hat{\rho}}(\underline{\hat{\eta}}, \underline{u}(k)) \right]^T \\ &=\; \underline{\hat{\theta}}_M^T \underline{\varphi}_M(\underline{\hat{\eta}}, \underline{u}(k)) \quad . \end{aligned} \tag{4.9}$$

The result of Eq. (4.9) shows that the complete Hammerstein structure of the isometric force generation can be expressed as SNLP-model according to Eq. (2.5c). The parameter

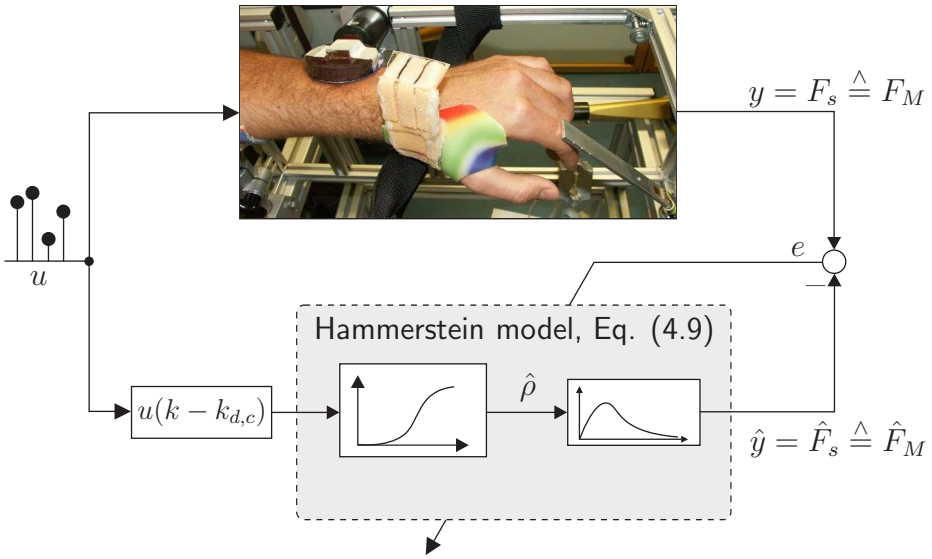

Fig. 4.1: Output error configuration for identification of the plant "muscle force generation".

space is given with $\hat{\underline{\theta}}_M \in \Omega_{\hat{\underline{\theta}}_M} \subset \mathbb{R}^{m_r}$ and $\underline{\hat{\eta}} \in \Omega_{\underline{\hat{\eta}}} \subset \mathbb{R}^q$ with $q = \dim(\underline{\hat{\eta}})$. Hence, the complete number of parameters is given with $p = m_r + q$.

4.2.2 Identification Scheme

Output Error Configuration

The chosen output error configuration is depicted in Fig. 4.1. The magnetic pulses act upon the plant, and the according weighted discrete Dirac Delta functions $u(k)$ (compare to Eq. (3.2)) represent the model input. The hardware delay $T_{d,hw}$ (Section 3.4.1) and the physiological delay $T_{d,ph}$ (Section 3.4.2) are compensated by delaying the model input $u(k)$ by the complete delay time $T_{d,c} = T_{d,hw} + T_{d,ph}$. In discrete time, a delay of $k_{d,c} = \text{ROUND}\left({}^{T_{d,c}}/_{T_s}\right)$ is implemented. The experimental setup used for the isometric identification is explained in Section 3.4.1. As explained in Section 3.4.1, the sensor output F_s is equalized with the muscle force F_M.

Parameter Adaptation Algorithm

The model has an SNLP-structure whose output $\hat{y}$ is directly measurable. Therefore, the parameter adaptation is done according to error model C1 (Section 2.6.1). In particular, the nonlinear parameters $\underline{\hat{\eta}}$ are identified using the modified LM-algorithm as introduced in Section 2.3 and thus, the calculations necessary for EM C1-GN have to be carried out: The algorithm has to compute the update Eqs. (2.21), (2.22), (2.25) and (2.26) using the input regressor $\underline{\varphi}_M(\underline{\hat{\eta}}, \underline{u}(k))$ and its partial derivatives

$$\underline{\varphi}_{M,i}(\underline{\hat{\eta}}, \underline{u}(k)) = \frac{\partial \underline{\varphi}_M(\underline{\hat{\eta}}, \underline{u}(k))}{\partial \hat{\eta}_i} \quad .$$

With

$$\underline{\varphi}_M(\underline{\hat{\eta}}, \underline{u}(k)) = \left[\underline{\tilde{R}}\underline{\hat{\rho}}(\underline{\hat{\eta}}, \underline{u}(k))\right]^T = \underline{\hat{\rho}}(\underline{\hat{\eta}}, \underline{u}(k))^T \underline{\tilde{R}}^T \tag{4.10}$$

we have

$$\frac{\partial \underline{\varphi}_M(\underline{\hat{\eta}}, \underline{u}(k))}{\partial \hat{\eta}_i} = \underline{\hat{\rho}}_i(\underline{\hat{\eta}}, \underline{u}(k))^T \underline{\tilde{R}}^T \tag{4.11}$$

whereas

$$\underline{\hat{\rho}}_i(\underline{\hat{\eta}}, \underline{u}(k))^T = \frac{\partial \underline{\hat{\rho}}(\underline{\hat{\eta}}, \underline{u}(k))^T}{\partial \hat{\eta}_i} = [\hat{\rho}_i(\underline{\hat{\eta}}, u(k)) \dots \hat{\rho}_i(\underline{\hat{\eta}}, u(k-m))] \ .$$

In particular, the partial derivatives are calculated as

$$\hat{\rho}_1(\underline{\hat{\eta}}, u(k)) = \arctan(-\hat{\eta}_3\hat{\eta}_1) - \arctan(\hat{\eta}_3(u(k) - \hat{\eta}_1)) - \frac{\hat{\eta}_3(u(k) - \hat{\eta}_1)}{1 + \hat{\eta}_3^2(u(k) - \hat{\eta}_1)^2} - \frac{\hat{\eta}_2\hat{\eta}_1}{1 + \hat{\eta}_3^2\hat{\eta}_1^2} \ , \tag{4.12}$$

$$\hat{\rho}_2(\underline{\hat{\eta}}, u(k)) = \arctan(\hat{\eta}_4(u(k) - \hat{\eta}_2)) - \arctan(-\hat{\eta}_4\hat{\eta}_2) + \frac{\hat{\eta}_4(u(k) - \hat{\eta}_2)}{1 + \hat{\eta}_4^2(u(k) - \hat{\eta}_2)^2} + \frac{\hat{\eta}_4\hat{\eta}_2}{1 + \hat{\eta}_4^2\hat{\eta}_2^2} \ , \tag{4.13}$$

$$\hat{\rho}_3(\underline{\hat{\eta}}, u(k)) = \frac{(u(k) - \underline{\hat{\eta}}_1)^2}{1 + \hat{\eta}_3^2(u(k) - \hat{\eta}_1)^2} - \frac{\hat{\eta}_1^2}{1 + \hat{\eta}_3^2\hat{\eta}_1^2} \quad \text{and} \tag{4.14}$$

$$\hat{\rho}_4(\underline{\hat{\eta}}, u(k)) = -\frac{(u - \hat{\eta}_2)^2}{1 + \hat{\eta}_4^2(u - \hat{\eta}_2)^2} + \frac{\hat{\eta}_2^2}{1 + \hat{\eta}_4^2\hat{\eta}_2^2} \ . \tag{4.15}$$

The influence of the parameters $\hat{\eta}_3$ and $\hat{\eta}_4$ on the shape of $\hat{\rho}(\underline{\hat{\eta}}, u(k))$ is insignificant and hence, their gradients $\hat{\rho}_3(\underline{\hat{\eta}}, u(k))$ and $\hat{\rho}_4(\underline{\hat{\eta}}, u(k))$ are small, as well. Therefore, they are chosen constant and among the nonlinear parameters only $\hat{\eta}_1$ and $\hat{\eta}_2$ will be subject to adaptation.

4.2.3 System Excitation

Local and Monotonic Parameterization

Following the corollary 2.5.3 and corollary 2.6.1, local parameterization (Definition 2.5.1) of the original model equation $\hat{y}(\underline{\hat{\theta}}_M, \underline{\hat{\eta}}, k) = \underline{\hat{\theta}}_M^T \underline{\varphi}_M(\underline{\hat{\eta}}, \underline{u}(k))$ and strict monotonic parameterization of its transformed model equation

$$\hat{y}(\underline{\hat{\eta}}) = \underline{\varphi}_M(\underline{\hat{\eta}})^T \underline{\hat{\theta}}_M(\underline{\hat{\eta}}) = \underline{\varphi}_M(\underline{\hat{\eta}})^T \underline{\Pi} \underline{f}^{\hat{\theta}_M} \tag{4.16}$$

(compare to Eq. (2.96)) with respect to $\underline{\hat{\eta}}$ are necessary conditions.

Fig. 4.2 illustrates how the recruitment curve $\hat{\rho}(\underline{\hat{\eta}}, I)$ depends on the parameters $\hat{I}_{thr}$ and $\hat{I}_{sat}$. It is obvious that both parameters have an effect only on their respective activation region, and that these regions hardly overlap for physiologically meaningful values of $\underline{\hat{\eta}}$. Thus, the model $\hat{\rho}(I)$ can be considered as locally parameterized.

Definition 2.5.1 is given for a static function $\hat{y}(k) = n(\underline{\hat{\eta}}, u(k))$. In the static case, it follows from locality that at any time instant k, a change of the parameter $\underline{\hat{\eta}}_i$ has no effect on the output $\hat{y}(k)$ if $u(k) \notin \mathbb{V}_i$. Here, the static function $\hat{\rho}(\underline{\hat{\eta}}, u(k))$ is followed by the LTI-system of the activation dynamics. Hence, at the time instant k, the output $\hat{y}(k)$ is affected by $\underline{u}(k) = [u(k) \dots u(k-m)]^T$ with $m = 350$ and thus, locality of the complete Hammerstein model can be achieved only if at every time instant k, $\underline{u}(k)$ is not element of more than one activation region. Considering Eq. (3.2), it follows that stimulation intensity vector $\underline{I}(k) = [I(k) \dots I(k-m)]^T$ is required not to be element of more then one

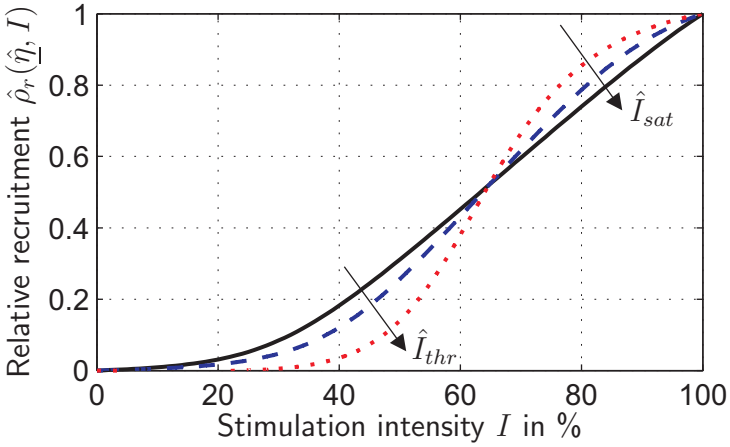

Fig. 4.2: Dependence of the recruitment curve on the parameters $\hat{I}_{thr}$ and $\hat{I}_{sat}$.

activation region $\hat{\rho}(\hat{\underline{\eta}}, I)$. This can be approximately achieved by choosing an input with hold times $k_h = \text{round}(T_h/T_s) >> m$ at which $I(k)$ stays within a particular activation region an with fast transient interphases.

In order to maintain the locality for the transformed model equation (4.16), the factor λ_d has to be chosen such that the exponential forgetting of the adaptation algorithm is fast enough to maintain the property of locality for the SLS error criterion. For this purpose, it is useful to calculate the time constant T_1 of the PT_1 behavior of exponential forgetting with Eq. (A.10). Since the input $u(k)$ first propagates through the "memory" of the Hammerstein model and subsequently through the "memory" of the adaptation algorithm, the hold time k_h has to be long enough in order to account for both memories. From experience it is proposed to choose the hold time as

$$k_h = m + \text{round}(T_1/T_s) \quad . \tag{4.17}$$

As illustrated in Fig. 4.2, $\hat{\rho}(\hat{\underline{\eta}}, I)$ is strictly monotonic with respect to $\hat{I}_{thr}$ and $\hat{I}_{sat}$. As stated in Section 2.6.1, strictly monotonic parameterization of the original model equation $\hat{y}(k) = \hat{\underline{\theta}}_M^T \underline{\varphi}_M(\hat{\underline{\eta}}, \underline{u}(k))$ does not imply strictly monotonic parameterization of the transformed model (4.16). Since it is nontrivial to show the strict monotonic parameterization of the transformed model equation (4.16) analytically, Fig. 4.3 illustrates its properties within a physiologically reasonable area of $\hat{\underline{\eta}}$. Obviously model (4.16) is strictly monotonically increasing with $\hat{\eta}_1$ and $\hat{\eta}_2$.

Persistent Excitation

For the adaptation of the nonlinear parameters, the modified LM-algorithm (Section 2.3), which is a second order GN-type method is used. Therefore, the input $u(k)$ has to meet the excitation requirements of EM C1-GN introduced in Section 2.6.1. Hence, the input signal has to be n.l.p.e with respect to the nonlinear parameters and l.p.e with respect to the linear parameters, i.e. the input regressor $\underline{\varphi}_M(\hat{\underline{\eta}}, \underline{u}(k))$ has to relax condition (2.44).

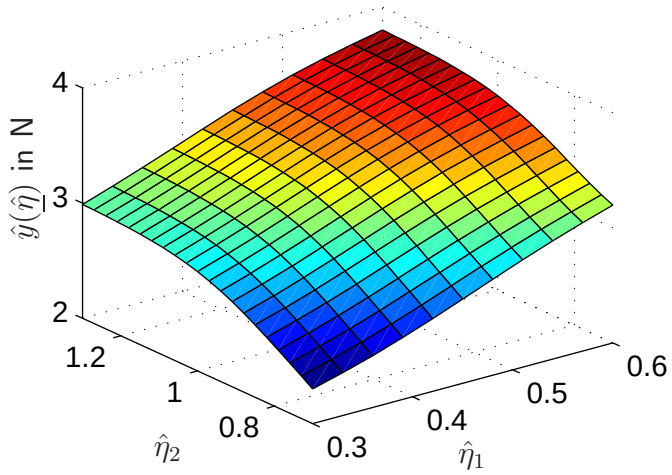

Fig. 4.3: Illustration of the monotonicity of the transformed model equation (4.16).

Additionally, the gradient vector $\underline{\psi}$ has to relax condition (2.71) and the requirements for maintaining local parameterization summarized above have to be fulfilled.

More intuitively, the input-output signals fed into the adaptation algorithm have to carry enough information to identify a model that is capable of describing the plant in all relevant operating conditions. For a nonlinear system, all frequencies of interest have to be excited in combination with all amplitudes spanned by the input space. During *RPMS*, the plant is excited with Dirac Delta functions which cause impulse responses that contain all information about the LTI-system. Choosing the stimulation intensity $I(k)$ as an amplitude modulated pseudo random binary (APRB-) signal with a uniform distribution of $0 \leq I(k) \leq 100\,\%$, combines all input amplitudes with all frequencies. However, when changing the amplitude of $I(k)$ with every pulse, the process has no time to settle due to the PT_1-dynamics of the temporal summation (see Section 3.4.4). Thus, the output $F_M(k)$ would cover mainly operating conditions around $F_M(k) \approx F_{M,\overline{rep}}(I = 50\%)$ such that the characteristics of $\rho(I)$ are hardly visible at the output. To give the process enough time to settle, $I(k)$ has to be kept constant during a minimum hold time T_h, which could be chosen at $T_h \approx 2\overline{\overline{T}}_e$.

The requirements of the formal as well as of the intuitive derivation can be relaxed by choosing the stimulation intensity $I(k)$ as uniformly distributed APRB-signal with $0 \leq I(k) \leq 100\,\%$ with a constant hold time T_h.

The forgetting factor is chosen as $\lambda_d = 0.99\,\mathrm{s}$ which yields a time constant of exponetial forgetting of $T_1 = 0.1\,\mathrm{s}$. With the rule of thumb (4.17), the hold time $T_h = 450\,\mathrm{ms}$, i.e. $k_h = 450$ is obtained. Fig. 4.4 illustrates the input signal $u(k)$ and the corresponding output $F_M(k)$.

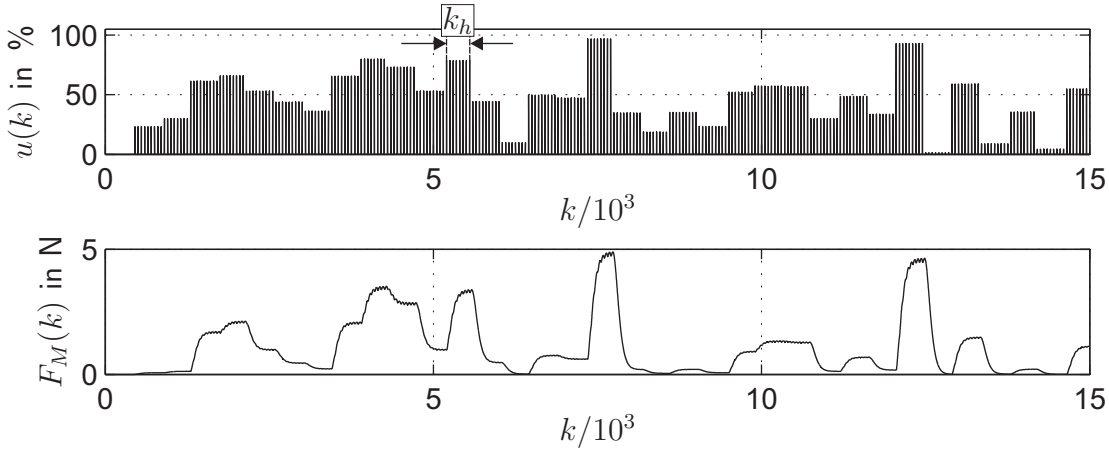

Fig. 4.4: Simulated input-output behavior of isometric *RPMS* with a persistently exciting input $u(k)$: The stimulation intensity $I(k)$ is modulated with an APRB-signal with constant hold time k_h.

4.2.4 Simulative Identification

Initialization

The activation dynamics are simulated according to Eq. (3.9) with $T_a = \overline{\overline{T}}_a = 28.4\,\text{ms}$ and the recruitment is simulated according to Eq. (3.19) setting $\alpha_{thr} = 5$, $\alpha_{sat} = 4$ and $\underline{\eta} = [48\,\%\ 98\,\%]^T$. The delay is set to $k_{d,c} = 15$ according to the average physiological delay $\overline{\overline{T}}_{d,ph} = 12.3\,\text{ms}$ and the hardware delay $T_{d,hw} = 2.6\,\text{ms}$.

The system is excited with the APRB-signal with a fixed hold time k_h as depicted in Fig. 4.4. The initialization and the choice of fiddle parameters of the adaptation algorithm and of the model equation are summarized Tab. 4.1.

Parameter Convergence

Once the simulation is started, the parameter estimates were adapted and converged to their true values. The parameter swarms $\hat{\underline{\eta}}(k)$ and $\hat{\underline{\theta}}_M(k)$ are illustrated in Fig. 4.5. Despite the bad initialization of $\hat{\underline{\eta}}(0)$, the algorithm converged after approx. 20 s.

In order to illustrate that the nonlinear parameters $\hat{\underline{\eta}}$ indeed converge to the global minimum, the SLS-error criterion $E_{k,2}(\hat{\underline{\eta}})$ was calculated according to Eq. (2.19) and plotted in Fig. 4.6. Note that $E_{k,2}(\hat{\underline{\eta}})$ changes with time and the plot shows $E_{k,2}(\hat{\underline{\eta}})$ only at a certain time instant. Because of the small forgetting factor $\lambda_d = 0.99$, the error criterion might have local minima during small time periods in between, due to inappropriate excitation. Therefore, the forgetting factor has been set to $\lambda_d = 0.9999$ in order to create Fig. 4.6. The locus of the parameter estimate is not perpendicular to the level curves since the direction of the Levenberg-Marquardt parameter drift differs from the steepest descent.

Tab. 4.1: Initialization and choice of fiddle parameters of the SLS-scheme, the modified LM-algorithm, and the model equation.

SLS scheme with modified LM-algorithm	
$\underline{\hat{\eta}}(0)$	$[20\,\%\ 40\,\%]^T$
$\underline{\hat{\theta}}_M(0)$	$\underline{0}$
$\underline{H}(0)$	$\mathrm{diag}(h_{11}\ldots h_{qq})$, $0 < h_{ii} \leq 0.001$, random uniform distribution
$\underline{\Pi}(0)^{-1}$	$\mathrm{diag}(h_{11}\ldots h_{qq})$, $0 < h_{ii} \leq 1000$, random uniform distribution
$\underline{\Pi}_i(0)^{-1}$	$\underline{0}$
$\underline{f}^{\underline{\hat{\theta}}_M}(0)$	$\underline{0}$
$\underline{f}_i^{\underline{\hat{\theta}}_M}(0)$	$\underline{0}$
λ_d	0.99
$\gamma_{\hat{\theta}}$	1
$\gamma_{\underline{\hat{\eta}}}$	1
$\delta(0)$	0.001
δ_s	0.01
κ	1.002
β	0.02
ν	1000
Model equation	
m	350
m_r	8
ζ	62
$\hat{\alpha}_{thr}$	5
$\hat{\alpha}_{sat}$	4

Evaluation

In Fig. 4.7, the plant output $y(k)$, the estimate $\hat{y}(k)$ and the model error $e(k) = y(k) - \hat{y}(k)$ during the adaptation process are depicted. The NMSE$(\underline{y}, \underline{\hat{y}})$ (Eq. (A.11)) calculated for $k = 20 \cdot 10^3 \ldots 30 \cdot 10^3$ yields $0.0028\,\%$.

Using formulae (4.5) and (4.7), the activation dynamics and the recruitment curve can be reconstructed from the parameter estimates. The reconstruction result is depicted in Fig. 4.8.

Remark 4.2.1 *The reconstruction of the Hammerstein model is not unique, since the gain of the complete system can be arbitrarily assigned either to the static nonlinearity or to the LTI-system.*

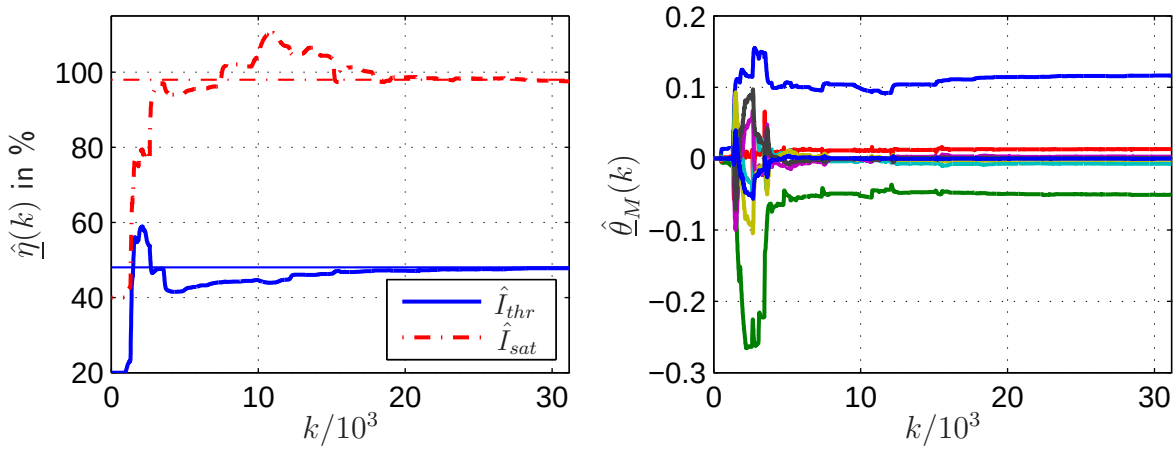

Fig. 4.5: Parameter swarms of $\hat{\underline{\eta}}(k)$ and $\hat{\underline{\theta}}_M(k)$. In the left graph, the true values $\underline{\eta}$ are indicated with straight lines.

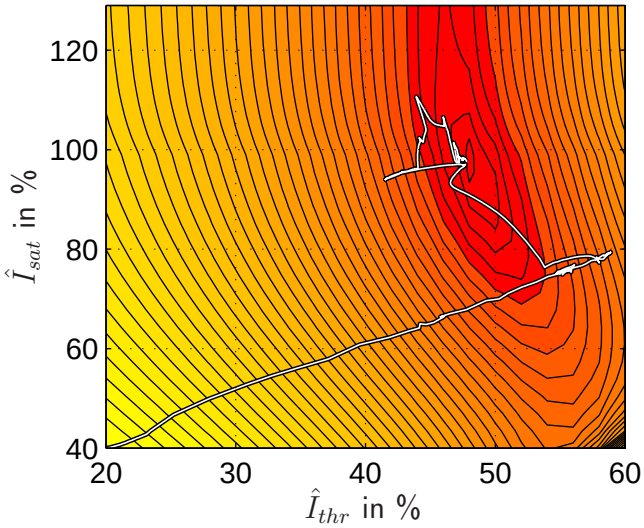

Fig. 4.6: Contour plot of the error criterion $E_{k,2}(\hat{\underline{\eta}})$ with locus of the parameter estimate $\hat{\underline{\eta}}(k)$.

Therefore, a constraint has to be introduced. Here, the gain of the impulse response $h(k)$ is determined such that the constant part of its step response (compare to Eq. (3.15)) is

$$\hat{F}_{M,\overline{rep}} \approx \frac{1}{k_{\text{rep}}} \sum_{k=0}^{f_s/1\text{Hz}} h(k) \stackrel{!}{=} 1 \tag{4.18}$$

when it is excited with a Dirac Delta pulse train with a repetition period of $k_{rep} = 50$ and amplitude one. As a result, the normalized activation dynamics $h(k)$ has no unit and the unit of the denormalized recruitment function is Newton. This constraint allows to directly infer the stationary value $\hat{F}_{M,\overline{rep}}(I) = \rho(I)$ from the recruitment curve.

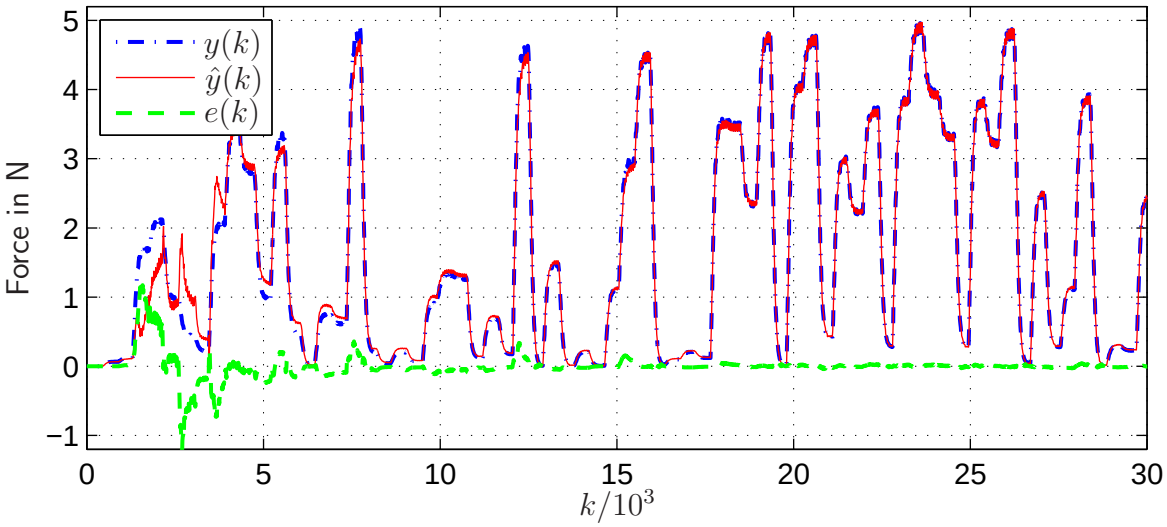

Fig. 4.7: Plant output $y(k)$, its estimate $\hat{y}(k)$, and output error $e(k)$ during parameter adaptation.

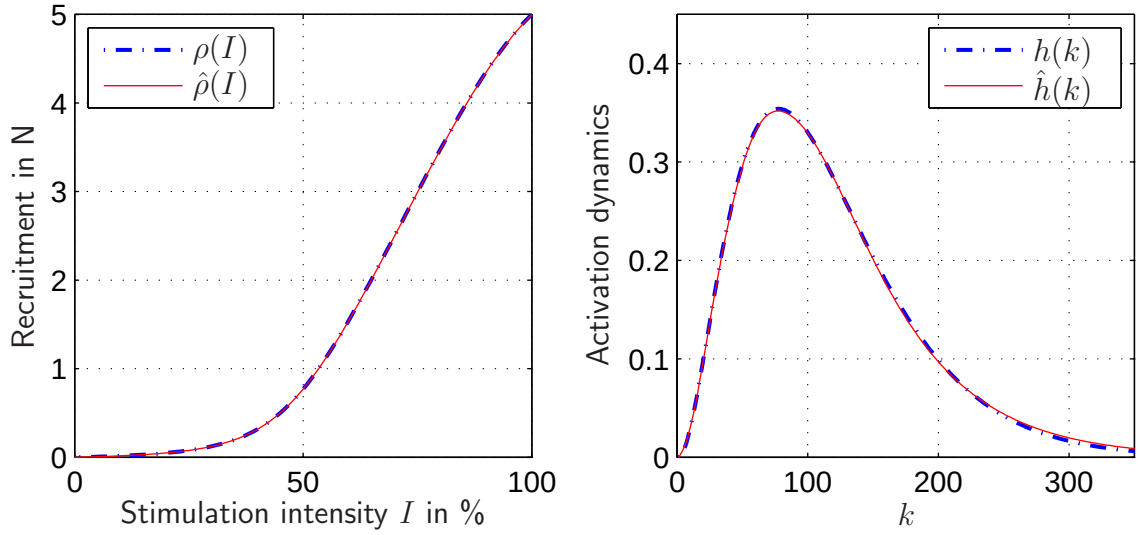

Fig. 4.8: Model reconstruction from the identification result: The blue dotted lines indicate the simulated plant. The identified approximations are plotted with red solid lines.

4.2.5 Experimental Identification

The identification scheme that is explained in Section 4.2.2 and summarized in Fig. 4.16 was applied to the data obtained from experiments with healthy subjects. The experiments that are describd in the following, aimed to evaluate the capabilities of the proposed model and identification algorithm under realistic conditions. The identification under nonisometric

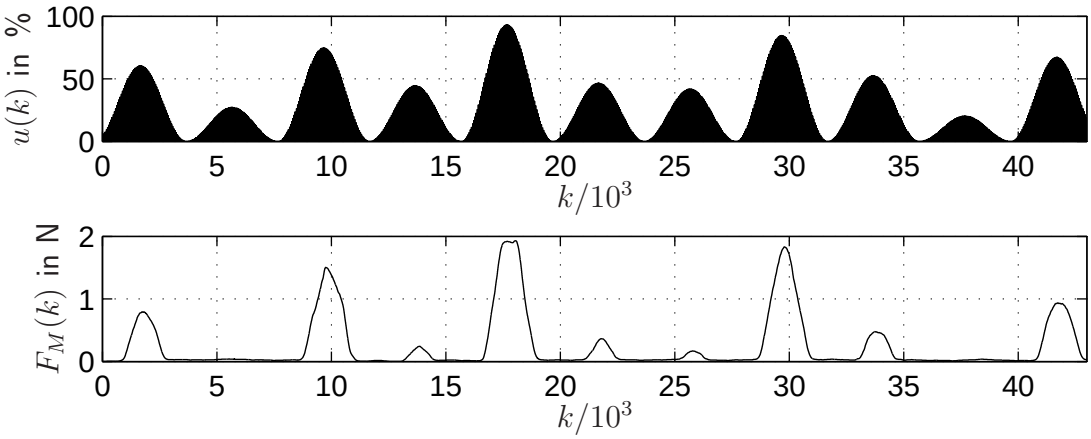

Fig. 4.9: Input-output behavior of isometric *RPMS* with a continuously modulated intensity $I(t)$.

conditions will be applied in the context of the position controlled movement induction as it will be presented in Chapter 5.

Methods

As summarized in Fig. 4.16, the plant of the *RPMS*-induced muscle force generation was identified in output error configuration with the example of the m. extensor indices proprius (EIP). Just as for the simulative identification, the model parameters were identified according to EM C1-GN using the modified LM-algorithm. Like all measurements under isometric conditions the experiments were carried out using the setup illustrated in Fig. 3.14.

All subjects were asked to relax as much as possible during stimulation. However, some subjects had difficulties to relax the EIP because of the sudden changes of the stimulation intensity as they occur in the APRB-signal (see Section 4.2.3). Therefore, to those subjects a continuous intensity modulation has been applied as depicted in Fig. 4.9. The intensity is modulated according to

$$I(k) = I_0 \sin(kT_s/T) \ , \tag{4.19}$$

with $T = 4\,\mathrm{s}$ and with $0\,\% < I_0 < 100\,\%$ randomly chosen for every period T. Clearly, the signal (4.19) relaxes the persistent excitation conditions derived in Section 4.2.3. However, with the sinusoidal excitation the parameters converge slower than with an APRB-signal since it takes more time to cover all operating conditions.

The small coils that were used for the EIP-stimulation have a small thermal capacity and overheat after a stimulation of approx. 40-50 s. The parameter estimates might need longer than that to converge. Therefore, for the experimental identification, the input-output data of the plant were saved first, and then fed into the adaptation algorithm as if they occur on-line. Thus, the stored data sequence could be repeated until the parameters were converged.

Tab. 4.2: Initialization and choice of those fiddle parameters that have been modified compared to Tab. 4.1 .

SLS scheme with modified LM-algorithm	
$\hat{\underline{\eta}}(0)$	$[47\,\%\ 85\,\%]^T$
λ_d	0.995
$\gamma_{\hat{\underline{\eta}}}$	0.1
Model equation	
ζ	42
$\hat{\alpha}_{thr}$	8
$\hat{\alpha}_{sat}$	7

Initialization

Some initializations and fiddle parameters that were chosen for the simulative identification were changed. These parameters are summarized in Tab. 4.2, the other parameters remained unmodified and can be taken from Tab. 4.1. The initial parameter estimate $\hat{\underline{\eta}}(0)$ has been chosen as a good empirical value in order to be close to the minimum. For the identification of experimental data, it turned out to be advantageous to choose a slightly greater forgetting factor λ_d than for the simulative identification. This results in a slower exponential forgetting and thus, the algorithm is more robust to disturbances like noise and movement artifacts. For similar reasons, the estimator gain $\gamma_{\hat{\underline{\eta}}}$ has been reduced. The identification turned out to be quite sensitive to the form factor ζ. An empirical value that yielded good results for the most data sets was determined as $\zeta = 42$. The algorithm is much less sensitive to the curvature-parameters $\hat{\alpha}_{thr}$ and $\hat{\alpha}_{sat}$. They have been chosen as average values that were obtained from the experiments described in Section 3.4.5.

Parameter Convergence

The parameter swarms $\hat{\underline{\eta}}(k)$ and $\hat{\underline{\theta}}(k)$ are illustrated with the plots of Fig. 4.10. Even though the initial parameters $\hat{\underline{\eta}}(0)$ have been chosen much closer to the minimum than for the simulation (compare to Fig. 4.5), the convergence is much slower. This is mainly due to the modified input signal and to some extent to the slower exponential forgetting. The parameter estimates $\hat{\underline{\eta}}$ remain constant after approx. 90 s. This experiment was conducted with a sinusoidal intensity modulation. When APRB-signals were used, convergence times of approx. 60 s were obtained.

In order to demonstrate that the parameter estimates indeed reach a the global minimum within a physiologically meaningful region, the error criterion $E_{k,2}(\hat{\underline{\eta}})$ (compare to Eq. (2.19)) was calculated. The contour plot together with the locus of $\hat{\underline{\eta}}(k)$ is depicted in Fig. 4.11. Note that $E_{k,2}(\hat{\underline{\eta}})$ changes with time so that the contour plot only illustrates the error criterion at a particular time instance k. Especially during the first samples after the algorithm is started, the input-output data are not informative enough to yield a benign

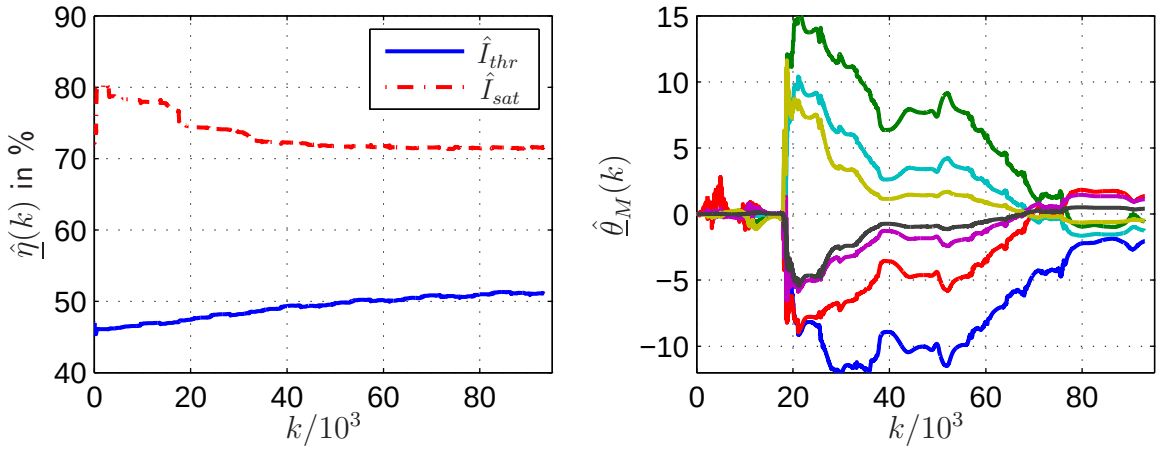

Fig. 4.10: Parameter swarms of $\hat{\underline{\eta}}(k)$ and $\hat{\underline{\theta}}_M(k)$.

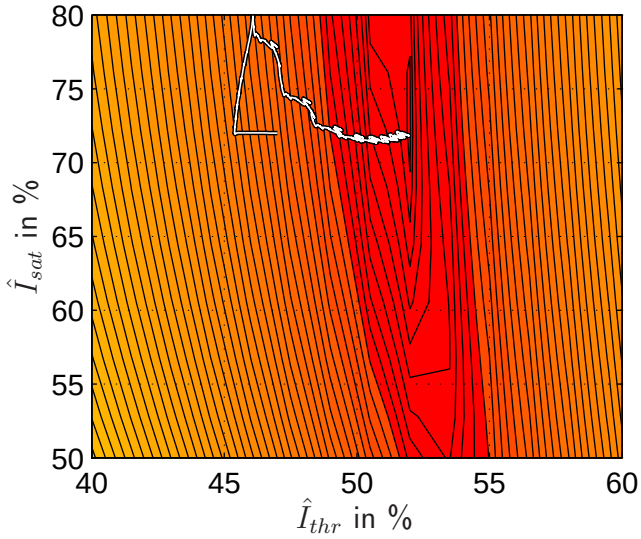

Fig. 4.11: Contour plot of the error criterion $E_{k,2}(\hat{\underline{\eta}})$ with locus of the parameter estimate $\hat{\underline{\eta}}(k)$.

error criterion. This explains the big parameter steps into the wrong directions at the beginning.

Evaluation

A comparison of the plant output y with its estimate $\hat{y}$ during the parameter adaptation process is depicted in Fig. 4.12. The model reconstruction of the simulative identification could be compared to the identified plant, since the true recruitment and activation dynamics were exactly known. In order to evaluate the model of recruitment and activation dynamics of the experimental identification, reference measurements have been carried out: The subject's forearm was fixated in the measurement orthosis, the coil was placed

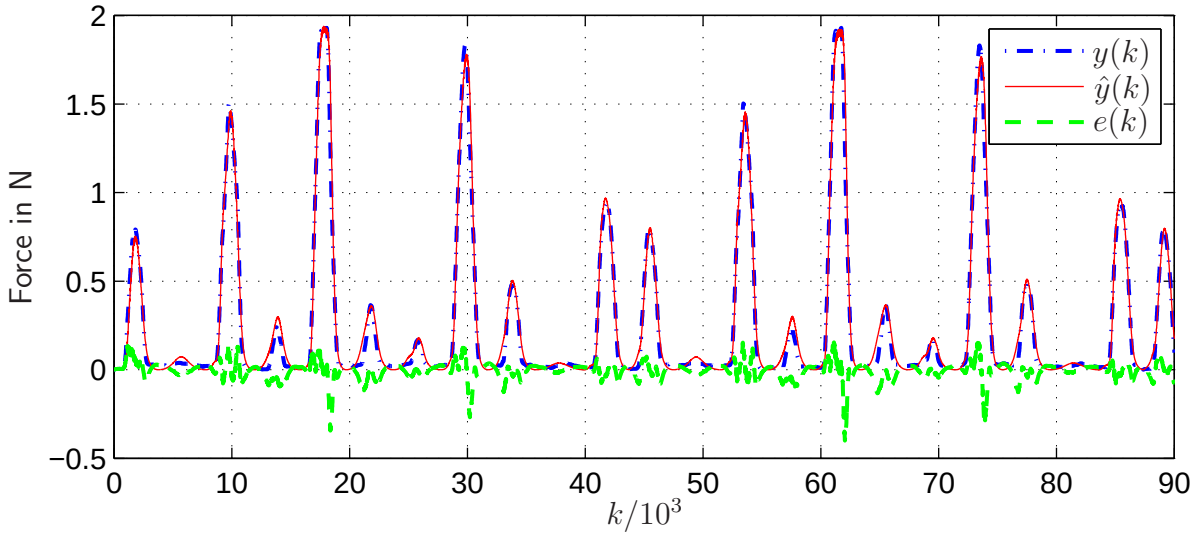

Fig. 4.12: Plant output $y(k)$, its estimate $\hat{y}(k)$ and output error $e(k)$ during parameter adaptation (data set of subject MB).

above the innervation zone of the EIP and the force sensor was arranged at the PIP-joint (compare to the schematic in Fig 3.14). Then, the absolute recruitment $\rho(I)$ was measured as described in Section 3.4.5, and the impulse response $h(k)$ was measured by application of single pulses as described in Section 3.4.3. Immediately after these reference measurements and without rearranging the coil, the stimulation sequence that was utilized for system identification (Fig. 4.4 or Fig. 4.9) was applied and the identification was carried out with the measured input-output data.

Exemplary reference measurements, and the model reconstruction of subject MB are depicted in Fig. 4.13. The experiment was carried out in total of six healthy subjects. The system identification of the data of two subjects did not converge and the model reconstruction yielded implausible results. Although the exact reason is unknown, it is possible that the subjects were not able to relax during identification so that the underlying model is inconsistent. Another two subjects had to be stimulated with the sinusoidal input sequence (4.19) since they had difficulties to relax with the APRB-signal. Two subjects felt comfortable with the APRB-signal. Accordingly, their parameter estimates converged faster than during the experiment depicted in Fig. 4.10 where a sinusoidal input signal was used.

The model reconstruction and the model output of the four subjects whose data sets converged were evaluated by calculating the NMSE (Eq. (A.11)). The results are summarized in Tab. 4.3.

4.2.6 Discussion

The identification of the simulated plant yields a negligible NMSE-value and an almost perfect model reconstruction. The implemented simulation is based on the model derived

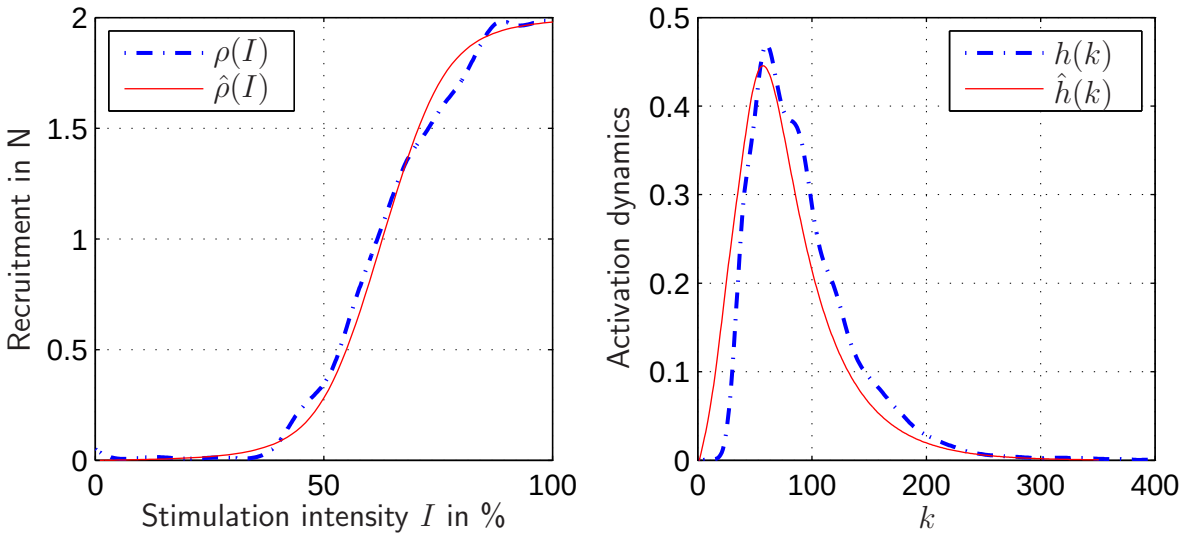

Fig. 4.13: Model reconstruction from the identification result: The blue dotted lines indicate the measured reference curves. The identified approximations are plotted with red solid lines.

Tab. 4.3: Evaluation of the experimental identification during isometric *RPMS*: The identified subplants $\hat{\rho}(I)$, $\hat{h}(k)$ as well as the model output $\hat{y}(k)$ were evaluated by calculating NMSE$(\rho(I), \hat{\rho}(I))$, NMSE$(\underline{h}, \underline{\hat{h}})$ and NMSE$(\underline{y}, \underline{\hat{y}})$. The results from the subjects whose data sets did not converge are excluded.

NMSE$(x, \hat{x})$ in % / Subject	$\hat{\rho}(I)$	$\hat{h}(k)$	$\hat{y}(k)$
MB	0.29	7.0	1.2
DM	0.37	5.3	1.3
BG	1.18	7.8	2.4
NN	0.6	4.6	1.5
Average	0.61	6.2	1.6

in Section 3.4. Since this model was proven to be a realistic approximation of the plant, it can be concluded that the proposed model equation is very well suited to approximate the plant of the isometric force generation.

The asymptotic stability of EM-C1 that was formally proved in Chapter 2 could be verified by means of a practical example and a real application. Since the parameter space of the nonlinear parameters is given with $\Omega_\eta \subset \mathbb{R}^2$, the error criterion and the locus of the parameter estimates $\underline{\hat{\eta}}(k)$ could be visualized in order to verify the convergence to the global minimum. The design rules for the adaptive system that have been derived in Sections 2.5.1 and 2.6.1 on the basis of theoretical insight were successfully applied and

turned out to be helpful guidelines. In particular, the design of a persistently exciting input signal was facilitated.

The experimental identification showed an additional requirement that was not revealed during simulation. The APRB-signal that was designed to meet the requirements of persistent excitation is characterized by a discontinuous modulation of the stimulation intensity $I(k)$. These intensity steps were sensed as unpleasant by four out of six subjects and hence they were not able to relax the stimulated muscles. Due to these disturbances the adaptation algorithm did not converge. For two subjects, this problem could be remedied by applying a smooth stimulation signal with a slow sinusoidal intensity modulation. This input signal still meets the excitation requirements though it yields a slower convergence. The data obtained from two of six subjects could not be identified at all. Probably, these subjects were not able to relax sufficiently.

During experimental identification, the parameters did not converge as fast as in simulation. This is due to measurement noise, model inconsistencies like voluntary muscle activity, and to the sinusoidal input signal. Nevertheless, the adaptation speed is fast enough to track slowly varying effects like muscle fatigue as it will be shown in Chapter 5.

A lot of design parameters (Tab. 4.1) have to be tuned in order to obtain a satisfactory performance of the adaptive system. However, the algorithm showed a critical sensitivity with respect to the exponential forgetting parameter λ_d and the form factor ζ, only. The initial guess $\hat{\underline{\eta}}(0)$ should be chosen within physiological meaningful intervals. Otherwise the properties of locality and monotonicity will be lost.

4.3 Identification under Nonisometric Conditions

Under nonisometric conditions, the plant depicted in Fig. 4.14 is considered. As was discussed for the identification under isometric conditions, the physiological delay is not integrated into the model equation but will be taken into account in the identification configuration.

Compared to Fig. 3.1 the muscle contraction dynamics are neglected which is explained and justified in Section 3.5. Furthermore, the block "Force transmission" is not considered since the tendon leverage can be approximated as constant factor (see Section 3.3). This constant will be implicitly integrated in the muscle force generation so that the output of the Hammerstein model is the muscular driving torque τ_M acting on the MCP-joint. It is equal to the torque τ_2 introduced in the coordinate systems in Figs. 3.10 and 3.20. For sake of a better readability, the MCP-joint angle α_2 is denoted as α since the angles α_1, α_3 and α_4 are not part of the model.

4.3.1 Model Equation

Model Structure

After applying block diagram manipulation to the plant depicted in 4.14, the equivalent system of Fig. 4.15 can be obtained. Assuming that the moment of inertia J and the relaxation characteristics are known, the structure of Fig. 4.15 divides the plant into a subplant with output τ, whose parameters are unknown, and a known LTI-system $\mathcal{W}$.

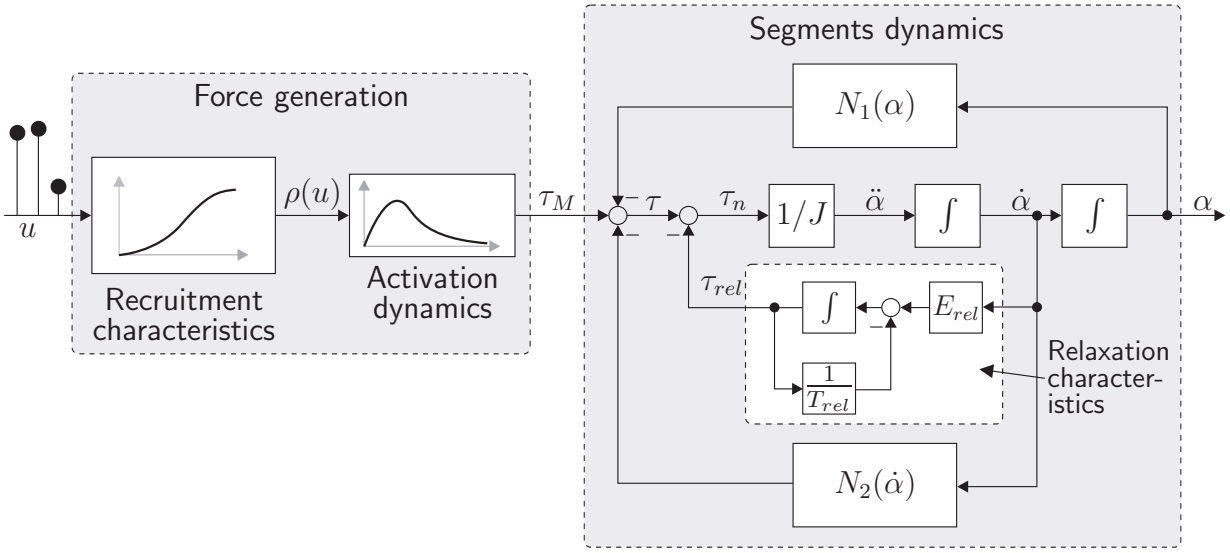

Fig. 4.14: Block diagram of the plant "*RPMS*-induced index finger extension".

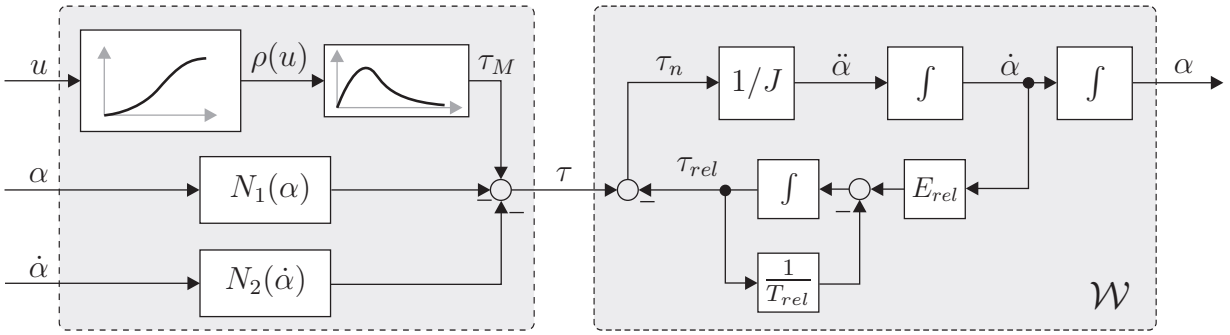

Fig. 4.15: Plant of the *RPMS*-induced index finger movement structured as a subplant with unknown parameters acting on a known LTI-system $\mathcal{W}$.

With

$$\underline{v} = [u\, \alpha\, \dot{\alpha}]^T \tag{4.20a}$$

$$y_n = \tau \tag{4.20b}$$

$$y = \alpha \tag{4.20c}$$

this structure coincides with the general identification structure introduced in Section 2.2. The state $\underline{\chi}$ of the subplant $\mathcal{W}$ is given as

$$\underline{\chi} = [\alpha\, \dot{\alpha}\, \tau_{rel}]^T \quad . \tag{4.21}$$

Parameterized Equation

The moment τ acting on $\mathcal{W}$ is calculated as

$$\tau = \tau_M - N_1(\alpha) - N_2(\dot{\alpha}) \ . \tag{4.22}$$

The muscle torque τ_M is the output of the Hammerstein structure of the force generation. According to derivation (4.9) its approximation is given as

$$\hat{\tau}_M(k) = \underline{\hat{\theta}}_M \underline{\varphi}_M(\underline{\hat{\eta}}, \underline{u}(k)) \ . \tag{4.23}$$

The static nonlinearities $N_1(\alpha)$ and $N_2(\dot{\alpha})$ comprise the gravitational torque, elastic properties of joint and attached muscles, viscous effects and spasticity, as explained in Sections 3.6 and 3.7. For the parameter identification, they are approximated by an artificial neural network whereas a Gaussian normalized radial basis function (NRBF) network (see [121], e.g.) is chosen, as proposed in [6]. Compared to multilayer perceptron (MLP-) networks, NRBF-networks show less accuracy and smoothness when approximating complicated functions and are ill-suited for high dimensional input spaces. However, due to their linear parameterization, fast adaptation algorithms can be used and there is no danger of local minima. Since the nonlinearities of the presented application are of simple shape and have a one dimensional input, NRBF-networks match the needs.

A Gaussian radial basis function (RBF-) network approximates static nonlinear functions by a weighted superposition of Gaussian functions

$$B_j(u) = \exp\left(-\frac{(u-\xi_j)^2}{2\sigma^2}\right) \tag{4.24}$$

with the function center ξ_j and the smoothing parameter σ that determines the width of the Gaussian function. In order to remedy the drawbacks of an RBF-network such as dips in the interpolation behavior the activation functions of an NRBF-network are normalized by the sum of all non weighted basis functions. This yields

$$A_j(u) = \frac{\exp\left(-\frac{(u-\xi_j)^2}{2\sigma^2}\right)}{\sum_{i=1}^{m_N} \exp\left(-\frac{(u-\xi_i)^2}{2\sigma^2}\right)} \ , \tag{4.25}$$

whereas the number of basis functions is given with m_N. The output y_{NRBF} of the NRBF-network is calculated as

$$y_{NRBF}(u) = \sum_{j=1}^{m_N} \hat{\theta}_j A_j(u) = \underline{\hat{\theta}}^T \underline{\varphi}(u) \ , \tag{4.26}$$

with the vector of network weights $\underline{\hat{\theta}} = [\hat{\theta}_1 \dots \hat{\theta}_{m_N}]^T$ and the input regressor $\underline{\varphi}(u) = [A_1(u) \dots A_{m_N}(u)]^T$. In the following, an equidistant distribution of the activation function over the whole input space $\mathbb{U} \subset \mathbb{R}$ with $\mathbb{U} = \{u | u_{min} \leq u \leq u_{max}\}$ is considered. Thus, the distance between two activation functions is calculated as $\Delta\xi = \frac{u_{min}-u_{max}}{m_N-1}$. In order to choose the smoothing factor σ independently of $\Delta\xi$, it is normalized according to $\overline{\sigma} = \sigma/\Delta\xi$

and thus, the activation functions are given as

$$A_j(u) = \frac{\exp\left(-\frac{(u-\xi_j)^2}{2\overline{\sigma}^2\Delta\xi^2}\right)}{\sum_{i=1}^{m_N}\exp\left(-\frac{(u-\xi_i)^2}{2\overline{\sigma}^2\Delta\xi^2}\right)} \quad . \tag{4.27}$$

The parameters $\Delta\xi$ and $\overline{\sigma}$ are heuristically predefined, therefore, only the network weights $\underline{\hat{\theta}}$ are subject to parameter identification.

According to Eq. (4.26), the nonlinearities can be approximated as

$$\hat{N}_1(\alpha) = \underline{\hat{\theta}}_{N1}^T\underline{\varphi}(\alpha) \quad , \tag{4.28a}$$

$$\hat{N}_2(\dot{\alpha}) = \underline{\hat{\theta}}_{N2}^T\underline{\varphi}(\dot{\alpha}_2) \quad . \tag{4.28b}$$

With $\underline{\hat{\theta}} = [\underline{\hat{\theta}}_M^T\,\underline{\hat{\theta}}_{N1}^T\,\underline{\hat{\theta}}_{N2}^T]^T$, $\underline{v}(k) = [\underline{u}(k)^T\,\alpha(k)\,\dot{\alpha}(k)]^T$ and with

$$\underline{\varphi}(\underline{\hat{\eta}},\underline{v}(k)) = [\underline{\varphi}_M(\underline{\hat{\eta}},\underline{u}(k))^T\ -\underline{\varphi}_{N1}(\alpha(k))^T\ -\underline{\varphi}_{N2}(\dot{\alpha}(k))^T]^T \tag{4.29}$$

$y_n = \tau$ can be approximated by

$$\hat{y}_n(\underline{\hat{\theta}},\underline{\hat{\eta}},k) = \underline{\hat{\theta}}^T\underline{\varphi}(\underline{\hat{\eta}},\underline{v}(k)) \tag{4.30}$$

which is an SNLP-model according to Eq. (2.5c). The parameter space is given by $\underline{\hat{\theta}} \in \Omega_{\underline{\hat{\theta}}} \subset \mathbb{R}^{m_r+m_{N1}+m_{N2}}$ and $\underline{\hat{\eta}} \in \Omega_{\underline{\hat{\eta}}} \subset \mathbb{R}^q$ with $q = \dim(\underline{\hat{\eta}})$. Hence, the complete number of parameters is given by $p = m_r + m_{N1} + m_{N2} + q$.

State Space Representation of $\mathcal{W}$

From the block diagram in Fig. 4.15, the system differential equations of $\mathcal{W}$ can be inferred as

$$\ddot{\alpha} = \frac{1}{J}(\tau - \tau_{rel}) \quad , \tag{4.31a}$$

$$\dot{\tau}_{rel} = E_{rel}\dot{\alpha} - \frac{1}{T_{rel}}\tau_{rel} \quad . \tag{4.31b}$$

With the output (4.20c) and the state (4.21), the state space representation becomes

$$\begin{aligned}\underline{\dot{\chi}} &= \underbrace{\begin{bmatrix}0 & 1 & 0\\ 0 & 0 & -1/J\\ 0 & E_{rel} & -1/T_{rel}\end{bmatrix}}_{\underline{A}_w}\underline{\chi} + \underbrace{\begin{bmatrix}0\\ 1/J\\ 0\end{bmatrix}}_{\underline{b}_w}\tau \quad ,\\ y &= \underbrace{[1\,0\,0]}_{\underline{c}_w^T}\underline{\chi} \quad .\end{aligned} \tag{4.32}$$

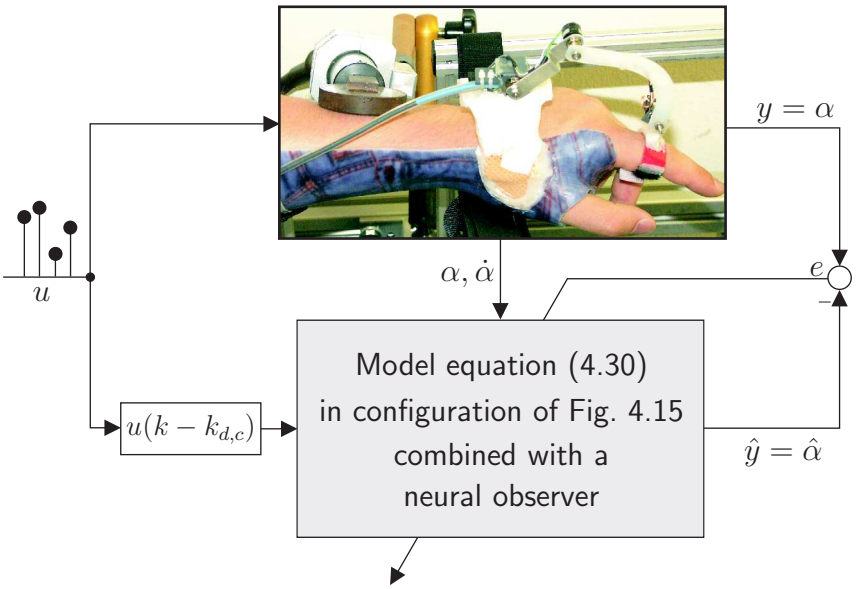

Fig. 4.16: Output error configuration of the identification of the *RPMS*-induced index finger extension.

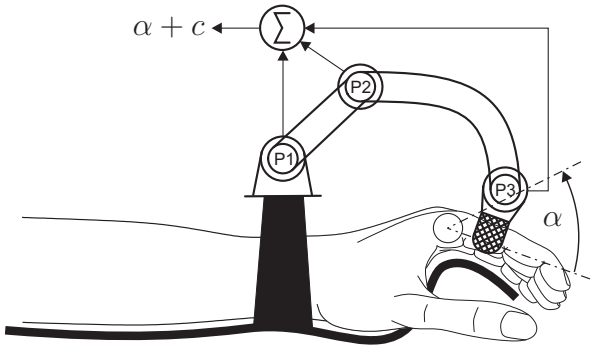

Fig. 4.17: Schematic illustration of the goniometer that measures the angle α: As easily derived from geometrical considerations, the angular sum of the three angles measured with the potentiometers P1-P3 is calculated as $\alpha + c$, with some constant value c.

4.3.2 Identification Scheme

Output Error Configuration

The identification configuration is depicted in Fig. 4.16. The input of plant and model and the compensation of the delay $k_{d,c}$ are equivalent to the isometric case explained in Section 4.3.2.

The experimental setup conforms with that depicted in Fig. 3.4.1 except for the force sensor which is replaced by a self-built goniometer (Fig. 4.17) that is attached to the index finger.

Parameter Adaptation Algorithm

The underlying parameter adaptation algorithm adapts the model parameters $\underline{\hat{\eta}}$ and $\underline{\hat{\theta}}$ according to EM C2 (Section 2.6.2) which incorporates a neural observer to obtain an asymptotically stable error transfer function. Similar to isometric conditions, the nonlinear parameters are identified with the modified LM-algorithm (Section 2.3). Therefore, the derivations of EM C2-GN apply. The algorithm has to compute the update equations (2.21), (2.22), (2.25) and (2.26) using the input regressor $\underline{\varphi}(\underline{\hat{\eta}}, \underline{v}(k))$ and its partial derivatives

$$\underline{\varphi}_i(\underline{\hat{\eta}}, \underline{v}(k)) = \frac{\partial \underline{\varphi}(\underline{\hat{\eta}}, \underline{v}(k))}{\partial \hat{\eta}_i} \ .$$

With the results (4.10)- (4.15) and with (4.29), $\underline{\varphi}_i(\underline{\hat{\eta}}, \underline{v}(k))$ is obtained as

$$\underline{\varphi}_i(\underline{\hat{\eta}}, \underline{v}(k))^T = [\underline{\varphi}_{M,i}(\underline{\hat{\eta}}, \underline{u}(k))^T \ \underline{0}^T \ \underline{0}^T] \ . \tag{4.33}$$

For the same reasons explained for isometric conditions, only $\underline{\hat{\eta}}_1$ and $\underline{\hat{\eta}}_2$ are subject to parameter identification and hence only $\underline{\varphi}_1$ and $\underline{\varphi}_2$ have to be calculated.

Neural Observer Design

The application of EM C2 requires the application of a neural observer if either the LTI-system $\mathcal{W}$ is not asymptotically stable, or the dynamic behavior is slow compared to the occurring signals. Since the system matrix of the state space representation (4.32) has not full rank, the system $\mathcal{W}$ is not asymptotically stable and a neural observer has to be implemented. The dynamics of the error transfer function $G_{w,obs}(s)$ should not have strong oscillating behavior and a short settling time T_{set}. These properties can be obtained by placing the observer poles according to the rules of optimal damping [152]. For second order systems, it is well known that the damping of $D = \sqrt{(2)}/2$ results in a minimum settling time. The rule of optimal damping is a generalization for systems of n^{th} order. For third order systems the desired denominator $d(s)$ of the transfer function is given as

$$d(s) = 8T_{sys}^3 s^3 + 8T_{sys}^2 s^2 + 4T_{sys} s + 1 \ , \tag{4.34}$$

whereas the system time constant T_{sys} is related to the settling time as $T_{set} = 13.28\, T_{sys}$. With the observer gain $\underline{l} = [l_1\, l_2\, l_3]^T$, the observer transfer function $G_{w,obs}(s) = \underline{c}_w^T(s\underline{I} - \underline{A}_w + \underline{l}\underline{c}_w^T)^{-1}\underline{b}_w$ of the system (4.32) is calculated as

$$G_{w,obs} = \frac{T_{rel}s + 1}{JT_{rel}s^3 + J(1 + T_{rel}l_1)s^2 + (E_{rel}T_{rel} + Jl_1 + JT_{rel}l_2)s + l_1E_{rel}T_{rel} + l_2J - l_3T_{rel}} \ . \tag{4.35}$$

Comparing the coefficients of Eq. (4.34) and of the denominator of Eq. (4.35) gives the observer gain $\underline{l}$.

The system time constant T_{sys} has to be chosen carefully. Choosing a small value yields fast dynamics of the error transfer function but results in a high observer gain $\underline{l}$. This may cause problems if the plant output y is not noise free since the noise will be amplified by

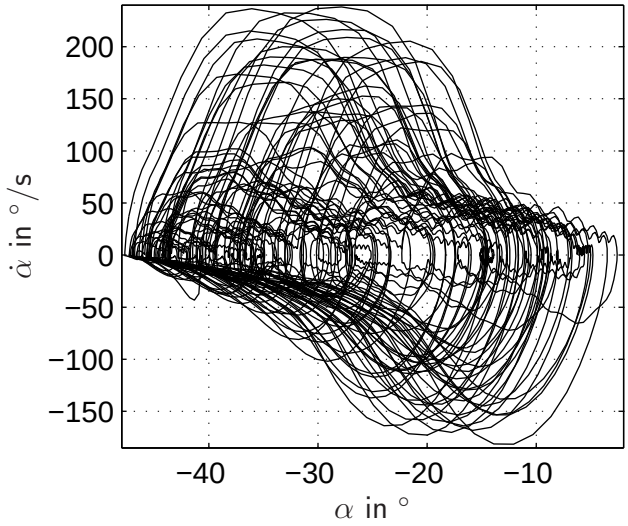

Fig. 4.18: Phaseplot of the signals $[\alpha(k)\,\dot{\alpha}(k)]^T$ that result from an APRB-input-signal $u(k)$.

$\underline{l}$. Based previous observations, the empirical value $T_{sys} = 0.01\,\mathrm{s}$ has been chosen which yields a settling time of $T_{set} \approx 133\,\mathrm{ms}$.

4.3.3 System Excitation

In case of an error transfer function with fast dynamics, EM C2 can be reduced to EM C1. Therefore, the considerations of Section 4.2.3 also apply for the nonisometric case. Since the input regressor has been extended by the NRBF-networks to approximate the nonlinearities $N_1(\alpha)$ and $N_2(\dot{\alpha})$, the linear persistent excitation condition can be relaxed if the complete input regressor (4.29) meets the condition (2.44), i.e. the covariance matrix $\underline{\Pi}^{-1}(k)$ remains invertible.

Since $\hat{N}_1(\alpha)$ and $\hat{N}_2(\dot{\alpha})$ are static functions, the specific excitation signal $[\alpha(k)\,\dot{\alpha}(k)]^T$ has to cover the complete input space of interest, and no requirements concerning any information about dynamics have to be fulfilled. The excitation of the plant with the APRB-signal of Fig. 4.4 results in a trajectory of $[\alpha(k)\,\dot{\alpha}(k)]^T$ that is depicted in Fig. 4.18. It can be expected that all covered operating points can be reproduced by the identification results. Due to the excellent interpolation behavior of NRBF-networks, operating points that are not excited in between should be reproducible.

4.3.4 Simulative Identification

As carried out for isometric identification, first a simulated plant is identified in order to evaluate the approximation performance of the model equation, and to test the ability of EM-C2 and the modified LM-algorithm with respect to this specific application. The theory of the error models A, B and C is based on the assumption that the LTI-system $\mathcal{W}$ is exactly known. However, in the presented application, the LTI-system consists of a double integrator and the relaxation dynamics. The relaxation parameters T_{rel} and

Tab. 4.4: Extension of Tab. 4.1: Additional fiddle parameters for nonisometric identification.

Model equation (NRBF-networks)	
$\overline{\sigma}$	0.55
m_{N1}	12
m_{N2}	12
$\alpha_{min} \ldots \alpha_{max}$	$-48\,^\circ \ldots 0\,^\circ$
$\dot{\alpha}_{min} \ldots \dot{\alpha}_{max}$	$-180\,^\circ/s \ldots 230\,^\circ/s$
Neural observer	
T_{sys}	0.01 s
T_{rel}	0.72 ± 0.09 s
E_{rel}	0.13 ± 0.02 Ncm/°

E_{rel} are not exactly known. Their average values were experimentally determined and the parameter uncertainty was quantified by calculating the 95 % confidence intervals (see Tab 3.8). Therefore, the robustness of the presented identification scheme with respect to an uncertain parameterization of $\mathcal{W}$ is evaluated with simulations.

Initialization

The force generation of the simulated plant is parameterized as explained for isometric identification. For the nonlinearities $N_1(\alpha)$ and $N_2(\dot{\alpha})$ (formulae (3.29) and (3.30)) typical functions as depicted in Fig. 3.21 have been used. The gravitational torque τ_g has been calculated with data from Tab. 3.6 and with simple geometrical considerations. For the moment of inertia J as well as for the relaxation parameters, the average values from Tab. 3.6 and Tab. 3.7 have been simulated.

The initialization of the identification algorithm and the choice of fiddle parameters has not been changed compared to the isometric case and therefore, the specifications of Tab. 4.1 apply. Additional fiddle parameters for the NRBF-networks are summarized in Tab. 4.4. The design of the neural observer is discussed in Section 4.3.2. The parameter identification was carried out with exact parameterization of the neural observer as well as with variations of T_{rel} and E_{rel} within the their 95 % confidence intervals.

Parameter Convergence

Fig. 4.19 depicts the convergence of $\hat{\underline{\eta}}(k)$, $\hat{\underline{\theta}}_M(k)$, $\hat{\underline{\theta}}_{N1}(k)$ and $\hat{\underline{\eta}}_{N2}(k)$ over time with exact parameterization of the neural observer. Although the initialization $\hat{\underline{\eta}}(0) = [20\,\%40\,\%]^T$ is far from the minimum, the algorithm converges after approximately 35 s. This convergence speed was obtained with inexact parameterization of the neural observer, too. Once the nonlinear parameters have settled, the linear parameters reach a steady state.

Fig. 4.20 shows a contour plot of the transformed error criterion $E_{k,2}(\hat{\underline{\eta}})$ that has been calculated according to Eq. (2.19) as already explained for the isometric case. It shows

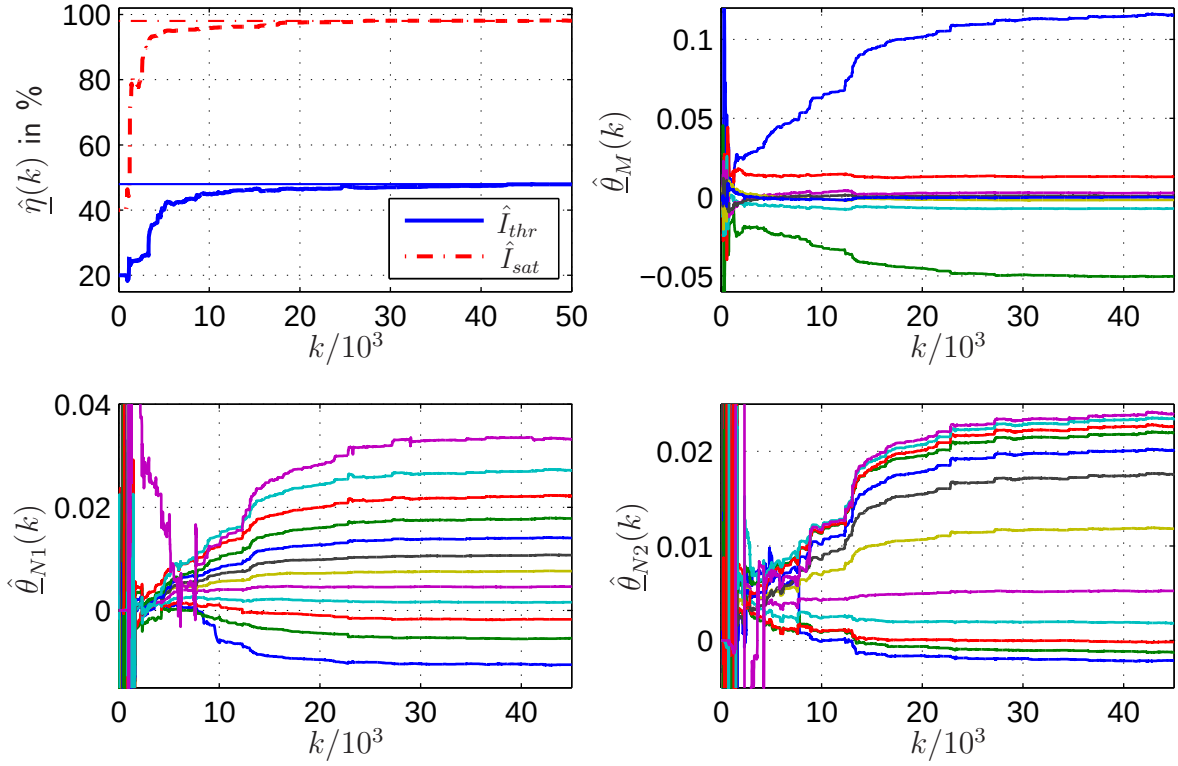

Fig. 4.19: Parameter swarms of $\hat{\underline{\eta}}(k)$, $\hat{\underline{\theta}}_{N1}(k)$, $\hat{\underline{\theta}}_{N1}(k)$ and $\hat{\underline{\theta}}_{N2}(k)$. In the top left graph, the true values $\underline{\eta}$ are indicated with straight lines.

that the true value $\hat{\eta} = [48\,\%\ 98\,\%]^T$ is indeed the only minimum within a physiologically meaningful region of $\hat{\underline{\eta}}$.

Evaluation

The lower graph of Fig. 4.21 shows the output error $e(k) = y(k) - \hat{y}(k)$ of the identification structure EM-C2 as it is depicted in Fig. 2.16. Since the output of the neural observer naturally follows the real output y, the observer error $\epsilon_{obs}(k) = e(k)$ is very small, even though the parameters have not yet converged. To evaluate the approximation performance, it is therefore reasonable to consider the error $e_n(k) = y_n(k) - \hat{y}_n(k)$ which is given as $e_\tau(k) = \tau(k) - \hat{\tau}(k)$ (Fig. 4.21 upper graph).

The model reconstruction is illustrated in Fig. 4.22. The Hammerstein model is reconstructed using the constraint explained in Remark 4.2.1 and the static nonlinearities are computed using Eq. (4.26).

Remark 4.3.1 *The identification of $\hat{N}_1(\alpha)$ and $\hat{N}_2(\dot{\alpha})$ is not unique since a constant offset can be added either to $\hat{N}_1(\alpha)$ or to $\hat{N}_2(\dot{\alpha})$ without changing the sum $\hat{N}_1(\alpha) + \hat{N}_2(\dot{\alpha})$. With the constraint*

$$\hat{N}_2(0) \stackrel{!}{=} 0 \tag{4.36}$$

a unique reconstruction is possible.

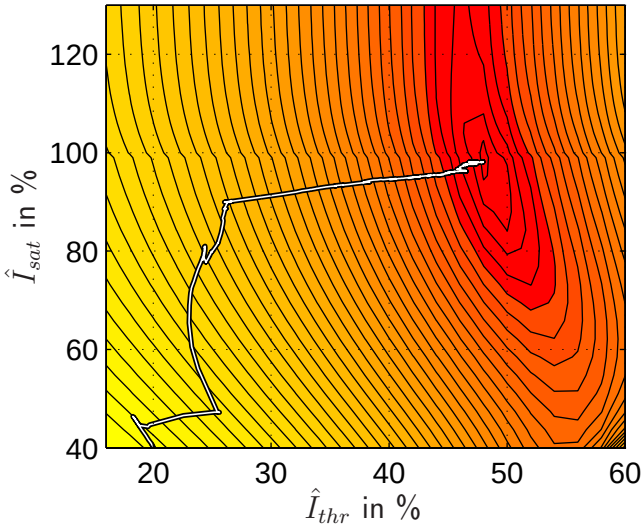

Fig. 4.20: Contour plot of the error criterion $E_{k,2}(\hat{\underline{\eta}})$ with locus of the parameter estimate $\hat{\underline{\eta}}(k)$.

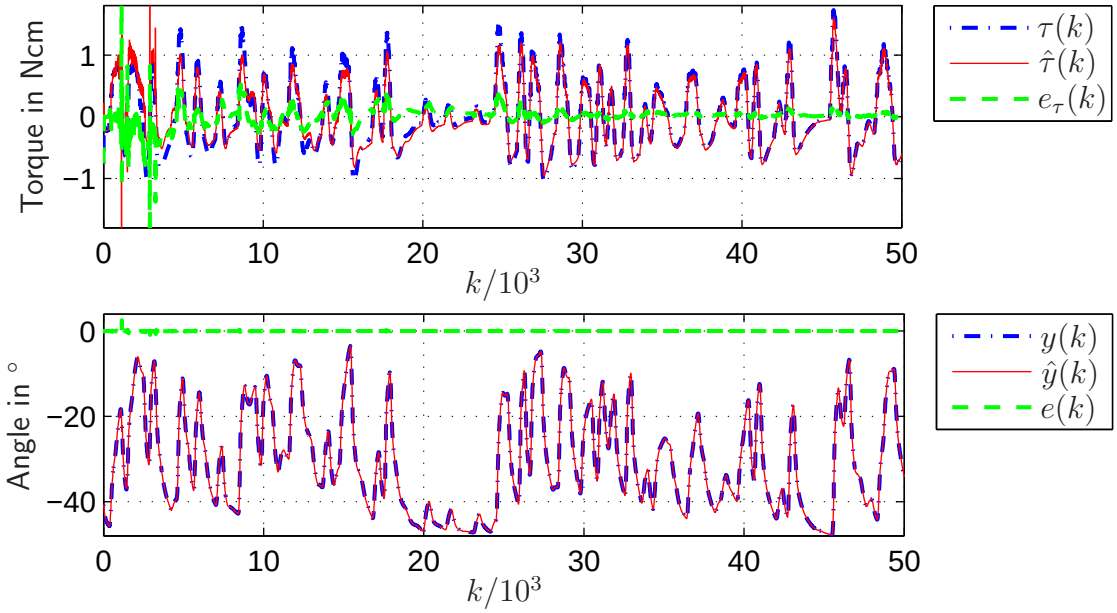

Fig. 4.21: Prediction errors during identification with exact parameterization of the neural observer: Upper graph: Torques $\tau(k)$, $\hat{\tau}(k)$ and prediction error $e_\tau(k) = \tau(k) - \hat{\tau}(k)$; Lower graph: Plant output $y(k)$, its estimate $\hat{y}(k)$ and output error $e(k)$.

The reconstruction in Fig. 4.22 shows the result obtained with exact parameterization of the neural observer as well as the worst results obtained with inexact parameterization. These reconstructions were obtained with the parameter variations summarized in the first column of Tab. 4.5. The reconstructions of all other parameterizations within the

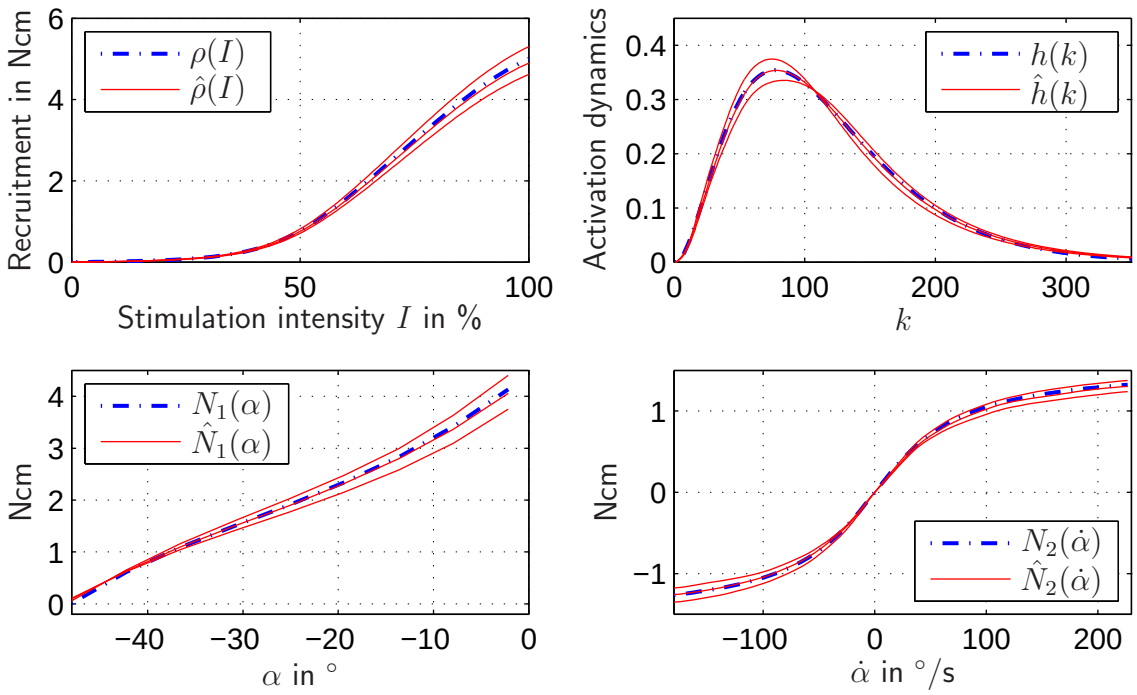

Fig. 4.22: Model reconstruction from the identification result: The blue dotted lines indicate the simulated plant. The identified approximations are plotted with red solid lines. The reconstructions obtained with exact parameterization are almost congruent with the given curves.

Tab. 4.5: NMSE-evaluation of the identification results: The results of the first row were obtained with an exact parameterization of the neural observer. The other results represent upper and lower error bounds obtained with an inexact parameterization within the 95 % confidence intervals of the relaxation parameters summarized in Tab. 3.8.

Observer parameterization \ NMSE$(x, \hat{x})$ in %	$\hat{\rho}(I)$	$\hat{h}(k)$	$\hat{N}_1(\alpha)$	$\hat{N}_2(\dot{\alpha})$	$\hat{\tau}(k)$
$\overline{T}_{rel}$ $\overline{E}_{rel}$	0.04	0.02	0.04	0.04	0.03
$\overline{T}_{rel} + 0.05\,\text{s}$ $\overline{E}_{rel} + 0.02\,\text{Ncm}/^\circ$	0.6	0.4	0.8	0.3	1.1
$\overline{T}_{rel} - 0.05\,\text{s}$ $\overline{E}_{rel} - 0.02\,\text{Ncm}/^\circ$	0.4	0.3	0.4	0.6	1.6

95 % confidence intervals showed a higher accuracy. The model accuracy was evaluated by means of NMSE-calculations. The results are summarized in Tab. 4.5.

4.3.5 Experimental Identification

In order to test the performance of the proposed identification scheme under realistic conditions, data from stimulation experiments with healthy subjects were recorded. The identification under nonisometric conditions will be applied in the context of spasticity quantification as it will be presented in Chapter 5.

Methods

As summarized in Fig. 4.16, the plant of the *RPMS*-induced index finger extension was identified in output error configuration. As described for the simulative identification, the adaptive system was implemented according to EM C2-GN using the modified LM-algorithm as adaptive law. The experimental setup conformed with the setup illustrated in Fig. 3.14. Instead of the force sensor, a goniometer (Fig. 4.17) was attached to the index finger.

The experiment was conducted with six healthy subjects. All subjects were asked to relax their hand as much as possible. However, just as during isometric stimulation, four subjects felt uncomfortable with the APRB-signal. Therefore, to those subjects the sinusoidal excitation (4.19) was applied. This kind of excitation leads to phase plots in the $\alpha - \dot{\alpha}-$plane as it is depicted in Fig. 4.23. Although the input space to the static nonlinearities $N_1(\alpha)$ and $N_2(\dot{\alpha})$ is covered incompletely, an identification is possible as the simulations have shown. This is due to the excellent interpolation behavior of NRBF-networks.

Just as during the isometric experiments, the small coils overheat after approx. 40-50 s. Since the convergence time might be longer, especially with the sinusoidal excitation, the input-output data are stored and fed into the adaptation algorithm as a repeating sequence.

Initialization

The algorithm was initialized similar to the simulative case. Parameters that have been changed are summarized in Tab. 4.6. As already explained for the experimental identification under isometric conditions, the forgetting factor λ_d was increased and the estimator gain $\gamma_{\hat{\underline{\eta}}}$ was decreased to make the algorithm more robust to disturbances. Also the parameters ζ, $\hat{\alpha}_{thr}$ and $\hat{\alpha}_{sat}$ were modified as it is explained for the isometric experiments. The number of basis functions was slightly increased which yielded a better convergence behavior. Lower and upper bounds for the approximation regions of the NRBF-network were individually adapted. The relaxation is parameterized according to experimental results described in Section 3.6.3. The moment of inertia J is individually calculated for every subject according to Eq. (3.28).

Parameter Convergence

The parameter swarms are illustrated in Fig. 4.24. The nonlinear parameters $\hat{\underline{\eta}}$ converge after approximately 90 s. This experiment was carried out with a sinusoidal intensity modulation. Using an APRB-modulation, a convergence time of approx. 60 s was achieved.

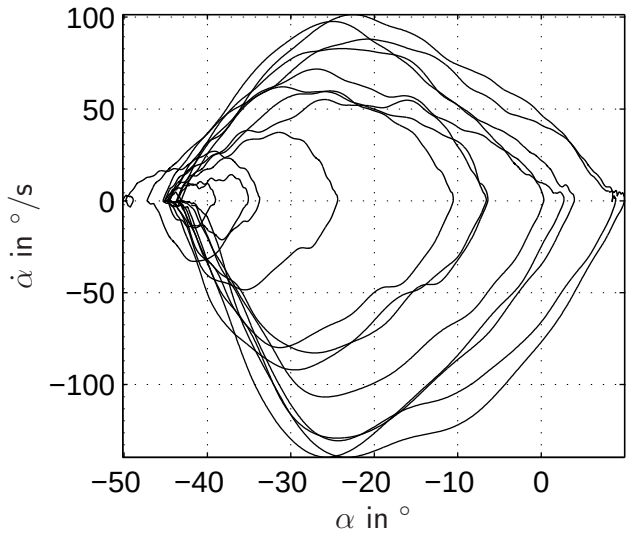

Fig. 4.23: Phaseplot of the signals $[\alpha(k)\,\dot{\alpha}(k)]^T$ that result from an input signal $u(k)$ with sinusoidal modulation of $I(k)$.

Tab. 4.6: Initialization and choice of the fiddle parameters that have been modified compared to Tab. 4.1 and Tab. 4.4.

SLS scheme with modified LM-algorithm	
$\hat{\underline{\eta}}(0)$	$[47\,\%\ 85\,\%]^T$
λ_d	0.995
$\gamma_{\hat{\underline{\eta}}}$	0.1
Model equation	
ζ	42
$\hat{\alpha}_{thr}$	8
$\hat{\alpha}_{sat}$	7
m_{N1}	16
m_{N2}	20
$\alpha_{min} \ldots \alpha_{max}$	Individual
$\dot{\alpha}_{min} \ldots \dot{\alpha}_{max}$	Individual
Neural observer	
T_{sys}	0.007 s
T_{rel}	0.72 s
E_{rel}	0.13 Ncm/°
J	Individual

The linear parameters follow immediately. The locus of the parameter estimate $\hat{\underline{\eta}}(k)$ plotted together with the error criterion in Fig. 4.25 shows that the nonlinear parameters

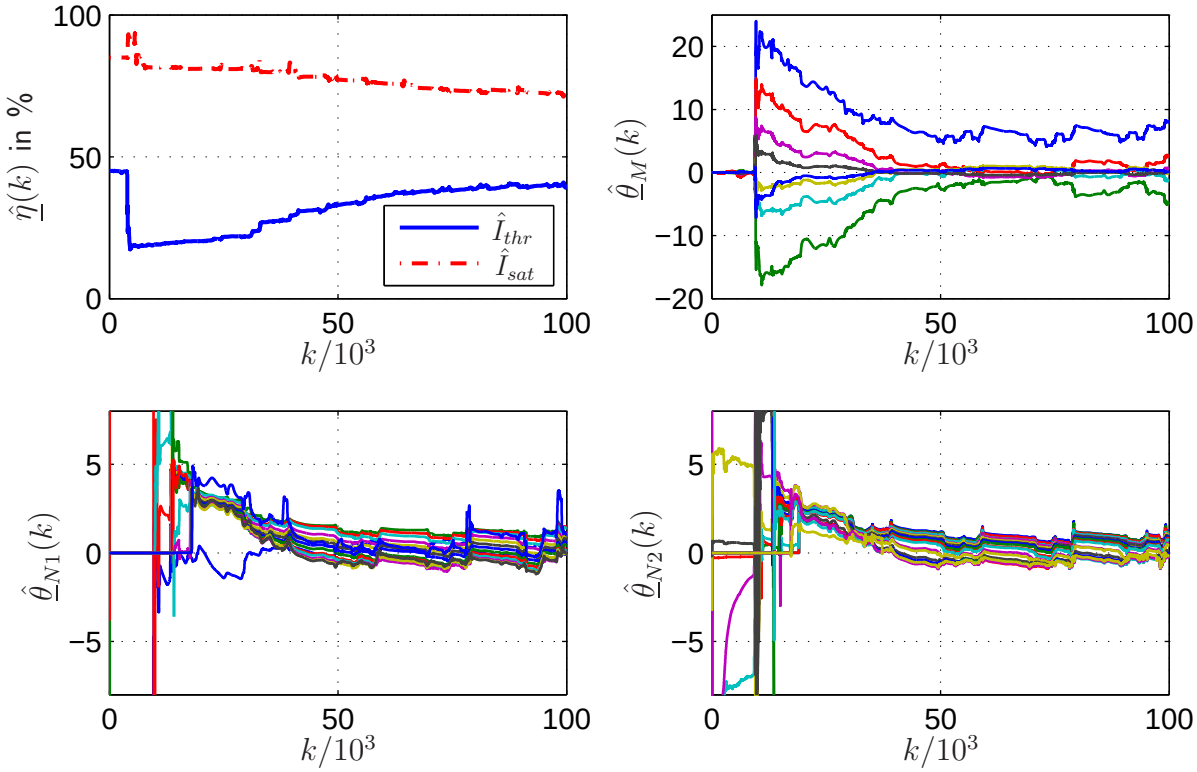

Fig. 4.24: Parameter swarms of $\hat{\underline{\eta}}(k)$, $\hat{\underline{\theta}}_M(k)$, $\hat{\underline{\theta}}_{N1}(k)$, and $\hat{\underline{\theta}}_{N2}(k)$.

indeed converge to the global minimum. Note, that $E_{k,2}(\hat{\underline{\eta}})$ changes with time so that the contour plot illustrates the error criterion at a particular time instance k, only. Especially during the first samples after the algorithm is started, the input-output data are not informative enough to yield a benign error criterion. This explains the big parameter steps into the wrong directions at the beginning.

Evaluation

The output error of the neural observer is very small due to the fast time constant T_{sys} of the neural observer and thus, its evaluation is not very meaningful. In order to evaluate the accuracy of the identified models, reference measurements were carried out. These reference measurements included isometric stimulations with force measurements on the one hand and measurements with the Fingertester (see Appendix C) on the other hand. The former was conducted immediately before the nonisometric stimulation sequence without rearranging the coil position. In this isometric setup, the absolute recruitment $\rho(I)$ and the impulse response $h(k)$ were measured as described in Sections 3.4.3 and 3.4.5. The measurements with the Fingertester were conducted in order to determine the nonlinear functions $N_1(\alpha)$ and $N_2(\dot{\alpha})$ as described in Section 3.6. Additionally, in a subsequent simulation, the identified models were run in parallel to the recorded data without observer feedback in order to calculate the NMSE$(y, \hat{y})$. An exemplary model reconstruction of subject MB in comparison to the respective reference measurements is depicted in Fig. 4.26.

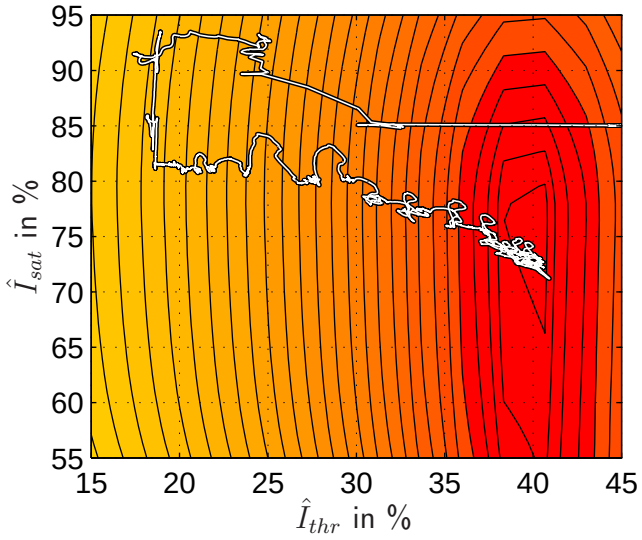

Fig. 4.25: Contour plot of the error criterion $E_{k,2}(\hat{\underline{\eta}})$ with locus of the parameter estimate $\hat{\underline{\eta}}(k)$.

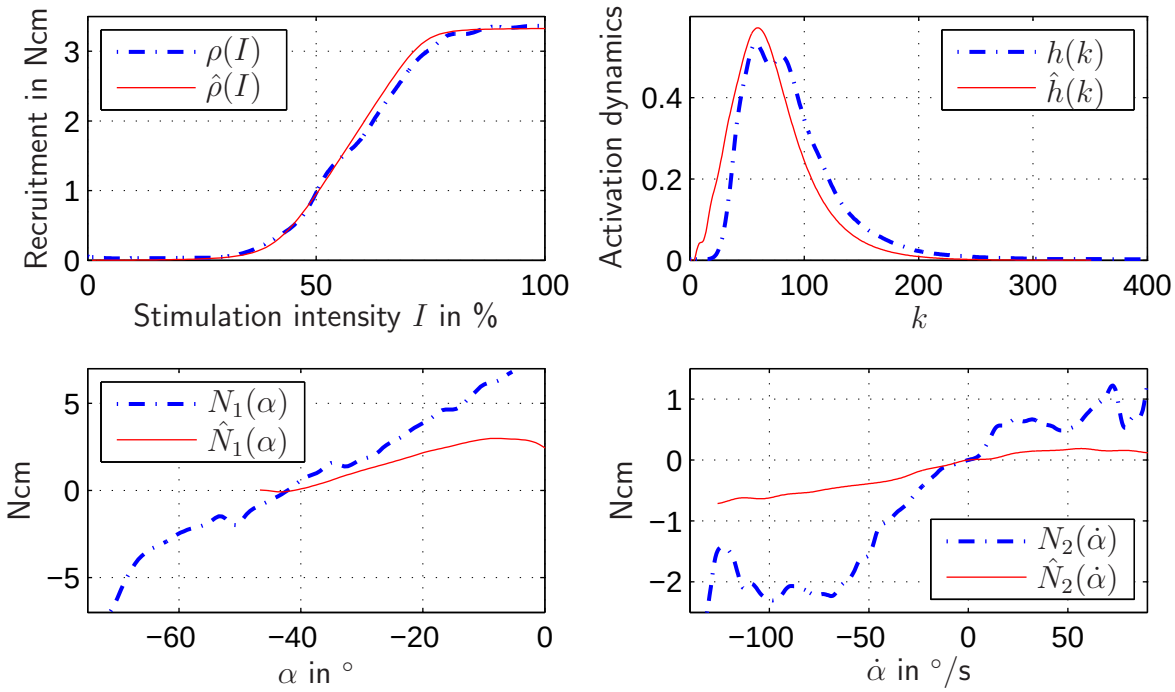

Fig. 4.26: Model reconstruction from the identification result: The blue dotted lines indicate reference measurements. The identified approximations are plotted with red solid lines.

The experiments were conducted with the same six subjects as the isometric identification. Again, two subjects felt comfortable with the APRB-signal, two had to be stimulated with

Tab. 4.7: NMSE-evaluation of the identification results obtained from experimental data. The results from the subjects whose data sets did not converge are excluded.

NMSE$(x, \hat{x})$ in % / Subject	$\hat{\rho}(I)$	$\hat{h}(k)$	$\hat{N}_1(\alpha)$	$\hat{N}_2(\dot{\alpha})$	$\hat{y}(k)$
MB	0.4	10.3	24.3	54.9	4.9
DM	0.6	3.2	26.8	48.3	5.2
BG	1.0	6.2	45.7	58.3	9.2
NN	0.5	3.0	20.7	61.3	6.1
Average	0.63	5.7	29.4	55.7	6.5

a sinusoidal intensity modulation and two subjects could not be identified at all. The four successfully identified curves as well as the model output of the parallel simulation were evaluated with NMSE-calculations. The results are summarized in Tab. 4.7.

4.3.6 Discussion

The simulative identification with exact parameterization of $\mathcal{W}$ yields an almost perfect model reconstruction with negligible small NMSE-values. Since the simulated plant is a verified model of the *RPMS*-induced index finger extension, it can be concluded that the proposed model equation is very well suited to approximate the real plant.

For the proposed approach, it is assumed that the relaxation parameters are known. This inevitably incorporates parametric uncertainties. In order to quantify the effect of these uncertainties on the overall identification result, worst case simulations were carried out. For this purpose, the model of the relaxation characteristics was parameterized with the boundary values of the 95% confidence intervals. Even with this worst case parameterization, the identification results yield NMSE-values smaller than 1.7 %. This robustness is due to the neural observer. The observer structure reduces the influence of parametric uncertainties on the output error just as it is known from the Luenberger observer. High gains of a Luenberger observer not only yield fast error dynamics, but also small influence of uncertain observer parameters on the observer output. The small NMSE-values indicate that the proposed observer design is well suited to suppress the parametric uncertainties that occur in the considered plant.

The asymptotic stability of EM C2 could be exemplified with a plant from a real application. The convergence to the global minimum was verified by visualizing the error criterion and the locus of $\hat{\underline{\eta}}(k)$. The design rules for the adaptation algorithm and the neural observer that were derived in Sections 2.5 and 2.6 based on stability analysis were successfully applied and turned out to be helpful guidelines. In contrary to other approaches of identification under nonisometric conditions (see state of the art in the Introduction 4.1), the EM C2 does not require the signal of angular acceleration. This is important for the on-line capabilities since numerical computation of a reasonable acceleration signal from a noisy position signal is often not possible. Clearly, the neural observer structure can

increase noise when the observer gain is chosen too high. Therefore, the observer has to be carefully designed.

The subjects that were identified were the same subjects that participated in the isometric experiments. Similarly, the data sets of two subjects could not be identified, two had to be stimulated with a sinusoidal input, and the other two felt comfortable with the APRB-signal. The identifications of the four successfully stimulated patients converged to the global minimum as it could be verified by visualizing the error criterion and the locus of the parameter estimate $\underline{\hat{\eta}}(k)$. The parameter convergence was slower than with simulated data which is due to the smaller estimator gain $\gamma_{\underline{\hat{\eta}}}$, the bigger forgetting factor λ_d and the faster observer time constant T_{sys}. These parameters were adjusted in order to increase the robustness of the adaptive system with respect to disturbances and model inconsistencies.

The comparison of the identified nonlinear functions $\hat{N}_1(\alpha)$ and $\hat{N}_2(\dot{\alpha})$ with their reference measurements shows significant differences. However, the identified recruitment, as well as the activation dynamics conform with the reference measurements. Since the NMSE-value of the overall model is small, it has to be concluded that the nonlinearities were identified correctly and indeed differ from those measured with the Fingertester. This conclusion can be justified by the physiology of sensorimotor integration:

Although the subjects are asked to relax, the muscles still show activity that is not caused by *RPMS*. This activity is due to synaptic noise and reflexes (see Appendix B.3.4) and results in a certain joint stiffness. This tonic joint stiffness is considered by the static nonlinear functions $\hat{N}_1(\alpha)$ and $\hat{N}_2(\dot{\alpha})$ since it can be modeled as a position and velocity dependent mechanical resistance. This fact will be utilized for the system identification based spasticity quantification that will be explained in Chapter 5. The activity of the α-motoneurons that conduct the action potentials from the CNS to the muscle is strongly affected by the *RPMS* which can mainly be ascribed to antidromic blocking and an increased Golgi tendon reflex. These effects have been reported in [93; 94; 111; 170]. Antidromic blocking is caused by the antidromic action potentials (see Section 3.2.1). During the time period in which an antidromic action potential propagates to the CNS, no orthodromic signal can be conducted through the same axon since colliding action potentials will be annihilated. The Golgi tendon reflex is caused by a change in muscle tension and has an inhibitory effect on the homonymous muscle. In comparison to voluntary muscle activation or to the externally applied movements of the Fingertester, the *RPMS*-enforced muscle contraction is less smooth. This is due to synchronous activation of the motor-units with a frequency of 20 Hz. Thus, the activity of the Golgi tendon organs is increased. Both, antidromic blocking, as well as the increased activity of the Golgi tendon organs, reduce the number of action potentials that reach the motor end plates of the axon. These inhibitory effects result in a smaller mechanical resistance of the attached joint, the MCP-joint in our case. All identification results of $\hat{N}_1(\alpha)$ and $\hat{N}_2(\dot{\alpha})$ showed a smaller gradients than the respective reference measurements $N_1(\alpha)$ and $N_2(\dot{\alpha})$. Therefore, it is well-conceivable that the identification results as well as the reference measurements are correct and reflect the varying innervatory muscle activity.

All known references concerning nonisometric identification consider "big" limbs like the forearm or the shank (see state of the art in the Introduction 4.1). In big limbs, the

gravitational component is dominant and relaxation phenomena can be neglected. Here, a "small" limb is considered where the gravitational torque is diminutive. Therefore, it was necessary to model and to account for the relaxation characteristics. The proposed approach is new and can easily be transferred to other small limbs.

4.4 Summary and Conclusions

The plant of the *RPMS*-induced index finger extension, consisting of force generation dynamics and segment dynamics including the relaxation behavior, can be accurately described with the proposed model. Thus, it can be concluded that the simplifying assumptions like the negligible influence of the length-velocity-dependencies and the constant tendon leverage apply, and that the approach of proposing a macroscopic model that only takes into account the dominant characteristics was successful.

It can further be concluded that the proposed model equations are well suited to individualize the model proposed in Chapter 3 to the respective subject. The equations can be considered as a gray box approach [122]. It allows incorporating a priori knowledge as far as it exists and is flexible to uncertainties where a priori knowledge is poor. A good knowledge exists about the segment dynamics and the characteristic shape of the recruitment function. The former is integrated by means of a white box model with known parameters and the latter by a nonlinearly parameterized function that a priori approximates the recruitment curve. Poor knowledge exists about the order of the activation dynamics. Although in Chapter 3 a third order model has been proposed, a predefined order as it could be realized with a difference equation does not yield satisfactory results. Therefore, a truncated convolution sum with input space compression by means of OBFs was used. This approach does not predefine the model order and was firstly proposed and successfully tested in [6]. Ultimately, this gray box approach is responsible for the good approximation behavior.

The adaptive system according to EM-C yields asymptotically stable parameter convergence with a reasonable speed, i.e. the parameter convergence is fast enough for slowly varying effects like muscular fatigue and spasticity. Robustness could be shown for uncertainties of the relaxation parameters whereas the expected uncertainties were bounded with the 95 % confidence intervals of the relaxation parameters. The experiments were not successful with 33 % of the subjects which is probably due to insufficient voluntary relaxation of the stimulated muscles. Since stroke patients suffer a partial or complete paresis, this problem might be reduced. It can therefore be concluded that the system identification is relevant for the further development of the *RPMS*-therapy.

The only work about nonisometric identification using a neural observer is presented in [6] where EM 4 [118] was implemented. Since EM 4 requires a linearly parameterized model equation, a model according to structure (2.5a) was developed. The linear parameterization leads to a bigger parameter space. Furthermore, it is more difficult to find good initial parameter guesses. Nevertheless, the results are comparable with those obtained with the SNLP-approach in this chapter. It is an advantage of the SNLP-approach that the parameters of the recruitment characteristics $\hat{I}_{thr}$ and $\hat{I}_{sat}$ have a direct physiological meaning which is not the case with an LP-approximation.

The identification was carried out isometrically as well as nonisometrically. The isometric experiment is easy to implement and can be useful for applications where on-line adaptations are not necessary like the design of the position controller that will be explained in Chapter 5. The implementation of the nonisometric case requires more expertise. However, during therapy, the index finger moves and thus, the on-line monitoring of patient parameters like muscle fatigue or spasticity has to be carried out under nonisometric conditions.

5 Enhancements for the RPMS-therapy

5.1 Introduction

As stated in Chapter 1, it is a major goal of the current research to improve the *RPMS*-therapy with the development an automated and objective therapy evaluation, an optimization of the proprioceptive input and an incorporation of the patient's voluntary activity. In this chapter, it will be shown how the system identification methods and the neuromuscular modeling introduced in the previous chapters make major contributions towards these goals: In Section 5.2 a system identification based quantification of spasticity and muscular fatigue will be introduced and Sections 5.3 and 5.4 will describe a position controlled and an EMG-driven position controlled *RPMS*-modes.

The quantification of spasticity is important for the assessment and planning of the therapy as well as to gather insight into the underlying neurophysiological mechanisms. Methods for spasticity assessment can be classified as clinical, electrophysiological and biomechanical (see [127; 177; 185] for a review). Standard clinical methods like the modified Ashworth scale [15] deliver subjective results. Their reliability is controversially discussed [126]. EMG-measurements are error prone and time-consuming [13]. Biomechanical methods comprise the measurement of joint-torque relations with dynamometers or exoskeleton robotic devices [1; 49; 77–79; 99; 113]. These measurements yield reliable results. However, expensive measurement devices are necessary and the attachment of the device to the patient might be time consuming. In [52; 150], system identification based methods for spasticity assessment were introduced which however are based on torque measurements. In this chapter, a method for spasticity quantification is introduced that is carried out during stimulation without using any extra equipment like force sensors or EMG-devices. It is based on the macroscopic models developed in Chapter 3 and the system identification method developed in Chapter 4. The novel method is tested and evaluated experimentally with stroke patients.

Prevention of muscular overexertion during *RPMS* is important since the therapeutic outcome is reduced, otherwise. During the position controlled movement induction, muscular fatigue cannot be observed by inspection since the controller just increases the controller output if the actuator (the muscle) becomes weaker. Therefore, similarly to the spasticity quantification, the muscle fatigue is monitored by means of system identification.

As explained in Chapter 1, proprioceptive input to the CNS is the basis of relearning the lost motor functions after having suffered stroke. The therapeutic outcome of relearning coordinated finger movements like grasping or the precision grip of index finger and thumb is still unsatisfactory [65]. In order to perform coordinated limb movements, the patient has to retrain complex spatiotemporal activation patterns. It is assumed, that the relearning of coordinated movements can be improved by task oriented therapy, i.e.

by inducing the same coordinated movements with muscle stimulation instead of inducing random uncoordinated patterns. In [131; 132; 172], it was demonstrated that task-oriented FES-therapy can improve voluntary reaching, grasping and walking functions in patients following stroke and spinal cord injury. In addition, the results presented in [2; 3] confirm this assumption. For these reasons, a coordinated *RPMS*-induced movement of the index finger is developed that aims to optimize the proprioceptive input to finally improve the therapeutic outcome. A model-based position controller is implemented to make the induced movement robust to disturbances and to provide the possibility of inducing movements at arbitrary velocities chosen by the supervising therapist. The capability of the proposed method is shown by means of experiments with healthy subjects.

So far, the only position controlled *RPMS*-induced limb motion can be found in [6] where the position of the elbow joint is controlled by dual *RPMS* of the m. biceps and m. triceps. Control strategies for FES-induced limb motion were developed mainly in the context of neuroprostheses for cyclic movements of the lower extremities. In [76; 146], sliding mode controllers were developed to control the knee-joint angle during quadriceps stimulation. In [40; 142], the same plant was controlled with model-based linearizing controllers and PID-control cascades. In [147], backstepping was used for position control of the knee-joint angle. The control performances of the proposed methods showed similar results. FES-induced hand and finger movements are commonly controlled with open-loop strategies. In [29; 59; 120; 145], various strategies for hand opening and closing are proposed with the purpose to implement grasping neuroprostheses. Comprehensive reviews on FES-induced grasping can be found in [130; 159]. A position controlled muscle stimulation induced extension and flexion of the MCP-joint of the index finger as it will be presented in this chapter, cannot be found in the current literature.

If a patient shows some ability to contribute to the therapy by voluntary force generation, this skill should be encouraged. In [42; 70; 88], it has been shown that active patient participation is essential for a successful motor rehabilitation. When using technical systems for rehabilitation, the patient's intention has to be detected and taken into account by the underlying algorithms in order to provide the possibility of active participation. In this chapter, an EMG-driven position control is introduced that incorporates the voluntary muscle activity that is sensed by means of electromyography (EMG). The proposed method ultimately yields the technical prerequisites to carry out a patient-cooperative therapy mode of the task oriented *RPMS*. In [139], the term "patient-cooperativity" is defined as the ability of the technical system to take into account the patient's intention and voluntary efforts, rather than imposing any predefined movement or inflexible strategy. In contrary to the position control with predefined trajectory, the EMG-driven mode adaptively generates the trajectory dependent on the patient's voluntary activity of the stimulated muscle. The effect is a force support by means of *RPMS* that assists the patient to carry out the intended motion. Thus, patients that are able to voluntarily generate a force that is not sufficient to initiate a movement obtain a direct biofeedback about their efforts. This kind of motivation is expected to increase the therapeutic outcome [138; 139].

The novel scientific contributions introduced in this chapter comprise a system identification based method for the quantification of spasticity and muscle fatigue, a position

controlled *RPMS*-induced extension and flexion of the index finger and an EMG-driven *RPMS*-induced position control with adaptive trajectory generation.

5.2 Quantification of Patient Parameters

5.2.1 Spasticity Quantification

Principle

In Section 3.7, a phenomenological model of the spastic joint torque in the MCP-joint of the index finger has been proposed. According to the formulae (3.35a) and (3.35b), the tonic and the phasic spasticity components $s_t(\alpha)$ and $s_{ph}(\dot{\alpha})$ can be integrated into the static nonlinearities $N_1(\alpha)$ and $N_2(\dot{\alpha})$ as additive terms[1]. In Section 4.3, it has been shown that the static nonlinearities can be identified on-line during nonisometric *RPMS*. All terms in (3.35a) and (3.35b) except the spasticity components are time invariant to a large extent. Therefore, a change of spasticity between the particular times t_1 and t_2 can be inferred as

$$\begin{aligned} \Delta s_t(\alpha) &= N_1(\alpha)\big|_{t_1} - N_1(\alpha)\big|_{t_2} \\ \Delta s_{ph}(\dot{\alpha}) &= N_2(\dot{\alpha})\big|_{t_1} - N_2(\dot{\alpha})\big|_{t_2} \quad . \end{aligned} \tag{5.1}$$

Thus, using on-line parameter identification, a change of spasticity can be observed in a time-continuous manner. In the following, a pilot study with four patients will be presented that aimed to evaluate the capability of this approach. The evaluation was done by means of comparative reference measurements. For this purpose, the spasticity was quantified in before-after manner instead of performing a time continuous tracking.

Experimental Protocol

The patients were treated with conditional *RPMS* [165; 166] for three days. During conditional *RPMS*, the flexor and extensor muscles of the upper and lower arm of the paretic side are stimulated with alternating coil positions. Every day, three stimulation sessions were carried out. During a stimulation session, magnetic pulse trains of 1.5 s, i.e. 30 pulses, followed by a 3 s break are applied for a total time of approx. 15 min.

Before the first treatment at day 1 (time t_1), the spasticity was quantified with system identification. Biomechanical reference measurements were carried out in order to evaluate the identification results. The same measurement protocol was carried out after the last stimulation session at day 3 (time t_2).

The experiments were conducted with four patients where three of them suffer from spastic paresis following a stroke. One patient suffered a cerebral hypoxia followed by spastic tetraparesis with dystonia (see Tab. 5.1).

[1] Throughout this chapter, the coordinate system introduced in Fig. 3.10 with the denotation $\alpha = \alpha_2$ applies.

Tab. 5.1: Relevant data of the patients. (L.o.l.: location of lesion, t.s.l.: time since lesion, Ashw. s. wr./fi.: Ashworth scale, wrist/fingers)

Patient	Sex	Age	L.o.l.	T.s.l. (yrs)	Symptoms	Ashw. s. wr./fi.	Sensory dysfunctions
CZ	f	63	complete middle cerebral artery infarction, right side	9	Paresis of the complete left hemisphere, spasticity in arm and finger flexors	2/2	Proprioceptive dysfunction in wrist and fingers, neglect of the complete arm
RG	f	64	vaso-spastic partial middle cerebral artery infarction, right side	6	Paresis of the upper left extremity, spasticity in arm and finger flexors	1-/2	Proprioceptive dysfunction in wrist and fingers, neglect of the complete arm
DL	m	71	intracerebral hemorrhage, right side, frontoparietal	5	Paresis of the upper left extremity, minimal voluntary flexion of finger and elbow, spasticity in arm and finger flexors	1/2	–
SU	f	37	Cerebral hypoxia	7	Spastic tetraparesis, ataxia, athetoid dystonia	–	–

System Identification Based Spasticity Quantification

The system identification of the *RPMS*-induced index finger extension was carried out as explained in Section 4.3. The EIP of the patients was stimulated with an APRB-modulated stimulation intensity $I(k)$ (compare to upper plot of Fig. 4.4) for a period of approx. 45 s. The data sets were identified with the identification scheme explained in Section 4.3.2 and the estimates $\hat{\rho}(I)$, $\hat{h}(k)$, $\hat{N}_1(\alpha)$ and $\hat{N}_2(\dot{\alpha})$ were obtained from the respective reconstructions. In Fig. 5.1, exemplary estimates $\hat{N}_1(\alpha)$ and $\hat{N}_2(\dot{\alpha})$ obtained from patient CZ are depicted. It can clearly be observed that both nonlinearities show a smaller amount of reset torque after the therapy at time t_2. According to the underlying model this change is ascribed to a reduction of the spasticity level. When comparing $\hat{N}_2(\dot{\alpha})$ in Fig. 5.1 with the identification results $\hat{N}_2(\dot{\alpha})$ obtained from healthy subjects (see Fig. 4.13), it can be observed that the amount of reset torque of the patient is higher and

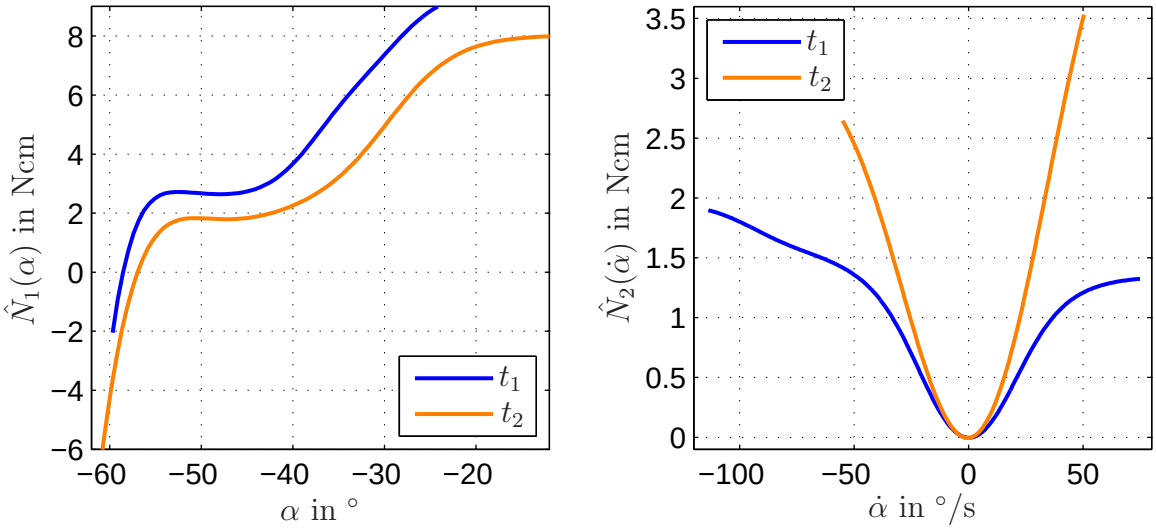

Fig. 5.1: Identification results of patient CZ before therapy (dark curves) and after therapy (bright curves).

that the patient's curve is positive for positive as well as for negative angular velocities $\dot{\alpha}$. Since this effect was observed at every patient and at none of the healthy subjects, it is well-conceivable that this characteristic is due to the spastic flexor activity.

In order to quantify the change of the tonic spasticity component, the mean difference

$$\Delta\bar{\hat{s}}_t = \overline{\hat{N}_1(\alpha)\big|_{t_1} - \hat{N}_1(\alpha)\big|_{t_2}} \tag{5.2}$$

is calculated as a characteristic number. As explained in the following section, the phasic component can be compared to the reference measurement at the angular velocities $\dot{\alpha} = 30\,°/\mathrm{s}$ and $\dot{\alpha} = 60\,°/\mathrm{s}$, only. Thus, the characteristic numbers

$$\begin{aligned} \Delta\hat{s}_{ph,30} &= \hat{N}_2(30°/\mathrm{s})\big|_{t_1} - \hat{N}_2(30°/\mathrm{s})\big|_{t_2} \\ \Delta\hat{s}_{ph,60} &= \hat{N}_2(60°/\mathrm{s})\big|_{t_1} - \hat{N}_2(60°/\mathrm{s})\big|_{t_2} \end{aligned} \tag{5.3}$$

are calculated.

Reference Measurements

The Fingertester (see Appendix C) was used to move the patient's MCP-joint of the index finger from its equilibrium position with constant angular velocity $\dot{\alpha}$ in order to measure the joint torque τ_{me} (compare to Fig. 3.22). In order to measure the tonic as well as the phasic spasticity component, the extension was carried out at three different angular velocities: $\dot{\alpha} = 15\,°/\mathrm{s}$, $\dot{\alpha} = 30\,°/\mathrm{s}$ and $\dot{\alpha} = 60\,°/\mathrm{s}$. An exemplary reference measurement of patient CZ is depicted in Fig. 5.2. Clearly the curves measured at time t_2 show a smaller amount of reset torque and no increase at velocities $\dot{\alpha} = 30°/\mathrm{s}$ and $\dot{\alpha} = 60°/\mathrm{s}$. From this

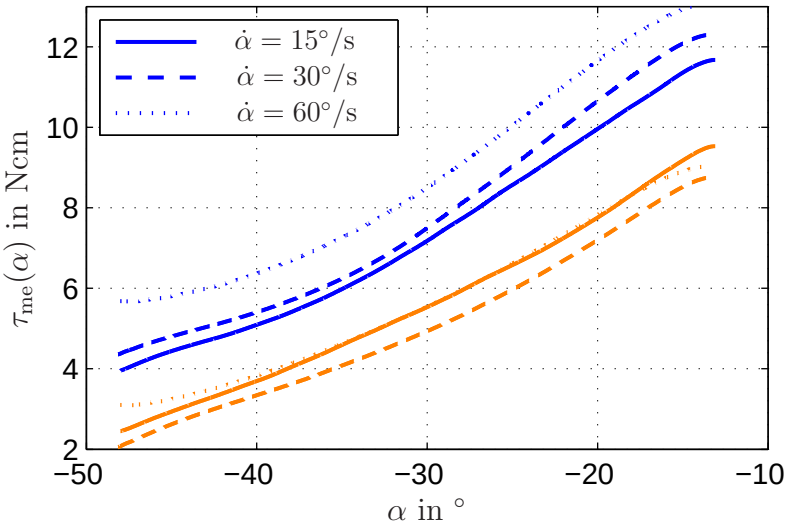

Fig. 5.2: Reference measurements of patient CZ: The index finger was extended at three different angular velocities. The dark curves indicate time t_1 and the bright curves indicate time t_2.

result it can be concluded that the tonic spasticity as well as the phasic spasticity have indeed decreased.

Since no phasic spasticity is expected at $\dot{\alpha} = 15\,°/s$, the characteristic number of the tonic spasticity component can be calculated as

$$\Delta\overline{s}_t = \overline{\tau_{\mathrm{me},15}(\alpha)\big|_{t_1} - \tau_{\mathrm{me},15}(\alpha)\big|_{t_2}} \quad . \tag{5.4}$$

The characteristic number $\Delta\overline{s}_{ph,30}$ that quantifies the phasic component at $\dot{\alpha} = 30\,°/s$ can be calculated as

$$\begin{aligned} \overline{s}_{ph,30}\big|_{t_1} &= \overline{\tau_{\mathrm{me},30}(\alpha)\big|_{t_1} - \tau_{\mathrm{me},15}(\alpha)\big|_{t_1}} \\ \Delta\overline{s}_{ph,30} &= \overline{s}_{ph,30}\big|_{t_1} - \overline{s}_{ph,30}\big|_{t_2} \quad . \end{aligned} \tag{5.5}$$

Eq. 5.5 is applied for $\dot{\alpha} = 60\,°/s$, too.

Results

The characteristic numbers were calculated for each patient according to Eqs. (5.4) and (5.5). In order to compare the identification-based results with the reference measurements, the relative differences

$$\begin{aligned} d_t &= \frac{\Delta\overline{s}_t - \Delta\overline{\hat{s}}_t}{\Delta\overline{s}_t} \\ d_{ph,30/60} &= \frac{\Delta\overline{s}_{ph,30/60} - \Delta\hat{s}_{ph,30/60}}{\Delta\overline{s}_{ph,30/60}} \end{aligned} \tag{5.6}$$

were calculated. The results of the characteristic numbers and the relative differences are summarized in Tab 5.2. The results indicate that the identification based spasticity quantification agree with the reference measurements by trend. An increase of the phasic component as it could be observed at patient RG has been often observed after conditional *RPMS*. The reason for the increase of tonic and phasic spasticity of patient SU is unclear.

Tab. 5.2: Results of the spasticity quantification: The unit of all "Δ"-numbers is Ncm, the relative differences d_t and d_{ph} are given in %. Patient CZ did not reach the angular velocity $\dot{\alpha} = 60°/\text{s}$ during stimulation at time t_1. Thus, $\Delta\hat{s}_{ph,60}$ could not be calculated. Note, that negative "Δ"-numbers indicate an increase of spasticity.

Patient	Tonic component			Phasic component					
	$\Delta\bar{\hat{s}}_t$	$\Delta\overline{s}_t$	d_t	$\Delta\hat{s}_{ph,30}$	$\Delta\hat{s}_{ph,60}$	$\Delta\overline{s}_{ph,30}$	$\Delta\overline{s}_{ph,60}$	$d_{ph,30}$	$d_{ph,60}$
CZ	1.6	1.7	6.8	0.9	-	1.0	1.4	10.4	-
RG	8.5	9.2	7.6	-3.1	-5.7	-4.2	-6.0	24.9	4.4
DL	1.5	1.8	16.1	2.0	6.8	1.4	3.7	-49.7	-84.3
SU	-2.9	-0.7	-325.5	-6.2	-9.4	-2.8	-3.3	-121.1	-189.1

5.2.2 Identification of Muscle Fatigue

Principle

In [135], a force generation model was developed on a physiological level, that incorporates the depolarization dynamics at the motor end plates, and in the T-tubuli as well as the dynamics of Ca^{2+}-release and Ca^{2+}-bonding (see also paragraph "Muscle Activation" in Appendix B.1.5). The process of fatiguing and recovery is ascribed to decrease and increase of Ca^{2+}-concentration in the sarcoplasmatic reticulum and modeled with a nonlinear first order differential equation. The proposed model was successfully verified with FES-experiments. On a phenomenological macroscopic level, the fatigue results in a smaller amount of force and in a different shape of the recruitment curve. The latter effect can be explained by the different recruitment characteristics of the different types of muscle fibers (see Appendix B.1.6). Slow muscle fibers show a higher recruitment threshold and a higher recruitment saturation than fast muscle fibers [66]. In the recruitment model 3.19 this is reflected with the parameters I_{thr} and I_{sat}. Since the fast fibers show a higher fatigability, during stimulation their contribution to the absolute recruitment $\rho(I)$ is reduced compared to the slow fibers. This results in increasing values of I_{thr} and I_{sat}.

The macroscopic force generation model developed in Section 3.4 can account for the phenomenological effects as described above. In the following, it will be shown, how the muscle fatigue can be tracked with on-line identification scheme introduced in Chapter 4. First, a simulation is described that evaluates the approximation capabilities of the

macroscopic model, subsequently, the experiment is described and evaluated. With our equipment, the EIP cannot be stimulated longer than approx. 45 s due to overheating of the small circular coils. Since the EIP does not show significant fatigue during this short stimulation period, the fatiguing experiments were conducted with the m. biceps brachii.

Simulation

The model from [135] was originally proposed for the electrically stimulated m. quadriceps. In [201], it was modified to approximate the magnetically stimulated m. biceps brachii. The model was verified by means of isometric experiments (see schematic of Fig. 5.3) and showed an excellent approximation behavior. The fatiguing parameters were manually tuned such that the significant muscle fatigue that can be observed at the m. biceps during a stimulation period of 60 s could be reproduced. The modified model was integrated as simulated plant into the identification scheme of Fig. 4.1 and identified as described in Section 4.2.

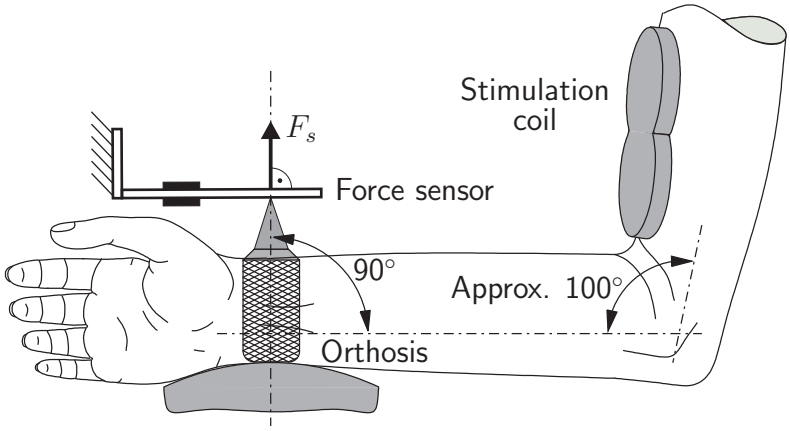

Fig. 5.3: Experimental setup for isometric stimulation of the m. biceps brachii. The sensor force F_s represents the plant output.

The plant output $y(k) = F_s(k)$, its estimation and the output error are plotted over time in Fig. 5.4. The motor unit recruitment $\hat{\rho}(I)$ and the muscle activation dynamics $\hat{h}(k)$ were reconstructed after 30 s, and 60 s. From the small output error $e(k)$, it can be concluded that the macroscopic model is capable of approximating the physiological model. The tracking performance of the on-line parameter identification is sufficient to follow the fatiguing process. From the reconstruction (Fig. 5.5), it can be inferred that the fatigue is accounted for with the recruitment model whereas the impulse response remains almost unchanged.

Experiment

The experiment was carried out according to the setup depicted in Fig. 5.3. The subject was stimulated over a period of 60 s. In [6], the contraction time of the m. biceps was determined as 450 ms. For this reason, the length m of the impulse response was chosen to 450. The curvature parameters were chosen at $\alpha_{thr} = 25$ and $\alpha_{sat} = 9$. In order to have an

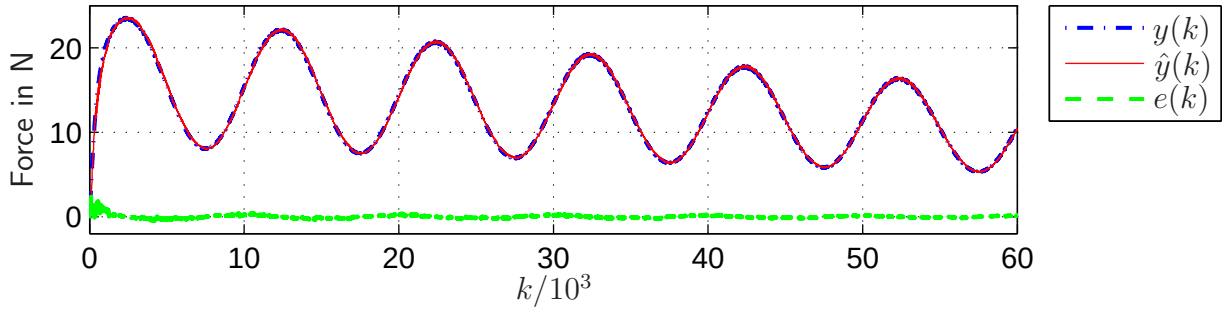

Fig. 5.4: Plant output $y(k)$, its estimate $\hat{y}(k)$, and output error $e(k)$ during simulative parameter adaptation.

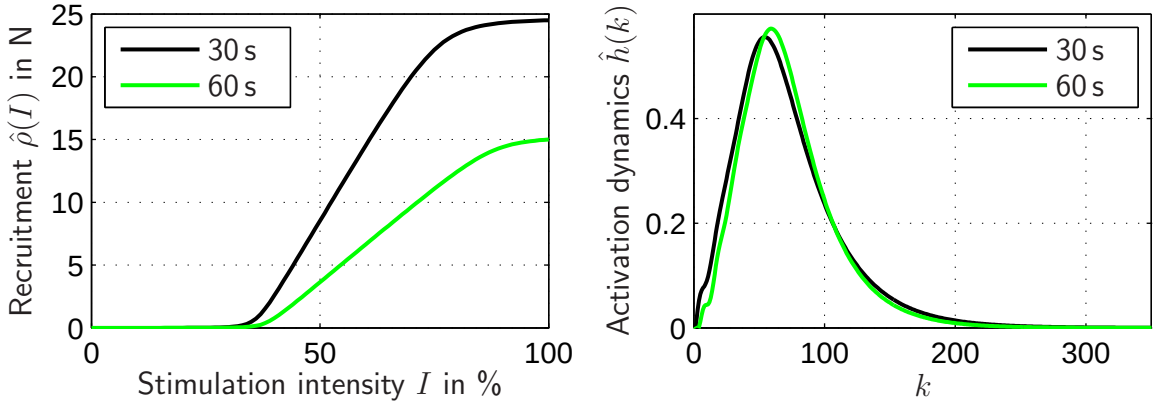

Fig. 5.5: Model reconstruction from the identified parameters after 30 s and after 60 s of simulation.

instant tracking of the plant, initial values $\underline{\hat{\eta}}(0)$ and $\underline{\hat{\theta}}_M(0)$ were obtained from a preceding parameter identification. The other fiddle parameters remained unchanged compared to Tabulars 4.1 and 4.2. Similar to Chapters 3 and 4, the sensor force F_s was defined as system output $y(k) = F_s(k)$.

The prediction error during identification is depicted in Fig. 5.6. The model was reconstructed after 30 s and after 60 s of stimulation. The experiment shows that the on-line identification is capable of tracking the fatiguing muscle, with a small prediction error. Similar to the simulation phase, the activation dynamics remain almost unchanged, and the muscle fatigue is reflected within the recruitment behavior. It can be observed that the values of I_{thr} and I_{sat} increase during stimulation. This observation coincides with the model of [135] that accounts for this effect with a different fatigability and a different recruitment behavior of slow and fast muscle fibers.

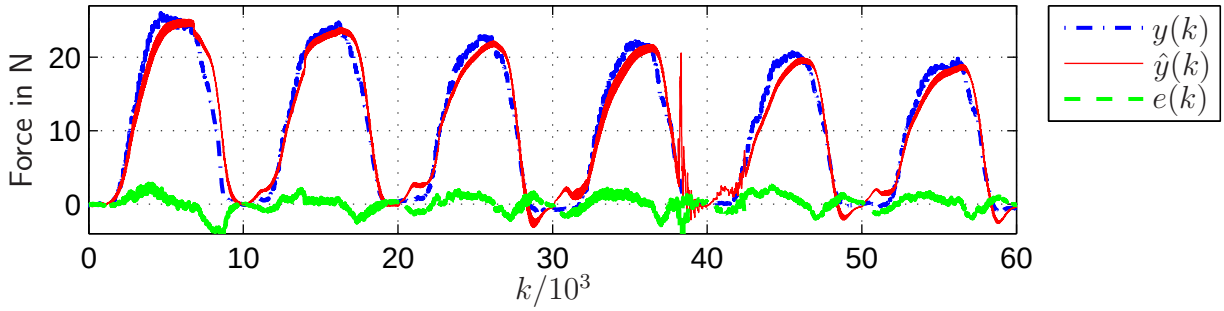

Fig. 5.6: Plant output $y(k)$, its estimate $\hat{y}(k)$, and output error $e(k)$ during parameter adaptation with experimental data.

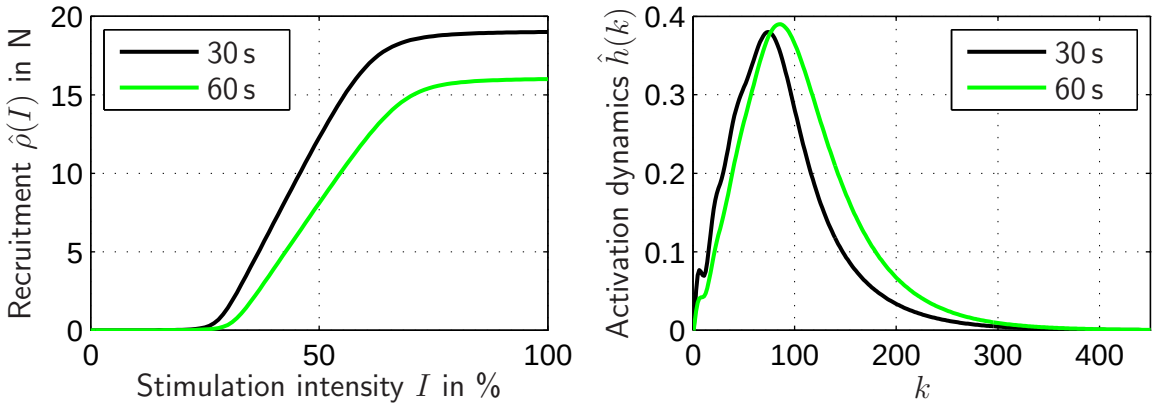

Fig. 5.7: Model reconstruction from the identified parameters after 30 s and after 60 s of stimulation.

5.2.3 Discussion

Spasticity Quantification

As already discussed in Section 4.3.6, the identified nonlinearities $\hat{N}_1(\alpha)$ and $\hat{N}_2(\dot{\alpha})$ (Fig. 5.1) differ from the reference measurements (Fig. 5.2). It is assumed that these variations are due to antidromic blocking and an increased Golgi tendon reflex. However, the characteristic numbers obtained from the before-after comparisons show similar tendencies of estimated and reference values. Among all the patients that could be identified, both methods conform to whether the spasticity has decreased or increased. Therefore, it can be concluded that spasticity quantification during therapeutic muscle stimulation based on system identification is possible. Patient RG showed a decrease of the tonic component whereas the phasic component increased. This effect is often observed after conditional *RPMS*.

It is important to note that the estimated nonlinearities $\hat{N}_2(\dot{\alpha})$ obtained from experiments with spastic patients qualitatively differ from those obtained from healthy subjects

(compare Fig. 4.13 with Fig. 5.1). The curves of spastic patients show positive torque values for positive, as well as for negative angular velocities. It is likely that this characteristic is due to the spastic flexor activity.

The proposed spasticity quantification represents an automated method that can be applied without using additional measurement devices. Since the underlying parameter identification can be applied on-line, a time-continuous spasticity monitoring during therapeutic stimulation can be implemented. However, the patient study revealed that there are patients whose spasticity level is too high to induce a significant movement with *RPMS*. The proposed method cannot be applied to such patients. For the further development of the spasticity quantification during stimulation, the direct influence of the *RPMS* on the joint stiffness (antidromic blocking, e.g.) has to be investigated. Moreover, it would be advantageous to map the torque-angle curves obtained from the system identification into a scheme such as the modified Ashworth scale that is easy to interpret, and familiar to neurologist and physiotherapists. Both problems can be attacked only by means of patient studies with a large number of participants which is beyond the scope of this thesis.

Identification of Muscle Fatigue

The macroscopic force generation model is capable of approximating the physiological model proposed in [135] that takes into account fatiguing and recovery processes and the on-line identification is capable of tracking the simulated as well as the real muscle fatigue. Thus, it can be concluded that system identification based quantification of muscle fatigue during therapy is possible.

Observing fatigue during therapy is important in order to avoid excessive strain. The proposed method yields time varying absolute recruitment curves from which the force generation ability can be inferred. In order to assess the muscle fatigue of the respective patient such that the therapy is stopped before overexertion occurs, the recruitment curve has to be mapped into a meaningful fatigue-parameter. Also for this purpose, a large data basis is required which can be obtained from studies with a large number of participants only.

5.3 Position Controlled Movement Induction

A position controlled *RPMS*-induced extension and flexion of the MCP-joint of the index finger was implemented with dual *RPMS* (see Fig. 5.8). The plant input is given with the magnetic pulses u_{ex} and u_{fl} that act upon the EIP and the FDS/FDP, respectively. The MCP-joint angle α is defined as plant output y.

In the following, first a simplified plant will be formulated. Subsequently, a controller design will be proposed, and experimental results will be presented.

5.3.1 Simplified Plant

A block diagram of the plant is depicted in Fig. 5.9. Compared to the plant that has been considered for the nonisometric identification (Fig. 4.14), the force generation has been

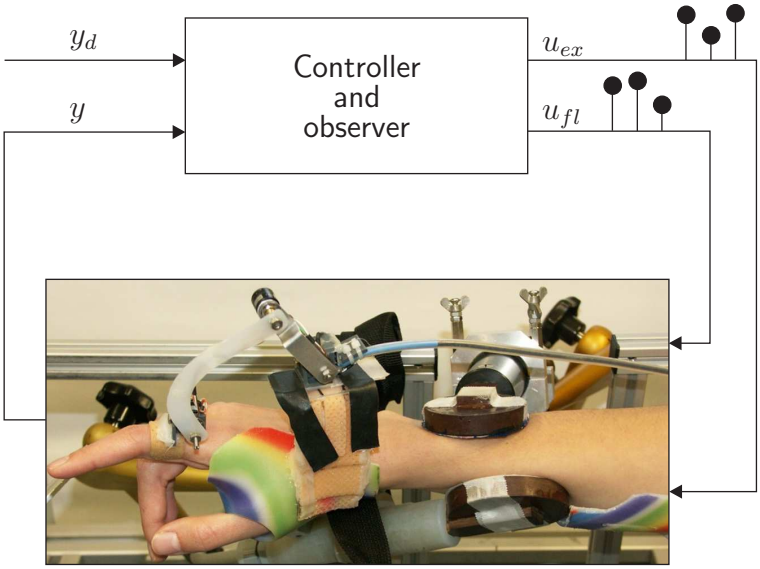

Fig. 5.8: Schematic of the position controlled movement induction with dual *RPMS*.

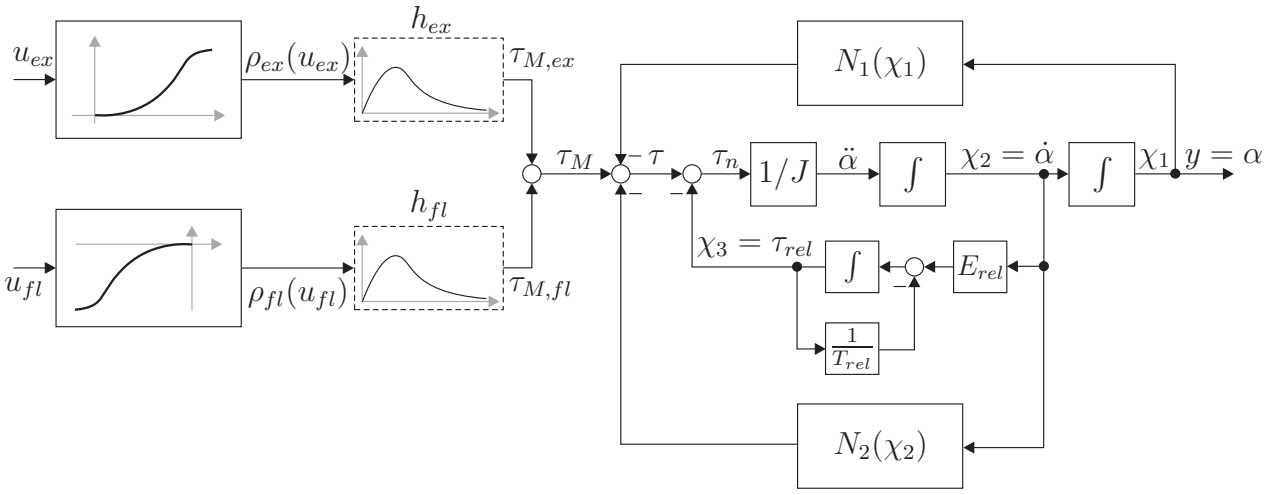

Fig. 5.9: Block diagram of the plant "*RPMS*-induced index finger extension and flexion" with dual *RPMS*.

extended by the recruitment $\rho_{fl}(u)$ and the activation dynamics h_{fl} of the flexor muscles FDS/FDP. The muscular driving torque τ_M, as well as the plant output $y = \alpha$ conform with the coordinate systems of Figs. 3.10 and 3.20 with $\tau_M = \tau_2$ and $\alpha = \alpha_2$. The flexor torque $\tau_{M,fl}$ counteracts the extensor torque $\tau_{M,ex}$ and therefore, the respective stimulators will never be active at the same time. This is accounted for by defining the input spaces as $u_{ex} := [0\,\% \ldots 100\,\%]$ and $u_{fl} := [0\,\% \ldots -100\,\%]$ and with a negatively defined absolute recruitment $\rho_{fl}(u_{fl})$ as indicated in Fig. 5.9.

During repetitive stimulation with $f_{rep} = 20\,\mathrm{Hz}$, the relation between $\rho(u)$ and τ_M is dominated by the dynamics of the temporal summation. As explained in Section 3.4.4, these dynamics can be approximated by a PT_1-system with an average time constant

$\overline{\overline{T}}_{e,opt} = 128,9\,\text{ms}$. Thus, the step response shows a settling time of approx. 0.45 s (compare to Fig. 3.17). This can be considered as fast compared to the dynamics of the desired trajectories y_d during therapy. Therefore, the activation dynamics h_{ex} and h_{fl} will be neglected for the following controller design. For sake of a simpler notation, the recruitment functions will be summarized as

$$\rho(u) = \begin{cases} \rho_{ex}(u) & \text{for} \quad u \geq 0 \\ \rho_{fl}(u) & \text{for} \quad u < 0 \end{cases} \quad . \tag{5.7}$$

Thus, the state space description of the simplified plant is given as

$$\begin{aligned} \dot{\underline{\chi}} &= \underbrace{\begin{bmatrix} 0 & 1 & 0 \\ 0 & 0 & -1/J \\ 0 & E_{rel} & -1/T_{rel} \end{bmatrix}}_{\underline{A}_p} \underline{\chi} + \underbrace{\begin{bmatrix} 0 \\ 1/J \\ 0 \end{bmatrix}}_{\underline{b}_p} (\rho(u) - N_1(\chi_1) - N_2(\chi_2)) \quad , \\ y &= \underbrace{[1\,0\,0]}_{\underline{c}_p^T} \underline{\chi} \quad , \end{aligned} \tag{5.8}$$

with the state $\underline{\chi}^T = [\alpha\, \dot{\alpha}\, \tau_{rel}]$.

5.3.2 Controller Design

Without formally applying the well-known method of exact input-output-linearization [74], the plant (5.8) can be linearized by introducing the nonlinear transformation

$$u = \rho^{-1}(\nu + N_1(\chi_1) + N_2(\chi_2)) \tag{5.9}$$

with the new virtual input ν. In the context of robot control, this method is known as "computed torque" (see [153], e.g.). The computed torque controller is depicted in Fig. 5.10 (a). Inserting the transformation (5.9) into (5.8) yields the linearized plant

$$\begin{aligned} \dot{\underline{\chi}} &= \underline{A}_p \underline{\chi} + \underline{b}_p \nu \\ y &= \underline{c}_p^T \underline{\chi} \quad . \end{aligned} \tag{5.10}$$

It can easily be shown that system (5.10) is controllable and observable. Therefore, a state feedback controller with an additional integral control loop to eliminate the stationary control error is proposed (Fig. 5.10 (b) and (c)). Following the standard pole placement procedure (see [125], e.g.), the system matrix $\underline{A}_c$ of the controlled system is given as

$$\underline{A}_c = \left[\begin{array}{c|c} \underline{A}_p - \underline{b}_p\, \underline{\kappa}^T & \underline{b}_p \kappa_I \\ \hline -\underline{c}_p^T & 0 \end{array}\right] \tag{5.11}$$

and the characteristic polynomial of the controlled system can be calculated as

$$P(s) = \det(s\underline{I} - \underline{A}_c) \quad . \tag{5.12}$$

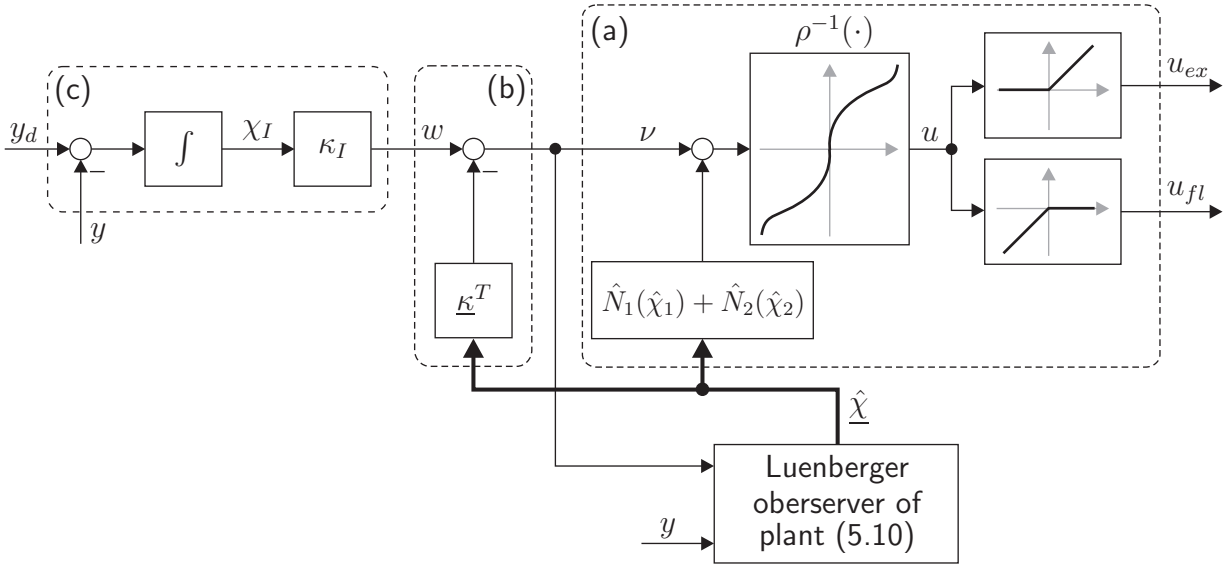

Fig. 5.10: Position controller: (a) Model based linearization by means of a computed-torque controller (b) State feedback controller (c) Integral controller cascade.

The poles of the controlled system are placed according to a forth order standard transfer function with optimal Integrated Time Multiplied Absolute Error (ITAE see [46], e.g.). The ITAE-criterion yields fast settling with a small overshoot, and is well-approved for many control applications. The desired fourth order polynomial is given as

$$P_d(s) = s^4 + 2.1\omega_0 s^3 + 3.4\omega_0^2 s^2 + 2.7\omega_0^3 s + \omega_0^4 \ , \tag{5.13}$$

whereas the settling time is given as $T_{set} \approx 5/\omega_0$. The controller parameters $\underline{\kappa}$ and κ_I can be determined by comparing the coefficients of (5.12) and (5.13). A Luenberger observer [125] for the linearized system (5.8) is implemented in order to estimate the system state $\underline{\chi}$. The observer dynamics are designed according to the ITAE-criterion as well. Its dynamic behavior is chosen to be twice as fast as that of the controlled plant by choosing $\omega_{0,obs} = 2\omega_0$.

5.3.3 Experimental Results

The position controller was tested with healthy subjects. As depicted in Fig. 5.8, the lower arm was fixated in an orthosis and a goniometer was attached to the index finger. The extensor coil was placed above the innervation zone of the EIP and the flexor coil was placed above the innervation zone of the FDS/FDP.

The controller of Section 5.3.2 requires estimates of the functions $N_1(\chi_1)$, $N_2(\chi_2)$, $\rho_{ex}(u_{ex})$ and $\rho_{fl}(u_{fl})$. Therefore, a system identification procedure was carried out that immediately preceded the control experiments. The EIP-recruitment $\rho_{ex}(u_{ex})$, $N_1(\chi_1)$ and $N_2(\chi_2)$ were identified with the nonisometric procedure explained in Section 4.3. The FDS/FDS-recruitment $\rho_{fl}(u_{fl})$ was identified under isometric conditions as explained in Section 4.2.

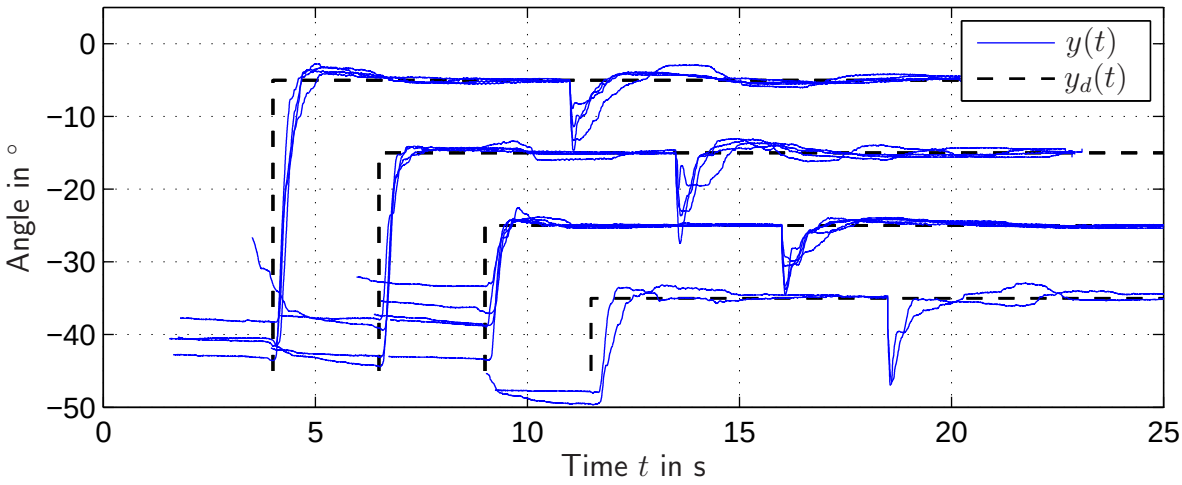

Fig. 5.11: Step responses at t_0 of the position controlled system with different step sizes: At $t = t_0 + 7$s the system was disturbed by hanging a 20 g load at the finger tip.

The controller performance was evaluated with two different experiments. The dynamics and the disturbance reaction of the controlled system (Fig. 5.11) was tested with steps of the desired output $y_d(t)$. When the set point was reached, a 20 g load was hung at the finger tip in order to disturb the system. The reference tracking behavior (Fig. 5.12) was tested by letting the controlled system follow ramp trajectories of $y_d(t)$. The characteristic frequency ω_0 of the desired polynomial (5.13) was chosen heuristically. In both experiments, the best results were obtained by choosing $\omega_0 = 10\,\mathrm{s}^{-1}$.

5.3.4 Discussion

The plant is simplified by neglecting the activation dynamics h_{ex} and h_{fl} as well as the delay $T_d = T_{d,hw} + T_{d,ph} \approx 15$ ms (see Section 3.4.1 and 3.4.2). A continuous time controller design is applied to the simplified plant. It can be shown by means of simulations that a controller design for the exact plant only yields a minimal improvement of the controller performance [212]. Furthermore, the higher order of the exact description requires a higher order state observer for the real implementation. Increasing the order also increases the sensitivity to noise that it will probably undo the small performance improvement.

The dynamics of the system are limited by the dynamics of the temporal summation and the delay T_d which result in an open-loop step response with a settling time of approx. 0.45 s (compare to Fig. 3.17). This limitation is considered by choosing the characteristic frequency to $\omega_0 = 10\,\mathrm{s}^{-1}$ which leads to a settling time of $T_{sys} \approx 5/\omega_0 = 0.5\,\mathrm{s}$. The experimental results of Fig. 5.11 approximately confirm this settling time. Faster dynamics could not be implemented due to the limited plant input. Thus, the dynamic performance or the proposed controller is close the practical limit.

Clearly, the development of a discrete time controller design for the exact plant that considers the periodic impulse characteristic of the plant input can be expected to yield slight improvements over the proposed methods, at least in theory. However, considering

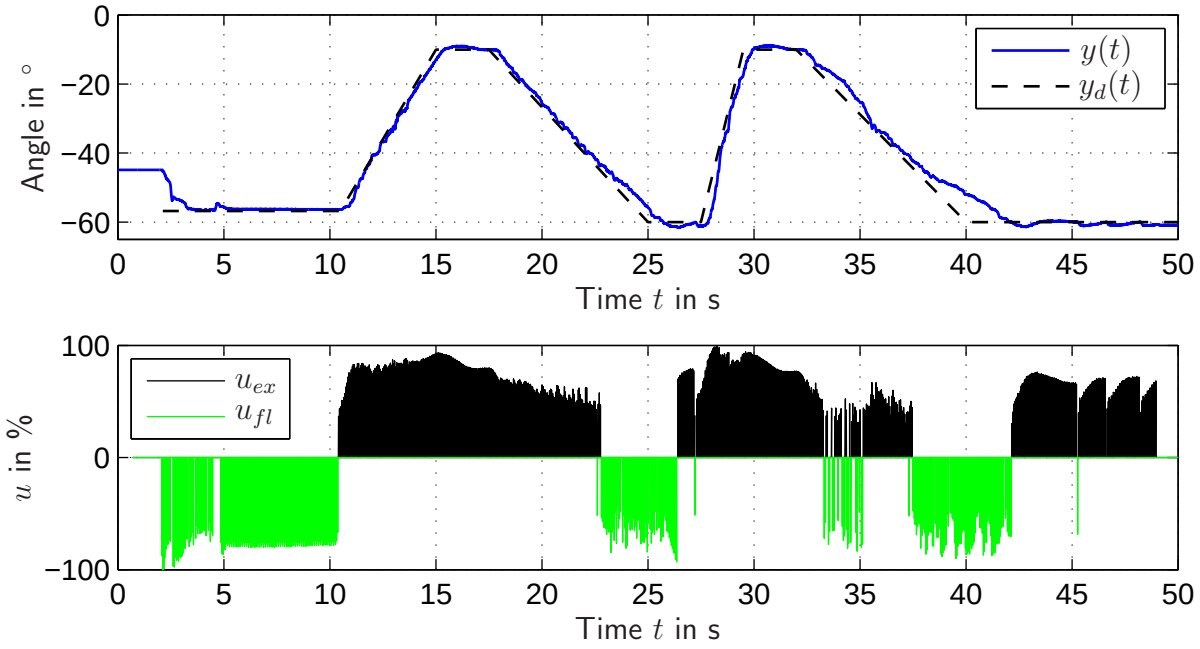

Fig. 5.12: Exemplary result of the trajectory tracking experiment: The upper graph depicts the trajectories of the desired and the actual angle, and in the lower graph the controller output is illustrated.

the slow movements during rehabilitation, the introduced method is reasonable. The results from the step response experiment as well as from the ramp-tracking show a small control error. Thus, it can be concluded that the performance of the proposed control algorithm is adequate for the therapeutic movement induction.

A system identification procedure was conducted preceding the actual position control experiments. Although, the experiment becomes more time consuming, the identification of the flexor recruitment was carried out under isometric conditions. Nonisometric identification of the flexor recruitment did not yield satisfactory results. This is due to two reasons: Firstly, the induced flexion movement is small ($|\Delta\alpha| \leq 20\,°$) and thus, the input of the identification algorithm has a small range. Secondly, the MCP-joint is flexed only indirectly as explained in Sections 3.2.2 and 3.3.2. This results in a delayed onset of the flexion movement, whereas the delay depends on the current geometrical configuration. This effect is not considered in the underlying model, since it is almost impossible to predict.

5.4 EMG-Driven Position Control

The position controller depicted in Fig 5.8 is enhanced with an adaptive trajectory generation driven by the voluntary activity of the stimulated muscle (see Fig. 5.13 a).

For the experiments of the EMG-driven position control, only the EIP is considered, and the controller of Fig 5.10 is reduced to the control output u_{ex}. As a consequence,

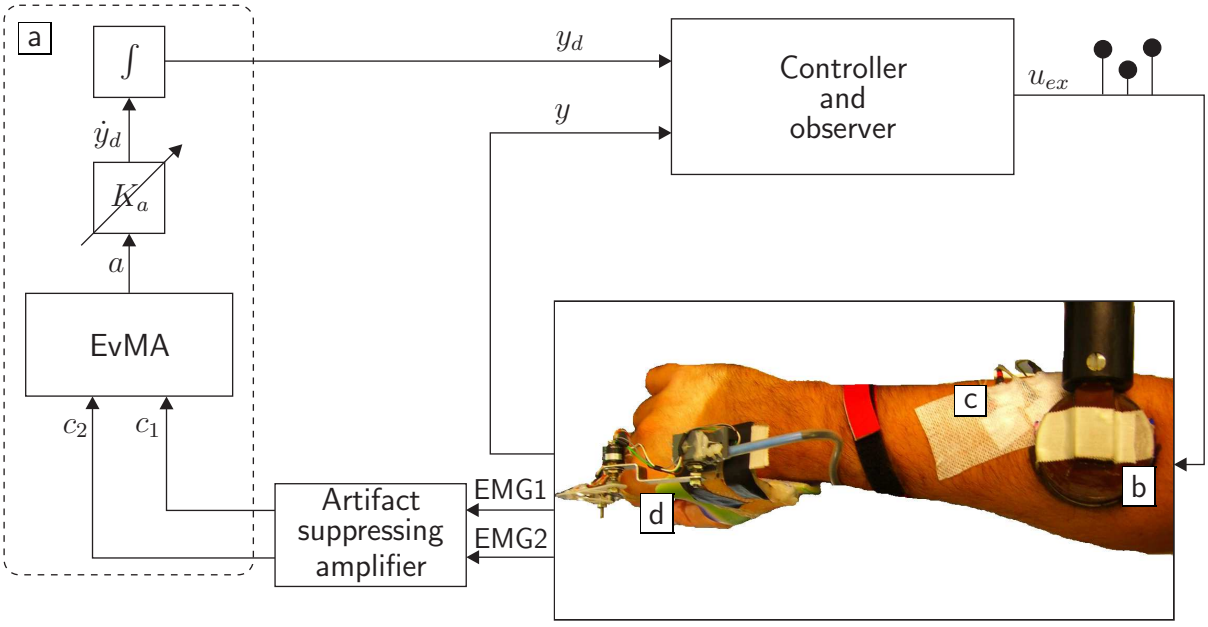

Fig. 5.13: Schematic of the EMG-driven position controlled index finger extension: (a) Adaptive trajectory generation (b) Extensor Coil (c) EMG-electrodes (d) Goniometer.

the index finger can only be extended from its equilibrium position and not flexed. This reduces the hardware complexity during experiments, but does not limit the generality of the introduced approach. Compared to the position control with predefined trajectory (Fig. 5.10), the experimental setup is enhanced by surface EMG-electrodes (Fig. 5.13 c) that are attached to the forearm above the innervation zone of the EIP. A short introduction into the electrophysiology of EMG can be found in Appendix B.2.

As it will be explained in Section 5.4.2, the muscular activity at the EIP is detected with a two-channel measurement. The raw EMG-signals are preprocessed by a self-built artifact suppressing EMG-amplifier [6; 187]. The amplifier outputs c_1 and c_2 are fed into the block EvMA (estimation of voluntary muscle activity). The EvMA represents a signal processing cascade that will be explained in Section 5.4.2. The output a of the EvMA is a measure for the voluntary muscle activity. This knowledge about the patient's effort is used to implement a patient cooperative therapy mode as it will be explained in Section 5.4.3.

Experiments have been carried out with healthy subjects. The results and the capability of the proposed method with respect to an application in a rehabilitation environment will be evaluated in Section 5.4.4.

The EMG-signals are sampled with a sampling period of $T_s = 1\,\text{ms}$ and processed in discrete time. Therefore, discrete time formulation with $k = t/T_s$ will be used throughout this section.

5.4.1 Stimulation Artifacts and Signal Preprocessing

In the literature pertaining EMG-measurements at FES-stimulated muscles [148; 155; 156], the EMG-signal is described as a superposition of three components:

Stimulation Artifacts that are evoked by the electromagnetic fields during stimulation.

M-Waves representing muscular activity due to the synchronous activation of motor units.

Voluntary activity caused by the patient's desire for muscular activity. Usually, the voluntary activity represents the wanted signal. It can be characterized as Gaussian band limited colored noise with time varying variance [24].

In order to reduce the stimulation artifacts, a a self-built artifact suppressing EMG-amplifier [6] is used. Stimulation artifacts can be subdivided in direct and indirect artifacts: The direct artifacts [6] caused by the magnetic pulses are suppressed by either short circuiting the EMG-electrodes or by connecting the EMG-electrodes to the constant voltage during a period S_1 (see Fig. 5.14) in which the pulse is fired. The constant voltage is set according to the last sensed voltage at the surface electrodes before the pulse. The first method causes indirect artifacts due to repolarization processes of the "skin-electrode-capacitor" [6]. These effects can be reduced by the second method which was used for the experiments in this chapter. In order to further reduce the effects of the indirect artifacts, the amplifier input is connected to ground during a period S_2 (see Fig. 5.14). Details about the amplifier functionality and the origin of the artifacts can be found in [6; 187].

In order to illustrate the characteristics of the artifacts, single pulses were applied to the EIP while a single channel EMG-signal $c(k)$ and the isometric force $F_s(k)$ (see setup depicted in Fig. 3.14) were recorded (Fig. 5.14). The pulses have been applied with stimulation intensities $I = 0 \ldots 100\,\%$. From the signals $c(k)$ in Fig. 5.14 an artifact pattern before S_2 and another right after S_2 can be observed. During S_2, no wanted signal can be extracted since the signal pathway is opened. The former artifact is ascribed to leakage currents of the stimulation device during the charging cycle that precedes the actual pulse. The latter could be either due to leakage currents, or due to the repolarization of the skin-electrode-capacitor. Both artifacts interfere with the EMG-signal of voluntary contraction and have to be suppressed with further signal processing. Furthermore, the experiment reveals that the artifacts are independent of the simulation intensity. The force recordings in the right graph of Fig. 5.14 indicate that the intensities $I = 0 \ldots 20\,\%$ are at subthreshold level, i.e., no motor units are activated. However, the artifacts of subthreshold stimulation do not differ from the others. From these measurements, it can be concluded, that an m-wave as observed in [148; 155; 156] is not part of the detected signal since no m-wave can be elicited with subthreshold stimulation.

5.4.2 Signal Processing

Fig. 5.16 yields an overview of the proposed signal processing cascade "EvMA". It combines the established EMG-processing methods of spatial decorrelation [71] and signal whitening [24] with an adaptive artifact filter and a weighted root mean square algorithm. Despite from simple blanking strategies that loose all EMG-information during the blanking period, several artifact removing strategies can be found in literature: Static comb filter [51; 62], high-pass filter [148] and a linear adaptive prediction (LAP-) filter [62; 155]. Since the LAP-filter performs best in removing the *RPMS*-artifacts [210] it is used as adaptive artifact filter for the EvMA-cascade.

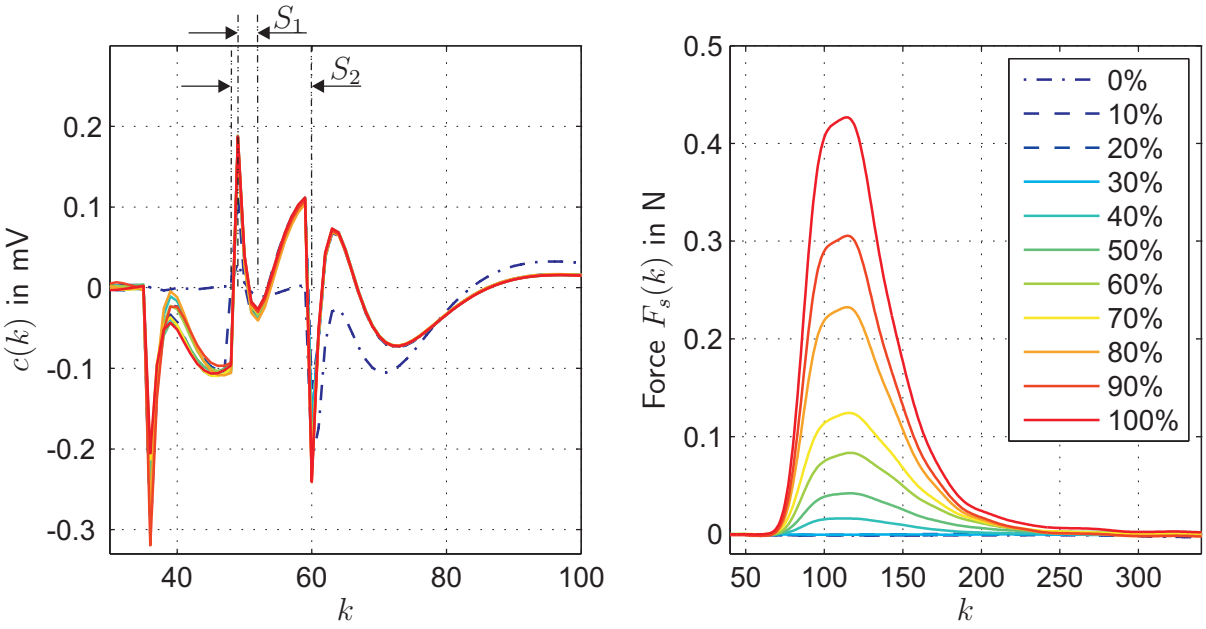

Fig. 5.14: Left: EMG-signals $c(k)$ during single *RPMS*-pulses at the EIP with stimulation intensities $I = 0 \ldots 100\,\%$. The periods S_1 and S_2 are indicated with vertical lines. Right: Corresponding force signals $F_s(k)$ recorded with the setup for isometric measurements (see Fig. 3.14). In both plots, the curves obtained from subthreshold stimulation are indicated with dotted and dashed lines.

In order to reduce random variations in the EMG-amplitude that disturb the mean amplitude of the muscular activity (see Appendix B.2), the EIP-activity is measured with two pairs of electrodes. Improving the detection of muscular activity with multiple site EMG-measurement was proposed and successfully evaluated in [26; 71; 164], e.g.. As depicted in Fig. 5.15, the electrode pairs measure the EIP-activity at different positions and thus the EMG-signals $c_1(k)$ and $c_2(k)$ carry different information. Both signals propagate through the EvMA-cascade in parallel and are averaged in the end. Fig. 5.15 shows an electrode configuration where both channels are aligned along the EIP-muscle fibers. Different configurations were tested whereas the presented yielded best signal quality. The issue of electrode arrangement is discussed in [210].

For sake of a better readability, the signal processing will be introduced for a single channel $c(k)$. Only for the introduction of the spatial decorrelation and the averaging both channels are considered. The individual signal processing blocks are introduced in the following paragraphs.

In order to illustrate the benefits of the particular processing steps, the EvMA is applied to the data set depicted in Fig. 5.17: The EIP of a healthy subject was stimulated under isometric conditions with a constant stimulation intensity of $I = 60\,\%$. The force generated by means of stimulation amounts to approx. 1.7 N. The subject was asked to generate an additional amount of force voluntarily. From the force signal it can be inferred that the subject first generated a constant force, subsequently a force ramp and three short force-periods. As it will be shown, the EvMA-cascade estimates the corresponding voluntary

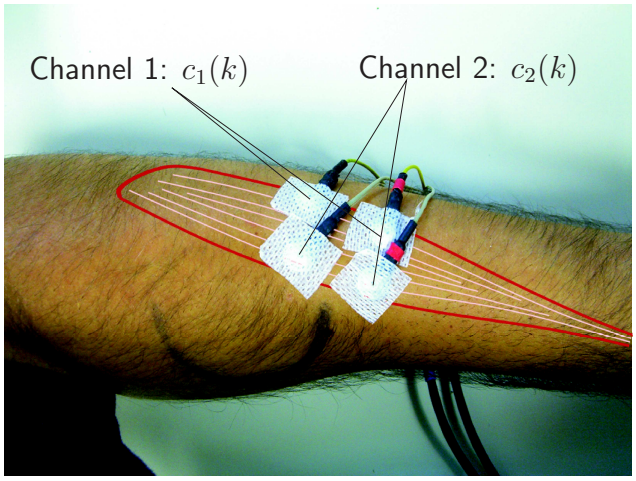

Fig. 5.15: Two channel electrode arrangement above the innervation zone of the EIP.

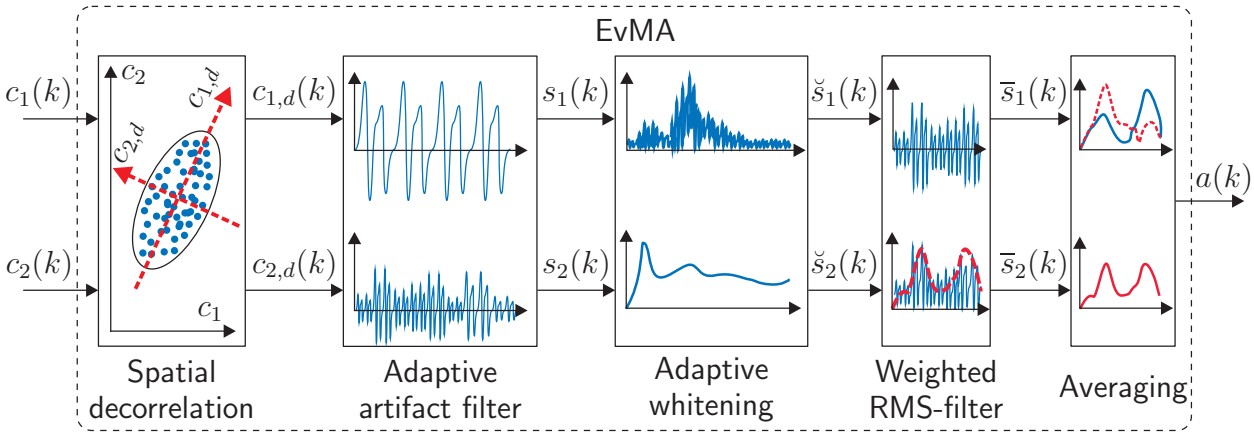

Fig. 5.16: EvMA-cascade: The voluntary muscle activity $a(k)$ is estimated from a two channel EMG-measurement.

muscular activity $a(k)$ that correlates with the voluntary force included in $F_s(k)$ from the signals $c_1(k)$ and $c_2(k)$.

Spatial Decorrelation

It is clear from intuition that simple averaging of the channels $c_1(k)$ and $c_2(k)$ will reduce random signal variations. However, in [26; 71; 164], it was shown that a spatial decorrelation of EMG-channels measuring the same muscle prior to computing the average, improves the reduction of signal variations. Each of the electrode pairs covers a certain region of the innervation zone where it is likely that the regions overlap. Thus, $c_1(k)$ and $c_2(k)$ carry information from the intersection as well as from the non-overlapping part of their respective regions. The former information is redundant. The spatial decorrelation aims to equally weight the mutually uncorrelated information from each channel which finally yields an optimal signal after averaging [24].

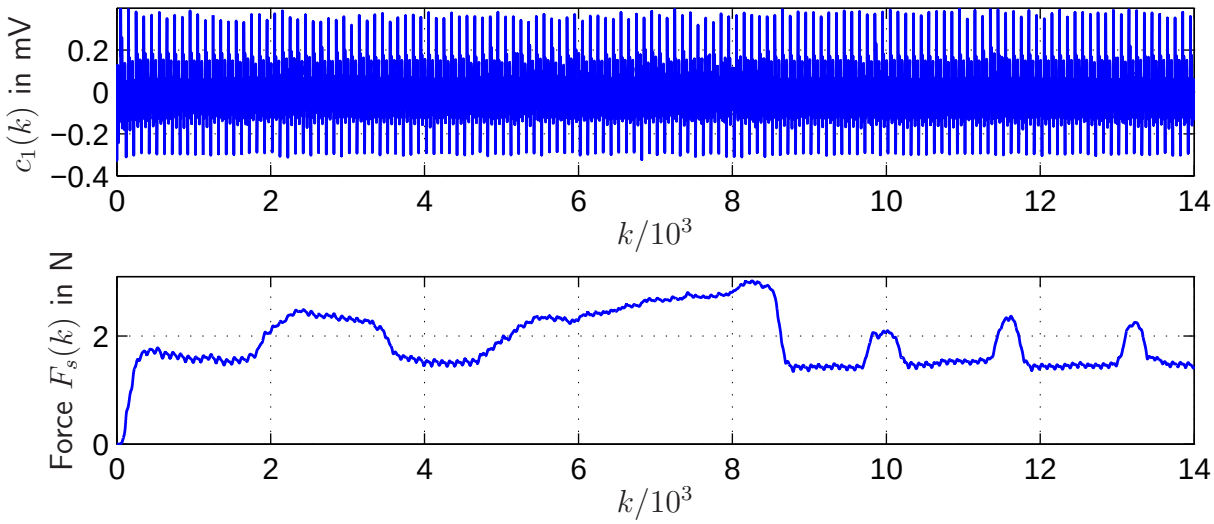

Fig. 5.17: Raw EMG-signal $c_1(k)$ of channel 1 and isometric force $F_s(k)$ during stimulation with constant intensity. The *RPMS*-induced force shows a nearly constant level of approx. 1.7 N. The subject was asked to generate voluntary force that adds to the *RPMS*-induced force. This additional forces occur at approx. 1.9 s-3.8 s, 4.8 s-8.7 s, and at approx. 10 s, 11.5 s and 13.1 s.

As indicated in the first block of Fig. 5.16 the decorrelation can be achieved by simply applying a principle component analysis (PCA) to the data of the channels c_1 and c_2 that yields a coordinate transformation into the new axis $c_{1,d}$ and $c_{2,d}$. According to the standard PCA-procedure (see [43], e.g.), the principle components of a two dimensional data set are obtained as the major and minor axes of the ellipse spanned by the data set (see first block in Fig. 5.16). The effect of the coordinate transformation is simply to rotate the coordinate system so that an uncorrelated data set $c_{1,d}$ and $c_{2,d}$ is obtained. Following the derivation in [71], where the coordinate transformation matrix $\underline{\Xi}$ is calculated using the covariance method, the covariance matrix

$$\underline{\Psi} = \underline{C}^T \underline{C} = \begin{bmatrix} \sigma^2_{c1,c1} & \sigma^2_{c1,c2} \\ \sigma^2_{c2,c1} & \sigma^2_{c2,c2} \end{bmatrix} \tag{5.14}$$

has to be calculated, whereas

$$\underline{C} = \begin{bmatrix} c_1(0) & c_2(0) \\ c_1(1) & c_2(1) \\ \vdots & \vdots \\ c_1(N) & c_2(N) \end{bmatrix} . \tag{5.15}$$

With $\underline{\Psi}$ symmetric, the spectral theorem [9] can be applied and $\underline{\Psi}$ can be written as

$$\underline{\Psi} = \underline{\Gamma \Lambda \Gamma}^T \quad , \tag{5.16}$$

whereas the matrix $\underline{\Gamma}$ summarizes the eigenvectors $\underline{\gamma}_i$ of $\underline{\Psi}$ and the diagonal matrix $\underline{\Lambda}$ contains the respective eigenvalues λ_i. Similar to the standard PCA, in [71] the transformation matrix is calculated as

$$\underline{\Xi} = \begin{bmatrix} \frac{1}{\sqrt{\lambda_1}} & 0 \\ 0 & \frac{1}{\sqrt{\lambda_2}} \end{bmatrix} \underline{\Gamma}^T = \begin{bmatrix} \frac{\gamma_{1,1}}{\sqrt{\lambda_1}} & \frac{\gamma_{1,2}}{\sqrt{\lambda_1}} \\ \frac{\gamma_{2,1}}{\sqrt{\lambda_2}} & \frac{\gamma_{2,2}}{\sqrt{\lambda_2}} \end{bmatrix} \tag{5.17}$$

and thus, the EMG-channels can be decorrelated as

$$\underline{c}_d(k) = \underline{\Xi}\,\underline{c}(k), \tag{5.18}$$

with $\underline{c}(k) = [c_1(k)\, c_2(k)]^T$ and with $\underline{c}_d(k) = [c_{1,d}(k)\, c_{2,d}(k)]^T$. Note that in standard PCA, a matrix Γ_N^T that contains the unit eigenvectors with length 1 is used as transformation matrix. The geometric interpretation is that the ellipse in Fig. 5.16 is only rotated and not scaled and thus, the variances of the transformed signals equal the variances of the original signals. The normalization of Eq. (5.17) has been proposed in [71]. It transforms the ellipse into a circle, and thus yields spatially uncorrelated signals $c_{1,d}(k)$ and $c_{2,d}(k)$ with equal variance. This yields further improvements in terms of reduction of random signal variations. More detailed derivations can be found in [26; 71]. For the practical application, the matrix $\underline{C}$ is obtained from calibration measurements that have to be carried out before the actual experiment. Implementational details can be found in [210]. The benefit of the spatial decorrelation can only be seen after smoothing and averaging, and is illustrated in Fig. 5.21: The activity signal $a(k)$ that was obtained when including the spatial decorrelation shows less variations than the signal $a(k)^{ws}$ that has been computed while omitting the spatial decorrelation. When comparing the signals with the force signal of Fig. 5.17, it can be observed that $a(k)$ is stronger correlated to the voluntarily applied force than $a(k)^{ws}$.

Adaptive Artifact Filter

The LAP-filter [62; 155] takes advantage of the periodic nature and the self-similarity of the stimulation artifacts, and the non-periodic and partly random nature of the wanted EMG-signal. The left plot of Fig. 5.18 shows the amplitude spectrum of $c_1(k)$ calculated with a discrete Fourier transform. In the frequency domain, the artifacts that occur with the *RPMS*-repetition $f_{rep} = 20\,\text{Hz}$ are represented with narrow amplitude peaks at $f_k = 20\,\text{Hz}$ and multiples of 20 Hz.

The output of the LAP-filter is calculated as

$$s(k) = c_d(k) - \sum_{j=1}^{M} b_j c_d(k - jk_{rep}) \quad , \tag{5.19}$$

with M filter coefficients b_j and with $k_{rep} = \text{round}(1/(f_{rep}T_s))$. For the adaptation of the filter coefficients b_j signal frames, each of length k_{rep} are considered. Hence, the k_{rep} samples of the signal $c_d(k)$ of the j^{th} frame are summarized as

$$\underline{c}_{d,j} = [c_d(-(j+1)k_{rep}+1)\; c_d(-(j+1)k_{rep})+2 \ldots c_d(-(j+1)k_{rep}+k_{rep}-1)\; c_d(-jk_{rep})]^T \tag{5.20}$$

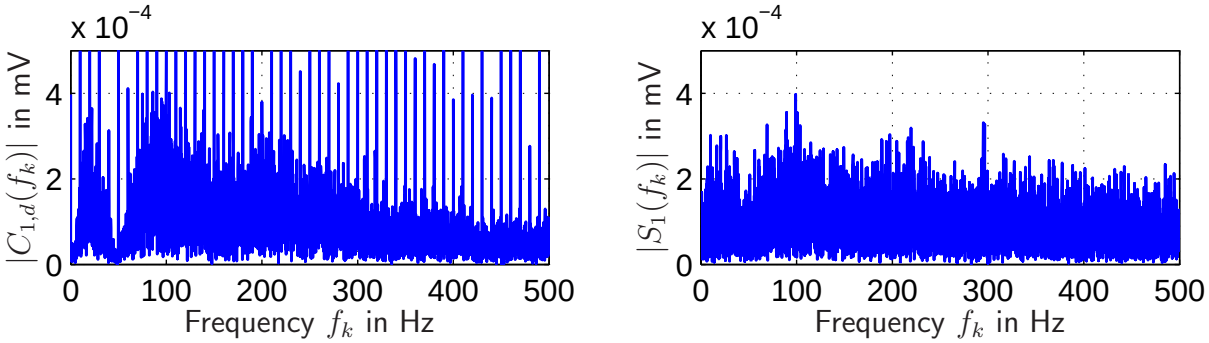

Fig. 5.18: Amplitude spectra of the signals $c_{1,d}(k)$ (left) and $s_1(k)$ (right).

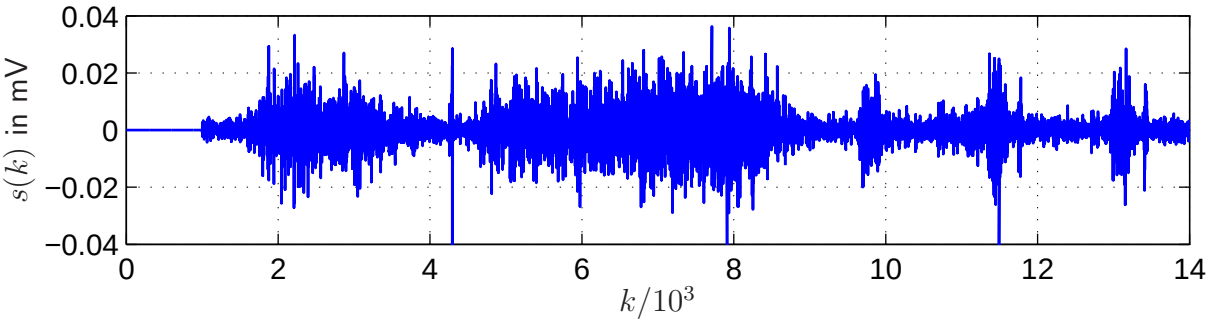

Fig. 5.19: EMG signal $s(k)$ after LAP-filtering.

and the latest output frame $\underline{s}_0$ can be written as

$$\underline{s}_0 = \underline{c}_{d,0} - \sum_{j=1}^{M} b_j \underline{c}_{d,j} \quad \text{with} \quad \underline{s}_0 = [s(-k_{rep}+1) \dots s(0))]^T \quad . \tag{5.21}$$

The optimal filter coefficients $\underline{b}_{opt}$ are found by minimizing the output energy $\underline{s}_0^T \underline{s}_0$ [62]. Thus, the linear quadratic minimum problem

$$\underline{b}_{opt} = \arg\min_{\underline{b}} (\underline{s}_0^T \underline{s}_0) \tag{5.22}$$

has to be solved. Intuitively spoken, the LAP-filter predicts the k_{rep}-periodic parts of the signal by a linear combination of the M frames $\underline{c}_{d,j}$ preceding the current frame $\underline{c}_{d,0}$ and eliminates the artifacts in the current frame $\underline{c}_{d,0}$ to a large extent by subtracting the prediction. Naturally, the LAP-filter causes a signal delay of $k_{rep}T_s = 50\,\text{ms}$. Further derivations and implementation details are presented in [210]. From the amplitude spectrum of the filtered signal $s_1(k)$, depicted in right plot of Fig. 5.18, it can be seen that the periodic peaks have been successfully removed. The time domain representation is depicted in Fig. 5.19. It is obvious that the wanted signal was separated from the artifacts to a large extent.

Adaptive Whitening

The amplitude estimation of EMG-signals can be improved by applying a whitening filter prior to smoothing (see [25; 44; 71], e.g.). Signal whitening has become an established EMG-processing method. One of the most successful approaches has been introduced in [24] as "adaptive whitening filter". It is integrated into the EvMA-cascade. Since the detailed filter design steps can be found in [24], in the following, only the main idea will be shortly described.

The filter cascade of [24] consists of a fixed whitening filter, and an adaptive Wiener filter together with an adaptive gain correction. It is assumed that the EMG-signal $s(k)$ can be modeled as

$$s(k) = a_i n(k) + \iota(k) \quad . \tag{5.23}$$

The signal amplitude a_i modulates a stationary Gaussian colored noise $n(k)$, additionally a stationary additive white background noise $\iota(k)$ is included. The whitening filter $H_{wh}(f_k)$ aims to generate a filtered signal $\tilde{s}(k) = a_i\tilde{n}(k)+\tilde{\iota}(k)$ with a white spectrum noise $\tilde{n}(k)$. It is assumed that the amplitude a_i is wide sense stationary (WSS), i.e. it remains constant over a time period that is considered to produce the amplitude estimate at time i. Moreover, the colored noise $n(k)$ is modeled as output of an LTI-system $H_t(f_k)$ that has a white noise $w(k)$ with unit intensity, i.e. a power spectral density (PSD) of $S_{ww}(f_k) = 1$, as input. By applying calibration measurements with 0 % maximum voluntary contraction (MVC) and with some other predefined value such as 50% MVC, e.g., the PSDs $S_{ss}(f_k)$, $S_{\iota\iota}$ and $S_{nn}(f_k)$ can be estimated. Thus, a filter $H_{wh}(f_k)$ with $|H_{wh}(f_k)| = |H_t^{-1}(f_k)|$ can be designed that whitens the spectrum of $n(k)$. As a result, the EMG-amplitude a_i modulates a noise signal $\tilde{n}(k)$ with a constant PSD and thus, the discretely sampled EMG-signal is orthogonalized [24]. That is, the correlation between successive EMG-samples is removed.

The adaptive Wiener filter $H_{wi}(f_k)$ aims to reduce the additive noise $\tilde{\iota}(k)$. Using the facts that the noise $\tilde{\iota}(k)$ occurs additive and that $S_{\tilde{n}\tilde{n}}(f_k) = 1$, the filter design is straightforward. In [24] it is described as

$$H_{wi}(f_k, a_i) = \frac{a_i^2}{a_i^2 + S_{\tilde{\iota}\tilde{\iota}}(f_k)} \quad . \tag{5.24}$$

Finally, an adaptive gain $d(a_i)$ is multiplied with the output of $H_{wi}(f_k, a_i)$ and thus, the complete adaptive whitening filter cascade can be written as

$$H_{awh}(f_k) = H_{wh}(f_k)H_{wi,a_i}(f_k)d(a_i) \quad . \tag{5.25}$$

The amplitude correction is necessary to maintain the variance of the unfiltered signal $s(k)$ such that $\sigma_s^2 = \sigma_{\breve{s}}^2$. Otherwise, amplitude information in $\breve{s}(k)$ is not consistent with the original EMG-signal. The computation of $d(a_i)$ can be found in [24]. The amplitude a_i is estimated from the signal $s(k)$ using a simple RMS-filter.

The benefit of the adaptive whitening filter can be observed best after signal rectification and smoothing. Therefore, Fig. 5.20 shows the signal $\overline{s}_1(k)$ compared to a signal $\overline{s}_1(k)^{nw}$ which has been obtained by omitting the adaptive whitening. It can be seen that the whitened signal better correlates to the different levels of voluntary force (see Fig. 5.17).

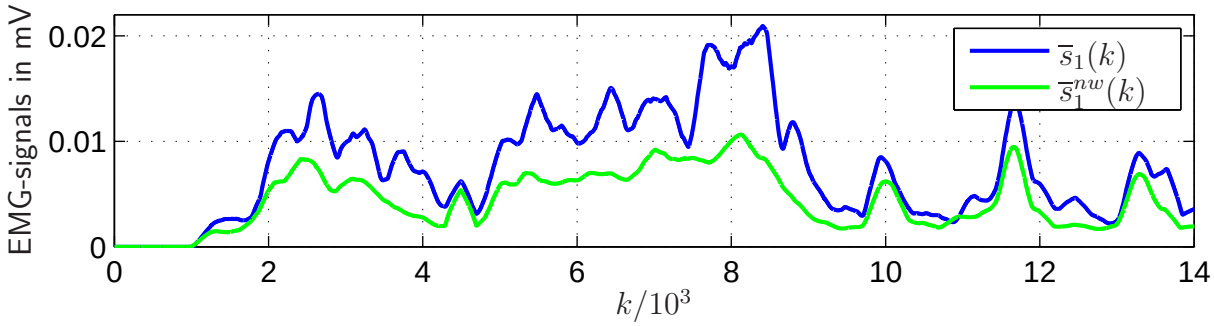

Fig. 5.20: EMG-signal $\overline{s}_1(k)$ compared to a signal $\overline{s}_1^{nw}(k)$ where the adaptive whitening has been omitted.

Weighted Root Mean Square Filter

Moving average (MA-) filters or root mean square (RMS-) processing are well-established methods for EMG-smoothing. Due to the signal squaring, the RMS-method emphasizes fast rises in the EMG-amplitude [50]. Thus, it is well suited for the on-line observation of a time varying EMG-level as is necessary for the EMG-driven position control. In order to further decrease the random variations of the EMG-amplitude, a weighted RMS-filter (wRMS) is developed. First, an RMS-signal

$$\overline{s}_{RMS}(k) = \sqrt{\frac{1}{K_{RMS}} \sum_{j=0}^{K_{RMS}-1} \breve{s}(k-j)^2} \tag{5.26}$$

is calculated, where K_{RMS} represents the length of the considered data window. The weighted smoothing aims to reduce strong deviations from the current average value $\overline{s}_{RMS}(k)$ by calculating

$$\overline{s}_{\upsilon}(k) = \overline{s}_{RMS}(k) + \text{sign}(|\breve{s}(k)| - \overline{s}_{RMS}(k)) W(\breve{s}(k), \overline{s}_{RMS}(k)) \tag{5.27}$$

with the weighting function

$$W(\breve{s}(k), \overline{s}_{RMS}(k)) = (|\breve{s}(k)| - \overline{s}_{RMS}(k))^{\upsilon} \quad . \tag{5.28}$$

Choosing $\upsilon < 1$, results in a signal $\overline{s}_{\upsilon}(k)$ where strong deviations from the average $\overline{s}_{RMS}(k)$ are stronger damped than small deviations. Finally, the weighted signal $\overline{s}_{\upsilon}(k)$ is RMS-filtered according to

$$\overline{s}(k) = \sqrt{\frac{1}{K_{RMS}} \sum_{j=0}^{K_{RMS}-1} \overline{s}_{\upsilon}(k-j)^2} \quad . \tag{5.29}$$

In [210], it is shown that the wRMS-filter yields a superior EMG-smoothing compared to an ordinary RMS-filter with a better correlation to the voluntary force. The wRMS-

Tab. 5.3: Choice of the design parameters of the EvMA-cascade.

Parameter	Value
M	15
υ	0.5
K_{RMS}	200

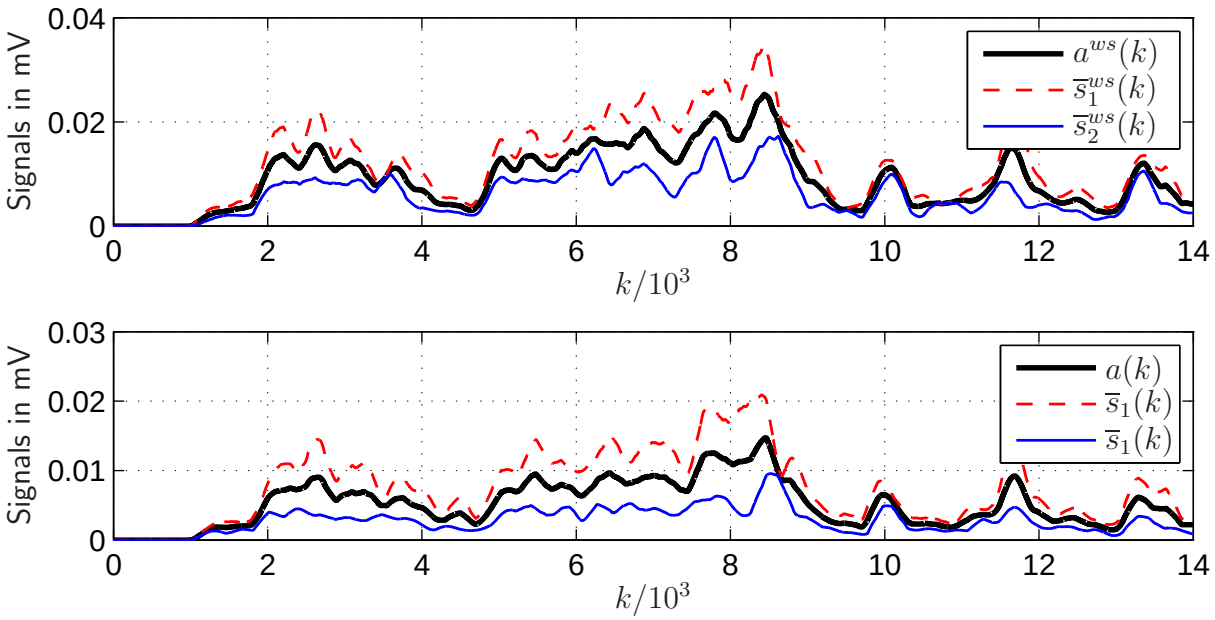

Fig. 5.21: Smoothed signals $\overline{s}_1(k)$ and $\overline{s}_2(k)$ and muscle activation signal $a(k)$: The upper graph shows the result when the spatial decorrelation is omitted. The lower graph depicts the result obtained when the raw signals propagate through the entire EvMA-cascade.

filtered signals $\overline{s}_1(k)$ and $\overline{s}_2(k)$ of the example in Fig. 5.17 are depicted in the lower graph of Fig. 5.21.

Averaging

The EMG-amplitude is calculated by simply averaging both channels according to

$$a(k) = \frac{1}{2}(\overline{s}_1(k) + \overline{s}_2(k)) \quad . \tag{5.30}$$

The output of the EvMA-cascade produced with the example of Fig. 5.17 is depicted in the lower plot of Fig. 5.21. The design parameters were chosen heuristically and are summarized in Tab. 5.3.

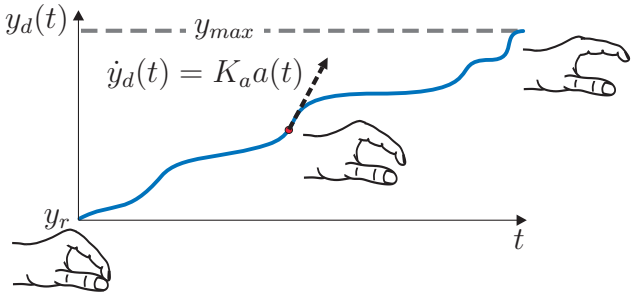

Fig. 5.22: Adaptive trajectory generation: The sketch shows a possible desired trajectory $y_d(t)$. The desired angular velocity is set to $\dot{y}_d(t) = K_a a(t)$.

5.4.3 Patient Cooperative Therapy Mode

In contrast to the position controlled movement induction with predefined trajectory, the patient cooperative therapy adaptively generates the desired trajectory depending on the patient's effort. As depicted in the block diagram of Fig. 5.13, the desired MCP-joint angle y_d is calculated as

$$y_d(t) = K_a \int a(t)\, dt \quad . \tag{5.31}$$

I.e., the desired angular velocity $\dot{y}_d$ is proportional to the voluntary activity a. Thus, a "servo steering" for the MCP-joint is implemented that takes into account the patient's effort: If the patient shows zero voluntary activity, the index finger will not move but if she/he shows a detectable amount of voluntary activity, the intended movement is supported by the *RPMS*-induced joint torque. The amount of *RPMS*-support can be adapted to the patient's needs with the gain K_a. This strategy aims to motivate the patient to actively participate during rehabilitation.

In Fig. 5.22, a trajectory generation is proposed that starts at the resting position y_r. The patient has to reach a maximum extension y_{max} by generating voluntary muscle contraction. The movement is supported by *RPMS*. When the maximum y_{max} is reached, the algorithm is stopped, so that the finger returns into its equilibrium position.

5.4.4 Experiment and Results

Experiments were carried out with two healthy subjects. The experimental setup is depicted in Fig. 5.13. Before the experiment is started, calibration measurements for the EvMA and a nonisometric system identification of the controller have to be carried out. The first calibration measurement is done with 0 % MVC in order to measure the background noise $\nu(k)$. Secondly, an EMG-measurement at approx. 50 % MVC and thirdly, an increasing contraction from 0 %-100 % are recorded. The latter measurements are needed to estimate the PSDs of $n(k)$ and $s(k)$ (comp. to Eq. 5.23), and to calculate the decorrelation matrix $\underline{\Xi}$.

During the experiments, K_a was chosen heuristically to 150°/mVs. Due to background noise and unfiltered artifacts, the activity signal $a(t)$ is always slightly greater than zero

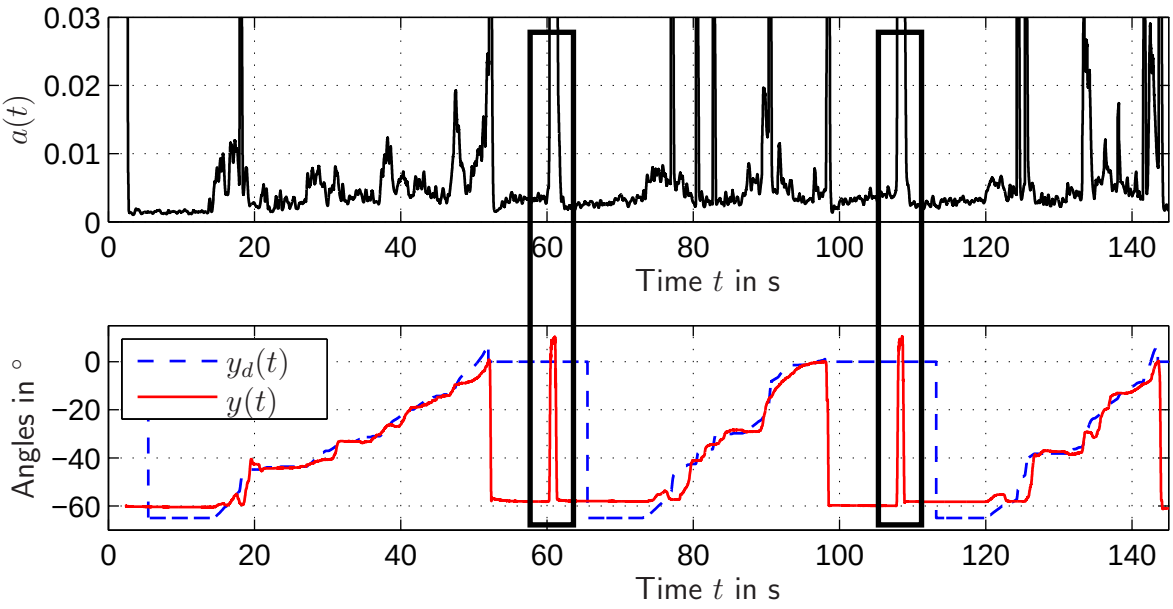

Fig. 5.23: Experimental result of the EMG-driven position control: The subject was asked to repeat the sequence illustrated in Fig. 5.22 three times. During this experiment, the algorithm was restarted after every sequence by a myoelectric signal generated with a full finger extension (rectangles at $t \approx 60\,\mathrm{s}$ and $t \approx 107\,\mathrm{s}$). The upper graph shows the subject's voluntary activity a(t).

even if the subject is passive. Therefore, a threshold value $a_{thr} = 0.005\,\mathrm{mV}$ was implemented that had to be surpassed in order to generate a desired velocity of $\dot{y}_d > 0$.

The subjects were asked to activate their EIP so weakly that hardly any motion was caused. The EIP-activation was detected by the EvMA and the trajectory $y_d(t)$ was generated according to Eq. 5.31. An exemplary result is depicted in Fig. 5.23. In this example, the subject repeated the extension sequence three times. The maximum angle y_{max} was set at $y_{max} = 0\,°$. A sequence was stopped when the subject reached y_{max}. A new sequence was started with a myoelectric trigger signal. The graphs clearly show that the angular velocity correlates with the voluntary activity. At $t = 20\,\mathrm{s}$, e.g., the finger is held at constant position since the activity $a(t)$ is below the threshold a_{thr}, whereas a high velocity occurs at $t = 40\,\mathrm{s}$. Both subjects reported that the implemented algorithm indeed feels like a servo steering that facilitates the index finger extension.

In order to evaluate the applicability of our setting to stroke patients, the minimum amount of detectable voluntary joint torque τ_M was experimentally determined as $\tau_{M,min} = 0.88\,\mathrm{Ncm}$. Using the Fingertester (see Appendix C), the zero degree voluntary contraction ZVDC torque which is in average needed to perform a zero degree extension, was determined to $\tau_{M,ZDVC} = 4.88\,\mathrm{Ncm}$. Therefore, the minimum amount of the detectable joint torque can be expressed as

$$\frac{\tau_{M,min}}{\tau_{M,ZDVC}} = 18\,\% \quad . \tag{5.32}$$

Hence, the patient has to be able to generate less than one fifth of the amount of force that is necessary for a zero degree extension. Considering that the ZDVC is far below 100 %MVC, 18 %ZDVC is a small amount of force and it can be expected that many patients meet this technical requirement.

5.4.5 Discussion

With the EMG-driven position control, a method is introduced that facilitates the implementation of a patient cooperative therapy mode with *RPMS*. Within the proposed approach, the EvMA-cascade represents the key issue. It is able to separate the wanted signal from the stimulation artifacts and to produce an activation signal that correlates with the voluntary muscle activation. Due to the windowed signal processing of the LAP-filter and due to the RMS-smoothing, the information in the activation signal $a(k)$ is delayed. The total delay can be adjusted by the choice of window length K_{RMS} of the RMS-filter. The heuristic choice of $K_{RMS} = 200$ yields a practical trade-off between delay and smoothing: It results in a total delay of approx. 250 ms. Since none of the participants reported a distracting effect, the delay of 250 ms can be considered as irrelevant for the desired application.

The artifacts depicted in Fig. 5.14 are specific to our stimulator and to our artifact suppressing EMG-amplifier. However, artifacts caused by other hardware configurations will be periodic, as well. As long as the artifacts show a self-similarity, it can be expected that the LAP-filter will perform equally well with other hardware, too.

A fundamentally different idea for the force support of patient intended movement has been presented in [137] with the method "patient driven motion reinforcement" (PDMR). The PDMR estimates the driving joint torque necessary to perform the current movement based on a model of the equations of motion. The obtained torque estimate is commanded as feed forward control to the plant. For the PDMR, no EMG-measurement is necessary. However, the patient has to be able to initiate a detectable motion in order to initiate the algorithm. The proposed EMG-based method can detect muscle contraction that does not suffice to initiate any motion. This is particularly important for spastic patients where the spastic joint torque counteracts the extension and thus considerable amount of force is necessary to move the index finger.

The experiments with healthy subjects showed that a detection of a relatively small amount of voluntary contraction can be detected at the stimulated muscle. Therefore, it can be expected that patients with a small amount of voluntary contraction will be able to use the proposed approach as rehabilitative therapy.

5.5 Summary and Conclusions

In this chapter, rehabilitation engineering solutions were presented that have the capability to improve the motor rehabilitation with *RPMS*.

First, a quantification of the patient parameters "spasticity level" and "muscle fatigue" was introduced. The spasticity quantification was tested in a pilot study with patients and evaluated by means of reference measurements. The results showed that the spasticity

data obtained from the system identification coincides with the reference measurements by trend. I.e., both methods agreed on whether the spasticity increased or decreased. It can therefore be concluded that system identification based spasticity quantification during therapy is possible. However, the absolute quantification results differ from the biomechanical reference measurements. As discussed in Section 5.2.3, this is possibly due to antidromic blocking and an increased Golgi tendon reflex during *RPMS*. Thus, a spasticity scale that applies during muscle stimulation has to be developed, in order to establish the proposed method. Similarly, information regarding tolerable amounts of muscle fatigue has to be gathered in order to extract meaningful conclusions from the identified fatigue parameters.

Secondly, a position controlled extension and flexion of the MCP-joint with dual *RPMS* was presented. The controller was applied to six healthy subjects and the performance in terms of tracking accuracy and disturbance compensation was shown to be absolutely sufficient for the desired application. The controller design comprises a model-based linearization similar to computed torque and a state feedback controller with an additional integral control loop. A task oriented *RPMS*-therapy could be further optimized by inducing a coordinated movement of index finger and thumb to perform a precision grip motion. The presented identification method and the control algorithm can be applied to the thumb, as well. The hardware has to be extended by two more stimulators and coils whereas one coil stimulates the m. abductor pollicis longus/brevis and the m. extensor pollicis longus (thumb abduction, i.e. opening of the precision grip) and the other coil stimulates the m. flexor pollicis longus (thumb adduction, i.e. closing the precision grip). As a simplification, the EIP and the thumb abductor muscles can be recruited with a single coil.

In order to evaluate the therapeutic effect of the position controlled *RPMS*, studies with a large number of patients have to be carried out. A major shortcoming of the current hardware is the fast overheating of the small coils used at the forearm that appears after approx. 45 s of stimulation. For a therapy, stimulation periods of at least five minutes are desirable. Thus, it is the most important step towards the establishment of the proposed therapy to develop coils that are small enough to be placed at the forearm, produce a sufficiently focal magnetic field, and do not overheat. A promising coil cooling approach was introduced in [61] where the coil winding is made with circular hollow conductors. The coil is cooled by circulating a cooling liquid through the conductors. Unfortunately, the coils are too big and the magnetic field is not focal enough for a forearm application.

Another drawback of the current mechanical setup that might limit the clinical application is the time consuming process of coil positioning. Every subject shows a slightly different anatomy and thus, requires different coil configuration. However, once a proper position is identified, a repositioning could be much faster. Thus, a setup has to be developed where the patient specific coil positions can be memorized. This can be achieved by coil fixation arms with pitch lined scales at each joint so that the coil positions specific to each patient can be measured and recorded. Furthermore, a spastic patient is usually not able to place his forearm on an arm rest that is located too far away, such as next to the chair she/he is sitting on. Therefore, the setup has to be ergonomic, i.e. the arm rest (measurement orthosis in Fig. 3.14) has to be adjustable to the patient's needs.

With the EMG-driven position control, a method has been presented that allows to enhance the *RPMS*-therapy by a patient cooperative therapy mode. The tests with healthy subjects showed that the EvMA-cascade is capable of detecting small amounts of voluntary muscle activity (≈18 %ZDVC) at the stimulated muscle. Thus, it can be concluded that the method can be applied to patients that are capable of generating some voluntary activity.

The system identification method introduced in Chapter 4 requires the subject to relax as much as possible during identification. Since the EMG-measurement provides a method to quantify the voluntary force, it is seductive to incorporate this information into the system identification. This would broaden the applicability since the system identification could be carried out even if the subject does not behave passively. As the comparison of the EvMA-output with the measured voluntary force indicates, it can be detected whether the subject is active or not and tendencies about the activity level can be inferred. This information is adequate for the EMG-driven position control. However, a reliable quantitative prediction of the voluntary force is not possible since the signal variations that do not correlate with the force are too big (see also [210]). Therefore, it can be expected that the incorporation of the EMG-information into the system identification will not yield satisfactory results.

6 Conclusion

6.1 Major Results

Spastic paresis is a clinical picture that can occur after CNS-lesions. After a stroke, the patients often suffer from hemiparesis in combination with spasticity. Hemiparesis is a reduced ability to perform voluntary motor actions on one side of the body. Spasticity is a motor disorder characterized by an increase of muscle tone in response to limb motion, particularly in the flexor muscles. The most common rehabilitation methods are physiotherapy, constraint movement therapy and robot aided movement therapy sometimes in combination with virtual reality applications. Although the therapy has progressed, often recovery levels are reached that are unsatisfactory concerning the patient's ability to perform daily life activities. Particularly the restoring of arm and hand functions like reaching and grasping is still a major concern. Thus, there is a strong research demand for innovative neurorehabilitation methods.

The *RPMS* represents such an innovative rehabilitation approach with a high potential of improving the therapeutic outcome as it has been shown in numerous clinical studies. The current research on *RPMS* aims to further explore the underlying neurophysiological mechanisms and active principles of the rehabilitative effects. Furthermore, it is the aim to optimize the proprioceptive input patterns for a further improved therapeutic outcome with the ultimate goal to facilitate the relearning of functional movements like reaching and grasping objects.

This thesis contributes towards these goals by developing control engineering methods and applying them to the physiological system of the *RPMS*-induced index finger motion. Therefore, new methods for parameter identification in the presence of linear, nonlinear and separable nonlinear parameterization are introduced. Here, these methods are applied to the *RPMS*-problem. However, the proposed theoretic framework is generic and can be applied to a variety of systems. Moreover an adequate biomechanical and neurophysiological model is developed that includes the *RPMS*-induced force generation, the segment dynamics, a dynamic relaxation effect as well as a simplified model of the spastic joint torque.

In the following, the major results of this thesis are summarized.

Parameter Identification
In Chapter 2, novel methods for parameter identification in the presence of linear, nonlinear and separable nonlinear parameterization are presented. The parameter convergence of the presented methods is analyzed using a stability framework of nonlinear dynamic systems: Based on Lyapunov's theory asymptotic stability, i.e., parameter convergence to the global minimum, is proven under certain conditions. Thus, verified methods are pro-

vided that broaden the class of identifiable systems. In case of linear parameterization the well-known error models 1-4 [118] are shown to converge using the RLS-algorithm instead of LMS. This yields a faster and more robust convergence. For nonlinear parameterization, conditions are formulated that guarantee stability using simple gradient based algorithms like GS, GN, or LM. These algorithms are well-known, easy to implement and are available as standard routines. Finally, adaptive systems with mixed linear/nonlinear parameterization are analyzed and verified. The possibility to formulate model equations with mixed parameterization yields additional freedom of design to the user and thus, facilitates the incorporation of a priori knowledge about the system.

Neuromuscular and Biomechanical Modeling
In Chapter 3, a model of the *RPMS*-induced index finger movement is presented. It includes a force generation model that is developed by means of experiments with healthy subjects under isometric conditions. The generated force acts on the finger segments that are modeled with dynamic equations of motion. The segment dynamics model incorporates a non negligible relaxation effect and is developed and verified with experiments that are conducted with healthy subjects. Based on the neurophysiology of spasticity, a simplified mathematical description of the spastic joint is proposed that consists of two additive static nonlinear functions that depend on the MCP-joint angle and the angular velocity. The model is experimentally verified by conducting biomechanical measurements with six spastic paretic patients.

Automated Model Individualization
In Chapter 4, a system identification approach is presented that individualizes the qualitative model to a respective subject. For this purpose, the model proposed in Chapter 3 is formulated with a mixed linear/nonlinear parameterization. Using the error models presented in Chapter 2, adaptive systems are implemented. It is shown in simulations as well as experimentally that the adaptive systems are asymptotically stable and thus converge to the global minimum. The experiments are carried out under isometric and nonisometric conditions.

Control Engineering Contributions to *RPMS*
In Chapter 5, it is shown how the methods, algorithms, and models proposed in the previous chapters can contribute towards an improvement of the *RPMS*-therapy. The system identification during *RPMS* yields the basis for a therapy assessment and monitoring by identifying the spasticity level and the muscular fatigue. The method is tested and evaluated in a pilot study with four spastic paretic patients. Furthermore, a model based position controller with dual *RPMS* is implemented that provides the possibility to extend and to flex the MCP-joint according to arbitrarily chosen trajectories. Finally, the position control mode is extended by a patient driven adaptive trajectory generation. This patient-cooperative mode supports the intended movement only as much as necessary and thus motivates the patient to actively contribute during therapy. For this purpose, an EMG-signal processing cascade is proposed that detects voluntary muscle activity at the stimulated muscle.

6.2 Conclusions and Outlook

The fundamental research on nonlinear parameter identification presented in this thesis has enhanced the current state of the art and broadened the class of identifiable systems. A major benefit of nonlinear parameterization is the capability of approximating systems with their "natural" physical equations. Thus, the parameters to be identified have a direct meaning and the user can incorporate a prior knowledge as far as it exists. Often, equations that arise from laws of physics or chemistry show nonlinear parameterization. However, theoretic frameworks for nonlinear systems are usually not as nicely generalizable as it is the case with linear systems. For this reason, there remain many classes of nonlinearly parameterized systems that cannot be robustly identified with available methods. Particularly, there arise unsolved problems from systems with non-monotonic and non-convex parameterization. Therefore, it can be concluded that it is worth to further enhance the theory of adaptive systems with nonlinear and separable nonlinear parameterization.

Models of physical, chemical or physiological processes play an important role for system analysis, controller design or monitoring purposes. In medical research, there are in general two applications for models: On the one hand, they help to gain insight into physiological processes and thus can yield important findings for the research on pathophysiology. Ultimately, this results in a smaller number of human experiments. Furthermore, models can be used for diagnostics and patient monitoring as it is presented in this thesis. On the other hand, models can predict the system behavior which is used in the context of control strategies where the human is part of the plant. The major challenge for the system designer is to find a "good" model: A good model is only as detailed as necessary to sufficiently describe the characteristics of interest with a decent prediction error. Thus, the designer has to identify the dominant characteristics of a plant and to justify the disregard of the others.

In this thesis, a macroscopic model of the *RPMS*-induced index finger is presented where dominant effects like the relaxation characteristics are included and other phenomena like the force-length- and the force-velocity curves are neglected. The model includes a static spasticity approximation that is a simplification of the real process, as well. However, from the experimental model verifications, it can be concluded, that the proposed simplifications are justified and the incorporation of the relaxation is necessary for obtaining sufficiently small prediction errors.

Physiological modeling has been a research area for several decades. Nevertheless, researchers are still making efforts on developing adequate models. As implied above, this is due to the variety of applications that require different types of models with different foci and a different level of details. Therefore, it should be the subject of future research to develop libraries of models with a modular structure. This would provide the potential of implementing models that satisfy the respective application requirement in a fast and flexible manner. One of the first approaches towards this idea is presented in [21] with an object-oriented model of the human cardiovascular system.

From the parameter identification experiments during *RPMS*, it can be concluded that the proposed models and the proposed identification algorithms have the capability to identify a highly nonlinear dynamic plant. Experiments on muscular fatigue showed that

the on-line identification is capable of tracking slow parameter variations as they occur during the *RPMS*-therapy. From experiments with spastic paretic patients, it can be concluded that the spasticity level can be determined by means of system identification during *RPMS*. However, it could be shown, that the spastic joint torque is directly affected by the *RPMS* and thus, it is not directly comparable to spastic joint torques that occur during passive movements as they are assessed with the modified Ashworth-scale, e.g.. Therefore, future work should develop a spasticity scale that applies during muscle stimulation in order to establish the proposed method. For this purpose, experiments with a large number of participants have to be carried out.

The exemplary implementation of a dual coil position control of the index finger MCP-joint showed a performance that is absolutely sufficient for the desired application of therapeutic limb manipulation. The major benefit of a closed loop control over an open loop implementation is the capability of tracking arbitrary trajectories that have been predefined by a physiotherapist. This is important since a physiotherapist takes extremely care to determine the velocity and range of the limb manipulation. According to her/his experience, she/he adapts the training to the therapeutic progress of the respective patient. With the position controlled *RPMS* this individual motion induction can be maintained.

Although in this thesis, the control engineering problems for an *RPMS*-induced induction of functional movements have been solved, there are a few practical issues that have to be tackled in future work to facilitate the applicability in broad clinical studies. First of all, coils have to be developed that do not overheat during a sufficiently long time period and at the same time, generate a magnetic field that is focal enough to selectively activate particular muscles in the forearm. Our current coils used for the stimulation of the EIP and the FDP/FDS produce a very focal field. The focality is achieved by a small size of the winding. This results in a relatively small thermal capacity and thus, overheating occurs after approx. 45 s. A promising coil cooling approach was introduced in [61] where the coil winding is made with circular hollow conductors. The coil is cooled by circulating a cooling liquid through the conductors. Unfortunately, the coils are too big and the magnetic field is not focal enough for the application at the forearm. Secondly, a fixture system has to be developed where the arm of a spastic patient can be placed and fixated in a way that is convenient for the patient. Thirdly, an adaptive and easy to use coil fixation system has to be developed. To sum up, the practical requirements are non-overheating and focal coils, patient-ergonomic positioning, fast and flexible coil mounting. These requirements are nontrivial and have to be tackled by engineers *together* with physiotherapists *and* patients.

The experiments with the EMG-driven position control show that the proposed signal processing cascade is capable of separating the wanted EMG-signal from the direct and indirect stimulation artifacts. Thus, the technical prerequisites for a patient driven *RPMS*-therapy are created. From the experiments with healthy subjects it can be concluded that the algorithm is capable of detecting small amounts of voluntary muscle activity as it will be generated by paretic patients. The therapeutic benefits need to be evaluated in studies with a large number of patients to address statistical significance.

A Derivations and Auxiliary Results

A.1 Derivations concerning the SLS-Algorithm

In the following, it will be shown that Eq. (2.27) represents an RLS-algorithm. The matrix inversion lemma (MIL) expresses the following inversion:

$$(\underline{A} + \underline{u}\underline{v}^T)^{-1} = \underline{A}^{-1} - \frac{\underline{A}^{-1}\underline{u}\underline{v}^T\underline{A}^{-1}}{1 + \underline{v}\underline{A}^{-1}\underline{u}} \quad . \tag{A.1}$$

Applying the MIL to the update equation (2.21) yields

$$\begin{aligned} \underline{\Pi}(k) &= \left(\lambda\underline{\Pi}(k-1)^{-1} + \underline{\varphi}(k)\underline{\varphi}(k)^T\right)^{-1} \\ &= \frac{1}{\lambda}\underline{\Pi}(k-1) - \frac{\frac{1}{\lambda^2}\underline{\Pi}(k-1)\underline{\varphi}(k)\underline{\varphi}(k)^T\underline{\Pi}(k-1)}{1 + \frac{1}{\lambda}\underline{\varphi}(k)^T\underline{\Pi}(k-1)\underline{\varphi}(k)} \\ &= \frac{\underline{\Pi}(k-1)}{\lambda + \underline{\varphi}(k)^T\underline{\Pi}(k-1)\underline{\varphi}(k)} \quad . \end{aligned} \tag{A.2}$$

From Eq. (2.27) it follows

$$\underline{f}^{\hat{\theta}}(k-1) = \underline{\Pi}(k-1)^{-1}\underline{\hat{\theta}}(k) \tag{A.3}$$

With Eqs. (2.22), (A.2), and (A.3) the parameter update (2.27) can be written as

$$\begin{aligned}
\hat{\underline{\theta}}(k+1) &= \frac{1}{\lambda}\left(\underline{\Pi}(k-1) - \frac{\underline{\Pi}(k-1)\underline{\varphi}(k)\underline{\varphi}(k)^T\underline{\Pi}(k-1)}{\lambda + \underline{\varphi}(k)^T\underline{\Pi}(k-1)\underline{\varphi}(k)}\right)(\lambda\underline{\Pi}(k-1)^{-1}\underline{\theta}(k) + \underline{\varphi}(k)y(k)) \\
&= \hat{\underline{\theta}}(k) + \frac{1}{\lambda}\underline{\Pi}(k-1)\underline{\varphi}(k)y(k) - \frac{\underline{\Pi}(k-1)\underline{\varphi}(k)\underline{\varphi}(k)^T\underline{\Pi}(k-1)\underline{\Pi}(k-1)^{-1}\hat{\underline{\theta}}(k)}{\lambda + \underline{\varphi}(k)^T\underline{\Pi}(k-1)\underline{\varphi}(k)} \\
&\quad -\frac{1}{\lambda}\frac{\underline{\Pi}(k-1)\underline{\varphi}(k)\underline{\varphi}(k)^T\underline{\Pi}(k-1)\underline{\varphi}(k)y(k)}{\lambda + \underline{\varphi}(k)^T\underline{\Pi}(k-1)\underline{\varphi}(k)} \\
&= \hat{\underline{\theta}}(k) + \frac{(\lambda + \underline{\varphi}(k)^T\underline{\Pi}(k-1)\underline{\varphi}(k))\frac{1}{\lambda}\underline{\Pi}(k-1)\underline{\varphi}(k)y(k) - \underline{\Pi}(k-1)\underline{\varphi}(k)\underline{\varphi}(k)^T\hat{\underline{\theta}}(k)}{\lambda + \underline{\varphi}(k)^T\underline{\Pi}(k-1)\underline{\varphi}(k)} \\
&\quad -\frac{\frac{1}{\lambda}\underline{\Pi}(k-1)\underline{\varphi}(k)\underline{\varphi}(k)^T\underline{\Pi}(k-1)\underline{\varphi}(k)y(k)}{\lambda + \underline{\varphi}(k)^T\underline{\Pi}(k-1)\underline{\varphi}(k)} \\
&= \hat{\underline{\theta}}(k) + \frac{\underline{\Pi}(k-1)\underline{\varphi}(k)y(k) - \underline{\Pi}(k-1)\underline{\varphi}(k)\underline{\varphi}(k)^T\hat{\underline{\theta}}(k)}{\lambda + \underline{\varphi}(k)^T\underline{\Pi}(k-1)\underline{\varphi}(k)} \\
&= \hat{\underline{\theta}}(k) + \frac{\underline{\Pi}(k-1)}{\lambda + \underline{\varphi}(k)^T\underline{\Pi}(k-1)\underline{\varphi}(k)}\underline{\varphi}(k)\underbrace{\left(y(k) - \hat{\underline{\theta}}(k)^T\underline{\varphi}(k)\right)}_{e(k)} \quad .
\end{aligned} \tag{A.4}$$

Inserting (A.2) into (A.4) yields

$$\hat{\underline{\theta}}(k+1) = \hat{\underline{\theta}}(k) + \underline{\Pi}(k)\underline{\varphi}(k)e(k) \quad . \tag{A.5}$$

Choosing the estimator gain $\gamma = 1$, this is exactly the RLS-update rule introduced in Tab. 2.1, and hence, Eq. (2.27) is an RLS-algorithm.

A.2 Positive Semidefiniteness of $\underline{M} = \underline{a}\underline{a}^T$

For a matrix $\underline{M} = \underline{a}\underline{a}^T$ the quadratic form $\underline{v}^T\underline{M}\underline{v}$ is calculated as

$$\underline{v}^T\underline{M}\underline{v} = \underline{v}^T\underline{a}\underline{a}^T\underline{v} = (\underline{v}^T\underline{a})^2 \geq 0 \quad .$$

Since $\underline{v}^T\underline{a} = 0$ not only for $\underline{v} = \underline{0}$ but also for $\underline{v}$ and $\underline{a}$ linearly dependent, the matrix $\underline{M} =$ is only positive semidefinite and not positive definite.

A.3 Update Equations Interpreted as PT_1-Filter

A.3.1 Continuous Time

The time continuous update laws with the exponential forgetting factor λ_c from table 2.1 conform with the equation

$$y(t) = \int_0^t \lambda_c^{t-\tau}u(\tau)d\tau \quad . \tag{A.6}$$

The output of an LTI-system with input $u(t)$ that is described with its impulse response $g(t)$, can be calculated with the convolution integral

$$y(t) = \int_0^t g(t-\tau)u(\tau)d\tau \quad . \tag{A.7}$$

The impulse response of a PT_1-system with the transfer function $G(s) = \frac{1}{1-sT_1}$ is given with $g(t) = e^{-\frac{t}{T_1}}$ and thus, with Eq (A.7), its output is calculated as

$$y(t) = \int_0^t e^{-\frac{t-\tau}{T_1}} u(\tau)d\tau \quad . \tag{A.8}$$

By inserting the reformulation

$$\lambda_c^t = \left(e^{\ln \lambda_c}\right)^t = e^{t \ln \lambda_c} = e^{-\frac{t}{-1/\ln \lambda_c}}$$

into Eq. (A.6) and by comparing the resulting term with Eq. (A.8), it becomes obvious that Eq. (A.6) describes the response of a PT_1-system with $T_1 = -1/\ln \lambda_c$, $K = -1/\ln \lambda_c$ and to the input $u(t)$.

A.3.2 Discrete Time

The discrete time update laws with the exponential forgetting factor λ_d from table 2.1 conform with the equation

$$y(k) = \lambda_d y(k-1) + u(k) \tag{A.9}$$

which is basically the equation of a discrete time PT_1-filter. Using the Explicit Euler Method, the time constant T_1 of the equivalent continuous time signal calculated as

$$T_1 = \frac{T_s}{1-\lambda_d} \quad . \tag{A.10}$$

A.4 Model Evaluation

A.4.1 Normalized Mean Square Error (NMSE)

The model accuracy can be evaluated by calculating the normalized mean square error (NMSE)

$$\mathrm{NMSE}(\underline{y}, \underline{\hat{y}}) = \frac{\left\|\underline{y} - \underline{\hat{y}}\right\|_2^2}{\left\|\underline{y}\right\|_2^2} 100\% \tag{A.11}$$

with the reference data set $\underline{y} = [y(0)\, y(T_s)\, y(2T_s)\, \ldots\, y(kT_s)]^T$ and the approximation to be evaluated $\underline{\hat{y}} = [\hat{y}(0)\, \hat{y}(T_s)\, \hat{y}(2T_s)\, \ldots\, \hat{y}(kT_s)]^T$. Note that in literature, the model accuracy is often evaluated by means of the "variance accounted for" (VAF). The VAF is related to the NMSE by

$$\mathrm{VAF} = 100\% - \mathrm{NMSE} \quad . \tag{A.12}$$

A.4.2 Relative Model Error

Another more intuitive measure for the model accuracy is given with the relative model error

$$e_r = \frac{\|\underline{e}\|_1}{\|\underline{y}\|_1} 100\,\% = \frac{\|\underline{y} - \underline{\hat{y}}\|_1}{\|\underline{y}\|_1} 100\,\% \quad . \tag{A.13}$$

The usage of the NMSE is more common since by squaring, big model errors are weighted stronger then small ones. Thus, this measure more significantly evaluates the model accuracy.

A.5 Calculation of the Moments of Inertia for the Index Finger Phalanges

The moment of inertia of a solid homogeneous cylinder with radius R and length L with respect to the axis of rotation y (see Fig. A.1) is calculated as

$$J_{cyl,y}(R, L) = m \left(\frac{R^2}{4} + \frac{L^2}{12} \right) \quad . \tag{A.14}$$

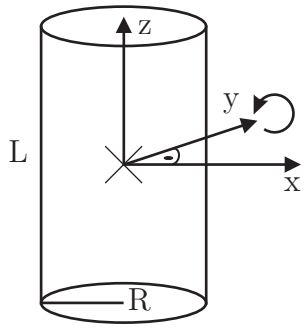

Fig. A.1: Cylinder with centered coordinate system.

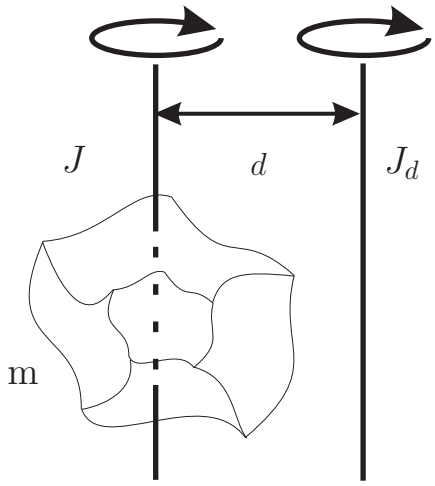

Fig. A.2: Illustration of Steiner's theorem: Given J and d, the moment of inertia J_d can be calculated.

According to Steiner's theorem, given the moment of inertia J of an object (mass m) with respect to an axis through the object's center of mass, the moment of inertia J_d with respect to a parallel axis with perpendicular distance d can be calculated as

$$J_d = J + md^2 \quad , \tag{A.15}$$

(see Fig. A.2). Using Eq. (A.15), the moment of inertia J_{1,y_2} of the proximal phalanx is calculated as

$$\begin{aligned} J_{1,y_2} &= J_{cyl1,y}(R_1, L_1) + m_1 \left(\frac{L_1}{2}\right)^2 \\ &= m_1 \left(\frac{R_1^2}{4} + \frac{L_1^2}{3}\right) \ . \end{aligned} \tag{A.16}$$

The moment of inertia J_{2,y_2} of the medial phalanx is given by

$$\begin{aligned} J_{2,y_2} &= J_{cyl2,y}(R_2, L_2) + m_2 d_2^2 \\ &= m_2 \left(L_1^2 + \frac{L_2^2}{3} + \frac{R_2^2}{4} + L_1 L_2 \cos\alpha_3 \right) \end{aligned} \tag{A.17}$$

whereas d_2 is given by the distance between the center of mass of the cylinder approximating the medial phalanx and the origin of the coordinate system S_2. The moment of inertia J_{3,y_2} of the distal phalanx is calculated as

$$\begin{aligned} J3, y_2 &= J_{cyl3,y}(R_3, L_3) + m_3 d_3^2 \\ &= m_3 \Big(L_1^2 + L_2^2 + \frac{R_3^2}{4} + \frac{L_3^2}{3} + L_2 L_3 \cos\alpha_4 + 2 L_1 L_2 \cos\alpha_3 + \\ &\qquad + L_1 L_3 \cos(\alpha_3 + \alpha_4) \Big) \end{aligned} \tag{A.18}$$

with the distance d_3 between the center of mass of cylinder three and the origin of S_2.

B The Sensorimotor System and Sensorimotor Deficits

B.1 Relevant Neuromuscular Anatomy and Physiology

B.1.1 The Nervous System and Functional Nerve Cell Classes

The nervous system coordinates and controls our body functions. It is composed of trillions of nerve cells which constitute a network that reaches from the brain through the spinal cord into the periphery. The brain and the spinal cord form the central nervous system (CNS) and the peripheral nerves, the autonomous nervous system (control of blood vessels and internal organs) and the enteric nervous system (control of the gut activity) make up the peripheral nervous system.

The nerve cells (also called neurons) can be divided into three functional classes: Afferent neurons, efferent neurons and interneurons. Afferent neurons transmit information from the periphery into the CNS whereas efferent neurons act vice versa. Interneurons connect neurons within the CNS. They integrate afferent and efferent neurons into reflex circuits and account for 99% of all neurons.

B.1.2 The Neuron

The individual neuron is the basic unit of the nervous system. A schematic of a neuron is depicted in Fig. B.1. The cell body (soma) contains the nucleus. The branches originating at the soma are called dendrites. They receive information from other neurons. The neuron transmits information to other neurons or muscles, e.g. via a threadlike extension of the soma called axon. Axons are often referred to as nerve fibers. Their length may extend a meter or even longer. They may be either myelinated or unmyelinated. Myelinated axons are covered by a thick layer of fatty material called myelin. In peripheral nerves the myelin layer is formed by Schwann cells. The myelin sheath is interrupted by at regular intervals by gaps called nodes of Ranvier. The axon branches at its end. The contacts between the terminal branches and the target are accomplished by synapses. Synapses may be made between nerve cells or between an axon and a non-neuronal cell such as a muscle fiber. In the latter case they are called motor end-plates or neuromuscular end-plates (see also Sec. B.1.5). The functional principle of synapses is not explained here but can be found in [128; 183], e.g..

Outside the CNS, axons run in bundles called fascicles. The fascicles are summarized in trunks that run alongside the major blood vessels and provide structural support. Some nerve trunks transmit information from specific sensory organs to the CNS (sensory nerves)

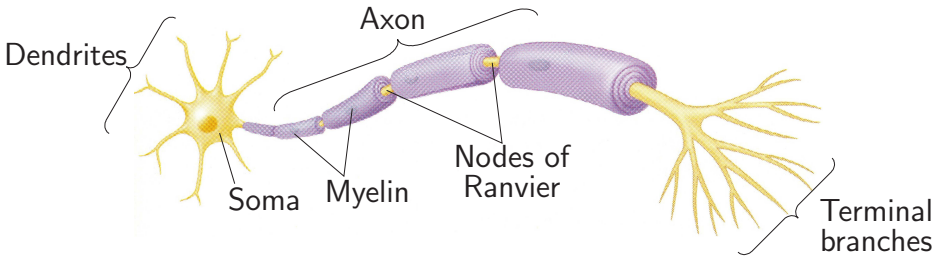

Fig. B.1: Myelinated nerve cell (modified from [183]).

Tab. B.1: Two kinds of peripheral nerve fiber classification taken from [128]: Erlanger and Gasser in column 3, Lloyd and Hunt in column 4 whereas the former differentiates the conduction velocity and the latter intends to indicate the position of innervation of specific types of receptors. Lloyd/Chang applies to afferent (sensory) fibers only.

Diameter in μm	Conduction velocity in m/s	Fiber classification	Cutaneous nerve classification	Function
15-20	70-120	Aα	-	Motor: Control of skeletal muscles
15-20	70-120	Aα	Ia	Sensory: Innervation of primary muscle spindles
			Ib	Sensory: Innervation of Golgi tendon organs
5-10	30-70	Aβ	II	Sensory: Cutaneous senses, secondary innervation of muscle spindles
3-6	15-30	Aγ	-	Motor: Control of Intrafusal Muscle fibers
2-5	12-30	Aδ	III	Sensory: Cutaneous senses, especially pain and temperature
$\approx$3	3-15	B	-	Motor: Autonomic preganglionic nerve fibers
0.5-1.0	0.5-2.0	C	-	Motor: Autonomic postganglionic nerve fibers
0.5-1.0	0.5-2.0	C	IV	Sensory: Nociceptors and cutaneous senses - pain and temperature

whereas others transmit signals from the CNS to specific effectors (motor nerves). Nerve trunks that contain both fibers are called mixed nerves.

Table B.1 summarizes a classification of peripheral nerve fibers with respect to their function and conduction velocity.

B.1.3 Neuronal Signaling

Resting Membrane Potential and Action Potential

In order to transmit information, nerve cells change their membrane potential from its resting level. In this context, the terms resting membrane potential and action potential are important. The resting membrane potential is the steady transmembrane potential of a cell that is not producing an electric signal. It is measured as voltage difference between the intracellular and extracellular potentials. It exists because of an excess of negative ions inside the cell and an excess of positive ions outside. Its magnitude varies from -5 to -100 mV, depending on the type of cell. In neurons it is generally -70 mV.

Nerve and muscle cells are capable of producing action potentials. Their membranes are called excitable and among many other functional units they contain voltage gated ion channels. Among many types of ion channels the sodium and potassium channels mediate the neuronal action potentials.

To generate an action potential, the membrane requires an electrical stimulus (change of resting potential) that is greater than a certain minimum known as depolarization threshold. Then the voltage gate ion channels open and hence the respective ions can move between the intra and extracellular plasma down their electrochemical gradient. The threshold of most excitable membranes is about 15 mV above the resting potential. During the action potential the membrane potential reaches a peak value of +40 to +50 mV before repolarizing to its resting level. The exact mechanisms can be found in [128; 183], e.g.. The entire cycle lasts about 4 ms and during so called refractory period (1-15 ms) which follows the action potential a second action potential cannot be generated. The refractory period limits the firing frequency. Action potentials occur maximally or they do not occur at all which is called the all-or-none principle.

Action Potential Propagation

When an action potential has been elicited, it propagates along the entire axon. As illustrated in the upper picture of fig. B.2, the zone where the action potential takes place will be at a different potential than the resting membrane. Hence, an electrical current will flow between the two regions. This local circuit depolarizes the neighboring region and thus, the action potential propagates. Thanks to the refractory period that occurs after an action potential the direction of propagation is always orthodromic [1]. The signal propagation in myelinated axons differs from that in unmyelinated axons. Since the axon membrane is in contact with the extracellular fluid only at the Nodes of Ranvier, and insulated in between, the local current circuit is completed between two nodes. Therefore, the action potential "jumps" from one node to the next which is called saltatory conduction. This results in a much higher conduction velocity.

[1] An orthodromic impulse runs along an axon in its normal direction, away from the soma. An antidromic impulse in an axon refers to conduction in the opposite direction.

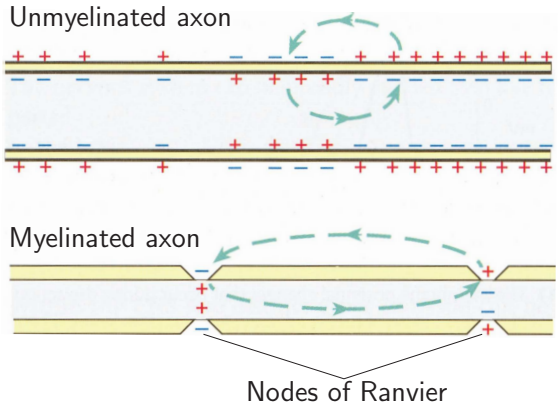

Fig. B.2: Simplified schematic for illustration of the action potential propagation (modified from [128]).

B.1.4 Skeletal Muscle Anatomy

A schematic illustration of the human skeletal muscle is depicted in Fig. B.3. Every muscle is connected with the skeleton at least at two fixation points, the origo and the insertio. The muscle is composed of many bundles of muscle fibers called fascicles. The muscle fiber length amounts between a few millimeters and approx. 30 cm and the thickness amounts 40-100 μm. Muscle fibers are among the largest cells in the body. They are coated with the sarcolemma, the cell membrane of a muscle cell. Every muscle fiber contains thousands of protein filaments called myofibrils. The myofibrils are the contractile elements of the muscle cell. Each myofibril has a consistent pattern of dark and light bands (A-band and I-band). Therefore, the skeletal muscle is also called striated muscle. The small sections between two Z-lines are called sarcomeres. The sarcomeres consist out of two contractile proteins: The actin filaments and the myosin filaments. Actin filaments have a diameter of 5-8 nm and are fixated at the Z-lines. The myosin filaments have a diameter of 12-14 nm, and are aligned in between the actin filaments. The myosin filaments overlap with the actin filaments also when the muscle is relaxed. The area within a sarcomere where there are only actin filaments is called I-band. In between two I-bands lies the A-band that contains actin and myosin filaments as well. The H-zone only consists of myosin filaments and the M-Line that controls the spacing between the myosin filaments.

B.1.5 Skeletal Muscle Physiology: Innervation, Activation and Contraction

Muscle Innervation

The commands that result in a muscle action are generated in the motor cortex and propagate via the spinal cord and via motoneurons into the muscle. Every skeletal muscle is innervated by motoneurons that originate from the anterior horn of the spinal cord. Before entering the muscle, every motor neuron splits up into a couple of terminal motor branches. Every terminal motor branch is connected with one muscle fiber at the so called

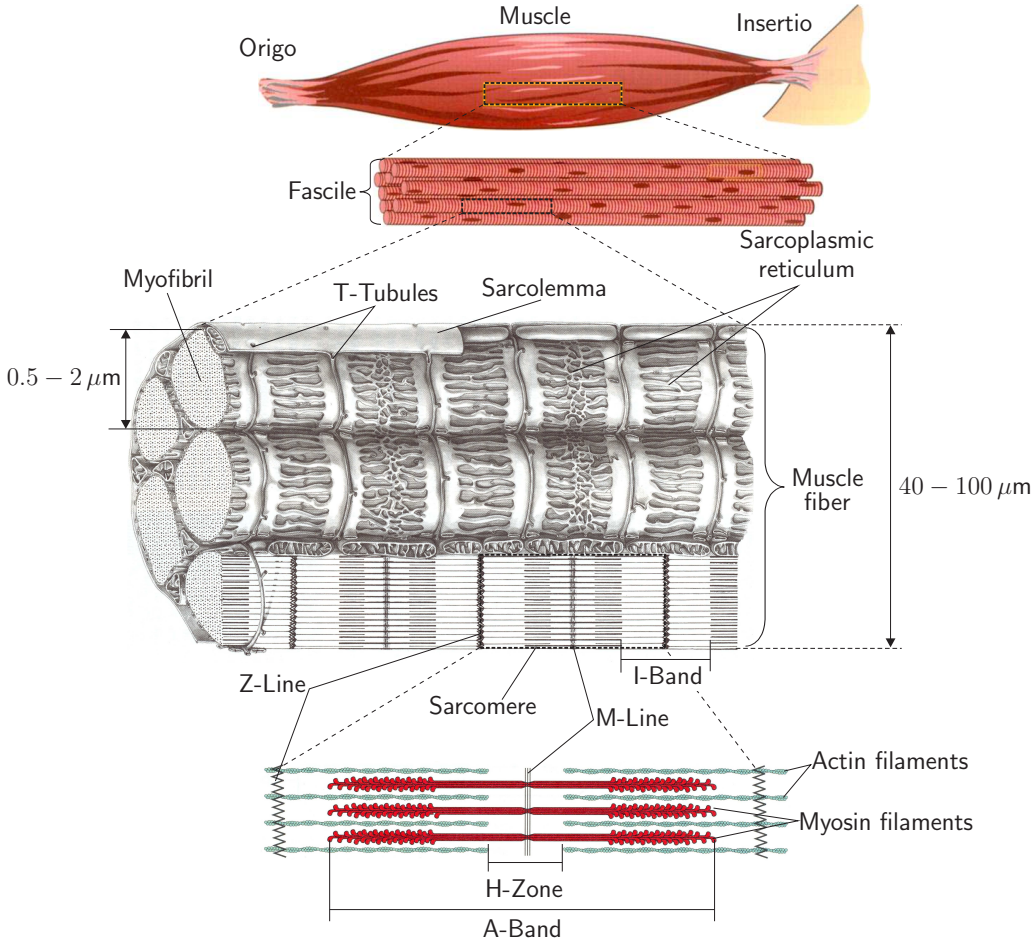

Fig. B.3: Histological and structural schematic of the skeletal muscle (modified from [149] and [32]).

neuromuscular end-plates. A motoneuron with its terminal branches and every muscle fiber it innervates constitute a motor unit (MU). The number of muscle fibers within each MU can vary: Thigh muscles can have a thousand fibers in each unit, eye muscles might have ten. In general, the number of muscle fibers innervated by a motor unit is a function of a muscle's need for refined motion.

Muscle Activation

The activation resulting from an incoming action potential requires an electromechanical coupling between electrochemical signals and the actual muscle force generation. When an action potential arrives at the neuromuscular end-plate it causes local membrane depolarization in the region of the end-plates (end-plate potential). This end-plate potential elicits a muscle action potential (MAP) that propagates first in longitudinal direction along the sarcolemma (see Fig. B.3) with a velocity of 2-6 m/s by mechanisms similar to those described for nerve cells. Subsequently, the signal propagates in transversal direction along the T-tubules. Thus, the electrical pulse spreads inside the entire muscle fiber. The

depolarization of the sarcolemma and the T-tubules causes a release of Ca^{2+} in the sarcoplasmic reticulum (see Fig. B.3) which is an interconnected network of tubules, vesicles and cisternae that surrounds the myofibrils. This release of Ca^{2+} ions causes the muscle contraction.

Muscle Contraction

The calcium ions Ca^{2+} diffuse into the cytoplasm where they get into contact with the myosin and actin filaments and bind with the troponin molecules of the actin filaments. This enables the myosin molecule heads to "grab and swivel" their way along the thin filament which is the driving force of muscle contraction. This procedure is called the cross-bridging cycle and requires adenosine triphosphate (ATP) as energy source. During muscle contraction the actin filaments are drawn closer together. Thus, the ends of the sarcomere are drawn in and the sarcomere shortens. During this shortening of the sarcomeres, there is no change in the length of the filaments. This is known as the sliding-filament mechanism. In order to finish the muscle contraction, a calcium pump transports the Ca^{2+} ions back into the tubules of the sarcoplasmic reticulum so that the bindings between actin and myosin filaments open up, and the muscle relaxes.

B.1.6 Skeletal Muscle Force Generation

The amount of force exerted by a muscle depends on many factors: The frequency at which the MUs are activated, the number of active MUs, the current length and the shortening velocity of the muscle. In the following, the underlying mechanisms will be shortly described.

Temporal Summation

The force response of a single muscle fiber to a single action potential is called muscle twitch (Fig. B.4). Following the MAP, there is an interval of a few milliseconds before the tension of the muscle fiber begins to increase. During this latency, the processes associated with the electromechanical coupling of the muscle activation are occurring. Then, the activated muscle fiber exerts a dynamic force response that may take 10 to 400 ms. The duration of the twitch depends on the muscle fiber type and is called contraction time.

If a muscle is repetitively with an inter-stimulus time that is below the contraction time, the generated force increases. This increase is called temporal summation. The principle is illustrated in Fig. B.5. A maintained force generation is called tetanus, whereas the unfused and fused tetanus is distinguished. The fusion begins at a stimulus-frequency of approximately 20 Hz. By increasing the activation frequency the generated force will be increased, as well. Due to the muscle fiber refractory period, the minimum inter-stimulus time amounts approx. 8 ms.

Spatial Summation

The spatial summation controls the exerted muscle force by the number active motor units. The process of increasing the number of active MUs is called recruitment. According to

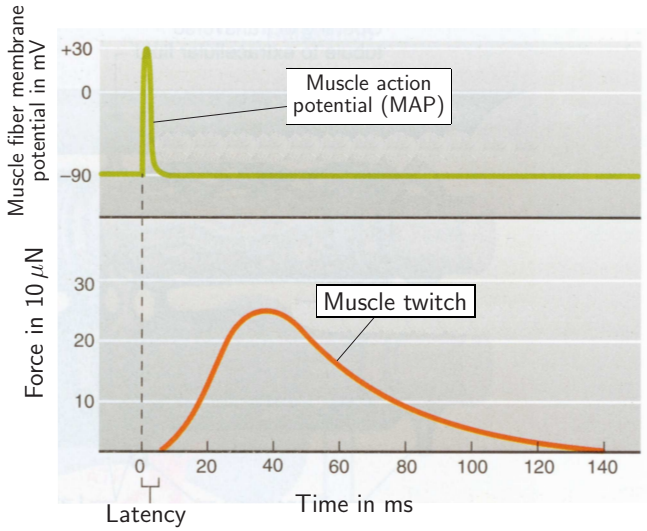

Fig. B.4: A muscle twitch generated by a single muscle fiber following a muscle action potential (MAP) (modified from [183]).

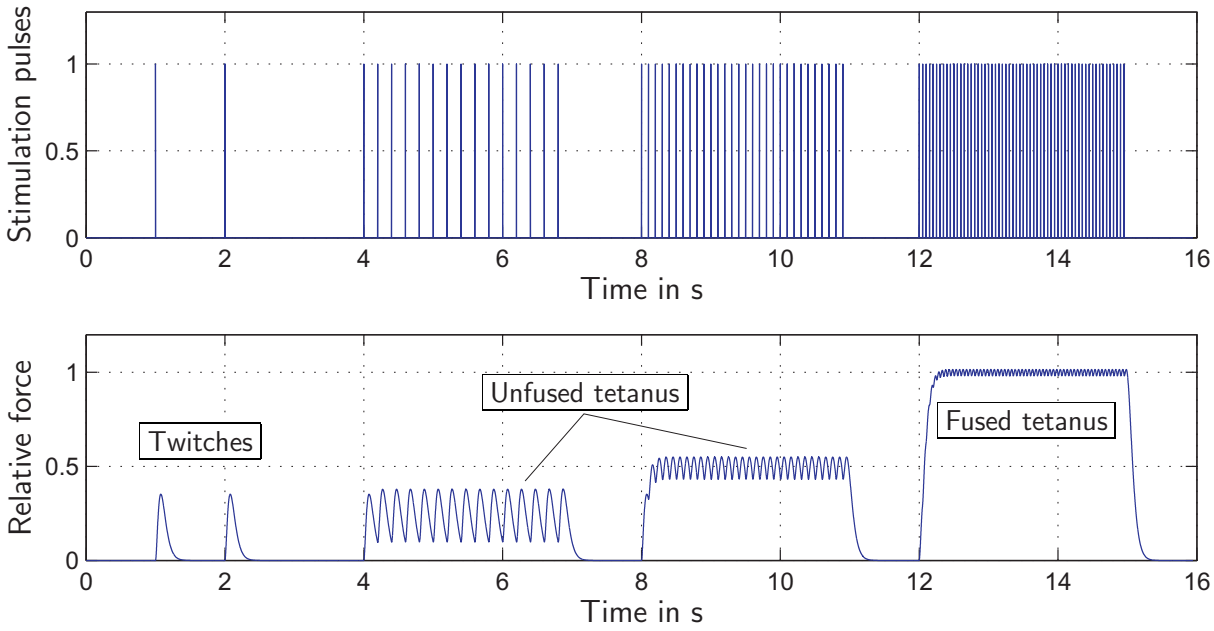

Fig. B.5: Principle of temporal summation illustrated by simulated force responses of a muscle to stimuli with repetition rates $f_{rep} = 1\,\text{Hz}$, $f_{rep} = 5\,\text{Hz}$, $f_{rep} = 10\,\text{Hz}$ and $f_{rep} = 20\,\text{Hz}$.

the size principle of motor unit recruitment [64; 110], first, the small and slow muscle fibers are recruited that are less sensitive to fatigue. Larger fibers that can produce a greater force but are fast fatiguing will be additionally recruited if a greater amount of force is required.

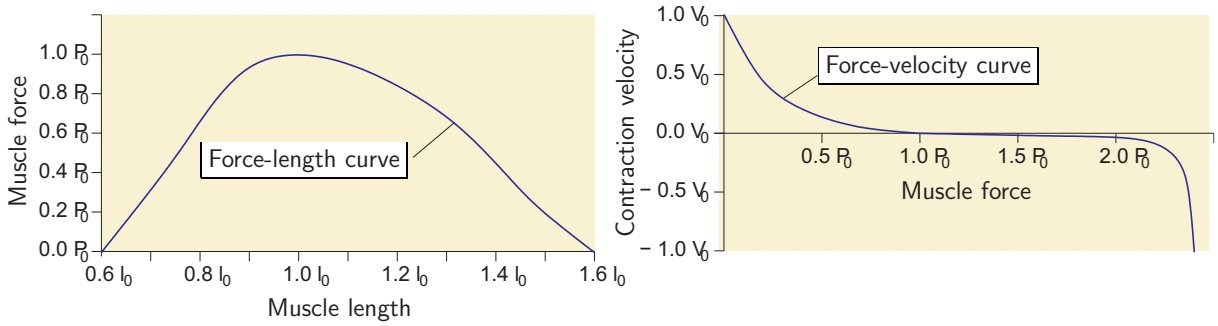

Fig. B.6: Qualitative characteristics of the muscle's ability to generate force depending on its length and velocity configuration. Left: Force-length curve. The maximum Force P_0 is generated at the optimal length l_0 Right: Force-velocity curve: The maximum contraction velocity V_0 occurs at zero load (modified from [6]).

There are major differences between physiological recruitment and enforced recruitment by *RPMS*. In order to avoid fatigue, naturally alternating MUs are activated during a maintaining force generation. During *RPMS* however, always the same MUs are recruited. Thus, the artificially stimulated muscle exhausts much faster than during physiological excitation.

Force-Length and Force-Velocity Relation

If a skeletal muscle is stretched, the amount of actively generated force will vary with length (See Fig. B.6). The equilibrium length of a relaxed muscle is near the optimal length l_0 at which it can produce the maximum force. This relationship can be explained in terms of the sliding-filament mechanism. The amount of overlap between actin and myosin filaments is optimal at the muscle length l_0. Stretching as well as shortening result in suboptimal overlapping configurations.

The ability of force generation also varies with the contraction velocity. With increasing load, the sliding of the filaments starts later, and becomes slower and smaller. The maximum shortening velocity depending on the applied muscle force, the so called force-velocity curve is sketched in Fig. B.6. During muscle shortening, the myosin filaments have to break up their bindings with the actin filaments more often which results in a smaller number of cross-bridges. Thus, the force generation capability decreases. At contraction velocity zero the maximum isometric force P_0 is generated. Interestingly, the amount of generated force increases further if the active muscle is stretched. During this so called lengthening contraction cross-bridges are broken up by force which requires a greater amount of force then maintaining in isometric contraction.

Muscle Fatigue and Muscle Fiber Types

When a skeletal muscle is repeatedly stimulated, the force it develops decreases. This decline of muscle tension is known as muscle fatigue. Many factor can contribute to the fatiguing process which is not yet fully understood. Two effects that could be proven are

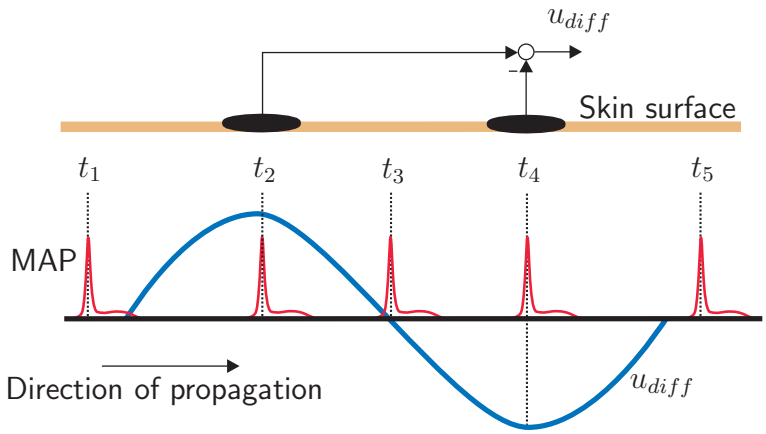

Fig. B.7: Principle of surface EMG: The MAP propagates along the muscle fiber and thus, a potential difference u_{diff} can be measured at the surface electrodes.

increase of potassium ions inside the T-tubules [183] that inhibits the conduction of muscle action potentials and a decrease of calcium ion concentration in the sarcoplasmic reticulum [45].

Muscle fatigue varies considerably with the muscle fiber types. As described earlier, muscle fibers are summarized in MUs. Since all the fibers of one MU are of the same type we can assign types of MUs instead of fibers. Basically there are three types of fibers: slow-twitch oxidative fibers (Type I), fast-twitch oxidative fibers (Type IIa) and fast-twitch glycolytic fibers (Type IIb). Oxidative and glycolytic fibers have different metabolic characteristics. Oxidative fibers have a rich blood supply an aerobic metabolism and are slowly fatiguing. Glycolytic fibers are surrounded by fewer blood vessels, they produce their energy by means of anaerobic metabolism and are fatiguing much faster.

Most muscles are composed of all three muscle fiber types. Depending on the proportions, the muscles differ considerably in contraction speed, strength and fatigability.

B.2 Surface Electromyography

Electromyography (EMG) is method that detects muscular activity by means of voltage measurements. Muscle action potentials (MAPs, see Section B.1.5) that propagate along a muscle fiber can be detected by measuring potential differences at the skin surface (Fig. B.7). As described in Section B.1.5, a MU consists of a motoneuron that innervates several muscle fibers. Due to the spatial distribution of the motor end plates, the MAPs of a single MU are temporally shifted. The superposition of these MAPs represents a motor unit action potential (MUAP) as illustrated in Fig. B.8. During muscle activation, MUAPs are elicited at certain activation rates and numerous MUs are active. As a consequence, numerous MUAP-wave-trains are generated. Contrary to needle electrodes that are capable of detecting single MUAPs, surface electrodes measure a superposition of MUAP-wave-trains as illustrated in Fig. B.9.

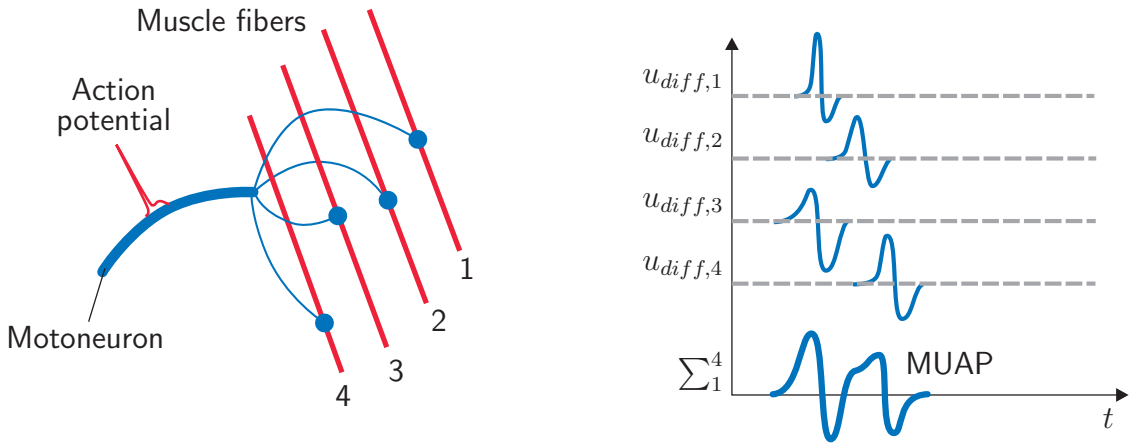

Fig. B.8: Left: Schematic of a MU with four innervated muscle fibers. Right: A MUAP results from the superposition of the temporally shifted MAPs.

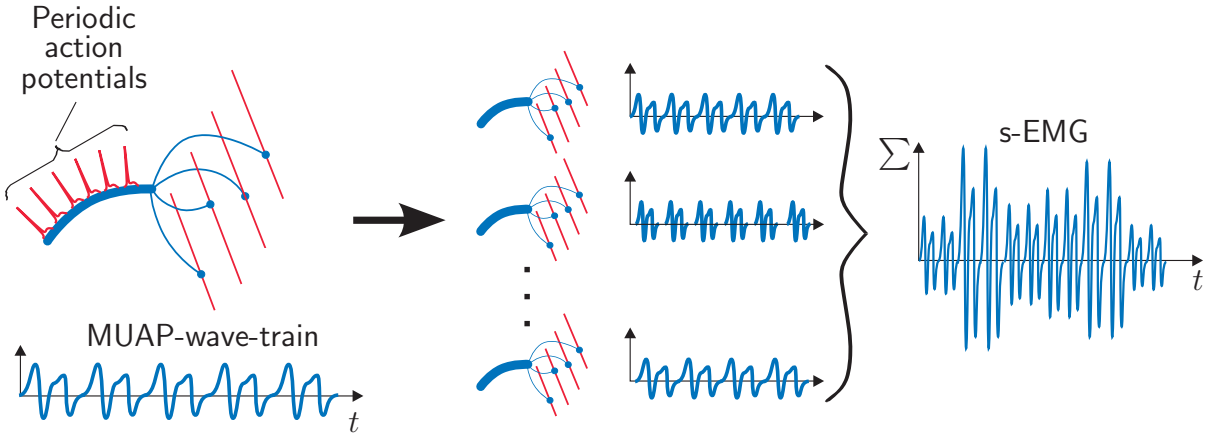

Fig. B.9: Generation of a MUAP-wave-train by periodic elicitation and superposition of all MUAPs to a surface EMG signal (s-EMG).

The quality of a s-EMG signal depends on many factors. The most important are: Electrode position, electrode-skin contact, depth of the muscle to be sensed below the skin surface and signal processing methods. In general, there exists a monotonic relationship between the amplitude of the EMG-envelope and the generated muscle force if the EMG-signal is sufficiently smoothed. However, the amplitude of the surface EMG is a random variable and its instantaneous value is not monotonic with respect to the force value. Under non-isometric conditions the EMG-signal amplitude may change due to anatomical modifications such as the muscle diameter. However, even during nonisometric contraction with constant force the amplitude of the EMG-envelope is not constant since the spatial configuration of the activated MUs changes. Thus, a strong signal is detected if more MUs are active that are close to the electrodes and a weaker signal is detected otherwise. Furthermore, constructive and destructive superpositions of MUAPs occur which also leads

to variance in the EMG-amplitude that does not represent the variance in the muscle activation. For further reading the references [50; 102; 103] are recommendable.

B.3 Motor Control and Sensorimotor Integration

Coordinated and purposeful movement is a fundamental aspect of human existence. There are two types of voluntary motor functions: Maintenance of position (posture) and goal-directed movements. Posture as well as movements are achieved by precise activation patterns of many motor units in various muscles. Reflexes represent a basic mechanism involved in both types of voluntary actions. Although reflexes are involuntary actions, they are modified by commands from the CNS and from sensory inputs in order to support the task execution.

Physiological understanding of what happens in the CNS during the execution of voluntary movements is still insufficient. Nevertheless, many key mechanisms are understood. They will be shortly summarized in this section: The conceptual hierarchical organization of the neural systems controlling the body movement, the integration of peripheral sensors in motor control (sensorimotor integration) and the mechanisms of reflexes.

In this context, the terms afferent and efferent neural pathways are important. Therefore, a short clarification appears necessary. Afferent neurons carry nerve action potentials from the periphery towards the CNS. The corresponding signals are referred to as afferent signals or afferent input. Vice versa, efferent neurons transport signals away from the CNS into the periphery.

B.3.1 The Brain Motor Centers and Descending Motor Pathways

The major areas inside the brain that are involved in motor task execution are depicted in Fig. B.10. The premotor, supplementary motor, primary motor, somatosensory and parietal lobe association cortices make up the sensorimotor cortex.

The primary motor cortex (sometimes simply called motor cortex) as well as the somatosensory cortex can be somatotopically subdivided with a mapping of peripheral areas to regions in the cortices. This somatotopic organization can be illustrated with the famous motor homunculus and somatosensory homunculus (see [183], e.g.).

Beneath the cortex lies the brainstem with numerous highly interconnected structures. It interacts with the cortex in order to control movements. It is not known to what extent, if any, these structures initiate movements, but they play an important role in movement planning and monitoring.

The cerebellum plays a vital role in the coordination of posture and rapid muscular activity. It supplements the activities of other motor areas. It may also contribute to motor learning.

The Thalamus is a major area for processing information from the sense organs. The basal nuclei (also called basal ganglia) are located next to the Thalamus and form an important link between the frontal lobes and the motor cortex. Their importance in the control of motor functions is clear from movement dysfunctions in patients with lesions of the basal ganglia.

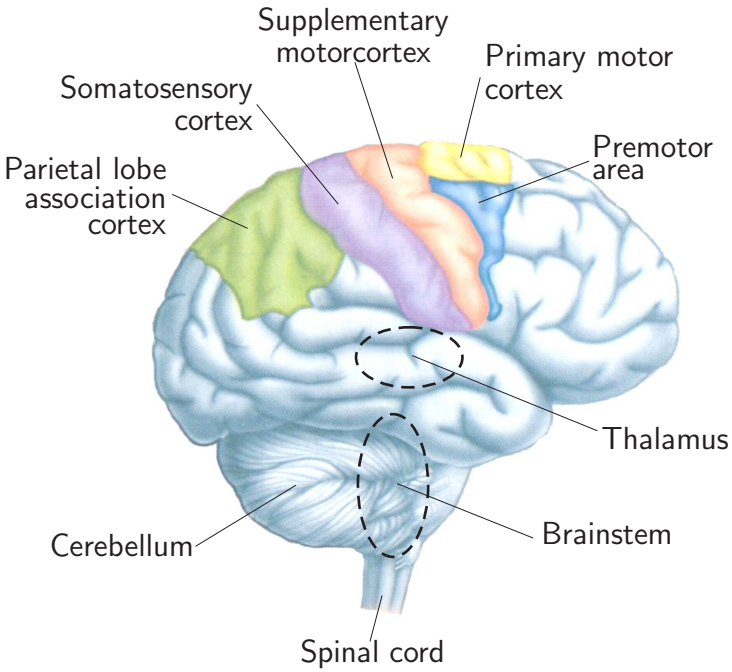

Fig. B.10: Major sensorimotor areas of the cerebral cortex and functional units in the brain involved in motor task execution (modified from [183]). The brain division where the somatosensory and the association cortex are located is called parietal lobe. The motor cortices are located in the frontal lobe. The brainstem consists of the midbrain, pons and medulla oblongata. Note that the brainstem and the thalamus are not visible in the picture. They are located below the cortices in the area of the respective dashed ellipses.

The connection between the sensorimotor cortex and the brainstem with the motoneurons and the interneurons in the spinal cord is accomplished by two types of descending pathways: The corticospinal pathways (also called pyramidal tracts) that origin in the sensorimotor cortex and the brainstem pathways (also called extrapyramidal pathways) originating in the brain stem.

B.3.2 The Hierarchical Structure of Motor Control System

The motor control system is formed by all functional units involved in the control of purposeful muscle contraction. These units are organized hierarchically as illustrated in Fig. B.11.

The initiation of a motor act begins with the intention and the appropriate plan that is generated in the highest level of the motor control hierarchy. Very little is known where exactly the plan is formed in the brain.

The middle level comprises parts of the sensorimotor cortex, the cerebellum, the basal nuclei, the thalamus and the brainstem. Here, all the afferent information (from sensors in the muscles, tendons and skin) is combined and integrated with the commands from the higher level in order to create a motor program, i.e. the activation pattern that is required to perform the desired movement. Postural control originates mostly in the

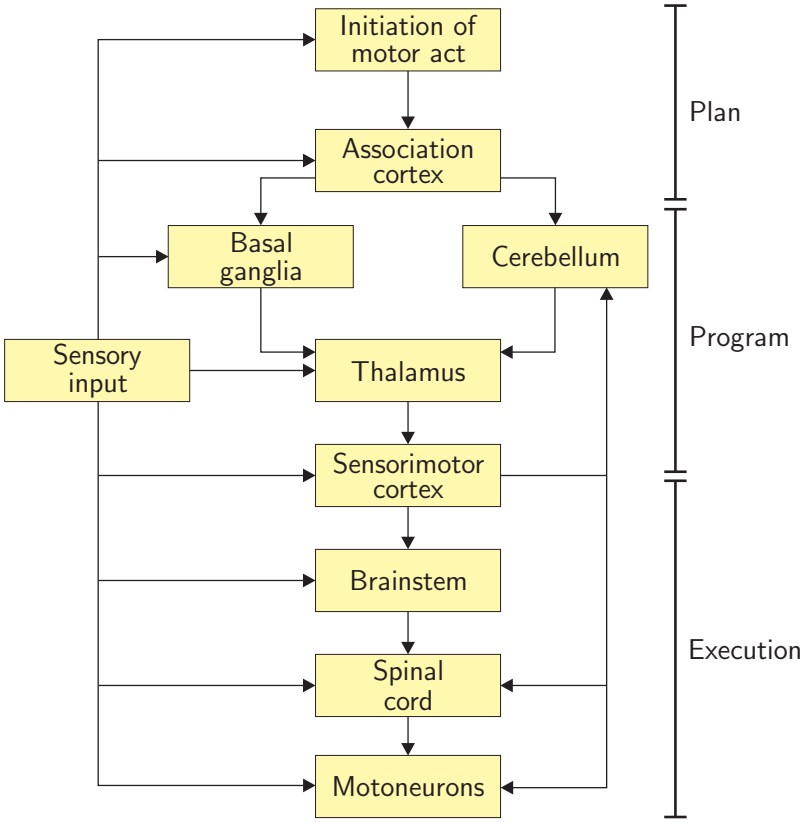

Fig. B.11: Hierarchical representation of the human motor systems (modified from [128]).

brainstem, whereas goal directed movements additionally require the participation of the sensorimotor cortex. The basal ganglia and the cerebellum play an important role in motor control although they are not directly connected with the motoneurons. Instead, they influence the sensorimotor cortex by way of the thalamus.

The motor program information generated in the middle level is transmitted via descending pathways to the lowest level of the motor control hierarchy in order to execute the motor task. The motoneurons that innervate the muscles originate in the brainstem and in the spinal cord.

B.3.3 Muscle Sensors: The Proprioceptors

In order to carry out controlled movements, sensory information about muscle length, velocity, and force are necessary. The receptors that provide appropriate signals are called proprioceptors. The main proprioceptors are the muscle spindles and the Golgi tendon organs.

Muscle Spindles

Muscle spindles are the proprioceptive position and velocity sensors and can be found in most skeletal muscles. Their basic structure is illustrated in Fig. B.12.

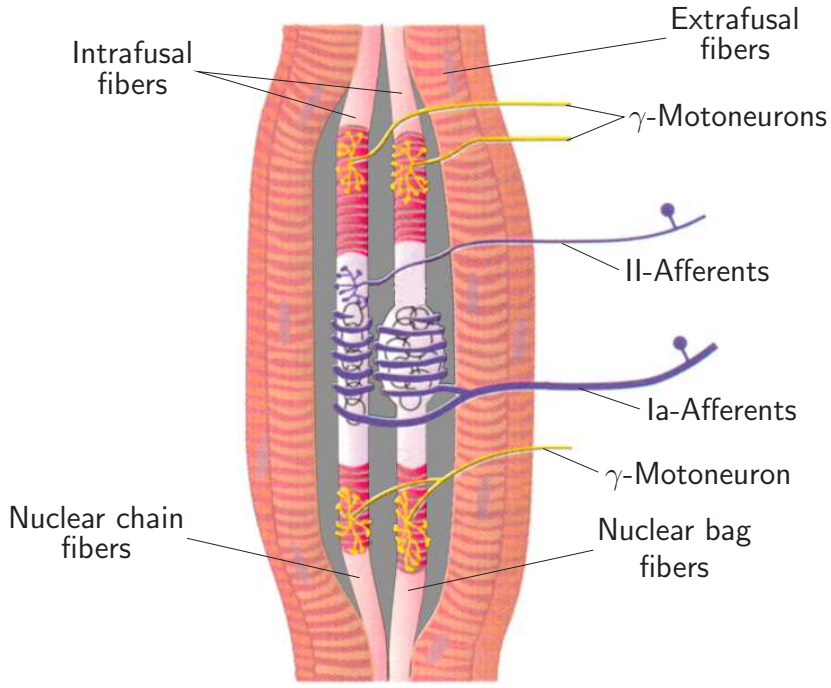

Fig. B.12: Anatomy of a muscle spindle (modified from [149]).

The muscle spindles are embedded in the muscle fibers. The functional units inside the muscle spindle are formed by special types of muscle fibers called intrafusal fibers. The fibers surrounding the spindle are called extrafusal fibers.

There are two different types of intrafusal fibers: The nuclear bag fibers and the nuclear chain fibers (the terms reflect the arrangements of their nuclei). The afferent nerve fibers originating in the muscle spindle are also of two types. The group Ia-fibers (compare Tab. B.1) wind around the middle sections of both, bag and chain fibers. Fibers of group II innervate almost exclusively the nuclear chain fibers. The two nerve groups respond to muscle stretch in different ways. The rate of action potential firing in both kinds is proportional to the muscle spindle length, i.e. the muscle stretch. However, the Ia fibers, that innervate the nuclear bag fibers, too, are much more sensitive to changes of muscle length. Therefore, Ia fibers (or primary fibers) carry position as well as velocity information and group II fibers (or secondary fibers) transport position information, only. The medical terms for position and velocity information are tonic and phasic information.

Contrary to the extrafusal fibers that are innervated by α-motoneurons, intrafusal fibers are innervated by γ-motoneurons (see also Tab. B.1). The axons of the γ-motoneurons are also known as fusimotor fibers. They innervate chain as well as bag fibers which contract when activated. This mechanism changes the sensitivity of the spindles by adjusting the tension of the intrafusal fibers.

Golgi Tendon Organs

The Golgi tendon organs are mechanoreceptors that lie within the tendons in the area of the attachments to the muscle fibers. They are stimulated by the muscle tension and

hence, act as force sensors. Their sensor information is transported to the CNS by group Ib afferent fibers.

B.3.4 Reflexes

A reflex is an involuntary movement as response to a certain stimulus. A classic example is the well known knee jerk or tendon-tap reflex. A reflex action is mediated via the reflex arc that includes at least two neurons, an afferent sensory neuron and an efferent motor neuron. They are interconnected in the spinal cord via just one synapse. Therefore, such reflexes are known as monosynaptic reflexes unlike polysynaptic reflexes where interneurons are interposed between the afferent and efferent neurons. Reflexes often are modulated by the CNS, i.e. they can be inhibited as well as excited by neural input from higher levels.

Since understanding of the principles of the muscle stretch reflex and its interrelated reflexes is important in the context of CNS lesions, they will be explained in the next section.

Muscle Stretch Reflex, Flexion Reflex and Golgi Tendon Reflex

The muscle stretch reflex is illustrated on the left side of Fig. B.13. If a muscle is stretched, the muscle spindles will generate action potentials. The primary afferent neurons are directly connected to the α-motoneurons of the homonymous muscle (same muscle in which spindle is located). Apart from this monosynaptic reflex loop, a disynaptic excitation of α-motoneurons from group II afferents is mediated by excitory spinal interneurons. Since group Ia as well as group II afferents contribute to stretch reflex actions, there is a phasic as well as a tonic reflex component.

The stretch reflex contributes to muscle tone and helps to maintain posture. The flexion reflex is an interrelated protective reflex that aims to rapidly withdraw a limb from a threatening stimulus. In order to withdraw a limb, the flexors have to contract. This is achieved by activation of the stretch reflex mechanism. At the same time the extensors acting on the same joint have to relax. Therefore, the Ia afferents involved in the monosynaptic stretch reflex also inhibit the motor neurons controlling the antagonistic muscles (see Fig. B.13). This pathway is mediated by inhibitory spinal interneurons and is known as reciprocal inhibition.

Also the Golgi tendon reflex is strongly interconnected with the muscle stretch reflex to which it acts complementary. For sake of simplicity it is not explicitly illustrated in Fig. B.13. The Golgi tendon organs are connected to inhibitory interneurons (gray circles) that act on the α-motoneuron of the homonymous muscle and to excitory interneurons acting on the motoneurons of the respective antagonist. This reflex contributes to the maintenance of posture.

A further mechanism that can inhibit reflex action is mediated by Renshaw cells. Some motor axons branch back into the spinal cord and make contact with small interneurons called Renshaw cells which are part of the postsynaptic inhibition acting on the α-motoneurons. This self-inhibiting loop is known as recurrent inhibition.

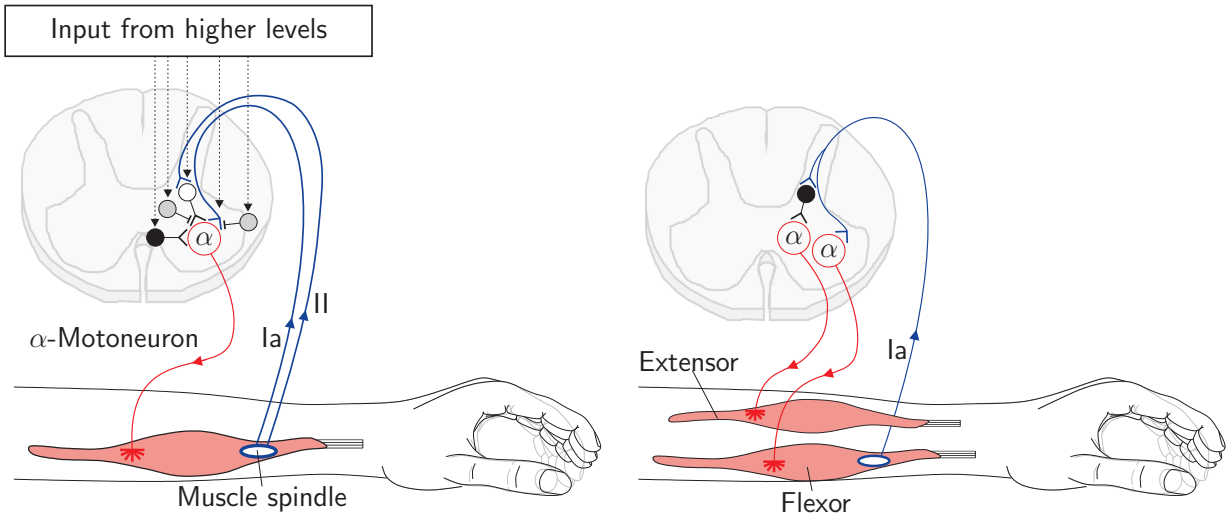

Fig. B.13: Left: Most important mechanisms of the muscle stretch reflex as a simplified schematic. Right: Functional principle of the reciprocal inhibition. Gray circles: Inhibitory spinal interneurons, presynaptic inhibition of group Ia- or group II-afferents. Black circle: Inhibitory spinal interneurons, postsynaptic inhibition from Ia-afferents (reciprocal inhibition), from Ib-afferents and recurrent inhibition (Renshaw cells). White circles: Excitory spinal interneurons in excitory dysynaptic pathways from group II-afferents. The actions of inhibitory as well as excitory interneurons can be modulated by input from higher levels.

B.4 Paresis and Spasticity

The Research Group for Sensorimotor Integration aims to improve the rehabilitation of sensorimotor dysfunctions after CNS-lesions, in particular after stroke. Usually, the patients suffer from hemiparesis which is a paresis in one body hemisphere. Paresis is defined as a reduced ability to perform voluntary motor actions. A Paresis is less severe than a plegia which is a condition of paralysis of parts of the body. In stroke survivors, hemiplegia will often improve to hemiparesis over time. Often paresis occurs in combination with spasticity which will be explained in the next paragraphs.

Spasticity is a motor disorder characterized by a velocity- and position-dependent increase of muscle tone in response to limb motion [12; 92]. Spasticity occurs as a result of lesions in the CNS - either in the spinal cord or within the sensorimotor cortex. As a consequence, signals with inhibitory effects on the stretch reflexes (see Section B.3.4) do not reach the spinal motoneurons, or they are not any more generated. It is generally agreed that the main factor underlying spasticity is a hyperexcitability of α-motoneurons. A number of different factors contribute to spasticity and there arise still some open questions. In [75], there is an excellent review of the current knowledge concerning the origins of spasticity. The main known factors are

- **Reduced presynaptic inhibition**
  Studies on presynaptic Ia inhibition lead to the conclusion that the inhibition is generally weaker in spastic patients than in healthy subjects, see [33; 73; 117], e.g..

- **Reduced reciprocal inhibition**
  A weak reciprocal Ia-inhibition has been reported in [16; 72; 186].

- **Defective activation Ib Interneurons and reduced recurrent inhibition**
  It could be shown, that inhibitory pathways in Ib afferents or Renshaw cells are no longer excited after CNS lesions, see [10], e.g..

- **Increased activation of excitory interneurons**
  Interneurons mediating the disynaptic excitation of α-motoneurons from group II afferents could be shown to have increased excitability, see [36; 115; 171], e.g.. Reflexes of secondary afferents have been found to be significantly enhanced in patients with hemiparesis [108] due to increased excitability of the respective interneurons.

As the above list implies, the term spasticity comprises not only the clinical appearance of increased mechanical resistance during joint motion but all the underlying complex pathologies affecting the reflex arcs. Nevertheless, the term spasticity is often used with the meaning of spastic joint torque, since the level of spasticity can be assessed by joint torque measurements during limb motion. Also within the thesis at hand the denominations spasticity and spastic joint torque are used synonymously.

C The Fingertester

The Fingertester (Fig. C.1) is a self-built actuated measurement device that extends and flexes the index finger at the MCP-joint. The angle α_2 (see coordinate system in Fig 3.10) is position controlled and the joint torque τ_{me} is measured with a self-built torque sensor (see also Fig. 3.22).

The subject's forearm and the palm lie on the ground plate and are immobilized with the fixation plates F and E. As it is illustrated in the side view (c), the pitch angle of the ground plate can be adjusted. This is important to fit the complete device to the subject's forearm pronation[1]. Especially spastic patients often show a abnormal pronation of the affected arm. If the device would force the arm into a position with less pronation, spasticity could increase and bias the measurement.

The index finger is attached to the Fingertester with the collar D, made of elastic plastic material. Different sizes have been assembled in order to guarantee a tight fitting. The collar is attached to the torque sensor C in a slot and can be fixated manually with a knurled thumb screw. The torque is measured with a U-shaped strain-gauge beam arrangement. This idea has been proposed and successfully evaluated in [189]. The axis of rotation of the motor B has to be centered over the axis of rotation of the MCP-joint. Therefore, the position of the motor can be adjusted arbitrarily in the plane of the ground plate. The angle α_2 of the MCP-joint is measured with an incremental encoder.

For safety reasons, the subject holds a dead man's switch with the hand that is not attached to the Fingertester. If the switch is released, a relay in motor supply circuit is released, too and the motor has no power. Additionally, torque and angle are supervised by a software-watchdog that switches the device off if predefined limits are exceeded.

The Fingertester shows an angular resolution of $0.24\,^\circ$ limited by the number of ticks the encoder provides. The torque sensor shows a resolution of 0.08 Ncm. Also the evaluation in terms of accuracy, linearity and crosstalk yielded an excellent performance with respect to the application. The Fingertester has been developed within a student project and further details can be reviewed in the project documentation [214].

[1] Pronation is an anatomical term to describe a rotation movement of a limb . Pronation is the opposite of supination. We see our palm if the forearms are in supination position and if the forearms are in pronation position the backs of the hands becomes visible.

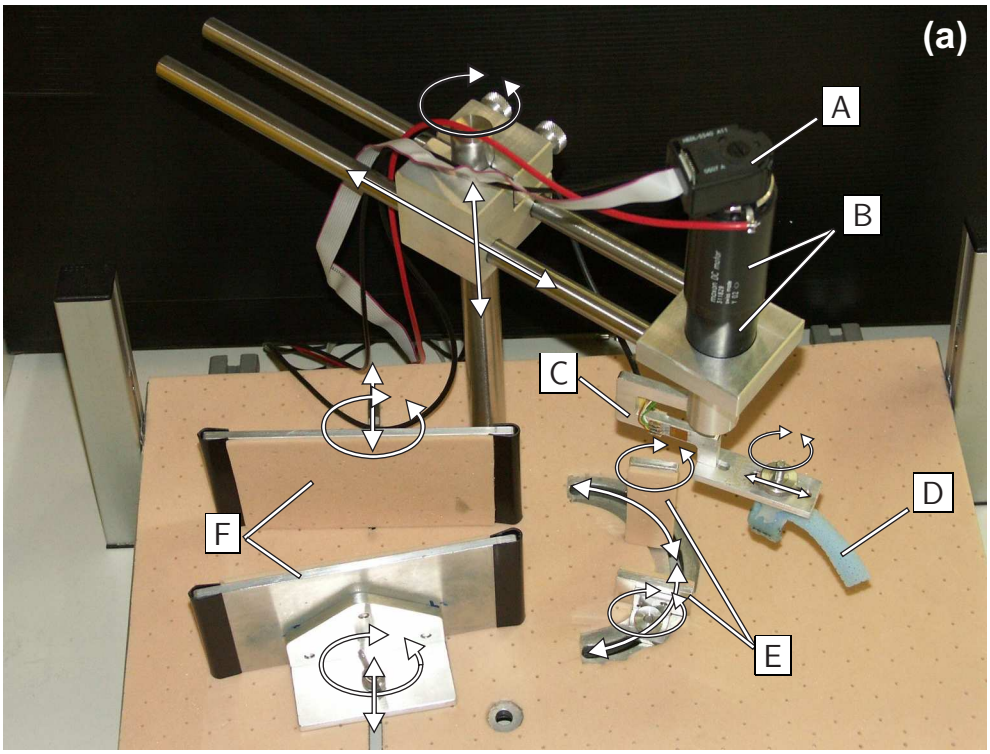

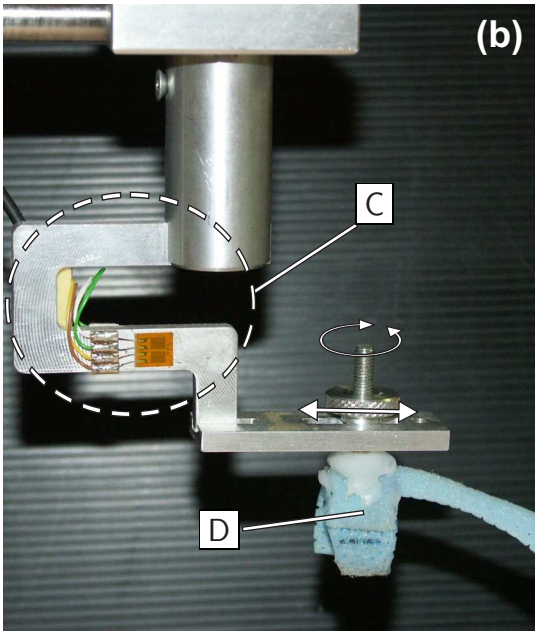

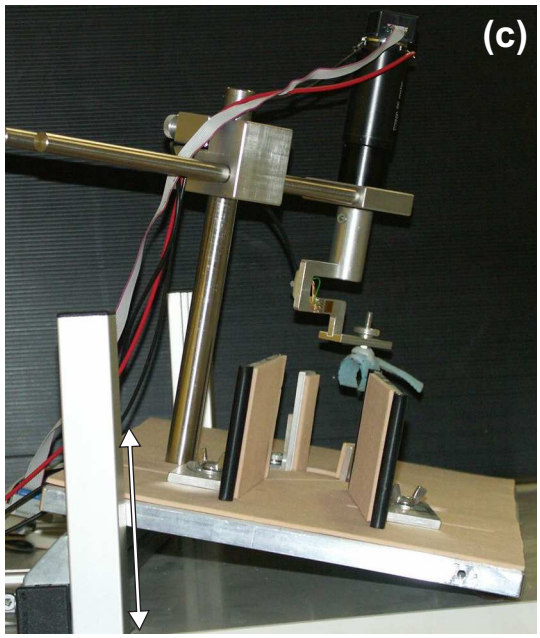

Fig. C.1: The Fingertester: (a) Complete device in top view. (b) Force sensor and collar for the connection to the index finger. (c) Side view, the angle of the ground plate can be adapted. A: Encoder, B: Motor and gear, C: Self built torque sensor, D: Finger collar to connect the index finger to the Fingertester, E: Adjustable palm fixation, F: Adjustable fixation plates for the forearm

Bibliography

[1] M. N. Akman, R. Bengi, M. Karatas, S. Kilinc, S. Sozay, and R. Ozker. Assessment of spasticity using isokinetic dynamometry in patients with spinal cord injury. *Spinal Cord*, 37(9):638–643, 1999.

[2] G. Alon, A. F. Levitt, and P. A. McCarthy. Functional electrical stimulation enhancement of upper extremity functional recovery during stroke rehabilitation: A pilot study. *Neurorehabilitation and Neural Repair*, 21(3):207–215, 2007.

[3] G. Alon, A. F. Levitt, and P. A. McCarthy. Functional electrical stimulation (FES) may modify the poor prognosis of stroke survivors with severe motor loss of the upper extremity: a preliminary study. *Am. J. of Physical Medicine and Rehabilitation*, 87(8):627–636, 2008.

[4] K.N. An, Y. Ueba, E.Y. Chao, W.P. Cooney, and R.L. Linscheid. Tendon excursion and moment arm of index finger muscles. *Journal of Biomechanics*, 16(6):419–425, 1983.

[5] E. Anderson, Z. Bai, C. Bischof, S. Blackford, J. Demmel, J. Dongarra, J. Du Croz, A. Greenbaum, S. Hammarling, A. McKenney, and D. Sorensen. *LAPACK User's Guide*. SIAM, Philadelphia, USA, 3rd edition, 1999.

[6] B. Th. Angerer. Fortschritte in der Erforschung der repetitiven peripheren Magnetstimulation. Dissertation, Fakultät für Elektro- und Informationstechnik, Technische Universität München, München, Germany, January 2006.

[7] B. Armstrong–Hélouvry. Stick slip and control in low-speed motion. *IEEE Trans. on Autom. Control*, 38(10):1483–1496, October 1993.

[8] K. Åström and B. Wittenmark. *Adaptive Control*. Addison-Wesley Publishing Company, 2nd edition, 1995.

[9] S. Axler. *Linear Algebra Done Right*. Springer, Berlin, Germany, 7th edition, 1997.

[10] F. Baldissera, H. Hultborn, and M. Illert. Integration in spinal neuronal systems. In V. B. Brooks, editor, *Handbook of Physiology, the nervous system, motor control, vol. II*, pages 509–595. American Physiology Society, Bethesda, MD, USA, 1981.

[11] P. Basser and B. Roth. New currents in electrical stimulation of excitable tissues. *Annu Rev Biomed Eng*, 2:377–397, 2000.

[12] R. Benecke. General aspects of motor physiology and pathology. In M. Emre and R. Benecke, editors, *Spasticity: The current status of research and treatment*, pages 15–26. The Parthenon Publishing Group, Park Ridge, New Jersey, USA, 1989.

[13] F. Biering-Sørensen, J. B. Nielsen, and K. Klinge. Spasticity-assessment: a review. *Spinal Cord*, 44:708–722, 2006.

[14] James Biggs and Ken Horch. A three-dimensional kinematic model of the human long finger and the muscles that actuate it. *Medical Engineering & Physics*, 21:625–639, 1999.

[15] R. W. Bohannon and M. B. Smith. Interrater reliability of a modified Ashworth scale of muscle spasticity. *Physical Therapy*, 67(2):206–207, 1987.

[16] G. Boorman, M. Hulliger, R. G. Lee, K. Tako, and R. Tanaka. Reciprocal Ia inhibition in patients with spinal spasticity. *Neuroscience letters*, 117:57–60, 1991.

[17] J. Boskovic. Stable adaptive control of a class of first-order nonlinearly parameterized plants. *IEEE Trans. on Autom. Control*, 40(2):347–350, feb 1995.

[18] J. Boskovic. Adaptive control of a class of nonlinearly parameterized plants. *IEEE Trans. on Autom. Control*, 43(7):347–350, jul 1998.

[19] I.E. Brown, E.J.Cheng, and Gerald E. Loeb. Measured and modeled properties of mammalian skeletal muscle: II. The effect of stimulus frequency on force-length and force-velocity relationships. *Journal of Muscle Research and Cell Motility*, 20:627–643, 1999.

[20] I.E. Brown and Gerald E. Loeb. Measured and modeled properties of mammalian skeletal muscle: IV. Dynamics of activation and deactivation. *Journal of Muscle Reseach and Cell Motility*, 20:33–47, 2000.

[21] A. Brunberg, R. Autschbach, and D. Abel. Ein objektorientierter Ansatz zur Modellierung des menschlichen Herz-Kreislauf-Systems. *at-Automatisierungstechnik*, 56(9):476–482, 2008.

[22] C. Cao, A. M. Annaswamy, and F. Kojic. Parameter convergence in nonlinearly parametrized systems. *IEEE Transactions on Automatic Control*, 48(3):397–412, March 2003.

[23] H. J. Chizeck, S. Chang, R. B. Stein, A. Scheiner, and D. C. Ferencz. Identification of electrically stimulated quadriceps muscles in paraplegic subjects. *IEEE Transactions on Biomedical Engineering*, 46(1):51–61, 1999.

[24] E. A. Clancy and K. A. Farry. Adaptive whitening of the electromyogram to improve amplitude estimation. *IEEE Trans. on Biomed. Eng.*, 47(6):709–719, 2000.

[25] E. A. Clancy and N. Hogan. Single cite electromyograph amplitude estimation. *IEEE Trans. on Biomed. Eng.*, 41(2):159–167, 1994.

[26] E. A. Clancy and N. Hogan. Multiple site electromyograph amplitude estimation. *IEEE Trans. on Biomed. Eng.*, 42(2):203–211, 1995.

[27] J. Classen, F. Binkofski, E. Kunesch, and R. Benecke. Magnetic stimulation of peripheral and cranial nerves. In A. Pascual-Leone, N. J. Davey, J.C. Rothwell, E. M. Wassermann, and B. K. Puri, editors, *Handbook of Transcranial Magnetic Stimulation*, chapter 17, pages 185–195. Arnold Publishers, London, United Kingdom, January 2002.

[28] A. B. Conforto, A. Kaelin-Lang, and L. G. Cohen. Increase in hand muscle strength of stroke patients after somatosensory stimulation. *Annals of Neurology*, 51(1):122–125, January 2002.

[29] P. E. Crago, W.D. Memberg, M.K. Usey, M.W. Keith, R.F. Kirsch, G.J. Chapman, M.A. Katorgi, and E.J. Perrault. An elbow extension neuroprosthesis for individuals with tetraplegia. *IEEE Transactions on Rehabiliation Engineering*, 6(1):1–6, March 1998.

[30] P. E. Crago, J. T. Mortimer, and P. H. Peckham. Closed–loop control of force during electrical stimulation of muscle. *IEEE Transactions on Biomedical Engineering*, 27(6):306–312, June 1980.

[31] P. Dayan and L. Abbott. *Theoretical Neuroscience: Computational and Mathematical Modeling of Neural Systems*. MIT-Press, Camebridge, MA, 2001.

[32] P. Deetjen and E.-J. Speckmann. *Physiologie*. Urban & Schwarzenberg Verlag, München, Germany, 2. überarbeitete edition, 1994.

[33] P. J. Delwaide and G. Pennisi. Tizanidine and electrophysiologic analysis of spinal control mechanisms in humans with spasticiy. *Neurology*, 44:21–27, 1994.

[34] S. J. Dorgan and R. B. Reilly. A model for human skin impedance during surface functional neuromuscular stimulation. *IEEE Transactions on Rehabilitation Engineering*, 7(3):341–348, September 1999.

[35] H. El Edrissi, M.H.G. Verhaegen, B.R.J. Haverkamp, and C.T. Chou. Off- and on-line identification of discrete time LTI-systems using separable least squares. In *Proceedings of the 37th IEEE Conference on Decision and Control, Dec. 1998, Tampa Florida*, volume 1, pages 720–724. IEEE, 1998.

[36] J. Eriksson, B. Olausson, and E. Jankowska. Antiseptic effects of L-Dopa. *Exp. Brain Res.*, 111:296–304, 1996.

[37] A. Esteki and J.M. Mansour. An experimentally based nonlinear viscoelastic model of joint passive moment. *Journal of Biomechanics*, 29(4):443–450, 1996.

[38] J. Fee and A. Foulds. Neuromuscular modeling of spasticity in cerebral palsy. *IEEE Transactions on Neural Systems and Rehabilitation Engineering*, 12(1):55–64, 2004.

[39] J. W. Fee. The leg drop pendulum test in spastic cerebral palsy: The addition of active elements to a passive, nonlinear, second order model. In *Proceedings of the 1995 Fourteenth Southern Biomedical Engineering Conference*, pages 104–106, 1995.

[40] M. Ferrarin, F. Palazzo, R. Riener, and J. Quintern. Model–based control of FES–induced single joint movements. *IEEE Transactions on Neural Systems and Rehabilitation Engineering*, 9(3):245–257, September 2001.

[41] M. Ferrarin and A. Pedotti. The relationship between electrical stimulus and joint torque: A dynamic model. *IEEE Transactions on Rehabilitation Engineering*, 8(3):342–352, 2000.

[42] M. Ferraro, J.J. Palazzolo, J. Krol, H. I. Krebs, N. Hogan, and B. T. Volpe. Robot-aided sensorimotor arm training improves outcome in patients with chronic stroke. *Neurology*, 61(11):1604–1607, 2003.

[43] S. Field. *Discovering Statistics with SPSS*. ISM Introducing Statistical Methods. SAGE Publications Ltd, 1 Oliver's Yard, 55 City Road, London EC1Y 1SP, 2. edition, 2005.

[44] G. C. Filligoi and P. Mandarini. Some theoretic results in a digital EMG-signal processor. *IEEE Trans. on Biomed. Eng.*, 31(4):333–341, 1984.

[45] R. H. Fitts. Cellular mechanisms of muscle fatigue. *The American Physiological Society*, 74:49–95, 1994.

[46] O. Foellinger. *Regelungstechnik – Einführung in die Methoden und ihre Anwendungen*. Hüthig Buch Verlag, Heidelberg, Germany, 8th edition, 1994.

[47] N.K. Fowler, A.C. Nicol, B. Condon, and D. Hadley. Method of determination of three dimensional index finger moment arms and tendon lines of action using high resolution MRI-scans. *Journal of Biomechanics*, 34:791–797, 2001.

[48] H. M. Franken, P. H. Veltink, R. Tijsmans, R. Nijmeier, and H. B. K. Boom. Identification of quadriceps-shank dynamics using randomized interpulse interval stimulation. *IEEE Transactions on Rehabilitation Engineering*, 3(2):182–190, 1995.

[49] A. C. Franzoi, C. Castro, and C. Cardone. Isokinetic assessment of spasticity in subjects with traumatic spinal cord injury. *Spinal Cord*, 37(9):416–420, 1999.

[50] J. Freiwald, C. Baumgard, and P. Konrad. *Einführung in die Elektromyographie*. Spitta Verlag, Balingen, Germany, 1st edition, 2007.

[51] C. Frigo, M. Ferrarin, W. Frasson, E. Pavan, and R. Thorsen. EMG signals detection and processing for on–line control of functional electrical stimulation. *Journal of Electromyography and Kinesiology*, 10(5):351–360, October 2000.

[52] L. Galiana, J. Fung, and R. Kearney. Identification of intrinsic and reflex ankle stiffness components in stroke patients. *Experimental Brain Research*, 165(4):422–434, 2005.

[53] H. Gollee and K. J. Hunt. Nonlinear modelling and control of electrically stimulated muscle: a local model network approach. *International Journal of Control*, 68(6):1259–1288, 1997.

[54] H. Gollee, D. J. Murray–Smith, and J. C. Jarvis. A nonlinear approach to modeling of electrically stimulated skeletal muscle. *IEEE Transactions on Biomedical Engineering*, 48(4):406–415, April 2001.

[55] H.G. Golub and V. Perreyra. The differentiation of pseudoinverses and nonlinear least squares problems whose variables are separate. *SIAM Journal of Numerical Analysis*, 10:413–432, 1973.

[56] H.G. Golub and C.F. van Loan. *Matrix Computations*. The John's Hopkins University Press, 1989.

[57] J. Hahlen and H. K. Selbmann, editors. *Gesundheitsberichterstattung des Bundes*, chapter Krankheiten des zerebrovaskulären Systems. Statistisches Bundesamt / Robert Koch–Institut, Wiesbaden, Germany, November 2007. http://www.gbe-bund.de (Nov. 10. 2007).

[58] R. Happee. Inverse dynamic optimization including muscular dynamics, a new simulation method applied to goal directed movements. *Journal of Biomechanics*, 27(7):953–960, July 1994.

[59] R.L. Hart, K.L. Kilgore, and P.H. Peckham. A comparison between control methods for implanted FES hand-grasp systems. *IEEE Transactions on Rehabilitation Engineering*, 6(2):208–218, June 1998.

[60] H. Hatze. *Myocybernetic Control Models of Skeletal Muscle — Characteristics and Applications*. Unisa Press, Pretoria, South Africa, 1981.

[61] P. M. Havel. Geregelte Induktion von Reich- und Greifbewegungen am Menschen mittels repetitiver peripherer Magnetstimulation. Dissertation, Fakultät für Elektro- und Informationstechnik, Technische Universität München, München, Germany, May 2002.

[62] S. S. Haykin. *Adaptive Filter Theory*. Prentice Hall information and system sciences series. Prentice Hall PTR, Upper Saddle River, New Jersey (USA), 4. edition, 2002.

[63] B. Heldmann, G. Kerkhoff, A. Struppler, P. M. Havel, and Th. Jahn. Repetitive peripheral magnetic stimulation alleviates tactile extinction. *NeuroReport*, 11(14):3193–3198, September 2000.

[64] E. Henneman, G. Somjen, and D. Carpenter. Excitability and inhibitability of motoneurons of different sizes. *J. of. Neurophysiology*, 28:599–620, 1965.

[65] S. Hesse, C. Werner, and A. Bardeleben. Der schwer betroffene Arm ohne distale Willküraktivität — ein "Sorgenkind" der Rehabilitation nach Schlaganfall. *Neurologie und Rehabilitation*, 10(3):123–129, May 2004.

[66] M. Heyters, A. Carpentier, J. Duchatreau, and K. Hainaut. Twitch analysis as an approach to motor unit activation during electrical stimulation. *Can. J. of Appl. Physiol.*, 19(4):451–461, 1994.

[67] A. V. Hill. *Proceedings of the Royal Society of London*, volume 126 of *Series B, Biological Sciences*, chapter The heat of shortening and the dynamic constants of muscle, pages 136–195. Royal Society of London, London, United Kingdom, 1938.

[68] A. V. Hill. *Proceedings of the Royal Society of London*, volume 136 of *Series B, Biological Sciences*, chapter The heat of activation und the heat of shortening in a muscle twitch, pages 195–211. Royal Society of London, London, United Kingdom, 1949.

[69] S. Hofmann. Identifikation von nichtlinearen mechatronischen Systemen auf der Basis von Volterra–Reihen. Dissertation, Fakultät für Elektro- und Informationstechnik, Technische Universität München, München, Germany, April 2003.

[70] N. Hogan, H. I. Krebs, B. Rohrer, J. J. Palazzolo, L. Dipietro, S. E. Fasoli, J. Stein, R. Hughes, W. R. Frontera, and D. Lynch. Motions or muscles?: Some behavioral factors underlying robotic assistance of motor recovery. *Journal of Rehabilitation Research & Development*, 43(5):605–618, 2006.

[71] N. Hogan and R. W. Mann. Myoelectric signal processing: Optimal estimation applied to electromyography – part 1. derivation of the optimal myoprocessor. *IEEE Trans. on Biomed. Eng.*, 27(7):382–395, 1980.

[72] H. Hultborn and J. Malmsten. Changes in segmental reflexes following chronic spinal cord hemisection in the cat. II. Conditioned monosynaptic test reflexes. *Acta Physiol. Scand.*, 119:423–433, 1983.

[73] J. F. Iles and R. C. Roberts. Presynaptic inhibition of monosynaptic reflexes in the lower limbs of subjects with upper motoneuron disease. *J. of Neurol. Neurosurg. Psychiatry*, 49:937–944, 1986.

[74] A. Isidori. *Nonlinear Control Systems 1.* Springer–Verlag, Berlin, Germany, 3rd edition, 1995.

[75] E. Jankowska and I. Hammar. Spinal interneurons; how can studies in animals contribute to the understanding of spinal interneuronal systems in man? *Brain Research Reviews*, 40:19–28, 2002.

[76] S. Jezernik, R. G. V. Wassink, and Thierry Keller. Sliding mode closed-loop control of FES: Controlling the shank movement. *IEEE Trans. on Biomedical Engineering*, 51(2):263–272, 2004.

[77] A. Jobin and M. F. Levin. Regulation of stretch reflex threshold in elbow flexors in children with cerebral palsy: a new measure of spasticity. *Developmental Medicine and Child Neurology*, 42(8):531–540, 2000.

[78] T. H. Kakebeeke, H. Lechner, M. Baumberger, J. Denoth, D. Michel, and H. Knecht. The importance of posture on the isokinetic assessment of spasticity. *Spinal Cord*, 40(5):236–243, 2002.

[79] R. E. Kearney, R. B. Stein, and L. Parameswaran. Identification of intrinsic and reflex contribution to human ankle stiffness dynamics. *IEEE Trans. on Biomed. Eng.*, 44(6):493–504, 1997.

[80] G. Kerkhoff. Modulation and rehabilitation of spatial neglect by sensory stimulation. In C. Prablanc, D. Pélisson, and Y. Rossetti, editors, *Neural Control of Space Coding and Action Production*, volume 142 of *Progress in Brain Research*, chapter 16, pages 257–271. Elsevier Science B.V., Amsterdam, The Netherlands, 2003.

[81] G. Kerkhoff, B. Heldmann, A. Struppler, P. M. Havel, and Th. Jahn. The effects of magnetic stimulation and attentional cueing on tactile extinction. *Cortex*, 37(5):719–723, December 2001. Proceeding of the 19th European Workshop on Cognitive Neuropsychology (Bressanone 2001).

[82] H. K. Khalil. *Nonlinear systems*. Prentice Hall Inc., Upper Saddle River, New Jersey, USA, 2000.

[83] M. Khoo. *Physiological Control Systems: Analysis, Simulation, and Estimation*. John Wiley and Sons, Hoboken (USA), 1st edition, 1999.

[84] A. Killich. *Prozeßidentifikation durch Gewichtsfolgenschätzung*, volume 268 of *Fortschritt–Berichte VDI, Reihe 8*. VDI–Verlag, Düsseldorf, Germany, September 1991.

[85] K. Kitching, D. Cole, and D. Cebon. Performance of a semi-active damper for heavy vehicles. *ASME J. of. Dynamic Systems, Measurement and Control*, 122(3):498–506, 2000.

[86] D. V. Knudson. *Fundamentals of Biomechanics*. Kluwer Academic/Plenum Publishers, 1st edition, 2003.

[87] V. T. Krasteva, S. P. Papazov, and I. K. Daskalov. Peripheral nerve magnetic stimulation: influence of tissue non–homogeneity. *BioMedical Engineering OnLine*, 2(19):1–14, December 2003.

[88] H. I. Krebs, J. J. Palazzolo, L. Dipietro, and B. T. Volpe. Rehabilitation robotics: Performance-based progressive robot-assisted therapy. *Autonomous Robots*, 15(1):7–20, 2003.

[89] F. T. Krogh. Efficient implementation of a variable projection algorithm for nonlinear least squares problems. *Communications of the ACM*, 17(3):167–169, 1974.

[90] M. Krstic, I. Kanellakopoulos, and P. V. Kokotovic. *Nonlinear and Adaptive Control Design*. Wiley, New York, 1995.

[91] J. Kurth. *Identifikation nichtlinearer Systeme mit komprimierten Volterra–Reihen*, volume 459 of *Fortschritt–Berichte VDI, Reihe 8*. VDI–Verlag, Düsseldorf, Germany, September 1995.

[92] J. W. Lance. Spasticity: Disordered motor control. In R. G. Feldman, R. R. Young, and W. P. Koella, editors, *Year Book Medical Publishers*, pages 485–494. 1980.

[93] E. Langzam, E. Isakov, and J. Mizrahi. Evaluation of methods for extraction of the volitional EMG in dynamic hybrid muscle activation. *Journal of Neuroengineering and Rehabilitation*, 3(27), 2006.

[94] E. Langzam, Y. Nemirovsky, E. Isakov, and J. Mizrahi. Muscle enhancement using closed-loop electrical stimulation: Volitional versus induced torque. *Journal of Electromyography and Kinesiology*, 17(3):275–284, 2006.

[95] M. A. Lemay and P. E. Crago. A dynamic model for simulating movements of the elbow, forearm, and wrist. *Journal of Biomechanics*, 29(10):1319–1330, October 1996.

[96] K. Levenberg. A method for the solution of certain problems in least squares. *Quarterly of Applied Mathematics*, 2:164–168, 1944.

[97] L. Ljung. *System Identification — Theory for the User*. PTR Prentice Hall Information and System Sciences Series. Prentice Hall PTR, Upper Saddle River, New Jersey (USA), 2nd edition, 1999.

[98] L. Ljung and T. Söderström. *Theory and Practice of Recursive Identification*, volume 4 of *The MIT Press Series in Signal Processing, Optimization, and Control*. MIT Press, Cambridge, Massachusetts (USA), 1987.

[99] L. Lünenburger, G. Colombo, R. Riener, and V. Dietz. Clinical assessments performed during robotic rehabilitation by the gait training robot lokomat. In *International Conference on Rehabilitation Robotics (ICORR)*, pages 345–348, Chicago, June 2005.

[100] A.-P. Loh, A. M. Annaswamy, and F. P. Skantze. Adaptation in the presence of a general nonlinear parameterization: An error model approach. *IEEE Transactions on Automatic Control*, 44(9):1634–1652, September 1999.

[101] C. K. Low, P. Pereira, R. T. H. NG, Y. P. Low, and H. P. Wong. The effect of the extent of a1 pulley release on the force required to flex the digits. *Journal of Hand Surgery (British and European Volume)*, 23B(1):46–49, Februar 1998.

[102] J. C. De Luca. Physiology and mathematics of myoelectric signals. *IEEE Trans. on Biomedical Engineering*, 26(6):313–325, 1979.

[103] J. C. De Luca. The use of surface electromyography in biomechanics. *Journal of Applied Biomechanics*, 13:135–163, 1997.

[104] Magstim. Stimulating coils. Datasheet, The Magstim Company Ltd., Whitland, United Kingdom, December 2008. `http://www.magstim.com` (Dec. 2008).

[105] Magventure. Coils overview. Datasheets, MagVenture, Lucernemarken 15,3520 Farum Denmark, December 2008. `http://www.magventure.com/` (Dec. 2008).

[106] R. Marino and P. Tomei. Global adaptive output-feedback control of nonlinear systems, Part I: Linear parameterization; Part II: Nonlinear parameterization. *IEEE Trans. on Autom. contr.*, 38:17–48, 1993.

[107] D. Marquardt. An algorithm for least-squares estimation of nonlinear parameters. *SIAM Journal of Applied Mathematics*, 11:431–441, 1963.

[108] P. Marque, M. Simonetta-Moreau, E. Maupas, and C. F. Roques. Facilitation of transmission in heteronymous group II pathways in spastic hemiplegic patients. *J. of Neurol. Neurosurg. Psychiatry*, 70:36–42, 2001.

[109] Matlab. *The MathWorks, Inc.* `http://www.mathworks.com`.

[110] L. M. Mendell. The size principle: A rule describing the recruitment of motoneurons. *J. of Neurophysiology*, 93:3024–3026, 2005.

[111] P. A. Merton. The silent period in a muscle of the human hand. *Journal of Physiology*, 114(1-2):183–198, June 1951.

[112] P. C. Miranda, M. Hallett, and P. J. Basser. The electric field induced in the brain by magnetic stimulation: a 3–D finite–element analysis of the effect of tissue heterogeneity and anisotropy. *IEEE Transactions on Biomedical Engineering*, 50(9):1074–1085, September 2003.

[113] M. M. Mirbagheri, H. Barbeau, M. Ladouceur, and R. E. Kearney. Intrinsic and reflex stiffness in normal and spastic, spinal cord injured subjects. *Experimental Brain Research*, 141(9):446–459, 2001.

[114] J. J. Moré. The levenberg-marquardt algorithm, implementation and theory. *Lecture Notes in Mathematics*, 630:105–116, 1977.

[115] H. Morita, C. Crone, D. Christenhuis, N. T. Petersen, and J.B. Nielsen. Modulation of presynaptic inhibition and disynaptic reciprocal Ia inhibition during voluntary movement in spasticiy. *Brain*, 124:826–837, 2001.

[116] S. S. Nagarajan and D. M. Durand. Analysis of magnetic stimulation of a concentric axon in a nerve bundle. *IEEE Transactions on Biomedical Engineering*, 42(9):926–933, September 1995.

[117] K. Nakashima, J. C. Rothwell, B. L. Day, P. D. Thompson, K. Shannon, and C. D. Marsden. Reciprocal inhibition between forearm muscles in patients with writer's cramp, symptomatic hemidystonia and hemiparesis due to stroke. *Brain*, 112:681–697, 1989.

[118] K. S. Narendra and A. M. Annaswamy. *Stable Adaptive Systems*. PTR Prentice Hall Information and System Sciences Series. Prentice Hall, Inc., Englewood Cliffs, New Jersey (USA), 1989.

[119] K. S. Narendra and P. Kudva. Stable adaptive schemes for system identification and control - parts 1 and 2. *IEEE Transactions on Systems, Man and Cybernetics*, 4:542–560, November 1974.

[120] R. H. Nathan. Control strategies in FNS systems for the upper extremities. *Crit Rev Biomed Eng.*, 21(6):485–568, 1993.

[121] G. Nelles, W. Jentzen, M. Jueptner, S. Müller, and H. C. Diener. Arm training induced brain plasticity in stroke studied with serial positron emission tomography. *NeuroImage*, 13:1146–1154, June 2001.

[122] O. Nelles. *Nonlinear System Identification — From Classical Approaches to Neural Networks and Fuzzy Models*. Springer Verlag, Heidelberg, Germany, 2001.

[123] L. S. H. Ngia. Separable nonlinear least-squares methods for efficient off-line and on-line modeling of systems using kautz and laguerre filters. *IEEE Transactions on Circuits and Systems*, 48(6):562–579, June 2001.

[124] H.B. Nielsen. Damping parameter in marquardt's method. IMM, DTU, 1999. `http://www.imm.dtu.dk/~hbn/publ/TR9905.ps` (Dez. 2008).

[125] K. Ogata. *Modern Control Engineering*. Prentice Hall, Upper Saddle River, New Jersey, USA, 4th edition, 2002.

[126] A. Pandyan, G. Johnson, C. Price, R. Curless, M. Barnes, and H. Rodgers. A review of properties and limitations of the ashworth and the modified ashworth scales as measures of spasticity. *Clinical Rehabilitation*, 13(5):373–383, October 1999.

[127] T. Platz, C. Eickhof, G. Nuyens, and P. Vuadens. Clinical scales for the assessment of spasticity, associated phenomena, and function: A systematic review of the literature. *Disability and Rehabilitation*, 27(1-2):7–18, 2005.

[128] G. Pocock and C. D. Richards. *Human physiology – The basis of medicine*. Oxford University Press, Oxford, UK, 3rd edition, 2006.

[129] D. B. Popovic. Externally powered and controlled orthotics and prosthetics. In J. D. Bronzino, editor, *The Biomedical Engineering Handbook*, chapter 138, pages 2086–2099. CRC Press in Cooperation with IEEE Press, Boca Ranton, Florida (USA), January 1995.

[130] M. R. Popovic, D. B. Popovic, and T. Keller. Neuroprostheses for grasping. *Neurological Research*, 24:443–452, 2002.

[131] M. R. Popovic, T. A. Thrasher, M. E. Adams, V. Takes, V. Zivonovic, and M. I. Tonack. Functional electrical therapy: Retraining grasping in spinal cord injury. *Spinal Cord*, 44(3):143–151, 2006.

[132] M. R. Popovic, T. A. Thrasher, V. Zivonovic, J. Takaki, and V. Hajek. Neuroprosthesis for restoring reaching and grasping functions in severe hemiplegic patients. *Neuromodulation*, 8(1):60–74, 2005.

[133] F. Previdi. Identification of black-box nonlinear models for lower limb movement control using functional electrical stimulation. *Control Engineering Practice*, 10(1):91–99, 2002.

[134] F. Previdi and M. Lovera. Identification on non-linear parametrically varying models using seperable least squares. *Int. J. of Control*, 77, 2004.

[135] R. Riener. Neurophysiologische und biomechanische Modellierung zur Entwicklung geregelter Neuroprothesen. Dissertation, Fakultät für Elektro- und Informationstechnik, Technische Universität München, München, Germany, January 1997.

[136] R. Riener, M. Frey, T. Nef, M. Bernhardt, and G. Colombo. New developments in rehabilitation robotics. In *Proceedings of the IEEE conference on Mechatronics & Robotics 2004*, pages 1397–1402, sep 2004.

[137] R. Riener and T. Fuhr. Patient-driven control of FES-supported standing up. *IEEE Trans. On Rehab. Eng.*, 6:113–124, 1998.

[138] R. Riener, L. Lünenburger, and G. Colombo. Human-centered robotics applied to gait training and assessment. *Journal of Rehabilitation Research & Development*, 43(5):679–694, 2006.

[139] R. Riener, L. Lünenburger, S. Jezernik, M. Anderschitz, G. Colombo, and V. Dietz. Patient-cooperative strategies for robot-aided treadmill training: First experimental results. *IEEE Trans. on Neural Systems and Rehabilitation Engineering*, 13(3):380–393, 2005.

[140] R. Riener, J. Quintern, E. Psaier, and G. Schmidt. Physiologically based multi-input model of muscle activation. In A. Pedotti, M. Ferrarin, J. Quintern, and R. Riener, editors, *Neuroprosthetics from basic research to clinical application*, pages 95–114. Springer–Verlag, Heidelberg, Germany, 1996.

[141] Robert Riener and Thomas Edrich. Identification of passive elastic joint moments in the lower extremities. *Journal of Biomechanics*, 32:539–544, dec 1999.

[142] J. Riess and J. Abbas. Adaptive neural network control of cyclic movements using functional neuromuscular stimulation. *IEEE Trans. on Rehabilitation Engineering*, 8(1):42–52, 2000.

[143] J. Ruohonen, P. Ravazzani, J. Nilsson, M. Panizza, F. Grandori, and G. Tognola. A volume-conduction analysis of magnetic stimulation of peripheral nerves. *IEEE Trans. on. Biommed. Eng.*, 43:669–678, 1996.

[144] S. Sastry and M. Bodson. *Adaptive Control: Stability, Convergence and Robustness.* Prentice Hall, Englwood Cliffs, NJ, USA, 1989.

[145] S. Saxena, S. Nikolic, and D. Popovic. An EMG-controlled grasping system for tetraplegics. *J. of Rehabilitation Research and Development*, 32(1):17–24, 1995.

[146] T. Schauer, W. Holderbaum, and K. Hunt. Sliding-mode control of knee-joint angle: experimental results. In *Proceedings of the 7th conference of the international fes society*, pages 316–318, Ljubljana, Slovenia, September 2002.

[147] T. Schauer, N.O. Negard, F. Previdi, K.J. Hunt, M.H. Fraser, E. Ferchland, and J. Raisch. Online identification and nonlinear control of the electrically stimulated quadriceps muscle. *Control Engineering Practice*, 13:1207–1219, 2005.

[148] T. Schauer, R. Salbert, N. Negård, and J. Raisch. Detection and filtering of EMG for assessing voluntary muscle activity during fes. In *Proceedings of the 9th conference of the international fes society*, Bournmouth, UK, September 2004.

[149] R. F. Schmidt, editor. *Neuro- und Sinnesphysiologie*. Springer Lehrbuch. Springer–Verlag, Heidelberg, Germany, 3. edition, January 1998.

[150] B.D. Schmit and W.Z. Rymer. Identification of static and dynamic components of reflex sensitivity in spastic elbow flexors using a muscle activation model. *Annals of Biomedical Engineering*, 29(4):330–339, February 2001.

[151] D. Schröder, editor. *Intelligent Observer and Control Design for Nonlinear Systems*. Springer–Verlag, Heidelberg, Germany, 2000.

[152] D. Schröder. *Elektrische Antriebe — Regelung von Antriebssystemen*. Springer Lehrbuch. Springer–Verlag, Heidelberg, Germany, 2., überarb. u. erw. edition, 2001.

[153] L. Sciavicco and B. Siciliano. *Modelling and Control of Robot Manipulators*. Springer–Verlag, Berlin, Germany, 2nd edition, 2000.

[154] U. Seemann. Magnetstimulation am peripheren Nerven — Vergleich von Stärke und Fokalität elektrischer und magnetischer Stimulation in verschiedenen umgebenden Medien. Dissertation, Fakultät für Medizin, Technische Universität München, München, Germany, April 1998.

[155] S. Sennels, F. Biering-Sørensen, O.T. Andersen, and S. D. Hansen. Functional neuromuscular stimulation controlled by surface electromyographic signals produced by volitional activation of the same muscle: Adaptive removal of the muscle response from the recorded EMG-signal. *IEEE Transactions on Rehabilitation Engineering*, 5(2):195–206, 1997.

[156] S. Sennels, F. Biering-Sørensen, S. D. Hansen, and O.T. Andersen. Adaptive filters for muscle response suppression. In *18th Annual International Conference of the IEEE Engineering in Medicine and Biology Society, Amsterdam*, 1996.

[157] Sensoray. Embedded electronics. Datasheet, Sensoray Co., Inc., Tigard, Or 97223, USA, December 2008. `http://www.sensoray.com`.

[158] D. Seto, M. Annaswamy, and J. Baillieul. Adaptive control of nonlinear systems with a triangular structure. *IEEE Trans. on Autom. Contr.*, 39:1411–1428, 1994.

[159] L. R. Sheffler and J. Chae. Neuromuscular electrical stimulation in neurorehabilitation. *Muscle & Nerve*, 35:562–590, 2007.

[160] R. Shepherd and J. Carr. Scientific basis of neurological physiotherapy: Bridging the gap between science and practice. *Neurologie & Rehabilitation*, 11(1):1–6, March 2005.

[161] E. M. Siekierka, K. Eng, C. Bassetti, A. Blickensdorfer, M.S. Cameirao, V. Dietz, A. Duff, F. Erol, T. Ettlin, D.M. Hermann, T. Keller, B. Keisker, J. Kesselring, R. Kleiser, S. Kollias, J.P. Kool, A. Kurre, S. Mangold, T. Nef, P. Pyk, R. Riener, C. Schuster, F. Tosi, P.F. Verschure, and L. Zimmerli. New technologies and concepts for rehabilitation in the acute phase of stroke: a collaborative matrix. *Neurodegenerative Diseases*, 4(1):57–69, February 2007.

[162] J.-J. E. Slotine and W. Li. *Applied Nonlinear Control*. Pearson Education. Prentice Hall, Inc., Englewood Cliffs, New Jersey (USA), 1991.

[163] E. Sontag. Some new directions in control theory inspired by systems biology. *Systems Biology*, 1(1):9–18, 2004.

[164] D. Staudenmann, I. Kingma, A. Daffertshofer, D. F. Stegemann, and J. H. van Steen. Improving EMG-based muscle force estimation by using a high-density EMG-grid and principal component analysis. *IEEE Trans. on Biom. Eng.*, 53(4):712–719, 2006.

[165] A. Struppler, B. Th. Angerer, Ch. Gündisch, and P. M. Havel. Modulatory effect of repetitive peripheral magnetic stimulation (RPMS) on the skeletal muscle tone (stabilization of the elbow joint) on healthy subjects. *Experimental Brain Research*, 157(1):59–66, 2004.

[166] A. Struppler, P. M. Havel, and P. Müller-Barna. Facilitation of skilled finger movements by repetitive peripheral magnetic stimulation (RPMS) — A new approach in central paresis. *NeuroRehabilitation*, 18(1):69–82, May 2003.

[167] A. Struppler, C. Jakob, P. Müller-Barna, M. Schmid, H.-W. Lorenzen, M. Prosiegel, and M. Paulig. Eine neue Methode zur Frührehabilitation zentralbedingter Lähmungen von Arm und Hand mittels Magnetstimulation. *Zeitschrift für EEG und EMG*, 27:151–157, 1996.

[168] E. Taub and G. Uswatte. Constraint–Induced Movement Therapy: Bridging from the primate laboratory to the stroke rehabilitation laboratory. *Journal of Rehabilitation Medicine*, 35(Supplement 41):34–40, October 2003.

[169] E. Taub, G. Uswatte, and R. Pidikiti. Constraint–Induced Movement Therapy: A new family of techniques with broad application to physical rehabilitation — a clinical review. *Journal of Rehabilitation Research and Development*, 36(3):237–251, July 1999.

[170] P. Taylor and P. Chappell. Variation in system gain when using voluntary EMG to control electrical stimulation of the same muscle. In *Proceedings of the 9th Annual Conference of the International FES Society*, Bournemouth, UK, December 2004.

[171] A. F. Thilmann, D. J. Burke, and W. Z. E. Rymer. *Spasticity: Mechanisms and Management*. Springer, Heidelberg, Germany, 1993.

[172] T. A. Thrasher, H.M. Flett, and M. R. Popovic. Gait training regimen for incomplete spinal cord injury using functional electrical stimulation. *Spinal Cord*, 44(6):357–361, 2005.

[173] I. Tyukin, D. Prokhorov, and C. Leeuven. Adaptation and parameter estimation in systems with unstable target dynamics and nonlinear parameterization. *IEEE Trans. on Automatic Control*, 52(9):1543–1559, September 2007.

[174] I. Tyukin, D. Prokhorov, and V. Terekhov. Adaptive control with nonconvex parameterization. *IEEE Trans. on Automatic Control*, 48(4):554–567, April 2003.

[175] R. Vachenauer. Zur Optimierung der repetitiven Magnetstimulation. Dissertation, Fakultät für Elektro- und Informationstechnik, Technische Universität München, München, Germany, November 1998.

[176] P. H. Veltink, H. J. Chizeck, P. E. Crago, and A. El-Bialy. Nonlinear joint angle control for artificially stimulated muscle. *IEEE Transactions on Biomedical Engineering*, 39(4):368–380, November 1992.

[177] G. E. Voerman, M. Gregoric, and H. J. Hermens. Neurophysiological methods for the assessment of spasticity: The hoffmann reflex, the tendon reflex, and the stretch reflex. *Disability and Rehabilitation*, 27(1-2):33–68, 2005.

[178] T. von Lanz and W.Wachsmuth. *Praktische Anatomie, Erster Band / Dritter Teil, Arm*, volume 1. Erste Auflage, Verlag von Julius Springer, 1935.

[179] D.T. Westwick and R.E. Kearney. Separable least squares identification of nonlinear hammerstein models: Application to stretch reflex dynamics. *Annals of Biomedical Engineering*, 29(8):707–718, 2001.

[180] D.T. Westwick and R.E. Kearney. *Identification of Nonlinear Physiological Systems*. John Wiley and Sons, Hoboken (USA), 1st edition, 2003.

[181] Th. Weyh. Magnetstimulation neuronaler Systeme. Dissertation, Universität der Bundeswehr, Neubiberg, Germany, November 1995.

[182] Th. Weyh and K. Schreivogel. Technische und physikalische Grundlagen. In B.-U. Meyer, editor, *Die Magnetstimulation des Nervensystems*, chapter 2, pages 27–59. Springer–Verlag, Heidelberg, Germany, 1992.

[183] E.P. Widmaier, H. Raff, and K.T. Strang. *Vander's human physiology: The mechanisms of body function*. The McGraw Hill Companys, Boston Burr Ridge, IL, 10$^{\text{th}}$ edition, 2006.

[184] David A. Winter. *Biomechanics and Motor control of Human Movement*. John Wiley & Sons, New Jersey, University of Waterloo, Canada, 3. edition, 2000.

[185] D. E. Wood, J. H. Burridge, F. M. van Wijck, C. McFadden, R. A. Hitchcock, A. D. Pandyan, A. Haugh, J. J. Salazar-Torres, and I. D. Swain. Biomechanical approaches applied to the lower und upper limb for the measurement of spasticity: A systematic review of the literature. *Disability and Rehabilitation*, 27(1-2):19–32, 2005.

[186] N. Yanagisawa and R. Tanaka. Reciprocal Ia inhibition in spastic paralysis in man. *J. of Neurophysiology*, 28:545–554, 1978.

[187] S. Zehetbauer. Entwicklung eines artefaktunterdrückenden Verstärkers zur Elektromyogrammmessung während repetitiver peripherer Magnetstimulation. Diplomarbeit, Lehrstuhl für Messsystem- und Sensortechnik (Fakultät für Elektro- und Informationstechnik, Technische Universität München), München, Germany, October 2004.

Own Publications and Supervised Student Projects

[188] B. Th. Angerer, M. Bernhardt, A. Struppler, D. Schröder, and M. Buss. Isometric muscle contraction induced by repetitive peripheral magnetic stimulation. In *Proceedings of MCBMS 2006 — 6th IFAC Symposium on Modelling and Control in Biomedical Systems, Sep. 20–22, Reims (France)*, pages 123–128, September 2006.

[189] M. Bernhardt. Entwicklung und Implementierung eines Eingabegerätes für einen Desktop-Kniesimulator. Bachelorarbeit, Lehrstuhl für Steuerungs- und Regelungstechnik, Technische Universität München, June 2002.

[190] M. Bernhardt, B. Th. Angerer, M. Buss, and A. Struppler. Neural observer based spasticity quantification during therapeutic muscle stimulation. In *Proceedings of the 28th Annual International Conference of the IEEE Engineering in Medicine and Biology Society in New York, August 30th to September 3rd, 2006*, pages 4897 – 4900. IEEE EMBS, September 2006.

[191] M. Bernhardt, B. Th. Angerer, M. Buss, and A. Struppler. Isometric muscle contraction induced by repetitive peripheral magnetic stimulation - modeling and identification. *Journal of Biomedical Signal Processing and Control*, 2(3):180–190, 2007.

[192] M. Bernhardt, B. Th. Angerer, M. Buss, and A. Struppler. Nonlinear system identification in stroke rehabilitation. *at Automatisierungstechnik*, 55(11):570–579, 2007.

[193] M. Bernhardt and D. Meissner A. Struppler M. Buss. Spastikquantifizierung während therapeutischer Muskelstimulation. *at Automatisierungstechnik*, 56(9):457–466, 2008.

[194] M. Bernhardt, M. Buss, and A. Struppler. Repetitive periphere Magnetstimulation - Eine neue Methode zur Rehabilitation zentraler Lähmungen. In *Konferenzband zur Automed 2006*, pages 7–4, Frankfurt am Main, Deutschland, March 2006. Automatisierungstechnische Verfahren für die Medizin (AUTOMED) gemeinsam mit VDI/VDE GMA.

[195] M. Bernhardt, M. Frey, M. Anderschitz, G. Colombo, and R. Riener. Der virtuelle Therapeut: Kraftuntersstützende Regelungsstrategien für eine aktuierte Gangorthese. In *Konferenzband zur Jahrestagung der Deutschen Gesellschaft für biomedizinische Technik, Ilmenau, Deutschland*, pages 194 – 195, Septmber 2004.

[196] M. Bernhardt, M. Frey, G. Colombo, and R. Riener. Hybrid force-position control yields cooperative behaviour of the rehabilitation robot LOKOMAT. In *Proceedings of the IEEE International Conference of the IEEE on Rehabilitation Robotics, ICORR, Chicago, USA*, pages 536 – 539, 2005.

[197] M. Bernhardt, M. Frey, and R. Riener. Der Joy(n)tstick: Ein neuartiges Kraft-Momenten-Eingabegerät für einen Desktop-Kniesimulator. In *Konferenzband zur Jahrestagung der Deutschen Gesellschaft für biomedizinische Technik, Salzburg, Österreich*, Septmber 2003.

[198] M. Bernhardt, S. Kibler, and M. Buss A. Struppler. Spastikquantifizierung während therapeutischer Muskelstimulation. In *Tagungsband Automatisierungstechnische Verfahren für die Medizin 2007*, pages 3–4, Düsseldorf, Deutschland, 2007. VDI Verlag GmbH.

[199] M. Bernhardt, P. Lutz, M. Frey, N. Laubacher, G. Colombo, and R. Riener. Physiological treadmill training with the 8-DOF rehabilitation robot LOKOMAT. In *Konferenzband zur Jahrestagung der Deutschen Gesellschaft für biomedizinische Technik, Nürnberg, Deutschland*, Septmber 2005.

[200] M. Bernhardt, H. Vallery, H. van der Kooji, M. Buss, and A. Struppler. Improvement and assessment of motor rehabilitation with control engineering methods. In *In Proceedings of the 2. International Congress on Domotics, Robotics and Remote-Assistance for All, DRT4all, Madrid, Spain*, pages 205–216, 2007.

[201] B. Buchholz. Identifikation von Museklermüdung während repetitiver peripherer Magnetstimuation. Bachelorarbeit, Lehrstuhl für Steuerungs- und Regelungstechnik, Technische Universität München, September 2008.

[202] C. Buchkremer. Induktion alternierender Zeigefingerbewegungen mittels repetitiver peripherer Magnetstimlation. Diplomarbeit, Lehrstuhl für Steuerungs- und Regelungstechnik, Technische Universität München, November 2006.

[203] T. Ch. Chang, P. Jaroonsiriphan, M. Bernhardt, and Paul Ludden. Web-based command shaping of cobra 600 robot with a swinging load. *IEEE Transactions on Industrial Informatics*, 2(1):59–70, 2006.

[204] D. Dumke, B. Schmitz, and Q. Huang. Entwicklung einer animierten 3D-Darstellung der menschlichen Hand für Biofeedbackanwendungen in der Rehabilitation von Schlaganfallpatienten. Projektpraktikum, Lehrstuhl für Steuerungs- und Regelungstechnik, Technische Universität München, Januar 2006.

[205] M. Eibl. Implementierung eines automatisierten Ashworth-Tests. Bachelorarbeit, Lehrstuhl für Steuerungs- und Regelungstechnik, Technische Universität München, Dezember 2007.

[206] M. Frey, M. Bernhardt, G. Colombo, and R. Riener. Kooperative Regelungsstrategien in der Gangrehabilitation. In *Konferenzband zur Automedtagung, Saarbrücken, Deutschland*, Oktober 2004.

[207] D. Gurdan. Erkennung von Bewegungsintentionen aus EMG-Signalen für Biofeedbackanwendungen in der Rehabilitation von Schlaganfallpatienten. Hauptseminar, Lehrstuhl für Steuerungs- und Regelungstechnik, Technische Universität München, Januar 2006.

[208] Y. Ji. Einsatz eines Störgrößenbeobachters zur Erkennung von Willküraktivität während therapeutischer Muskelstimulation. Hauptseminar, Lehrstuhl für Steuerungs- und Regelungstechnik, Technische Universität München, Juli 2006.

[209] S. Kibler. Modellierung und Identifikation der passiven Gelenkeigenschaften des Zeigefingers. Bachelorarbeit, Lehrstuhl für Steuerungs- und Regelungstechnik, Technische Universität München, März 2007.

[210] A. Lindner. EMG-basierte Schätzung von willkürlicher Muskelaktivität während repetitiver peripherer Magnetstimulation. Diplomarbeit, Lehrstuhl für Steuerungs- und Regelungstechnik, Technische Universität München, September 2008.

[211] D. Meissner. Identifikation nichtlinearer Gelenkeigenschaften mit quasi-online Verfahren. Bachelorarbeit, Lehrstuhl für Steuerungs- und Regelungstechnik, Technische Universität München, Dezember 2007.

[212] N. Neusser. Entwicklung und Implementierung einer geregelten Fingerstreckung mittels repetitiver peripherer Magnetstimulation. Diplomarbeit, Lehrstuhl für Steuerungs- und Regelungstechnik, Technische Universität München, Mai 2006.

[213] A.-S. Seeger, B. Angerer, M. Bernhardt, and A. Struppler. Facilitation of goal directed motor tasks and position sense by repetitive peripheral magnetic stimulation (RPMS). Lübeck, March 2006. Symposium on Cortical control of higher motor cognition.

[214] T. Spittler. Entwicklung einer Messapparatur zur automatisierten Bestimmung des passiven Gelenkmomentes des Zeigefingers. Bachelorarbeit, Lehrstuhl für Steuerungs- und Regelungstechnik, Technische Universität München, June 2006.

[215] A. Struppler, F. Binkofski, B. Angerer, M. Bernhardt, A. Drzezga S. Spiegel, and P. Bartenstein. A fronto-parietal network is mediating improvement of motor function related to repetitive peripheral magnetic stimulation: A PET–H_2O^{15} study. *NeuroImage*, 36(suppl.):174–186, 2007.

[216] J. v. Zitzewitz. Entwicklung und Implementierung patientenkooperativer Regelungen für die robotergestützte Gangtherapie. Diplomarbeit, Institut für Automatik, Eidgenössiche Technische Hochschule Zürich.

[217] J. v. Zitzewitz, M. Bernhardt, and R. Riener. A novel method for automatic treadmill speed adaptation. *IEEE Transactions on Neural Systems and Rehabilitation Engineering*, 15(3):401–410, 2007.

[218] H. Vallery, M. Buss, M. Bernhardt, and T. Pröll. Control applications in rehabilitation and medical education. In *Proceedings of the 1st International Congress on Domotics, Robotics and Remote-Assistance for All, DRT4all, Madrid, Spain*, pages 171–188, 2005.